University of Southampton Research Repository

Copyright © and Moral Rights for this thesis and, where applicable, any accompanying data are retained by the author and/or other copyright owners. A copy can be downloaded for personal non-commercial research or study, without prior permission or charge. This thesis and the accompanying data cannot be reproduced or quoted extensively from without first obtaining permission in writing from the copyright holder/s. The content of the thesis and accompanying research data (where applicable) must not be changed in any way or sold commercially in any format or medium without the formal permission of the copyright holder/s.

When referring to this thesis and any accompanying data, full bibliographic details must be given, e.g.

Thesis: Author (Year of Submission) "Full thesis title", University of Southampton, name of the University Faculty or School or Department, PhD Thesis, pagination.

Data: Author (2018) Title. URI [dataset]

UNIVERSITY OF SOUTHAMPTON

FACULTY OF ENGINEERING AND PHYSICAL SCIENCES

SCHOOL OF CHEMISTRY

Applications of Microelectrodes and Scanning Electrochemical Microscopy (SECM) to Complex Environmental Interfaces

by

Ana Cristina Perdomo Marin

Thesis for the degree of Doctor of Philosophy

September 2018

UNIVERSITY OF SOUTHAMPTON

ABSTRACT

FACULTY OF ENGINEERING AND PHYSICAL SCIENCES

School of Chemistry

Thesis for the degree of Doctor of Philosophy

Applications of Microelectrodes and Scanning Electrochemical Microscopy (SECM) to Complex Environmental Interfaces

By Ana Cristina Perdomo Marin

During this research, microelectrodes were employed as sensors and scanning electrochemical microscopy (SECM) probes to further understand two complex environmental interfaces: the sea surface microlayer (SML), and the iron-groundwater interface at permeable reactive barriers (PRBs).

The water-air and water-SML interfaces were investigated through the oxidation current of a model redox pair at a Pt submarine microdisc. Chronoamperometry and cyclic voltammetry allowed us to determine the concentration and diffusion coefficients of the redox species at different tip-substrate distances with respect to each interface. The approach curves recorded revealed information regarding the stability of the water-air interface over time and its susceptibility to the acquisition mode, size of the meniscus and the ratio of glass/microwire of the tip (RG).

The iron-groundwater interface was investigated in terms of the corrosion activity and ReO_4^- uptake from groundwater of iron from different sources and particle sizes. The relationship between the corrosion of iron and the uptake of ReO_4^- was investigated using supplementary techniques like laser ablation inductively coupled plasma mass spectrometry (ICP-MS), scanning electron microscopy (SEM) and energy dispersive spectroscopy (EDX). The results obtained represented a basis to understand the TcO_4^- uptake from groundwater at PRBs.

Contents

List of Figures

List of Tables

Academic Thesis: Declaration of Authorship

I, Ana Cristina Perdomo Marin, declare that this thesis and the work presented in it are my own and has been generated by me as the result of my own original research.

Applications of Microelectrodes and Scanning Electrochemical Microscopy (SECM) to Complex Environmental Interfaces

I confirm that:

1. This work was done wholly or mainly while in candidature for a research degree at this University;

2. Where any part of this thesis has previously been submitted for a degree or any other qualification at this University or any other institution, this has been clearly stated;

3. Where I have consulted the published work of others, this is always clearly attributed;

4. Where I have quoted from the work of others, the source is always given. With the exception of such quotations, this thesis is entirely my own work;

5. I have acknowledged all main sources of help;

6. Where the thesis is based on work done by myself jointly with others, I have made clear exactly what was done by others and what I have contributed myself;

7. None of this work has been published before submission

Signed:

Date:

Acknowledgements

To CONACyT, the School of Chemistry of the University of Southampton, and GAU Radioanalytical for funding this project.

To my supervisor Dr. Guy Denuault, for his guidance and support through my MSc and PhD.

To Prof. Phil Warwick and Prof. Ian Croudance, for laying the foundations of this research.

To Dr. Peter Birkin, for his advice and interest in the project.

To present and past members of the Denuault group, and my project students Zsofia, Peter, George and Felix for sharing with me this research project.

To my family and friends, for being with me despite the distance. And last but no least, to my half orange Michael Cousins, for his unconditional love and support.

List of Abbreviations

ASV	Anodic stripping voltammetry
ASV-LSV	Anodic stripping voltammogram using linear sweep voltammetry in the stripping step
BiFMe	Bismuth film microelectrode
CV	Cyclic voltammogram
EDX	Energy dispersive spectroscopy
FcMeOH	Ferrocene methanol
ICP-MS	Inductively coupled plasma mass spectrometry
NOC	National Oceanography Centre
LSV	Linear sweep voltammogram
OCP	Open circuit potential
PRB	Permeable reactive barrier
RG	Ratio of the radius of glass over the radius of the microwire
SCE	Saturated calomel electrode
SMSE	Saturated mercury mercurous sulfate electrode
SECM	Scanning electrochemical microscopy
SECM G/C	Scanning electrochemical microscopy generation-collection mode
SEM	Scanning electron microscopy
SML	Sea surface microlayer
ZVI	Zero valent iron

Chapter 1

Preamble

1.1 Research aim

The aim of this project was to exploit the properties of microelectrodes and scanning electrochemical microscopy (SECM) to investigate the water-air interface and the iron-groundwater interface.

The water-air interface was investigated in order to develop a methodology to study the physichochemical properties of the sea surface microlayer (SML) *in situ*. This interface has been poorly studied due to its complexity, however, it plays a key role in the regulation of exchange of matter and gasses between the sea and the atmosphere. It also controls the absorption and reflection of UV radiation, it is home of *Neuston* species, and due to its unique physichochemical properties it is capable of accumulating pollutants that travel from the atmosphere or the bulk sea water.

The SML research has been addressed using a wide range of sampling methods, however, each method collects different thicknesses of SML and the challenge still remains to obtain reproducible samples with acceptable integrity. To overcome this, we propose the use of microelectrodes, whose small size provide a steady state response. They are also able to perform in difficult conditions, like in absence of ionic conducting media.

The investigation of the iron-groundwater interface was carried out to determine the suitability of iron from different sources and particle sizes as permeable reactive barrier (PRB) material. PRBs are a technology that aims to clean contaminated groundwater *in situ* through chemical reactions at a metallic iron barrier placed underground. This is relevant because of the release of radioactive subproducts to the environment due to the use of nuclear power and weapons.

1.2 Structure of the thesis

Chapter 2 is the introduction, which explains the relevance of the two interfaces studied: the sea surface microlayer and the iron-groundwater interface.

Chapter 3 is the experimental section, in which the fabrication of the electrodes, cells and instruments technical details are described.

Chapter 4 corresponds to the investigation of the water-air and water-SML interface. The physical and chemical parameters involved in the response obtained when investigating the two interfaces are detailed in this chapter.

Chapter 5 corresponds to the investigation of the iron-groundwater interface through the SECM generation/collection mode, SEM-EDX, and laser ablation ICP-MS.

Chapter 6 provides the conclusions and future work for each of the complex interfaces.

Chapter 2

Introduction

This chapter is focused on explaining the relevance of the two complex environmental interfaces studied in this work: the sea-air interface and the iron-groundwater interface.

In section 2.1.1, the unique chemical composition and structure of the sea surface microlayer (SML) are presented. The physical processes that occur in this unique interface and its role as ecosystem are discussed in section 2.1.2 and 2.1.3. Finally, in section 2.1.4 the sampling methods and devices developed to study the SML are reviewed.

The introduction to permeable reactive barriers (PRBs) for groundwater remediation in section 2.2.1 is essential to understand the importance of investigating the iron-groundwater interface. A brief overview of the corrosion mechanisms of iron under different conditions is given in section 2.2.2. Finally, in section 2.2.3 the chemistry of perrhenate (ReO_4^-), a chemical analogue of pertechnetate (TcO_4^-), used as a model contaminant during this research is discussed.

The electrochemical techniques employed in this research are reviewed in section 2.3. The unique properties of microelectrodes that allowed us to investigate the two complex interfaces are explained in section 2.3.1. The theoretical aspects and the application of scanning electrochemical microscopy (SECM) to the study of water-air, and corrosion are discussed in section 5.2.
Finally, in section 2.3.3, the use in this project of Tafel extrapolation and OCP measurements is justified.

2.1 The sea-air interface: the sea surface microlayer (SML)

The sea surface microlayer (SML) is a thin film made of biologically produced surfactants at the sea-air interface. It is typically referred as the top millimetre of the ocean and it is described as a slick with a gel-like consistency that remains stable at the sea surface. Its unique composition makes its physical, chemical, and optical properties completely different to the underlying seawater. The chemical composition of this complex interface and the different models that have been proposed to describe its structure are discussed in section 2.1.1.

2.1.1 Chemistry of the SML

Phytoplankton exudates are the main source of natural surface active molecules at the sea-air interface. These metabolic products are mostly carbohydrates with a small contribution of proteins and lipids. Particles and breakdown products of dead plankton such as oils, fats and proteins that remain floating are an additional contribution [1]. According to Williams *et al*, the ratio of carbohydrates, proteins and lipids in the SML is 10:4:1 respectively [2]. - The dissolved polysaccharides released by phytoplankton form aggregates as they associate to hydrophobic moieties which make them surface active and force them to concentrate at the sea-surface [3]. They form microgel particles as they associate with uronic acids, leading to the aggregation of macrogels and transparent exopolymer particles (TEP) [4]. TEP are known to be sticky and potentially responsible for the enrichment of trace metals and biological species at the top millimetre of the ocean [5, 6].

The influence of exopolysaccharides polymers with sulphate content in the intrinsic viscosity [7], and the low solubility in water of sulphur-containing algal carbohydrates [8] suggests that molecules with sulphate half-ester groups allow the SML to remain stable at the sea-air surface [5].

Hardy in 1982 described the SML as "a layer of natural lipids and fatty acids overlaying a polysaccharide-protein complex" [9]. Figure 2.1 shows the schematic representation of this description. According to this, the upper layer consists of a monomolecular lipid film of 10 Å to 20 Å thick. At 1 µm of depth, there is a polysaccharide protein layer of to 100 Å to 300 Å thickness associated to a layer of abiotic particulate matter, bacterioneuston and yeasts. Deeper layers contain microalgae (phytoneuston), ciliates, copepods and other zooneuston.

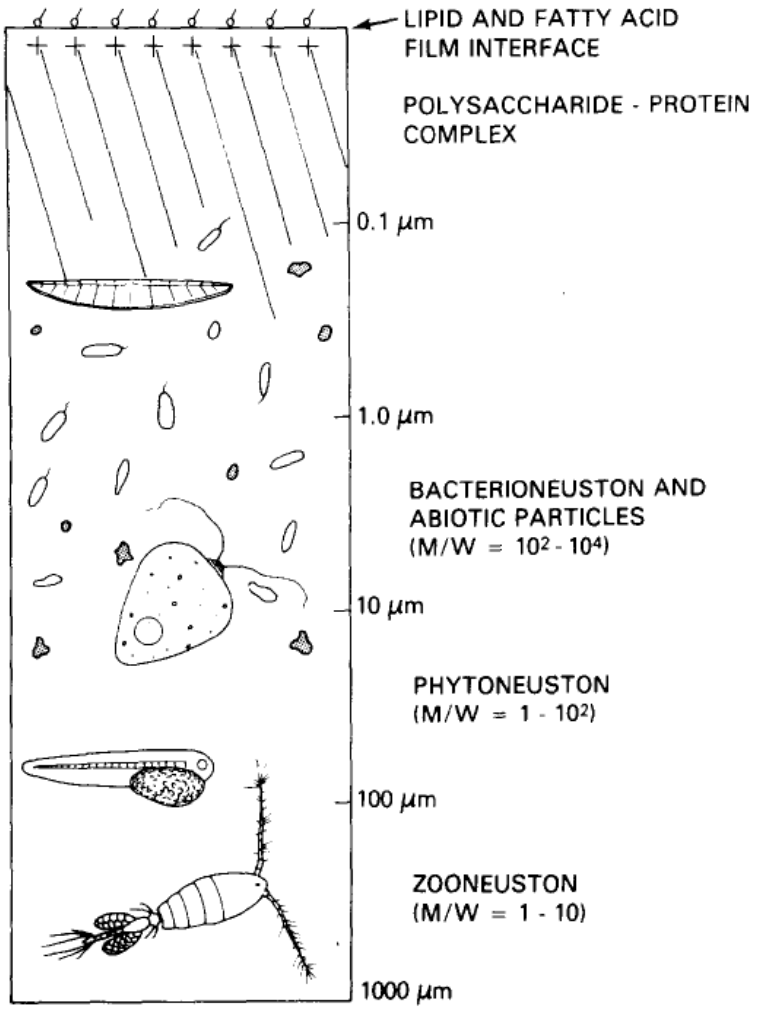

Figure 2.1: Conceptual model of the the SML. *Neuston* is the term that refers to the biological species living in the SML. M/W = typical microlayer to bulk sea water concentration ratios. Taken from [9].

Zhengbin *et al* described the SML as "the layer of sudden change of physicochemical properties with respect to sampling depth" [10]. They proposed the existence of several planes where physicochemical properties like pH, surface tension, density, and concentration of $Zn^{2+}, Cu^{2+}, Pb^{2+}$, and ammonia, change with respect to the depth. Further research led to Zhengbin *et al* in 2003 to report the thickness of the SML as $50\,\mu m \pm 10\,\mu m$ [11]. Figure 2.2 shows a scheme of their model. The properties increase from plane b_3 (bulk sea water) to b_2 (the subsurface layer) and then they reach a maximum at plane S, which represents the transitional plane between the gas and the liquid phase. The thickness of the SML is then the distance from plane S to b_1 and b_2.

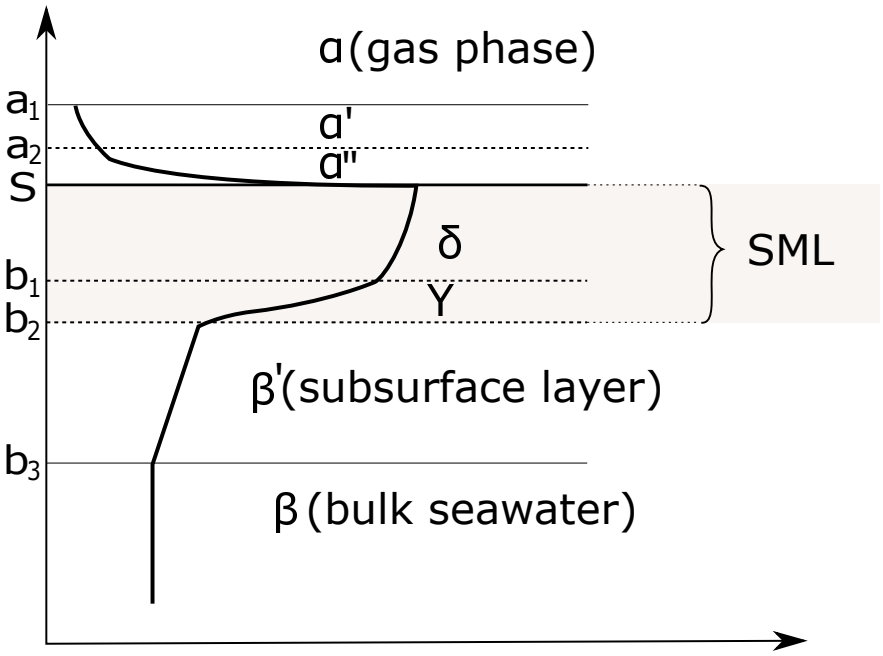

Figure 2.2: Multilayer model of the SML; β is the bulk sea water, β' is a subsurface layer. The SML is comprised by phase γ and δ. α is the gas phase, α' and α'', are gas sub-surfaces defined by planes a_1 and a_2. S is the dimensionless transitional phase; b_1, b_2 and b_3 are sub-surfaces boundaries. Adapted from [12].

The SML was described as "a highly hydrated loose gel of tangled macromolecules and colloids" [13] by Sieburth in 1983. Wurl in 2008 supported that description and proposed that the SML is "a hydrated gelatinous layer formed by a complex structure of polysaccharides, proteins and lipids". It was then depicted that the gelatinous layer is made of exopolymer particles (TEP) and breakdown products of dead plankton [3, 5, 14].

Despite the models proposed, the composition and availability of the SML changes with the season, meteorological and geographical conditions. More than a thin layer or a gel matrix, the SML is a complex interface in which the transport of gases, matter and momentum between the ocean surface and the atmosphere takes place.

The next section presents the wide range of physical processes that occur at the sea-air interface and their implications in key environmental processes.

2.1.2 Physical processes at the SML

The SML controls the sea-air gas exchange because it works as a physicochemical barrier. On either side of the sea-air interface gases pass through the "diffusive sub-layers", which are gradients of gas concentration that restrict the air–water gas exchange [15].

The gas transfer rate in air (ka) and in water (kw) are directly proportional to the gas diffusivity and inversely proportional to the diffusive sub-layer depth. kw depends on the composition and thickness of the SML and it is relevant for the transport of biogenic gases [16]. Laboratory studies have shown that kw decreases with the increasing concentration of soluble surfactants at the water-air interface [17].

The sea surface hydrodynamics is also defined by the unique SML composition [18]. The presence of surface active molecules at the sea-air interface leads to an energy barrier to the formation of robust wind wave fields [19]. In presence of SML, the formation of wind waves are subject to a critical wind speed, a threshold at which when wind speed is lower, waves do not form or grow at a small rate.

Transport of matter and gasses from the sea surface to the atmosphere can take place via the formation of wind-generated sea spray aerosols (marine aerosols), bursting bubbles, or evaporation [20]. Material from the atmosphere travels to the SML by wet or dry atmospheric deposition.

The dynamic nature of the sea surface drives the transport of matter from benthic sediments and water column to the SML by convection, diffusion, or bubbles. Bursting bubbles are responsible for the transfer of matter from the SML to the atmosphere and the transfer of matter from one region of the sea to another [21].

The mass transfer of gases at the bulk sea water is controlled by turbulence, while close to the sea-air interface molecular transport dominates."The viscous boundary layer" represents a transition layer in which molecular and turbulent transport coexist. Figure 2.3 shows a schematic representation of the mass transport mechanisms and the wide range of processes that occur at the sea-air interface.

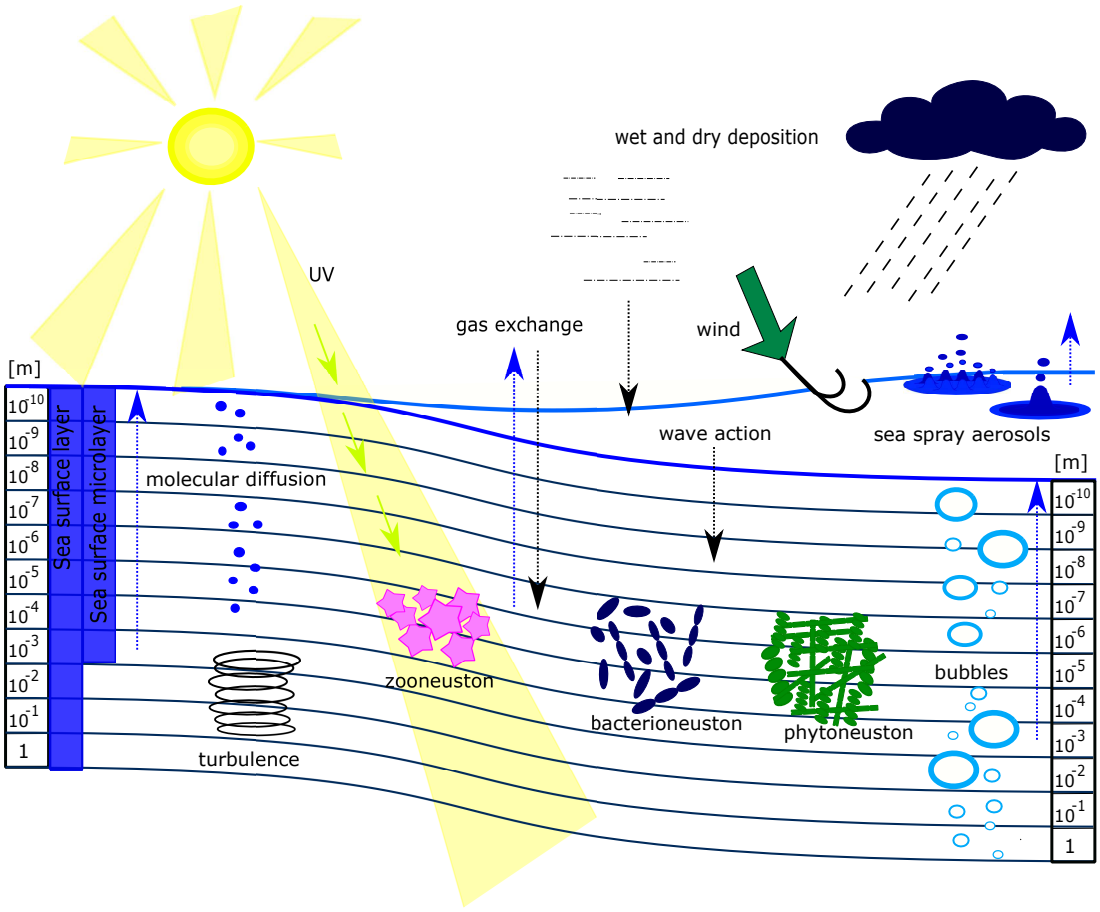

Figure 2.3: Schematic representation of the interconnections between the sea surface microlayer, the bulk sea water and the atmosphere. Adapted from [14].

The hydrophobicity of chlorinated hydrocarbons allows them to associate to the SML. Because of this, the accumulation of persistent organic pollutants (POPs), such as pesticides and polychlorinated biphenyls (PCBs), has been found to be 10 to 40 times higher in the SML than in the water column [22].

The enrichment of toxic metals at the SML has been proposed to occur by metal–ion complexation with organic ligands available at the sea surface [23]. The concentration of Pb and other toxic metals has been found to be 2 to 100 times higher in the SML than in the bulk sea water [22].

The measurement of ^{210}Po:^{210}Pb ratios in neuston species suggest that these mediate the flux of radionuclides from the bulk seawater to the sea surface [24]. Other radionuclides like Am, have been found in marine aerosols three orders of magnitude larger compared to bulk seawater concentrations [25].

The accumulation and transfer of pollutants at the SML represents a threat to the marine fauna. The importance of neuston species and the effect of specific pollutants

in their functions is discussed in the next section.

2.1.3 Biology of the SML

The sea surface allows organisms to live, reproduce and feed there [26]. It is home to neuston organisms that comprise bacterioneuston (bacteria), phytoneuston (plants), zooneuston (animals) and virioneuston (viruses).

Neuston organisms remain physically attached to the SML due to its high surface tension. Other association mechanisms involve secretion of mucilaginous extracellular buoyant material and bubble flotation [9].

Bacterioneuston are involved in the regulation of the global carbon cycle by degrading particulate organic matter (POM), including organic and anthropogenic chemicals accumulated at the SML, into dissolved organic matter (DOM) [27]. The production of DOM is relevant because it is a source of food for the marine fauna. Bacterioneuston also contribute to the sea-air gas exchange by consuming and producing traces of CO, H_2, CH_4, and N_2O [28, 29].

Photosynthetic neuston (phytoneuston) are usually found in sheltered bays and lagoons in a proportion 10-100 times higher with respect to underlying water phytoplankton [30]. Their abundance suggests that they play a key role in the conversion of atmospheric carbon into organic matter (primary production in the food chain).

It is believed that the metabolism of autotrophic and heterotrophic species of phytoneuston is responsible for the regulation of O_2 and CO_2 exchange between the sea and the atmosphere in inshore waters [31, 32].

The cyanobacteria *trichodesmium* is a common phytoneuston in tropical ocean water. It is the most important producer of organic matter from atmospheric or aqueous carbon dioxide. Also, it is responsible for the largest fraction of nitrogen fixation [26].

Neuston organisms can accumulate soluble pollutants. These, can take part in the planktonic food chain through the solubilization of airborne particles [33]. The photosynthetic carbon assimilation by the phytoneuston can decrease as a result of deposition of urban air particulate matter into the SML [34]. Compounds like polyaromatic hydrocarbons can inhibit the growth of phytoneuston [35].

It is therefore a key task to further investigate the enrichment of pollutants in the SML and its effects towards neuston species. The next section lists the common techniques to perform chemical and biological analyses of the SML; their advantages and disadvantages are discussed.

2.1.4 Techniques and methods to study the SML

The investigation of the SML has been performed using a combination of sampling methods and analytical techniques. Figure 2.4 shows a schematic representation of how membrane filters, screen samplers, glass plates and drums are used to sample the SML along with their corresponding sampling depth.

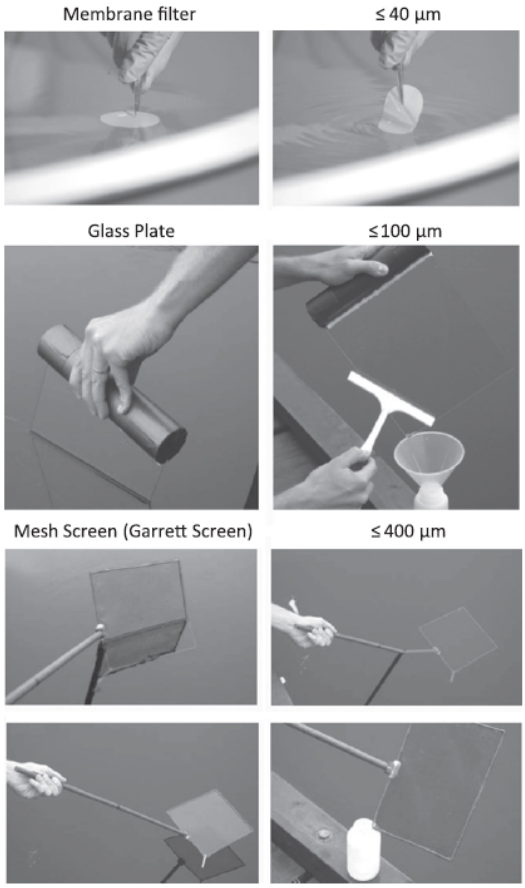

Figure 2.4: Typical SML sampling methods and their corresponding sampling depth. Taken from [6].

The membrane filters can be made of Nuclepore, polycarbonate or polytetrafluoroethylene (PTFE). They are usually dipped in the top 40 µm of the sea surface in order to get biological samples [36].

The glass plate consists of a sheet of glass that is immersed into the sea and pulled upwards at a controlled rate. The SML is removed after using a windscreen wiper blade. A similar procedure takes places when using a drum made of glass, Teflon or ceramic. It is slowly pushed forwards over the sea surface, and the SML is removed from the drum and collected continually. The sampling depths depend on the surface area of the drum, the number of rotations and the volume of seawater collected [37].

The screen samplers consist in a wire or plastic mesh that retains the surface layer within the mesh gaps by surface tension. They are usually employed in chemical analysis and the sampling depth is determined by the void area and the total volume of water collected.

The chemical or biological enrichment of samples collected by screen, plate and drum samplers is assessed by calculating the enrichment factor (EF). Equation 2.1 shows the definition of EF:

$$EF = [X]_\mu / [X]_b \tag{2.1}$$

Where $[X]_\mu$ is the concentration in the microlayer of a species X, and $[X]_b$ is the concentration of X in the bulk (usually collected 10-20 cm below the surface).
EF values larger than 1 indicate enrichment in the microlayer, and less than 1 indicate depletion.

The sample thickness of each sampling method is different, therefore the results of chemical or biological analysis cannot be directly compared. The calculation of the surface excess concentration (SE) allows to compare results between different sampler thickness. Equation 2.2 is used to calculate total excess concentration through a cross-section of the surface; however, this equation only allows comparisons between the screen and plate samplers, and the plate and rotating drum [26].

$$SE = ([X]_\mu - [X]_b) * d \tag{2.2}$$

Where $[X]_\mu$ is the concentration in the microlayer of a species X, $[X]_b$ is the concentration of X in the bulk and d is the sample thickness.

In order to address this issue, the sea surface autonomous modular unit (SESAMO) was designed to take samples with a controlled depth. Its main components are shown in Figure 2.5.

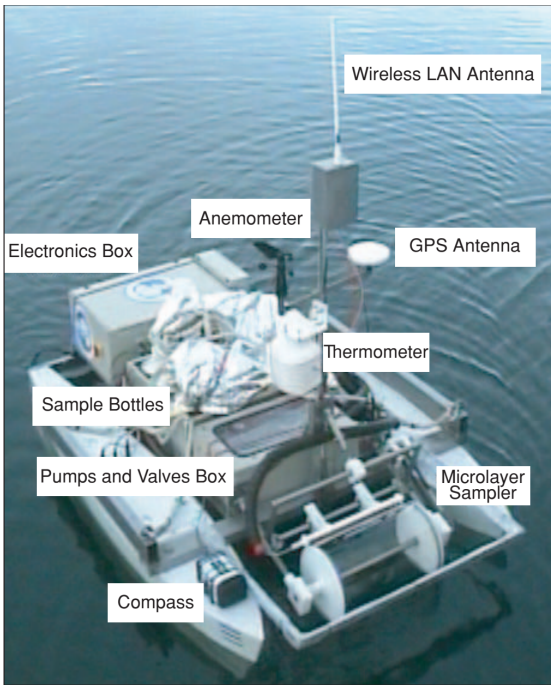

Figure 2.5: The components of the sea surface autonomous modular unit (SESAMO) platform. Taken from [38].

The geochemical fractionation of phosphorous and the transfer and enrichment of marine aerosols with radionuclides have been studied with devices like the bubble interfacial microlayer sampler (BIMS) and the Harwell bubble burst aerosol sampler [39, 40]. The collection apparatus of these samplers is also carried between the hulls of a catamaran. They produce bubbles from 200 to 1000 µm of diameter that after bursting are collected onto a Whatman 541 filter. The basic components of the Harwell bubble burst aerosol sampler are shown in Figure 2.6.

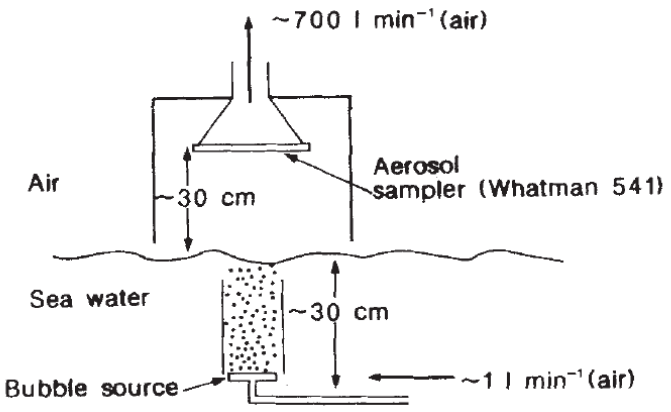

Figure 2.6: Schematic representation of the main components of the Harwell bubble burst aerosol sampler. Taken from [40].

Other sampling techniques have been developed; however, the collection of samples with acceptable integrity remains a challenge [22, 41].

The need for more devices to perform measurements *in situ* inspired this research project. The use of microelectrodes to do this was the main premise of this research. The results shown in chapter 4 will discuss the performance of microelectrodes to probe model water-air and water-SML interfaces.

The next section will focus on explaining the relevance of iron-groundwater interface, the second complex environmental interface that was investigated during this research.

2.2 The iron-groundwater interface

The increasing use of nuclear power and weapons has led to the release of radioactive subproducts of the induced fission of 235 U to the environment. Of interest to this research is 99 Tc, which is a pure β-emitter element with a half life of 2.11×10^5 years [42]. Removing 99 Tc from nuclear waste streams is a challenging task due to its long lifetime, toxicity, and high mobility in the environment as pertechnetate ion (TcO_4^-). Disposing of 99 Tc is historically the main weakness of nuclear power stations. The Sellafield plant in the UK releases 90 TBq of 99Tc (10% of produced 99Tc) into the Irish sea annually despite pre-treatment [43].
The technologies to remove contaminants from groundwater are discussed in section 2.2.1 making special emphasis on permeable reactive barriers (PRBs).

2.2.1 Permeable reactive barriers for the remediation of groundwater

The removal of radionuclides from groundwater has been addressed using the "pump and treat" method that involves pumping water from the subsurface to an above-ground treatment system [44]. Uptake by anion exchange resins, or iron sulfide adsorbents, and coprecipitation by ferrous sulfate or sodium hydroxide are some of the procedures followed to remove pertechnetate from groundwater [43, 45]. However, these leave secondary products like Na^+, SO_4^{2-} in the treated water [46].

Permeable reactive barriers (PRBs) are an emerging technology in which contaminants in groundwater can be removed by diverse *in situ* chemical reactions. Figure 2.7 shows a schematic representation of a functioning PRB. In these, a semipermeable material is placed in a trench at the flow path of underground water. As the water passes through it, contaminants are converted into a non-toxic or immobile species [47].

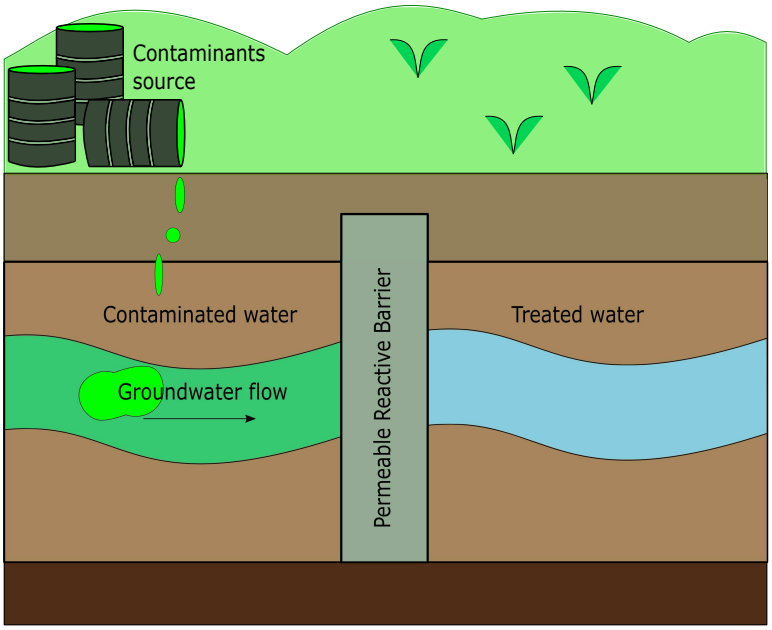

Figure 2.7: Schematic representation of a functioning permeable reactive barrier (PRB).

A PRB can be made with zeolites, oxides and zero valent metals, in particular zero valent iron (ZVI) [48]. Iron as Fe^0 and Fe^{2+} is capable of reducing redox active contaminants and chlorinated hydrocarbons from aqueous media [49–52].
Research has focused on developing iron nanoparticles and modified iron particles in order to improve the performance of iron as base material [53–56]. Making smaller iron particles increases the reactive surface area; however, iron nanoparticules smaller than 20 nm are too reactive to be used in this technology [54].
The reduction of metallic species at ZVI barriers obeys the thermodynamic predictions for any redox reaction in aqueous media, and the efficiency depends on the pH of the media and dissolved species; e.g. dichromates are reduced at pH lower than 10 and at low concentrations of dissolved oxygen [52].

The performance of iron as permeable reactive barrier is dependent on the wide range of reactions occurring at the iron-groundwater interface. These are discussed in section 2.2.2.

2.2.2 Reactions at the iron-groundwater interface

The corrosion of iron at a PRB is expected to occur according to the equation 2.3 in absence of dissolved oxygen:

$$Fe^0 + 2\,H_2O \longrightarrow Fe^{2+} + H_2 + 2\,OH^- \tag{2.3}$$

The main products consist of H_2 and OH^- ions. The formation of the later increases the local pH and leads to the formation of ferrous (oxo)hydroxides as shown in equation 2.4:

$$Fe^{2+} + 2\,OH^- \longrightarrow Fe(OH)_{2(s)} \tag{2.4}$$

The anaerobic oxidation of Fe^0 can also occur through the reduction of nitrate to ammonia or nitrogen [57], or by the biologically mediated reduction of sulfate to sulfide [58].

In presence of dissolved O_2 the oxidation of Fe^0 leads to the production of the ferrous and ferric ion, and a higher concentration of OH^- as follows:

$$2\,Fe^0 + O_2 + 2\,H_2O \longrightarrow 2\,Fe^{2+} + 4\,OH^- \tag{2.5}$$

$$4\,Fe^{2+} + 4\,H^+ + O_2 \longrightarrow 4\,Fe^{3+} + 2\,H_2O \tag{2.6}$$

$$Fe^{3+} + 3\,OH^- \longrightarrow Fe(OH)_{3(s)} \tag{2.7}$$

In the field, $Fe(OH)_2$ has been identified as the main corrosion product [59]. It can be further oxidise to magnetite or green rusts [60, 61]. The later are transient intermediates between $Fe(OH)_2$ and the ferric oxohydroxides goethite (α-FeO(OH)) and lepidocrocite (γ-FeO(OH)) [62]. Green rusts are believed to be the main reducing agent of heavy metals and radionuclides at the iron-groundwater interface [61, 63].

Other precipitates can cover the iron-groundwater interface and affect the reactivity of the PRB according to the composition of the groundwater. Carbonates and iron hydroxides have been reported to passivate the iron surface and decrease the long term performance of the PRB [64, 65].

On the other hand, laboratory experiments have shown that microbial-Fe^0 interactions enhance the efficiency of a PRB [66, 67]. In this case, hydrogen is an electron donor that promotes the biotransformation of reducible contaminants, such as chlorinated solvents and hexavalent chromium [68].

The reactions at the iron-groundwater interface that remove contaminants depend on the chemical nature of the contaminant and the composition of the groundwater. Chlorinated organics are removed via the coupling of the oxidation of Fe^0 with the reductive dechlorination of the organic, R-Cl [69]. Heavy metals and radionuclides are immobilised by a precipitation reaction at the iron-groundwater interface [70].

Equation 2.8 shows the chemical equation for the immobilization of the pertechnetate ion. This is proposed to occur by the reduction of Tc(VII) to Tc (IV), that translates into the precipitation of the TcO_4^- ion as TcO_2 at the PRB.

$$TcO_4^- + 4\,H^+ + 3\,e^- \longrightarrow TcO_2 + 2\,H_2O \tag{2.8}$$

In comparison to organic contaminants, which can be broken down to CO_2 and H_2O, heavy metals and radionuclides remain at the iron-groundwater interface and it is not possible to recover or further degrade them. Also, laboratory experiments suggest that the immobilised contaminants are likely to become soluble after a period of time according to geochemical conditions [54, 71].
In this research, the uptake of the TcO_4^- ion by iron from different sources and particle sizes was investigated using ReO_4^- as chemical analogue.
The next section will discuss the similarities between Tc and Re, including their redox chemistry in solution and the reduction mechanisms in different metallic interfaces.

2.2.3 Use of Re as Tc chemical analogue

The TcO_4^- ion uptake has being studied using ReO_4^- as chemical analogue [72–74]. This is possible because the chemistries of Tc and Re is very similar. The main difference between them is that Tc is a β-emiter and Re is not. Both have seven electrons occupying the outer orbitals, which allow them to acquire valence states between 0 and +7, however the most common oxidation state in solution and solid state for Tc and Re species is +7 followed by +4. The predominant forms of Tc and Re in aqueous solution are the pertechnetate (TcO_4^-) and perrhenate anions (ReO_4^-) [75].
The predominance of the Re species in aqueous solution as a function of the potential and pH is shown in the Pourbaix diagram in Figure 2.8. This shows that Re(IV) (ReO_4^-) is the most stable form of Re in presence of dissolved oxygen (at higher potentials than the oxidation of H_2O). In absence of oxygen, Re(III) is stable as Re_2O_3 according to thermodynamic data from Zouboz and Pourbaix (solid lines in Figure 2.8). However, data from Bard *et al* (dotted lines in Figure 2.8) suggest that the stable species in anoxic conditions is ReO_2 [76].

Kim *et al* proposed that Re(IV) is stable as $ReO(OH)_3^-$ in alkaline anoxic media, which is a similar environment to that at a PRB. On the other hand, they suggest that Re(III) can exist in the form of Re_2O_3 in absence of oxygen as a metastable species for being in equilibrium with dissolved Re(IV) in concentrations up to $10\,\mu mol\,L^{-1}$. This led them to propose that Tc(VII) could be reduced to either Tc(IV) or Tc(III) in

absence of dissolved oxygen or at concentrations in the range found at PRBs [76].

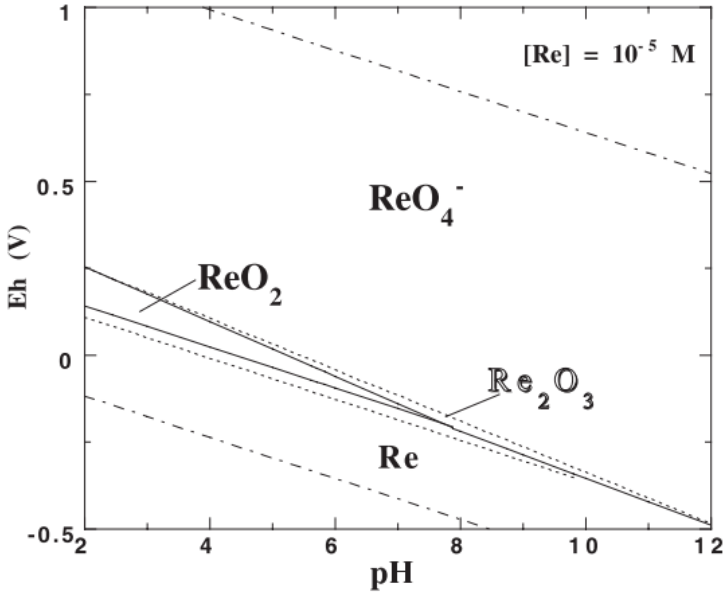

Figure 2.8: Re Pourbaix diagram. Total dissolved concentration of Re=1×10^{-5} M. The limits of stability of water are marked by the two dash-dotted lines. Thermodynamic data from Zouboz and Pourbaix (solid lines), data from Bard *et al* (dotted lines). Re_2O_3 is shown in a blackboard bold to highlight its metastable character. Taken from [76].

The reduction of ReO_4^- on different materials depends on their capacity of adsorbing H. With materials that are capable of adsorbing H atom ReO_4^- reduces to ReO_2, but with materials that are not capable of adsorbing H atom ReO_4^- reduces to Re. The adsorbed H atom works as a reducing agent and when a surface is not capable of adsorbing H, H_2 acts as a reducing agent [77].

On Pt, the formation of ReO_2 involves the participation of H adatoms (Had). These are electrochemically formed on the electrode surface and subsequently they reduce the ReO_4^- ions through a chemical reaction [78].

On Au, an initial formation of H_2 followed by metallic Re electrodeposition takes place. There is a competitive deposition on Au between ReO_2 and Re, the extent of each process depending upon the potential and the time of adsorption [78].

The reduction of ReO_4^- on iron nanoparticles has been reported to proceed according to the following equation:

$$ReO_4^- + 4\,H^+ + Fe^0 \longrightarrow ReO_2 + 2\,H_2O + Fe^{3+} \tag{2.9}$$

Having as major products ReO_2 and Fe^{3+} [74]. Lenell *et al* agreed with this,

and also found that the adsorption of ReO_2 on iron is pH and nitrate concentration dependent [73].

2.3 Electrochemical techniques

This section shows the theory behind the electrochemical techniques employed during this research. In section 2.3.1 the unique properties of microelectrodes that allowed us to investigate the water-air, water-SML and iron-groundwater interfaces are discussed. The principles of scanning electrochemical microscopy (SECM), the operation modes employed during this project and its applications to the investigation of the water-air interface and corrosion research are explained in section 2.3.2. Finally, the electrochemical techniques employed in corrosion research are described in section 2.3.3.

2.3.1 Microelectrodes

A microelectrode is defined as "an electrode with at least one dimension small enough that its properties are a function of its size" [79, 80]. In practice, an electrode with a critical dimension smaller than 50 µm is considered a microelectrode.

Microelectrodes with different geometries can be fabricated; however, during this project only microdiscs were employed. In a microdisc electrode, the critical dimension is the radius (a), which is given by the microwire size employed in the fabrication of the electrode. Figure 2.9 shows the basic components of one of the Pt discs employed in this research. The details of the fabrication are shown in chapter 3, section 3.3.

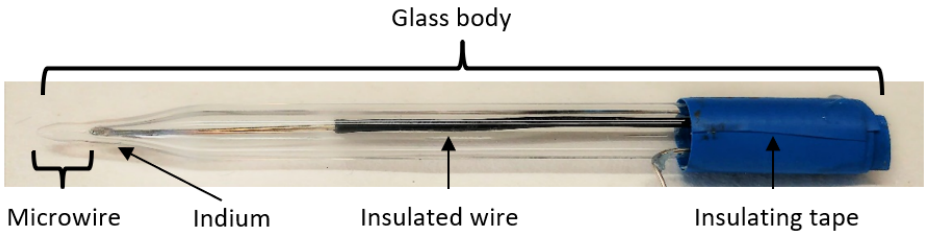

Figure 2.9: Micrograph showing the main components of a Pt disc electrode employed during this research.

The small electroactive area of a microelectrode provides several advantages when performing amperometric measurements, like decrease of the capacitive charging currents and lowering of the ohmic drop effects even in absence of ionic conducting media. Highly relevant to our research is the fact that microelectrodes provide steady state voltammetry. To highlight the unique behaviour of microelectrodes compare their

response to that at an electrode with a critical dimension larger than 50 µm (macroelectrode) after a potential step experiment.

At short times the diffusion layer thickness at the macroelectrode changes according to $\sqrt{\pi Dt}$. As the time of the experiment increases, the diffusion layer thickness expands further to the solution. This causes the concentration gradient at the electrode surface to decrease, along with it the current measured.

At a microelectrode, the diffusion layer thickness at short times also grows according to $\sqrt{\pi Dt}$. However, as the experiment progresses, the diffusion layer thickness grows until it is considerably larger than the electrode radius. At intermediate times a quasi-hemispherical diffusion field is observed and the material travelling from the bulk experiences edge effects at the microwire-glass boundary. This translates into an increase of flux of material traveling linearly and radially to the surface of the electrode. At long times, the diffusion layer thickness evolves into an hemisphere, whose growth is limited by the size of the electrode. Therefore, at long times the diffusion layer thickness becomes independent of time, but dependent of the size of the microelectrode. This causes the concentration gradient at the electrode surface to acquire a constant value. Then, the current measured reaches the steady state.

Figure 2.10 shows a schematic representation of the dependence of the evolution of the diffusion layer thickness with time at a macroelectrode and at a microdisc electrode.

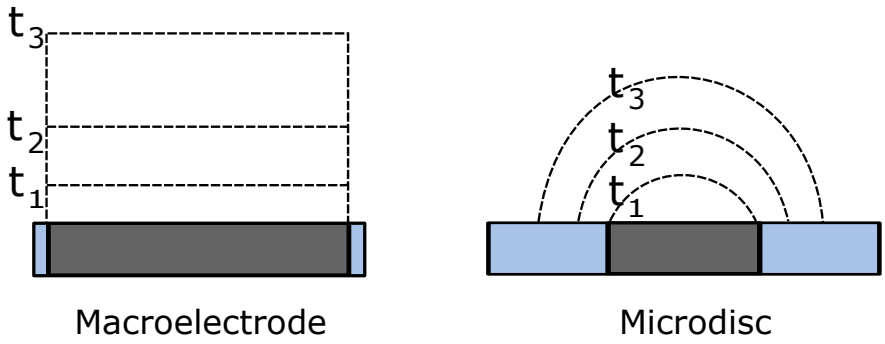

Figure 2.10: Diffusion field at a large electrode and at a microdisc electrode. t is time after the electrochemical perturbation.

At a macrodisc electrode, the current after a potential step is given by the first term of equation 2.10. However, at a microdisc electrode, the current measured is the sum of the transient current at short times and the steady state current at long times.

$$i = \frac{nFA\sqrt{DC}}{\sqrt{\pi t}} + \frac{4nFADC}{\pi a} \tag{2.10}$$

Where n is the number of electrons, F is the Faraday constant, C is the concentration of reactant, D the diffusion coefficient, A is the electrode area, and a the radius.

At long times, the contribution to the current of the first term of equation 2.10 becomes negligible and the steady state term determines the response. For a microdisc electrode of area πa^2 that term becomes equation 2.11.

$$i = 4nFDCa \tag{2.11}$$

However, equation 2.10 does not provide an accurate description of the current at intermediate times, when the contributions due to the edge effects are significant. Mahon and Oldham proposed equation 2.12, which is the most accurate mathematical model that describes the chronoamperometric response at all times for a microdisc electrode.

$$\begin{aligned} \frac{i_d(t)}{n\pi FCDa} &= \left\{ \frac{1}{\sqrt{\theta\pi}} + 1 + \sqrt{\frac{\theta}{4\pi}} - \frac{3\theta}{25} + \frac{3\sqrt{\theta^3}}{226} \right\} \\ & \qquad\qquad \theta \leq 1.281 \\ &= \left\{ \frac{4}{\pi} + \frac{8}{\sqrt{\pi^5}\theta} + \frac{25\sqrt{\theta^{-3}}}{2792} - \frac{\sqrt{\theta^{-5}}}{3880} - \frac{\sqrt{\theta^{-7}}}{4500} \right\} \\ & \qquad\qquad \theta \geq 1.281 \end{aligned} \tag{2.12}$$

Where,

$$\theta = \frac{Dt}{a^2} \tag{2.13}$$

During this research, the Mahon–Oldham equation was employed to determine the diffusion coefficient and the concentration of the redox species simultaneously through a non-linear regression. This was part of the methodology proposed to characterise the water-air and water-SML interface.

The diffusion regime at a microelectrode is a function of the experiment time scale. Linear diffusion is the mass transport regime at short times, and provides a current response similar to a macroelectrode. At intermediate times the quasi-hemispherical diffusion determines the shape of the voltammograms. An hemispherical diffusion regime is observed at long times, which gives a steady state voltammogram. Figure 2.11 shows the transition of the mass transport regimes at a microdisc electrode from planar, to quasi-hemispherical, and to hemispherical diffusion as the time of the experiment increases.

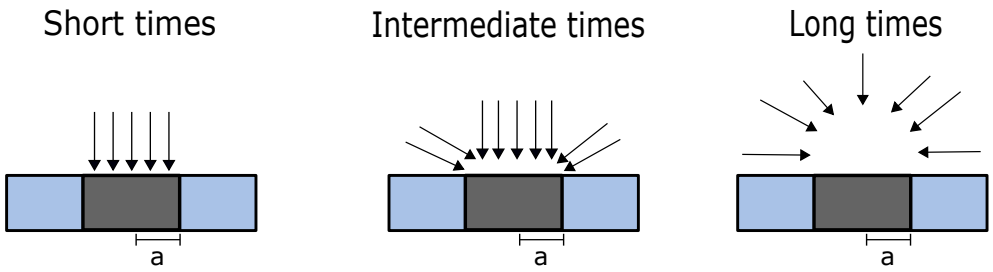

Figure 2.11: Schematic representation of the diffusion regimes at a microdisc electrode during an electrochemical experiment. Planar diffusion at short times, quasi-hemispherical diffusion at intermediate times and hemispherical diffusion at long times. a is the radius of the microdisc.

Figure 2.12 shows the amperometric response as the transition between diffusion regimes is observed at different time scales for a 25 µm Pt microdisc electrode. Cyclic voltammograms (CVs) recorded at high scan rates show the planar diffusion response. When the time scale is much larger than a^2/D, the characteristic diffusion time of the disc, hemispherical diffusion dominates and a steady state voltammogram is obtained.

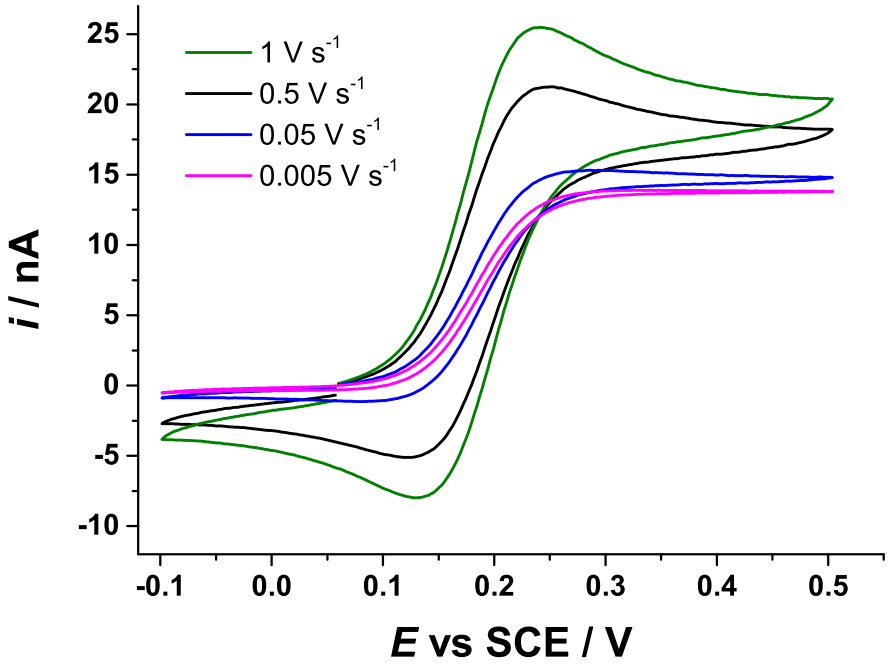

Figure 2.12: CVs recorded with a 25 µm diameter Pt disc at $0.005\,\mathrm{V\,s^{-1}}$, $0.05\,\mathrm{V\,s^{-1}}$, $0.050\,\mathrm{V\,s^{-1}}$, and $1\,\mathrm{V\,s^{-1}}$ in an aerated 4 mM ferrocyanide + 0.1 M KCl solution.

During this research, we employed linear sweep voltammetry and chronoamperom-

etry to investigate the water-air and water-SML interface. On the other hand, the iron-groundwater interface was investigated by acquiring CVs at a fixed distance from the iron surface. In order to characterise each interface, the microelectrode had to be positioned very accurately close to each interface. Because of this, scanning electrochemical microscopy was employed. The following section provides an overview of the principles of the technique and its applications to diverse interfaces.

2.3.2 Scanning electrochemical microscopy (SECM)

Scanning electrochemical microscopy (SECM) is a technique that employs a microelectrode as a probe to investigate the electrochemical properties of interfaces.

The instrumentation to perform an SECM experiment involves a micropositioner driven by piezoelectric elements that allow the movement of the microelectrode (tip) in the x, y and z directions. A potentiostat is used to control the potential of the tip and the substrate. A personal computer is needed to command the position and the speed of the tip, set the potential perturbation, and digitalise the current recorded. The principle of the technique relies on the modes of mass transport at microdisc electrodes. During an SECM experiment a steady state reaction is driven at the microdisc electrode. Assuming that hemispherical diffusion is predominant, the perturbation of the diffusion field by an interface provides a particular current response.

In the SECM feedback mode the microelectrode is moved towards a conducting, semiconducting or insulating substrate. The substrate is immersed in a solution that contains a redox species with a known concentration and whose reduction or oxidation will provide information regarding the substrate's properties. When the tip-substrate distance is larger than 10 times the radius of the electrode (a), the diffusion field is not perturbed and the current response corresponds to the steady state given by equation 2.11. The diffusion field at the microelectrode can be disturbed by a substrate once the tip-substrate distance is less than $7a$-$10a$. If the substrate is conductive, the regeneration of the redox species at the substrate's surface as the tip approaches produces an increase of current called positive feedback. Hindered diffusion is obtained when the diffusion field is blocked by an insulating substrate, which causes the steady state current to decrease. This is also known as negative feedback. In this case the ratio of glass surrounding the microwire (RG) plays an important role because a larger amount of glass around the microwire can also block the diffusion of material. Figure 2.13 shows the three modes of diffusion of material at a microdisc when performing an SECM experiment in the feedback mode.

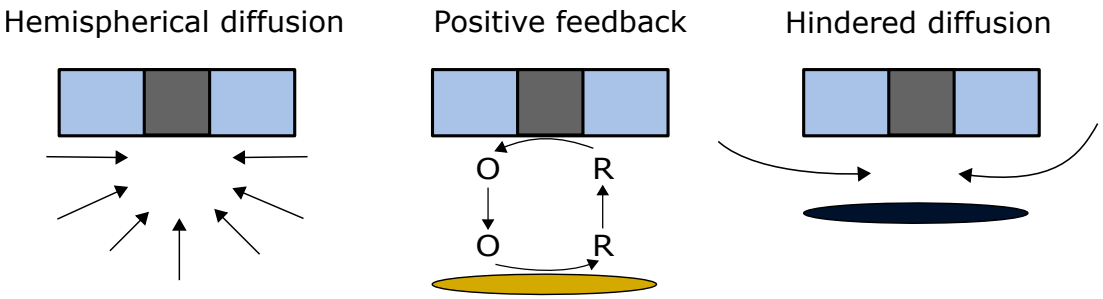

Figure 2.13: Diffusion regimes at a microdisc during an SECM experiment. Hemispherical diffusion at the bulk, positive feedback when positioned close to a conductive substrate, and hindered diffusion close to an insulating substrate. R is the reduced form of the redox species, and O the oxidized form.

The graph of the current acquired at the microelectrode as a function of the tip-substrate is known as an approach curve. Figure 2.14 shows an approach curve to a conductive and to an insulating substrate. The plot is presented in the dimensionless form I_T (the tip current divided by its value in the bulk) with respect to L (the tip substrate separation normalized by the tip radius) to show each case.

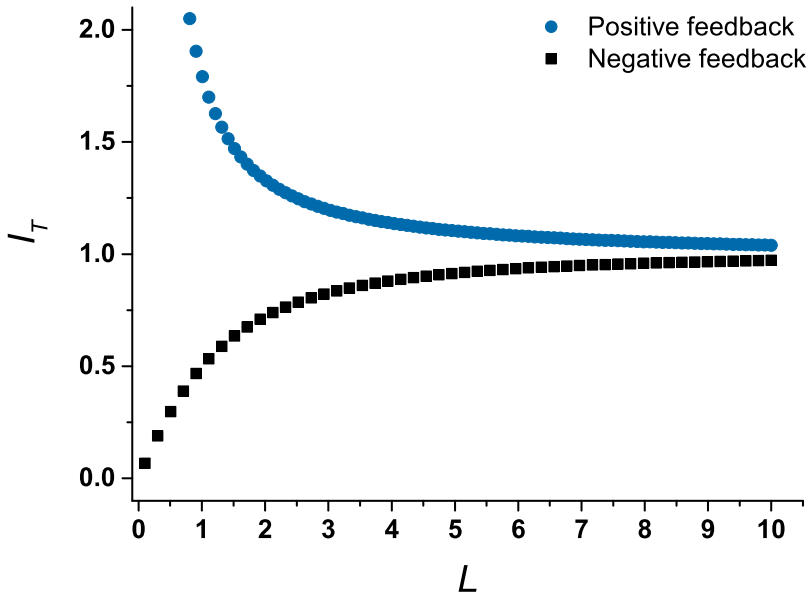

Figure 2.14: Theoretical approach curves for a redox species in solution with diffusion coefficient $1 \times 10^{-5}\,\mathrm{cm^2\,s^{-1}}$, concentration in solution $1 \times 10^{-6}\,\mathrm{mol\,cm^{-3}}$, undergoing a one electron transfer reaction at a Pt microdisc of 25 µm diameter with $RG = 10$. Generated through the function building tool in Origin lab 9.0. using equation 23 and 26 from [81].

In the SECM generation/collection mode (G/C), the collector works as an amperometric sensor that detects the electroactive species produced at the surface of the generator [82]. The typical electrochemical experiments performed at the collector are cyclic voltammetry and chronoamperometry. Figure 2.15 shows a scheme of the G/C modes when the tip and the substrate are generator or collector.

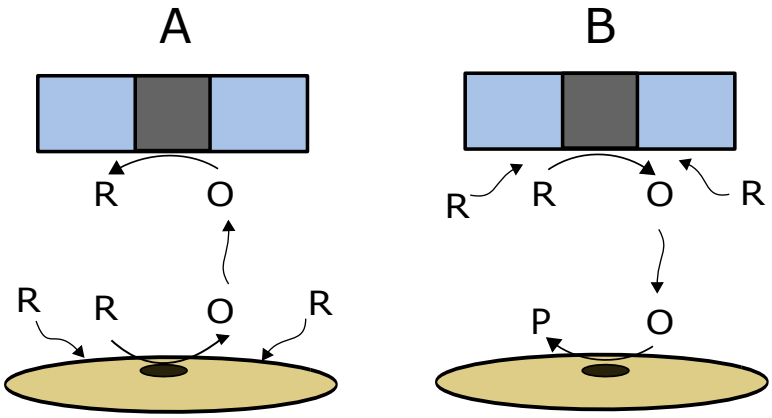

Figure 2.15: SECM substrate generation/tip collection (A) and tip generation/substrate collection (B). R is the reduced form of the redox species, and O the oxidized form. Adapted from [83].

During this research, we fabricated submarine microelectrodes that were employed as SECM probes to investigate the water-air and water-SML interface.

Submarine electrodes have been employed to measure the transfer of solutes and gases through phospholipid monolayers spread at the water-air interface using the feedback mode and the G/C mode [84–86]. The lateral H^+ diffusion in Langmuir monolayers deposited at a water-air interface have been also studied using submarine microelectrodes [87]. Other experiments used submarine microelectrodes to investigate the transport of chemical species across immiscible liquid organic/water interfaces [88].

On the other hand, the SECM G/C mode has been used to monitor localised corrosion of diverse metals [83, 89]. The corrosion of iron at the open circuit potential has been investigated under the assumption that the surface can be monitored by recording the Fe^{2+}, and the decrease of the oxygen reduction current (or protons according to pH) at a microdisc electrode [90, 91].

To investigate the iron-groundwater interface, the corrosion activity of iron from different sources and particle sizes was investigated using the SECM G/C mode. The corrosion activity of iron substrates was compared by recording CVs at different time intervals and tip-substrate distances when exposed to a fixed volume of synthetic ground-

water. These results were compared to those obtained using Tafel extrapolation and OCP measurements. The next section provides a summary of the theory behind the Tafel extrapolation and the information that can be obtained through this method.

2.3.3 Tafel extrapolation and open circuit potential (OCP) measurements

Among the classical electrochemical techniques to investigate corrosion, we find linear polarization resistance (LPR), impedance spectroscopy and Tafel extrapolation [92]. During this research we measured the open circuit potential (OCP) of iron electrodes over time, and we employed the Tafel extrapolation to obtain quantitative information of the corrosion of iron from different sources and particle sizes.

Tafel extrapolation involves the polarization of the iron surface ± 30 mV from the open circuit potential. By applying a linear perturbation and measuring the current, a plot of the *log i* vs E allows the determination of the corrosion current (rate) and corrosion potential. The relationship between the corrosion rate (i_{corr}) and corrosion potential (E_{corr}) and the net current density is analogous to the Butler-Volmer equation:

$$i = i_a + i_c = i_{corr}[e^{\frac{E-E_{corr}}{b_a}} + e^{\frac{-(E-E_{corr})}{b_c}}] \tag{2.14}$$

Where b_a (Equation 2.15), and b_c (Equation 2.16) are the Tafel slopes.

$$b_a = \frac{RT}{\alpha_a nF} \tag{2.15}$$

$$b_c = \frac{RT}{\alpha_c nF} \tag{2.16}$$

By separating 2.14 into the anodic and the cathodic semi-equations and applying base 10 logarithms equations 2.17 and 2.18 are obtained.

$$E - E_{corr} = 2.303 b_a \log i_a - 2.303 b_a \log i_{corr} \tag{2.17}$$

$$E - E_{corr} = 2.303 b_c \log(-i_c) - 2.303 b_c \log i_{corr} \tag{2.18}$$

Then, by writing the equations 2.17 and 2.18 in terms of overpotential η (equation 2.19), the Tafel equations are obtained (equations 2.20 and 2.21).

$$E - E_{corr} = \eta \tag{2.19}$$

$$\eta_a = b_a \log(\frac{i}{i_{corr}}) \tag{2.20}$$

$$\eta_c = -b_c \log(\frac{|i|}{i_{corr}}) \tag{2.21}$$

Figure 2.16 shows an example of a Tafel plot. When fitting a line to each of the cathodic and anodic current it is possible to obtain the Tafel slopes b_a and b_c. When the linear fit to the anodic and cathodic current intercepts, the log of the corrosion rate ($\log i_{corr}$) and the corrosion potential are obtained.

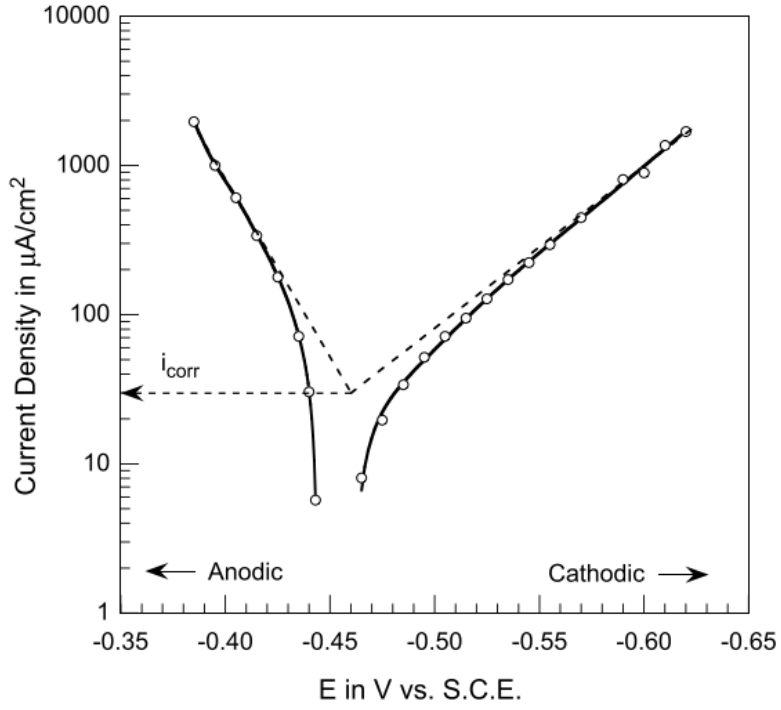

Figure 2.16: Tafel plot for iron in deaerated 1 M HCl. Taken from [93].

The measurement of the OCP is useful to identify the formation of new phases in the surface of the metal studied, assuming that the changes in potential are given by the iron going from passive to active state (Flade potential) [94].

During this research we fabricated iron electrodes to measure the corrosion rate of iron from different sources and particle sizes. Chapter 3 shows the fabrication methods for the diverse electrodes employed during this research, including iron electrodes, microelectrodes and reference electrodes.

Chapter 3

Experimental section

This chapter shows specifications of all the equipment, reagents and materials, fabrication of electrodes and substrates employed during this research.
In section 3.1 the specifications of all the equipment employed including potentiostats, optical and electron microscopes are listed.
The reagents and materials, including the details composition of the synthetic sea surface microlayer (SML) and the synthetic groundwater are shown in section 3.2.
The fabrication of all working and reference electrodes is described in section 3.3 and the fabrication of the iron substrates is shown in section 3.4.
Finally, the cells employed for the study of each complex interface are shown in section 3.5.

3.1 Equipment

A scanning electrochemical microscopy workstation, Uniscan instruments^{TM}, model 370, supported by the UiChem^{TM} software for Windows version 4.36.3928. was employed for the SECM experiments .
A Metrohm Autolab PGSTAT 101, supported by Nova 1.11, was employed for the corrosion measurements.
A Celestron Handheld Digital Microscope supported by microscope suite software was used to keep track of physical changes of the water-air interface and the iron substrates surface during the SECM experiments.
A Nikon eclipse LV100ND optical microscope was employed to obtain the optical micrographs shown in this thesis.
A FEI XL30 ESEM (Environmental Scanning Electron Microscope) with a W filament as electron source, an UltaDry EDX, 10 mm^2 detector in the low vacuum mode (wet mode) were employed to obtain the SEM images and EDX spectra.

Elemental analysis data was acquired using a New Wave NWR193 excimer laser ablation system coupled to a Thermo X-Series II quadrupole inductively coupled plasma mass spectrometry (ICP-MS).

3.2 Reagents and materials

The reagents employed during this project were used as received without further purification. Solutions were prepared using deionised water from a Purite select water purifying system (resistivity 18 MΩ cm). Table 3.1 shows a list of the chemical reagents employed in this project including their specifications.

Table 3.1: Chemical reagents and solvents employed during this project.

Name	**Formula**	**Purity %**	**Manufacturer**
Octaethyleneglycol mono n-hexadecyl ether	$C_{16}EO_8$	98.0	Aldrich
Ferrocene methanol	FcMeOH	97	Aldrich
Sodium Chloride	NaCl	99.5	Aldrich
Potassium sulphate	K_2SO_4	AR grade	Fisher scientific
Potassium chloride	KCl	AR grade	Fisher scientific
Sulphuric acid	H_2SO_4	99.999	Aldrich
Bismuth nitrate pentahydrate	$Bi(NO_3)_3 \cdot 5\,H_2O$	98	Aldrich
Lead Nitrate	$Pb(NO_3)_2$	99.999	Aldrich
Perchloric acid 70%	$HClO_4$	99.999	Aldrich
n-Heptane	C_7H_{16}	96	Aldrich
Ethanol	C_2H_6O	99.8	Aldrich

A list of the materials employed during this project including bulk metals, metal wires, polishing materials, epoxy resin kits, etc. is shown in table 3.2.

Table 3.2: Materials employed in this project.

Name	**Specifications**	**Manufacturer**
Alumina powder	5 µm,1 µm, and 0.3 µm	Buehler
Polishing pad	-	Buehler
SiC paper	grit 1200	3M
Platinum wire	25 µm, 99.9%	Goodfellow
Gold wire	500 µm 99.99%	Fisher scientific
Iron chips	98%	Aldrich
Iron powder	325 mesh, 97%	Aldrich
Conductive epoxy	Silver loaded	RS
Indium wire	0.5 mm, 99.999%	Goodfellow
Quick set epoxy resin	Tubes (2 x 16 g), cure in 5 min	RS
Standard Epoxy Adhesive	Tubes (2 x 16 g), cure in 8 hr	Alraldite
Epoxy resin set (Epofix resin)	Cure in 24 hr	Struers

Iron flakes and iron powder were provided by colleagues from the National Oceanography Centre. They obtained the iron powder from Aldrich and the iron flakes were provided by an industrial partner. We made iron of different sizes from the same source by making an iron chip from Aldrich, 98% purity into smaller pieces using an industrial drill. This yielded the large iron particles that ranged from 700 µm to 1000 µm. Medium size iron particles that ranged from 300 µm to 500 µm were obtained by filing an iron chip. Finally, the smallest size of iron particles ($\approx$ 70 µm) were obtained using a komet dental H141 104 010 by Brasseler drill tip as shown in Figure 3.1.

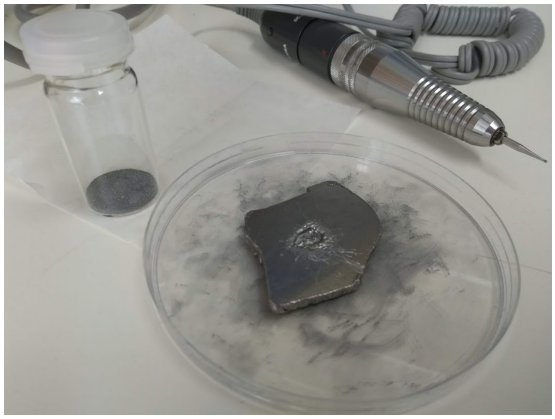

Figure 3.1: The iron chip being drilled into iron powder. The drill tip was a komet dental H141 104 010 by Brasseler drill.

3.2.1 The synthetic SML

A 30 w.t. % solution of octaethylene glycol monohexadecyl ether $C_{16}EO_8$ was used as synthetic SML in this research. These polyoxyethylene non-ionic surfactants are widely employed in Southampton University as templates to electrodeposit nanostructures [95–98]. $C_{16}EO_8$ form micelles above the critical micellar concentration (c.m.c), and liquid crystals at higher concentrations. The phase behaviour of $C_{16}EO_8$ in water is shown in Figure 3.2. According to this, our synthetic SML was in the boundary between the micellar and cubic phase.

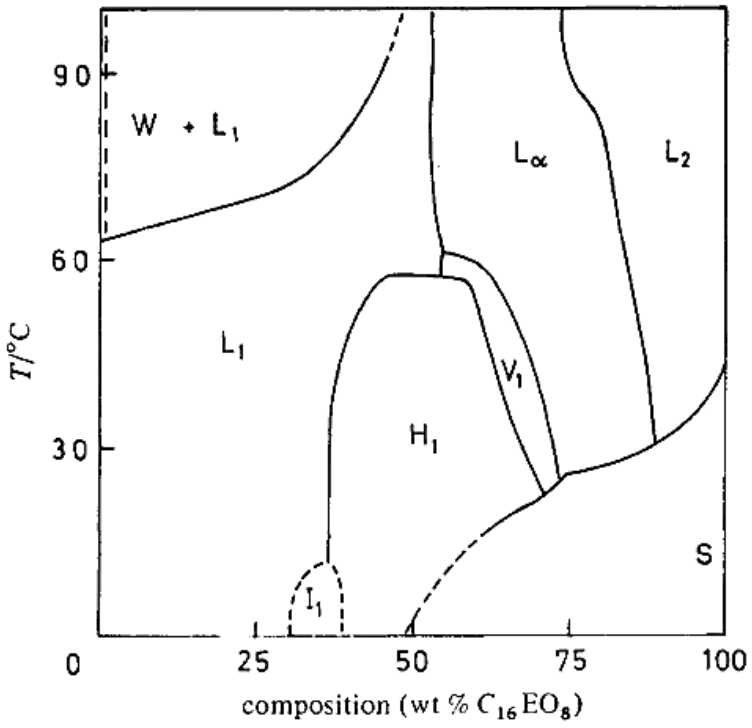

Figure 3.2: Phase diagram of $C_{16}EO_8$ water system over the temperature range 0 °C to 100 °C. L_1 corresponds to a micellar solution; L_2, to the liquid surfactant; I_1 to a cubic phase of close-packed spherical micelles; H_1, to the normal hexagonal phase; V_1, to the normal bicontinuous cubic phase and L_α to the lamellar phase. The presence of solid is indicated by S, and W is a phase that remains in equilibrium with the micellar solution below the cloud point (temperature where the surfactant is not soluble and starts precipitating). Taken from [99].

3.2.2 The synthetic groundwater

The composition of the synthetic groundwater, provided by researchers of the National Oceanography Centre contained Na^+ 25 mg L^{-1}, K^+ 5 mg L^{-1}, Ca^{2+}, 36 mg L^{-1}, Mg^{2+} 5 mg L^{-1}, HCO_3^- 49 mg L^{-1}, NO_3^- 18 mg L^{-1}, Cl^- 70 mg L^{-1}, SO_4^{2-} 19 mg L^{-1}. Table 3.3 shows the mass per litre of solution of each compound employed.

Table 3.3: Compounds employed in the preparation of 1 L of synthetic groundwater

Compound formula	**Mass / g**
$NaHCO_3$	0.0672
$NaNO_3$	0.0128
NaCl	0.0088
KNO_3	0.0138
$CaCl_2 \cdot 2\,H_2O$	0.1005
$MgSO_4 \cdot 7\,H_2O$	0.0493

3.3 Electrodes fabrication

3.3.1 Platinum microdiscs

The fabrication of all working electrodes, including Pt 50 µm and 25 µm diameter, and Au 250 µm diameter was carried out as described here.

A scheme of the procedure followed is shown in Figure 3.3. First, the metallic wire was inserted into a glass body and the end was sealed using a butane torch (A and B in Figure 3.3). Borosilicate glass capillaries of 2 mm diameter were used as glass bodies for the fabrication of the submarine microelectrodes. For the rest of the working electrodes, a soda glass body with the shape of a Pasteur pipette of 2 mm diameter was employed.

Once the end of the glass body was sealed, the open end of the glass body was plugged to plastic tubing connected to a vacuum pump. The sealed end of the glass body was placed inside the nichrome wire heating coil. The vacuum was turned on and the heat was increased in a controlled manner to a point in which the glass would melt at a reasonable rate (C in Figure 3.3). When the characteristic "V" shape appeared indicating the glass walls had collapsed around the microwire, the heating coil was moved further up to seal the rest of the wire. Once the wire was sealed, the glass body was unplugged from the vacuum pump and placed away from the heating coil (D in

Figure 3.3).

A small amount of microwire was left free to facilitate the contact with indium, which was inserted into the glass body from the top with the help of a copper wire. The whole arrangement was heated slightly using the heating coil until the indium melted between the microwire and the insulated copper wire. Non conductive epoxy was added at the top of the glass body to secure the stability of the electrical connection (E in Figure 3.3).

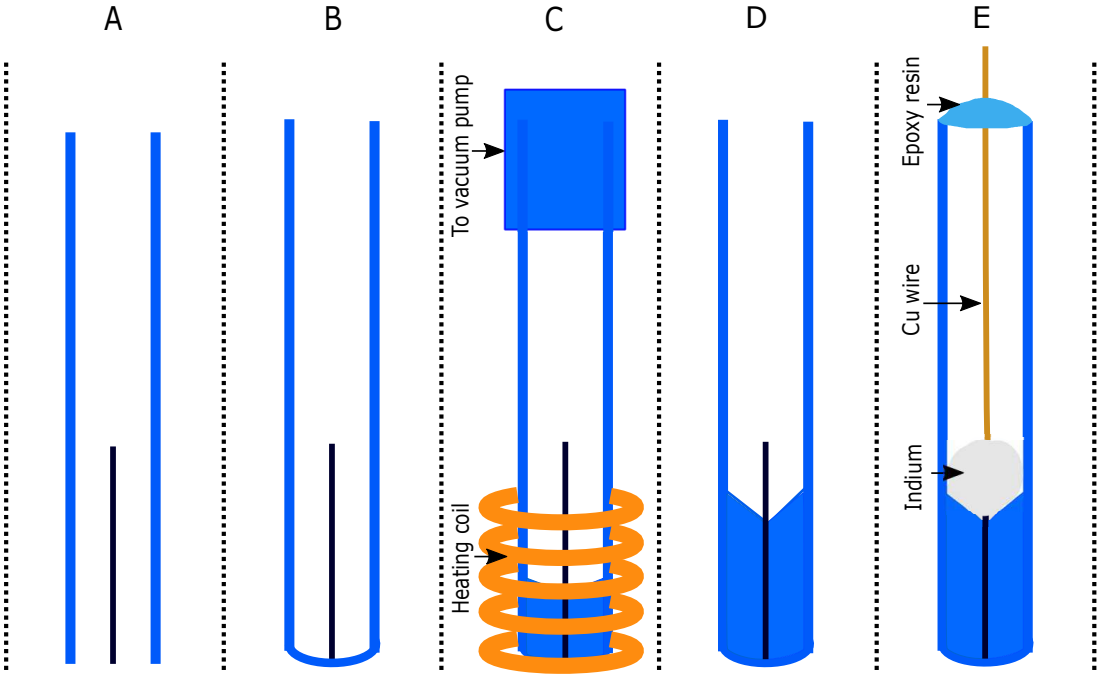

Figure 3.3: Schematic representation of the fabrication of a microdisc electrode. In blue the glass body, in black the microwire, in orange the nichrome heating coil.

The electroactive area was revealed using sand paper of 1200 grit, then the surface of the electrode was polished with 5 µm, 1 µm and 0.3 µm alumina powder on a polishing pad. The electrode was characterised by recording CVs in a deaerated 1 M H_2SO_4 solution. The response obtained is shown in figure 3.4, where the typical surface processes at the Pt surface are highlighted.

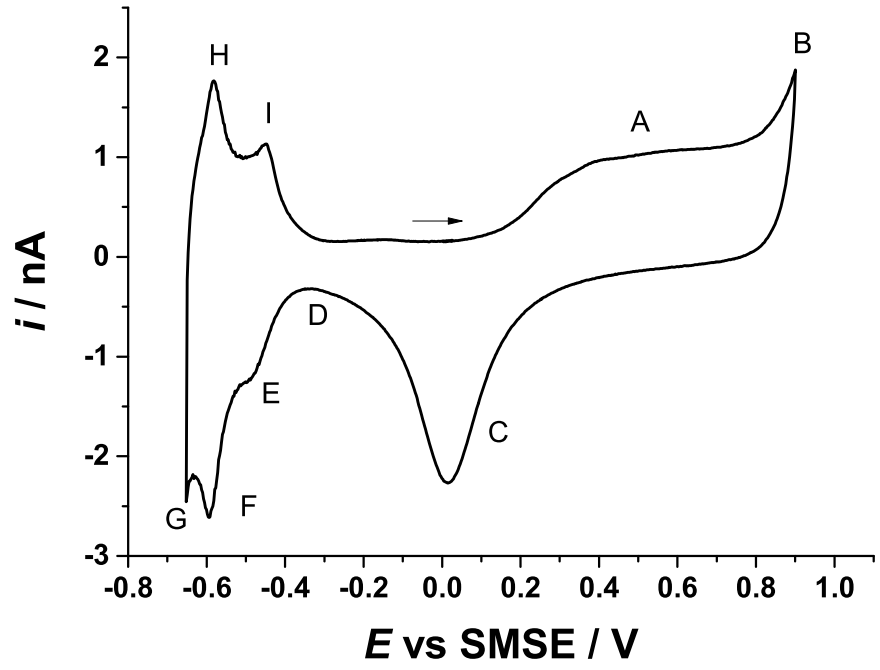

Figure 3.4: CV recorded with a 25 µm diameter Pt disc electrode in a deaerated 1 M H_2SO_4 solution at $0.1\,V\,s^{-1}$. *A* is the Pt oxide formation, *B* is the onset of oxygen evolution, *C* is the Pt oxide stripping peak, *D* is the double layer region, *E* and *F* the hydrogen adsorption peaks, *G* is the onset of hydrogen evolution, *H* and *I* are the hydrogen desorption peaks. The second cycle is shown.

3.3.2 Bismuth film microelectrodes (BiFMes)

The bismuth film microelectrodes (BiFMes) were fabricated by depositing a Bi film of 2 µm thickness onto a 50 µm diameter Pt disc by holding the potential at 0.05 V vs SCE. The optimum deposition potential was chosen after a cyclic voltammogram in a deaerated 20 mM $Bi(NO_3)_3.5\,H_2O$ in 0.5 M $HClO_4$ solution was recorded. Figure 3.5 shows the voltammetry in the plating solution where it is possible to appreciate the nucleation loop, the reduction wave of Bi(lll) onto the Pt electrode in the cathodic region and the oxidation of Bi(0) in the anodic region.

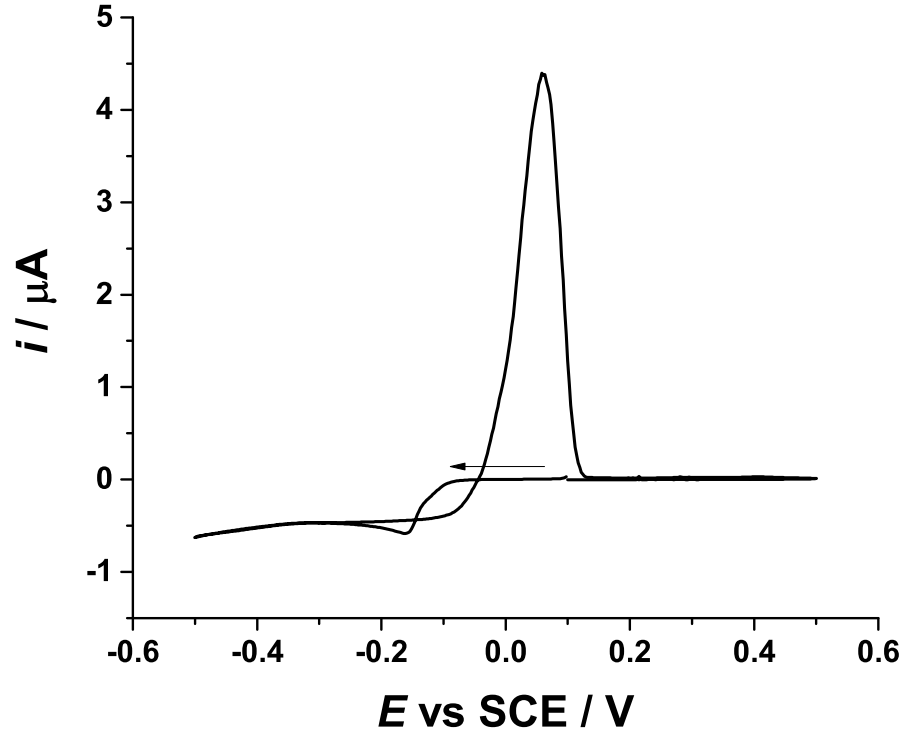

Figure 3.5: CV recorded with a 50 µm diameter Pt disc in deaerated 20 mM $Bi(NO_3)_3.5\,H_2O$ in 0.5 M $HClO_4$ solution at $0.05\,V\,s^{-1}$.

The charge needed to deposit a given thickness was calculated using the following equation:

$$Q = \frac{hnFdA}{M.W.} \tag{3.1}$$

Where Q is the charge, h is the thickness of the film, n is the number of electrons transferred, F is the Faraday constant, d is the metal density, A is the electrode area, and $M.W$ is the molecular weight of the deposited metal. For Bi the metal density is $9.78\,g\,cm^{-3}$ and the molecular weight $208.890\,g\,mol^{-1}$. The charge deposited was 5.32×10^{-5} C, and this provided a thickness circa 2 µm.

Figure 3.6 shows the current and charge as a function of time during the deposition.

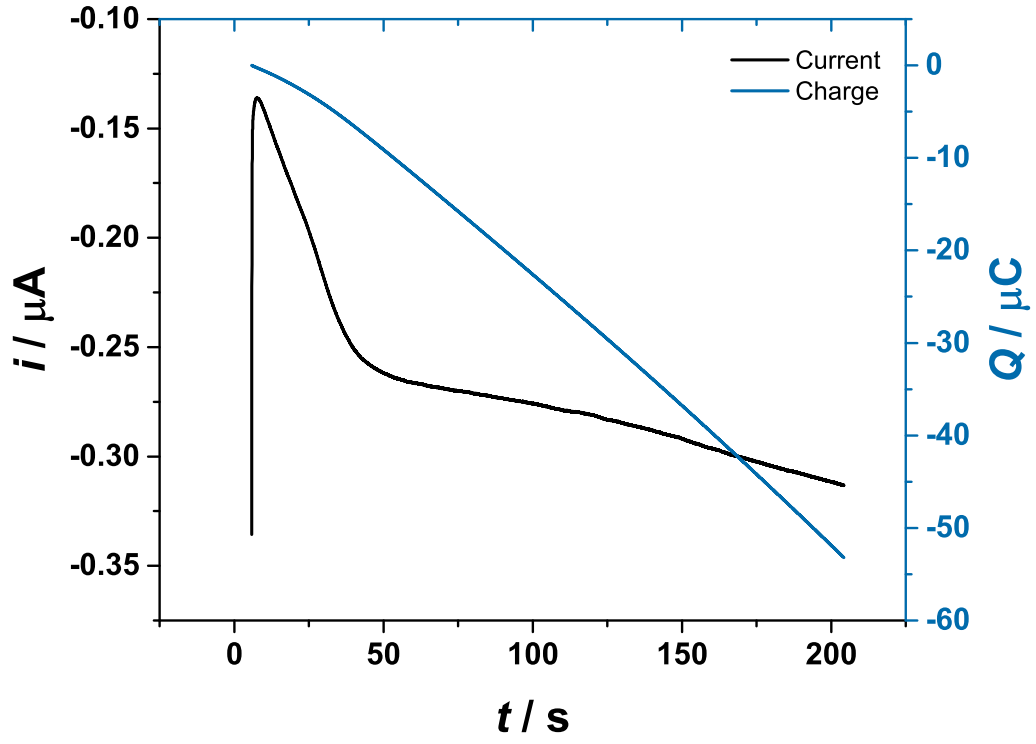

Figure 3.6: Current (i) and charge (Q) as a function of time (t) during the deposition of a 2 µm thickness Bi film onto a 50 µm diameter Pt disc.

Figure 3.7 shows an optical micrograph of the Pt disc before and after the electrodeposition.

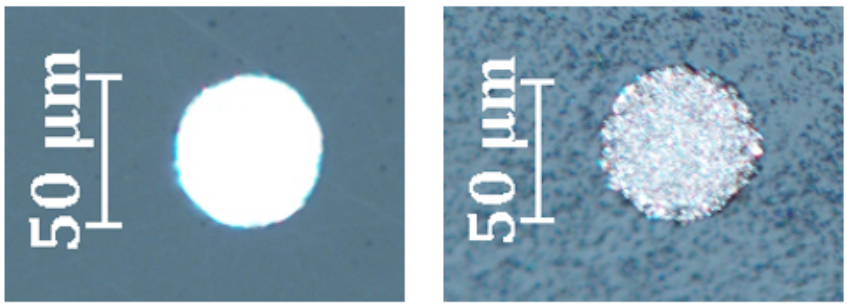

Figure 3.7: Micrographs of the Pt disc before and after the Bi deposition.

The Pt disc was characterised before and after the electrodeposition using a 5 mM $Ru(NH_3)_6^{3+}$ in 0.5 M KCl solution. The limiting current for the reduction of $Ru(NH_3)_6^{3+}$ was recorded to determine the radius of the Pt and Bi disc. Figure 3.8 shows the LSV recorded with the 50 µm diameter Pt disc before and after the electrodeposition. The limiting current is larger for the BiFMe because the Bi film

extends beyond the Pt disc.

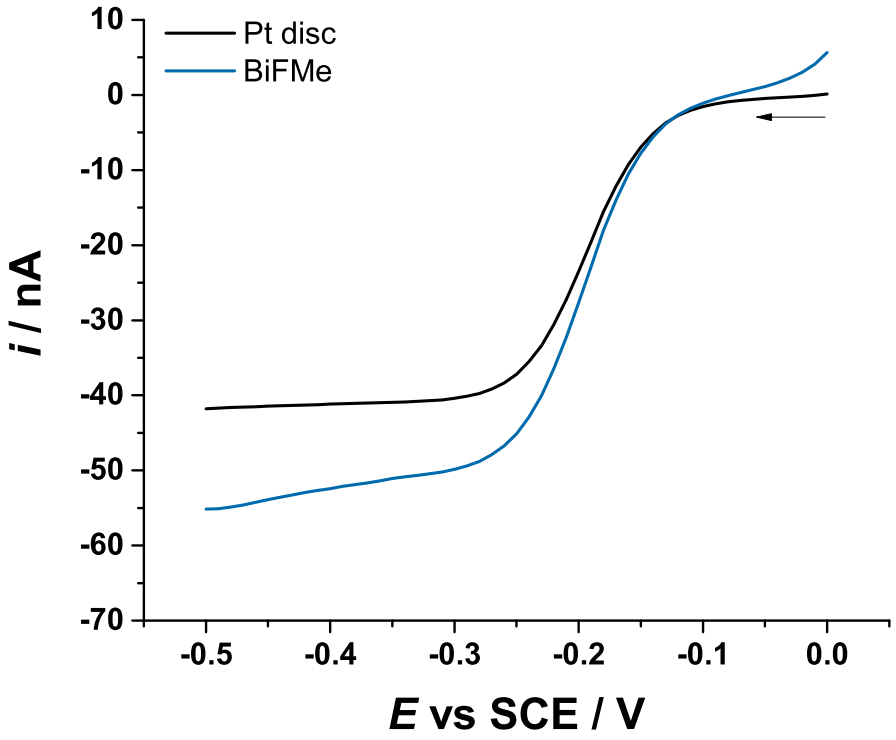

Figure 3.8: LSVs recorded with a 50 µm diameter Pt disc in deaerated 5 mM $Ru(NH_3)_6^{3+}$ in 0.5 M KCl solution at 0.001 V s^{-1} at 25.4 °C. The black curve corresponds to the Pt disc and the blue one to the BiFMe.

3.3.3 Reference and counter electrodes

The reference electrodes used in this work were the saturated calomel electrode (SCE) and saturated mercury mercurous sulfate electrode (SMSE). The mercury/mercurous salt couple was placed in a glass tube in contact with a Pt wire, and was sealed using glass wool. A plastic cap was fitted to the glass cap. Then, the two pieces were placed onto the glass body filled with the corresponding electrolyte solution, saturated KCl for SCE and saturated K_2SO_4. The electrodes were placed in a beaker containing the corresponding electrolyte in contact with the glass frit of the glass body. Figure 3.9 shows the main components of the mercury reference electrodes employed.

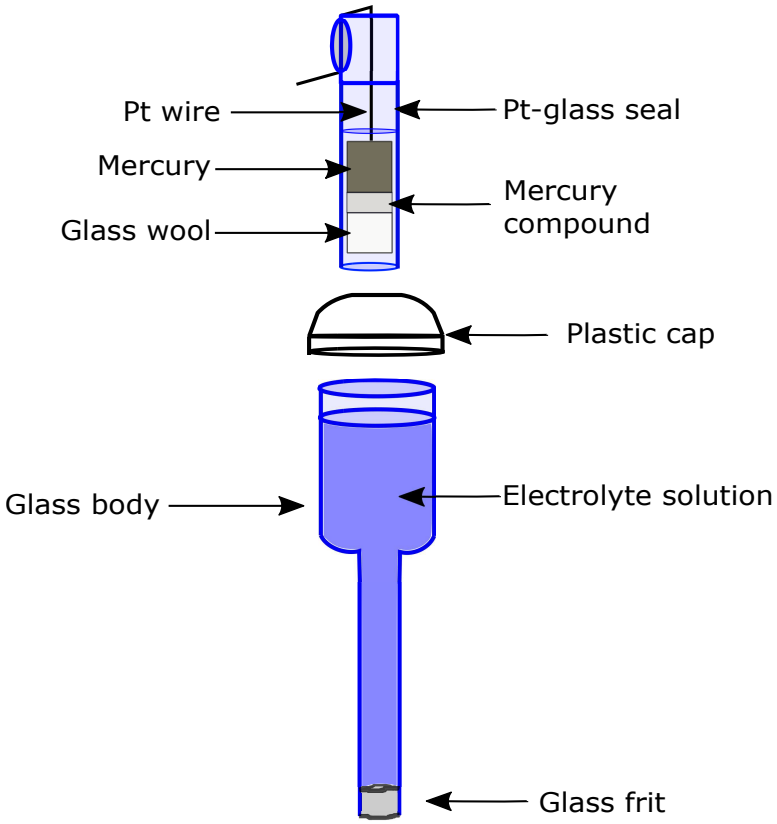

Figure 3.9: Scheme of the main components of the mercury reference electrodes. SMSE if the electrolyte solution was saturated K_2SO_4, and SCE if the electrolyte solution was saturated KCl.

The experiments were performed using a microelectrode as working electrode and a reference electrode as reference/counter due to the low magnitude of current passed at the microelectrodes. When experiments were conducted using electrodes larger than 50 µm, a carbon rod was used as a counter electrode.

3.3.4 Iron electrodes

3.3.4.1 Iron flake

Figure 3.10 shows a schematic representation of the fabrication of the iron flake electrode. A single iron flake was taken and the electrical connection to an insulated Cu wire was made using silver epoxy. This was placed in a truncated Pasteur pipette sealing the end with quick set epoxy resin. The cavity containing the iron flake was filled with Araldite and it was left to dry for 24 hours. Once the araldite was dry, the Pasteur pipette was broken and removed from the epoxy body.

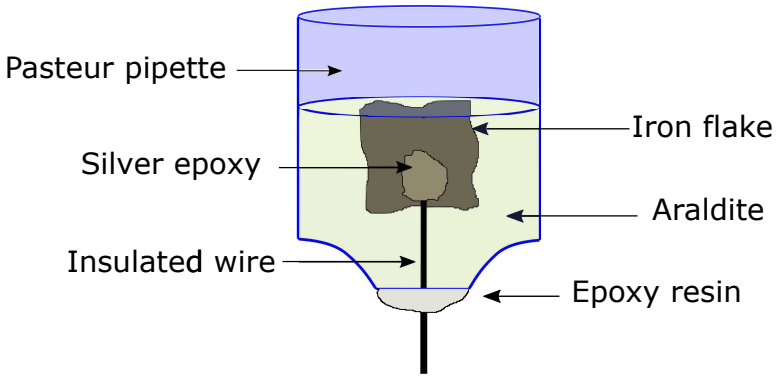

Figure 3.10: Schematic representation of the fabrication of the iron flake electrode.

The exposed iron surface was polished with alumina lapping film 5 µm, 1 µm and 0.3 µm prior to the start of the experiment.

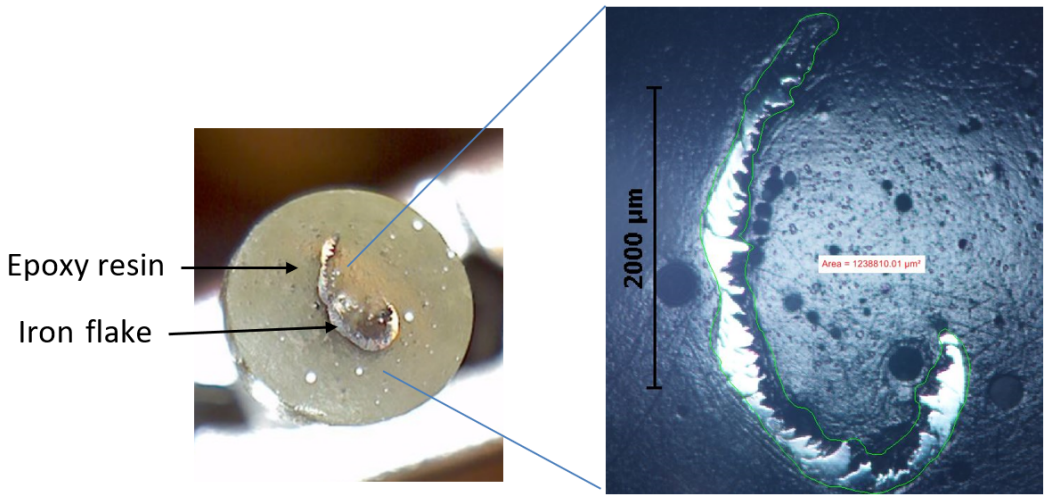

Figure 3.11: Exposed electrode surface (on the left) and optical micrograph of a section of the freshly polished iron electrode (on the right). The green line delimitates the area of the iron flake, which is displayed in the image, 0.0123 cm^2.

3.3.4.2 Iron powder

The iron powder electrode was made using a 500 µm diameter Au electrode (fabrication mentioned in section 3.3) that was electrochemically etched in an aerated NaCl 0.5 M by cycling the potential 5 times from -0.7 V to 1.3 V vs SCE at 0.1 V s. Figure 3.12 shows the CVs obtained when etching the Au electrode. The anodic peak at 1 V corresponds to the oxidation of Au to Au(lll) and Au(l) to form the soluble complexes $[AuCl_4]^-$ and $[AuCl_2]^-$ according to the following equations:

$$Au_{(s)} + 4\,Cl^- -> [AuCl_4]^- + 3\,e^- \tag{3.2}$$

$$Au_{(s)} + 2\,Cl^- -> [AuCl_2]^- + e^- \tag{3.3}$$

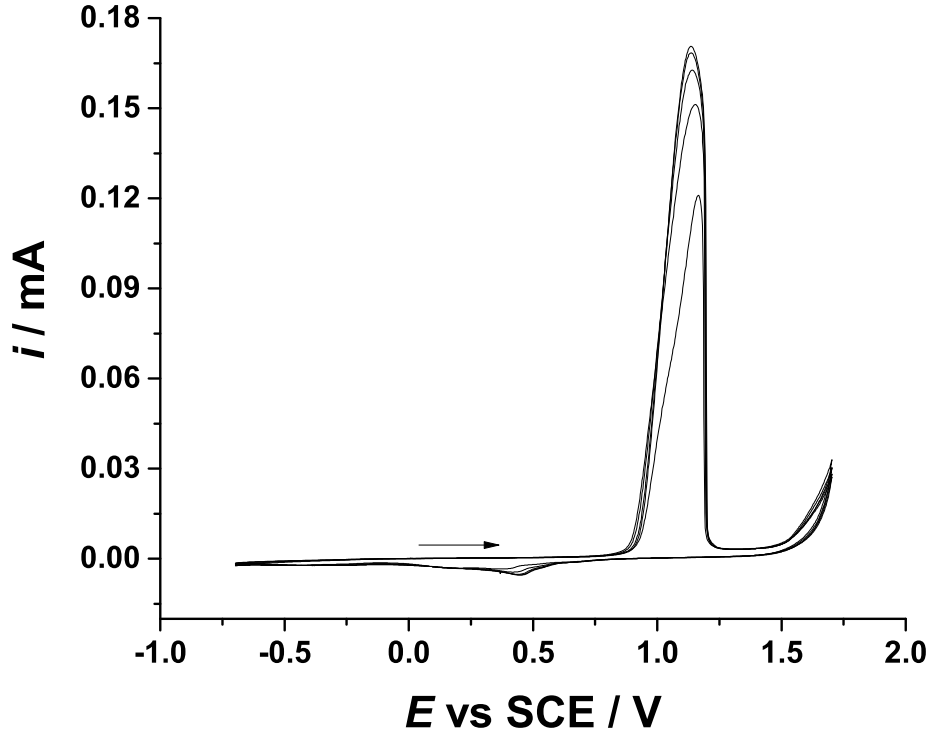

Figure 3.12: CVs recorded with a 500 µm diameter Au disc electrode in an aerated 0.5 M NaCl solution at $0.1\,V\,s^{-1}$. The 5 cycles are shown. The current of the anodic peak increased with the number of cycles.

The cathodic peak at 0.5 V is the reduction of gold oxide, and a possible contribution of the soluble species electrochemically formed; however there is no evidence of the latter [100]. The depth of the cavity is too deep to be determined electrochemically, however, micrographs suggest that the depth is about 150 µm.

The etched Au electrode was packed with iron powder by pushing the surface of the electrode towards a pile of iron powder on a microscope slide. Figure 3.13 shows from left to right a micrograph of the Au electrode before and after etching, and after packing with iron powder.

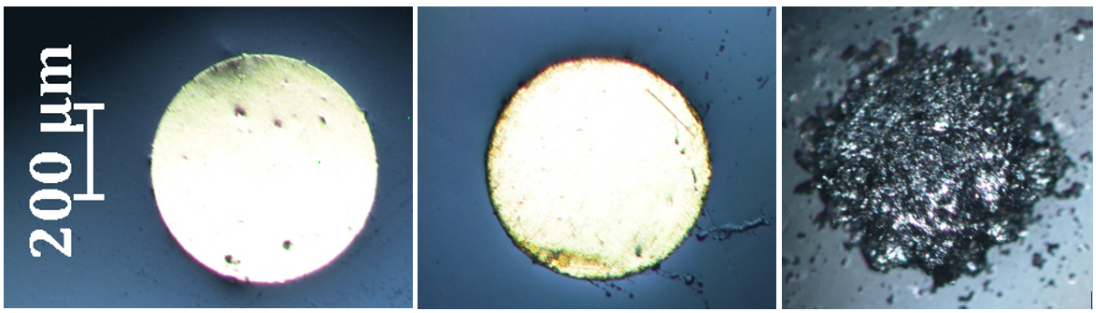

Figure 3.13: Optical micrographs of the gold electrode before etching, after etching and after filling with iron powder.

3.4 Iron substrates

3.4.1 Iron substrates for SECM

The iron substrates and the raw materials are shown in Figure 3.14. The size of the flakes ranged from 100 µm to 1000 µm, and the powder from 10 µm to 50 µm. The substrates were made by casting the iron flakes and iron powder in epoxy resin.

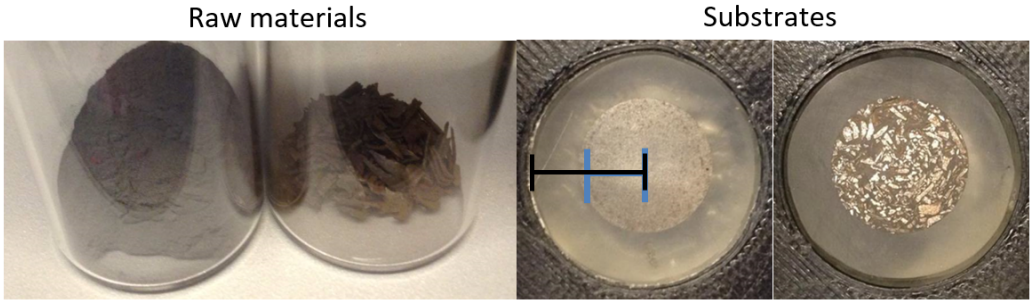

Figure 3.14: Photographs of the raw materials (on the left) and the substrates (on the right). The blue segment is the radius of the iron substrate (7.5 mm) and the black segment the radius of the whole substrate (12.5 mm).

Figure 3.15 and 3.16 show optical micrographs of the iron substrates to illustrate the particle size on each of them.

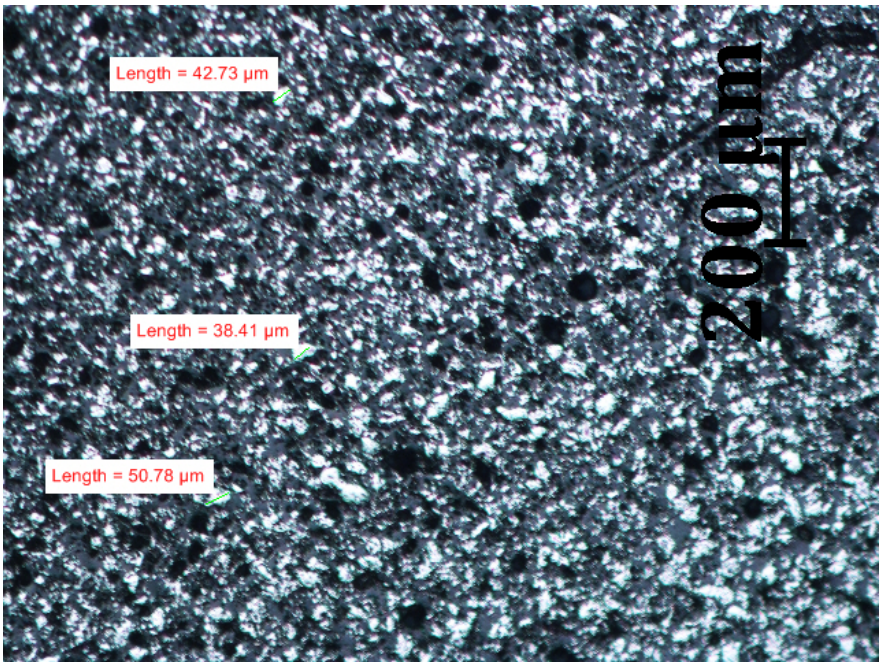

Figure 3.15: Optical micrograph of the substrate made with the iron powder produced by Aldrich. The dark areas correspond to the epoxy resin and the shiny areas to the iron particles. The green segments show the iron particle size.

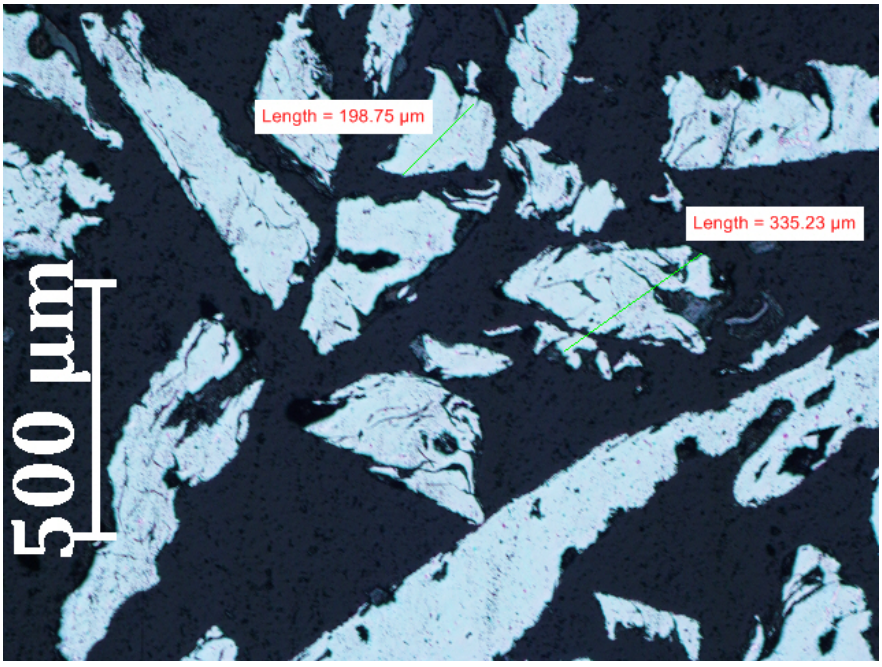

Figure 3.16: Optical micrograph of the substrate made with iron flakes. The dark areas correspond to the epoxy resin and the shiny areas to the iron particles. The green segments show the iron particle size.

3.4.2 Iron substrates for ReO_4^- uptake

The top of a 1000 µL pipette tip was cropped to obtain a cylindrical mould. This was glued to a glass microscope slide with quick epoxy resin. The iron particles were placed inside the cylindrical mould until a layer covered the whole diameter. After that, the cylindrical mould was filled with 24 hr. setting time epoxy. The substrates were revealed by cropping the cylindrical mould and were polished with sand paper 1200 grit, and with 5 µm, 1 µm and 0.3 µm alumina powder in a polishing pad.

Figure 3.17 shows a schematic representation of the fabrication of the iron substrates.

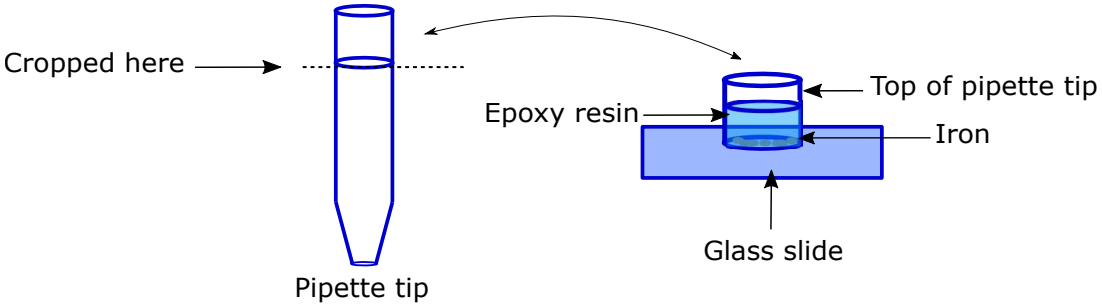

Figure 3.17: Scheme showing the fabrication of the iron substrates employed in the experiments of ReO_4^- uptake.

Figures 3.18, 3.19 and 3.20 show the substrates surface, highlighting the size of the iron particles obtained from the same iron chip.

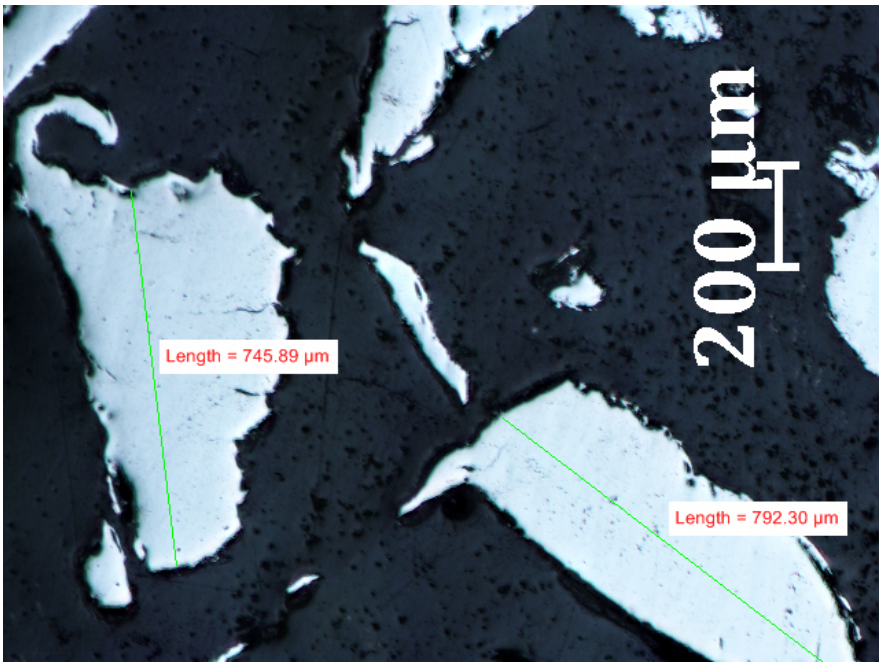

Figure 3.18: Optical micrograph of the large size iron substrate. The dark areas correspond to the epoxy resin and the shiny areas to the iron particles. The green segments show the iron particle size.

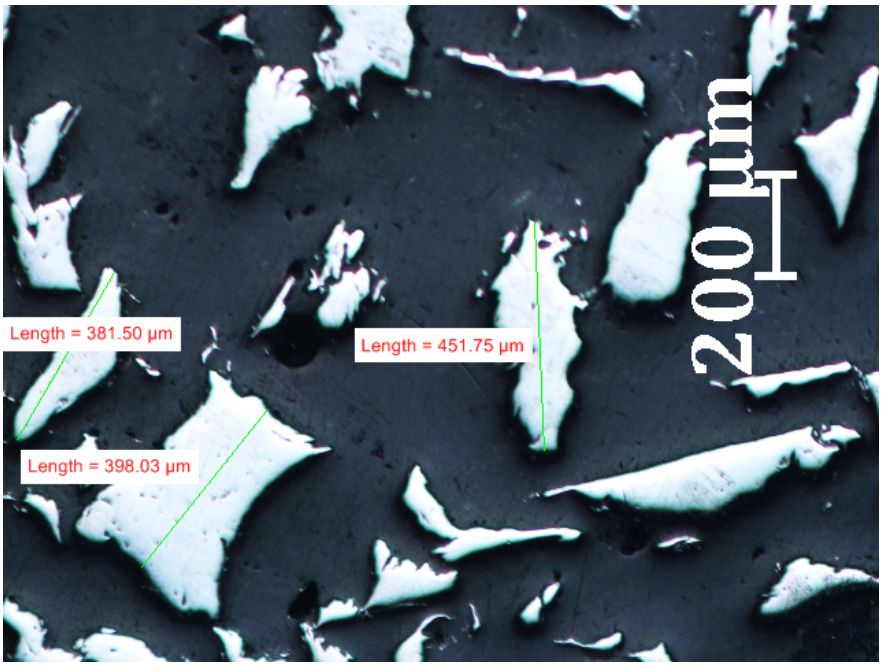

Figure 3.19: Optical micrograph of the medium size iron substrate. The dark areas correspond to the epoxy resin and the shiny areas to the iron particles. The green segments show the iron particle size.

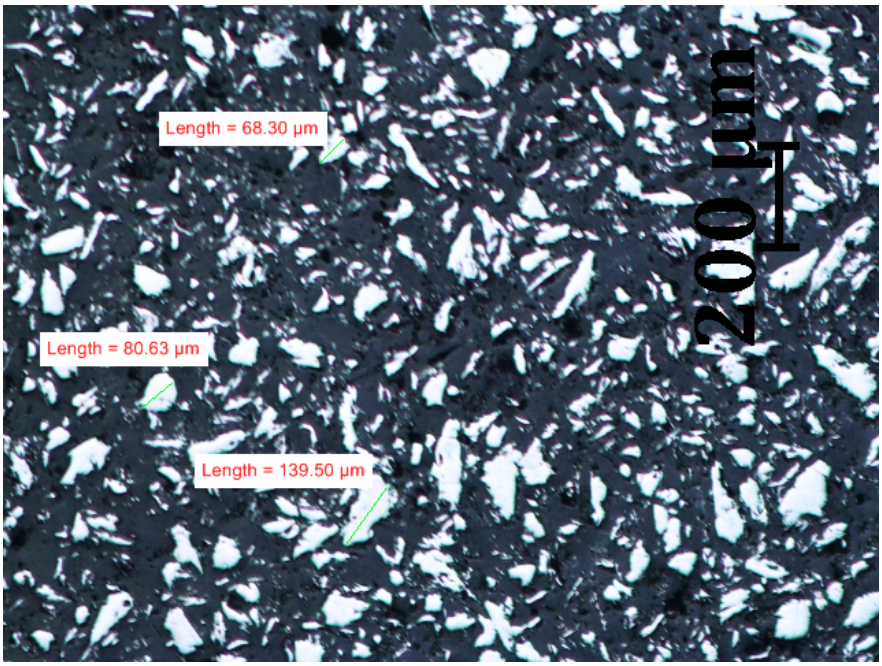

Figure 3.20: Optical micrograph of the iron powder substrate. The dark areas correspond to the epoxy resin and the shiny areas to the iron particles. The green segments show the iron particle size.

3.5 Cells

3.5.1 Cell for the water-air interface

Figure 3.21 shows the experimental arrangement used for the experiments regarding the water-air interface. A two electrode configuration was employed having an SCE as reference/counter electrode and a Pt disc of 25 µm diameter as working electrode. The cell was made of Perspex and a glass slide was glued to the sides to have visibility inside the cell.

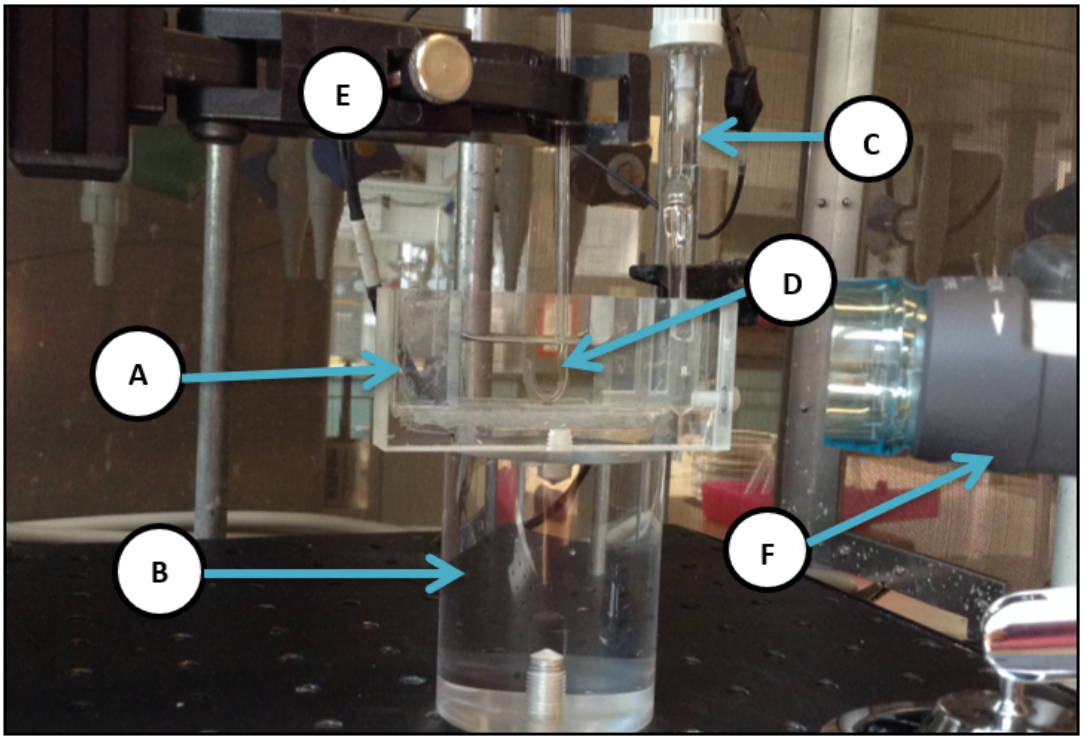

Figure 3.21: Experimental arrangement; *A* is the cell made of Perspex with two glass slides glued to the sides, *B* a Perspex cylinder fixed to the antivibration platform, *C* is the reference electrode, *D* is a submarine microelectrode, *E* is the clamp of the SECM, and *F* is a Celestron optical microscope.

The experimental set up was modified to investigate the the water-air interface due to its complexity. Figure 3.22 shows on the left a micrograph of the experimental configuration using a submarine microelectrode held by a Teflon clamp. The "unconfined meniscus" was a rectangle of 3.5 cm length and 1.5 cm width. A zoom on the water-air interface is shown on the right.

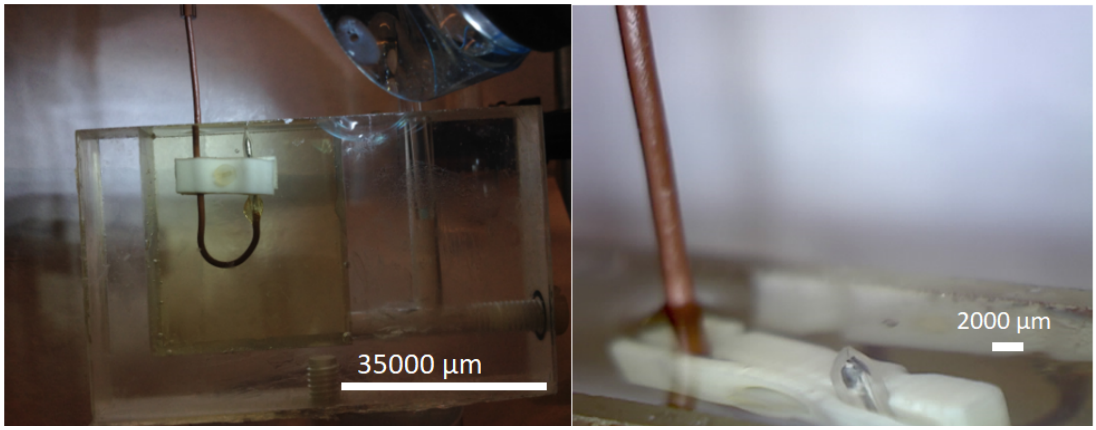

Figure 3.22: Experimental arrangement with an unconfined meniscus. The submarine microelectrode was held by a Teflon clamp. On the left, the whole configuration. On the right a zoom on the water-air interface.

Figure 3.23 shows a second experimental configuration. In this case, the meniscus was confined by placing a 0.5 mm thick polycarbonate sheet with a 6.5 mm diameter hole on top of the cell.

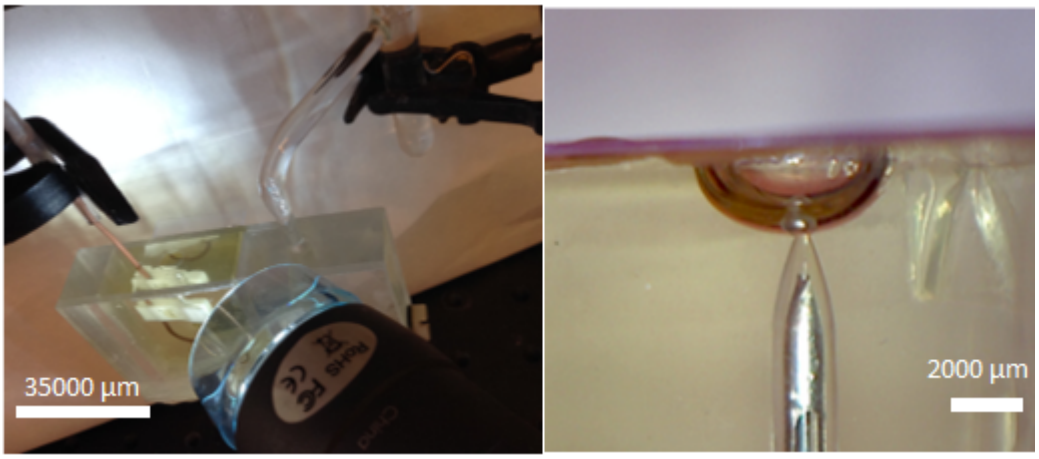

Figure 3.23: Experimental arrangement with a confined meniscus. The submarine microelectrode was held by a Teflon clamp. On the left, the whole configuration. On the right a zoom on the water-air interface confined by placing a 0.5 mm thick polycarbonate sheet with a 6.5 mm diameter hole.

3.5.2 Cell for Bi film microelectrodes (BiFMes)

The electrochemical set up for the determination of lead in water samples involved the use of a 5 neck glass cell. A three electrode system was employed to perform the electrodeposition, having a 50 µm Pt disc as working electrode, SCE as reference electrode and a Pt mesh as counter electrode. For the determination of Pb^{2+} in water

samples the configuration involved using the BiFMe as working electrode and SCE as reference/counter electrode.

3.5.3 Cell for the iron-groundwater interface

The electrochemical cell employed for the investigation of the iron-groundwater interface experiments was designed using Solid Works and printed using ABS (acrylonitrile butadiene styrene) in an Up Box 3D printer. A glass window was glued to the cell with quick set epoxy resin to provide visibility inside the cell. Figure 3.24 shows the scanning electrochemical microscope with the cell configuration that consisted of a 2 electrode system having an SMSE as reference/counter electrode and a Pt disc of 25 µm diameter as working electrode.

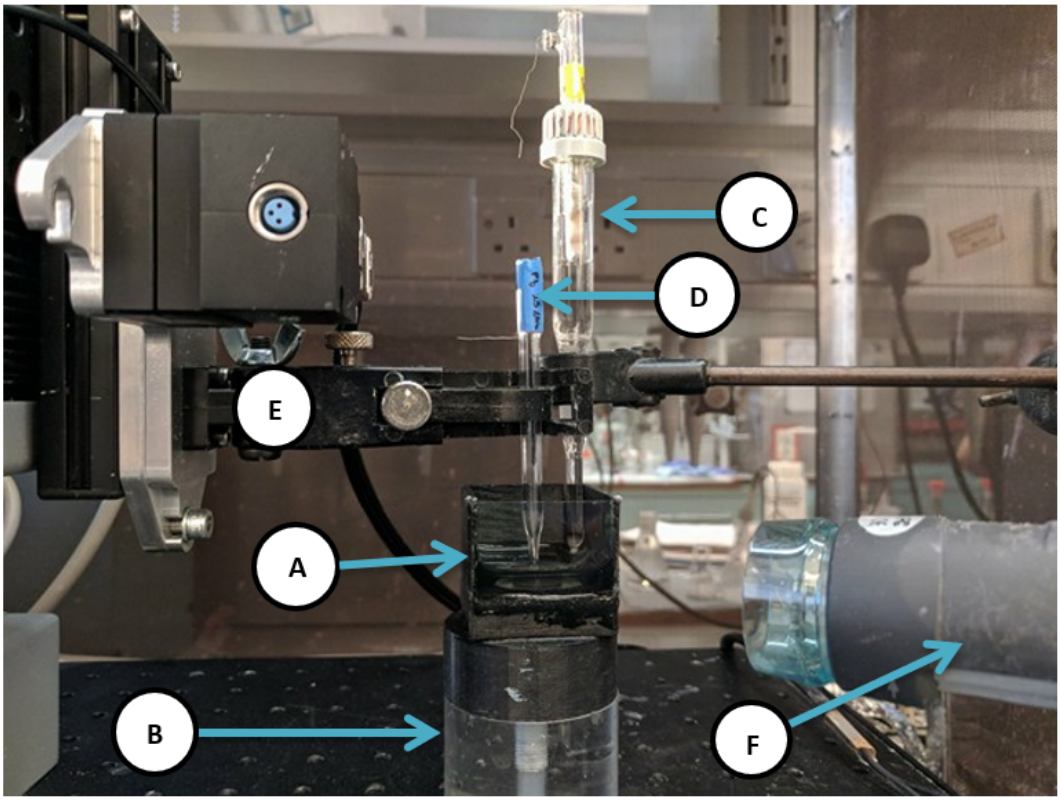

Figure 3.24: Experimental arrangement employed to investigate the iron-groundwater interface. *A* is the 3D pinted cell, *B* a Perspex cylinder fixed to the antivibration platform, *C* is the reference electrode, *D* is the Pt disc of 25 µm diameter, *E* is the clamp of the SECM, and *F* is a Celestron optical microscope.

The results obtained using each the experimental arrangement shown in Figure 3.24 are presented in chapter 5.

Chapter 4

SECM study of the properties of the water-air and water-SML interface

This chapter shows the results of the investigation of the physicochemical properties of the water-air interface and water-SML interface.

In section 4.1 and 4.2, the results of the experiments performed using submarine microelectrodes, linear sweep voltammetry, chronoamperometry and the SECM feedback mode, are analysed in terms of the size of the meniscus for each interface. Other factors affecting the amperometric response, like the electrode orientation and the acquisition mode in the approach curves, are discussed too.
The influence of the SML composition on the amperometric response is discussed in section 4.2.2. We compared the results obtained when the synthetic SML consisted in a mixture of 0.8 mL of a 30% w.t. $C_{16}EO_8$ with 0.2 mL of ethanol or heptane.

Section 4.3 shows experiments performed using a conventional shaped Bi film microelectrode (BiFMe) to characterise water samples in terms of Pb^{2+} trace concentrations using a calibrationless method.

4.1 The water-air interface

The results in this section show the investigation of the water-air interface through submarine microelectrodes, linear sweep voltammetry, chronoamperometry and the SECM feedback mode. The aim was to record the oxidation current of FeMeOH at different tip-substrate distances. Submarine microelectrodes were employed to be able to approach the water-air interface from underneath, without disturbing the meniscus of the solution. The methodology consisted in recording linear sweep voltammograms (LSVs) and chronoamperograms one after the other as the submarine microelectrode was moved in µm steps towards the water-air interface. After the electrode touched the meniscus of the solution, it was placed back in the bulk and electrochemically reconditioned by cycling the potential from 1 V to -1 V at $500\,\mathrm{mV\,s^{-1}}$. The approach curves were recorded using the step scan mode first and the sweep scan mode after.
Acquiring LSVs and chronoamperograms allowed us to know the concentration and diffusion coefficient of the redox species at different depths, which is similar to what we aim to achieve *in situ*. The approach curves allowed us to investigate the water-interface as an SECM substrate and compare the amperometric response between the three experiments.

Section 4.1.1.1 shows the experiments performed using an unconfined meniscus, which was formed by placing 10 mL of a 1 mM FcMeOH in 500 mM NaCl solution in the electrochemical cell.
Section 4.1.1.2 shows the investigation of water-air interface using a confined meniscus created by placing a 0.5 mm thick polycarbonate cover with a 6.5 mm diameter hole on top of the electrochemical cell.

4.1.1 Influence of the size of the meniscus

4.1.1.1 Unconfined meniscus

The water-air interface was created using the experimental arrangement shown in Figure 4.1. The U-shape electrode was held by a PTFE clamp, and the meniscus of the solution was only constrained by the cell walls. The position set as $d = 0\,\mu\mathrm{m}$ (the bulk) was arbitrarily fixed approximately 5000 µm underneath the water-air interface.

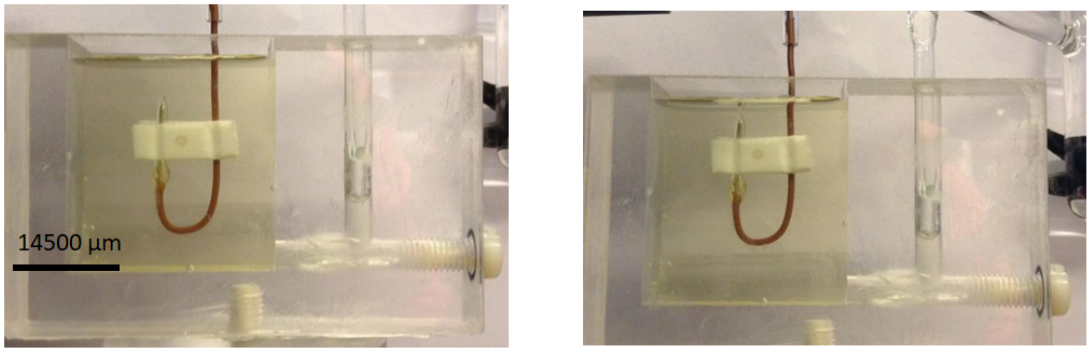

Figure 4.1: The experimental arrangement showing a submarine 25 µm diameter Pt disc at the position set as $d = 0$ µm (left) and at $d = 5000$ µm (right) in an aerated 1 mM FcMeOH in 500 mM NaCl solution.

Linear sweep voltammograms (LSVs) and chronoamperograms were recorded one after the other as the submarine microelectrode was moved in 1000 µm steps from $d = 0$ µm to $d = 4000$ µm, then every 100 µm, and 50 µm when getting closer to the water-air interface ($d = 5000$ µm). After the electrode touched the water-air interface, it was placed back in the bulk ($d = 0$ µm) and electrochemically reconditioned by cycling the potential from 1 V to -1 V at 500 mV s^{-1}.

Approach curves were recorded using the step scan mode first and the sweep scan mode after. In both modes the step size, the distance between two data points, and the scan velocity (how quickly the electrode travels) can be modified. In the step scan mode the electrode stops at the indicated step size before acquiring data. In the sweep scan mode the electrode acquires the data at regular intervals without stopping. This mode is known as "on the fly". The approach curves are shown using the normalized current (tip current divided by the limiting current recorded in the bulk), however the distance was not normalised by the radius of the electrode to facilitate the interpretation.

The LSVs shown in Figure 4.2, recorded from 0 µm to 4910 µm, correspond to the response when the electrode was in the bulk. At 4950 µm the current dropped to zero because the electrode touched the meniscus of the solution. At 5000 µm the meniscus was being broken by the electrode. The same trend was observed in the chronoamperograms recorded as shown in Figure 4.2. The plot in Figure 4.3 was built by extracting the limiting current from the LSVs and chronoamperograms to compare both experiments. From the LSVs the current was taken at E=0.4 V vs SCE and from the chronoamperograms at t=30 s.

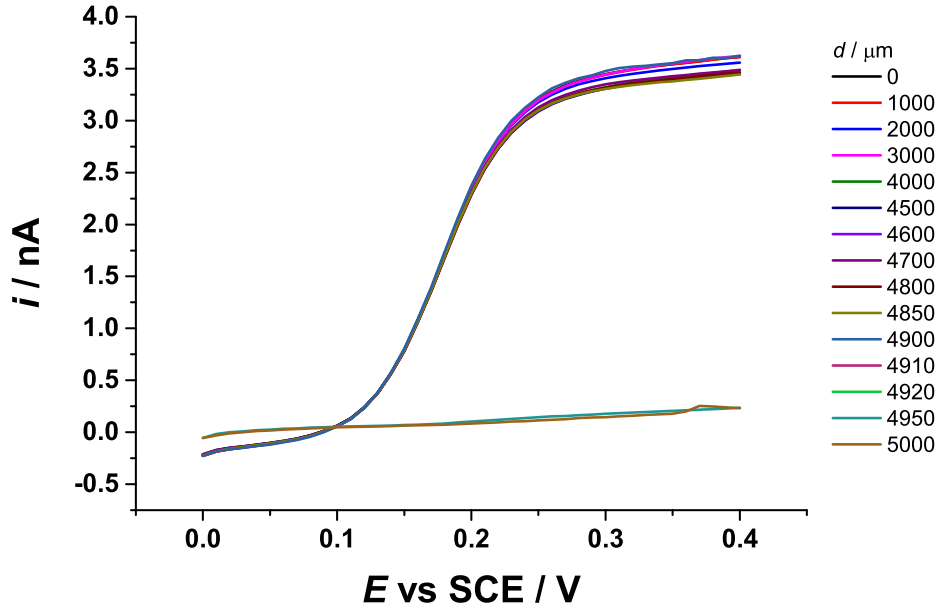

(a) LSVs

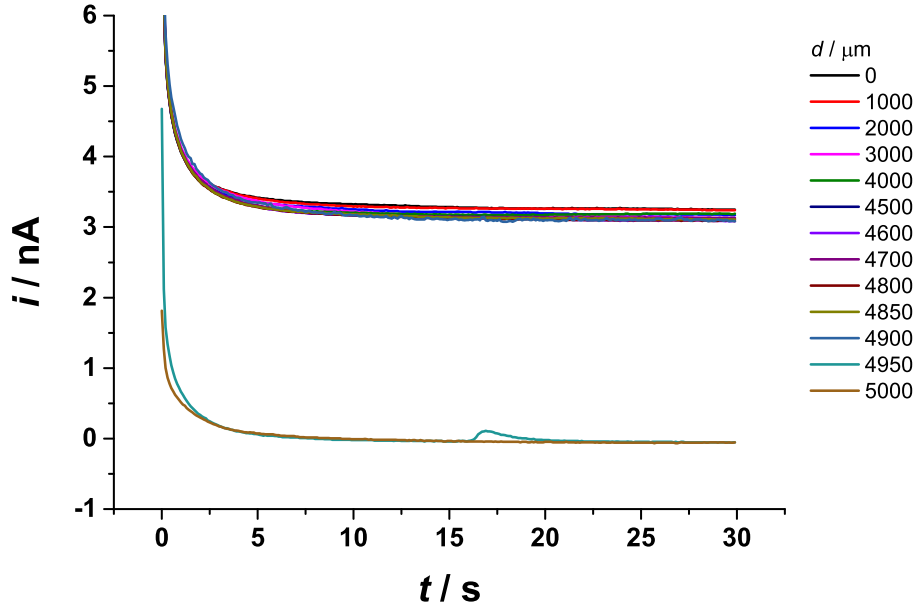

(b) Chronoamperograms

Figure 4.2: LSVs (a) and chronoamperograms (b) recorded with a submarine 25 µm diameter Pt disc at different distances to the water-air interface in an aerated 1 mM FcMeOH in 500 mM NaCl solution. The position $d = 0\,\mu m$ corresponds to the electrode in the bulk, and $d = 5000\,\mu m$ when it was touching the water-air interface. LSVs were acquired at $0.010\,V\,s^{-1}$. The potential was stepped from 0.0 V to 0.4 V vs SCE. $RG = 18$.

The trend observed in the reconstructed approach curves shows agreement between the current extracted from LSVs and chronoamperograms. It remains the same from $d = 0\,\mu m$ to $d = 4950\,\mu m$, then it drops to zero. However, according to theoretical expectations, the current should remain the same when the tip-substrate distance is up to 7 to 10 times the radius of the microdisc. Closer to the substrate, the diffusion field at the microdisc is affected by the substrate, and considering that the water-air interface is an insulator, we should expect hindered diffusion. Therefore, about 125 µm away from the water-air interface the current should decrease. This is not observed in Figure 4.3, so the trend was further investigated through the approach curves.

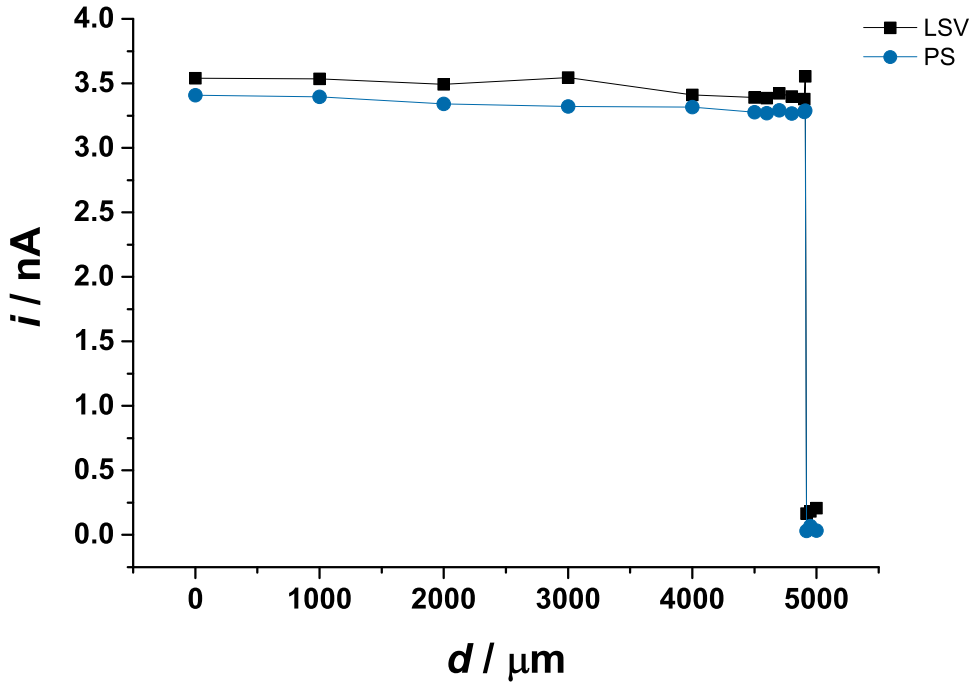

Figure 4.3: Limiting current from LSVs and potential steps (PS) as a function of the electrode water-air interface distance. The current from LSVs was extracted at E=0.4 V vs SCE, and at t=30 s in the chronoamperograms. The black points correspond to the limiting current from the LSVs, and the blue from the potential steps.

The approach curves were recorded after the electrode was placed back in the bulk and electrochemically cleaned before starting each measurement. The response obtained is shown in Figure 4.4.

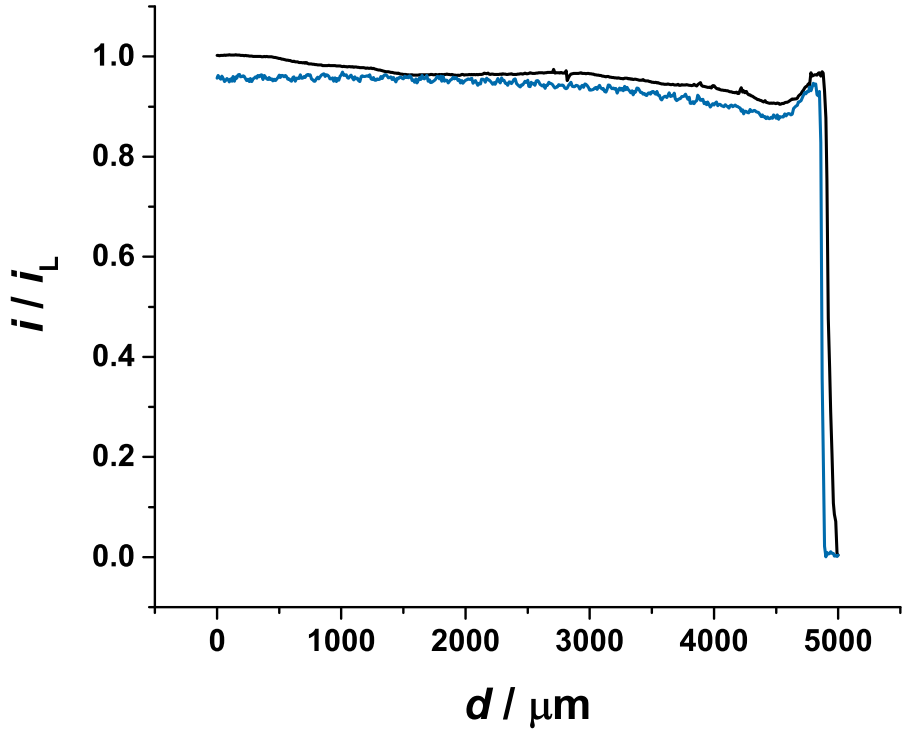

Figure 4.4: Approach curves recorded with a submarine 25 µm diameter Pt disc in an aerated 1 mM FcMeOH in 500 mM NaCl solution holding the potential at 0.4 V vs SCE. The current was conditioned by holding the potential at 0.4 V for 100 s. The data was acquired using the step scan mode (black) and the sweep scan mode (blue) using a step size of 10 µm at 10 µm s^{-1}. At 5000 µm the electrode reached the water-air interface. The electrode was normalized by $i_L = 3.07 \times 10^{-9}$ A. $RG = 18$.

The approach curves shown in Figure 4.4 agree with each other qualitatively and are also in agreement with the trend shown in 4.3. The response followed a similar trend to what was previously observed from $d = 0$ µm to $d = 4000$ µm, in which the current oscillated around 3.0 nA. Considering that the water-air interface is an insulator, hindered diffusion was expected when the electrode was 87.5 µm to 125 µm ($7a$ -$10a$) away from the interface. However, the current started decreasing at $d = 3000$ µm and a minimum was observed at 4500 µm, which is 900 µm away from the interface. After this, the current reached a maximum at $d = 4900$ µm and dropped to zero at $d = 5000$ µm. This behaviour could be explained by the fact that the water-air interface is not solid but more like an elastic barrier. When the unconfined meniscus was approached, the water-air interface was susceptible to environmental vibrations, natural

convection or convection from above the solution, and also changes of concentration due to solution evaporation if the experiment was long enough. Another aspect to consider is the interaction between the glass surrounding the microwire and the water-air interface. Because the glass surrounding the microwire is hydrophilic, it is possible that the electrode pushed away the water molecules "bending" the water-air interface from underneath. Figure 4.5 shows a micrograph of the microelectrode coming back to the bulk of the solution. There, it is possible to appreciate the meniscus being bent by the electrode when dragging a stagnant layer of solution towards the bulk.

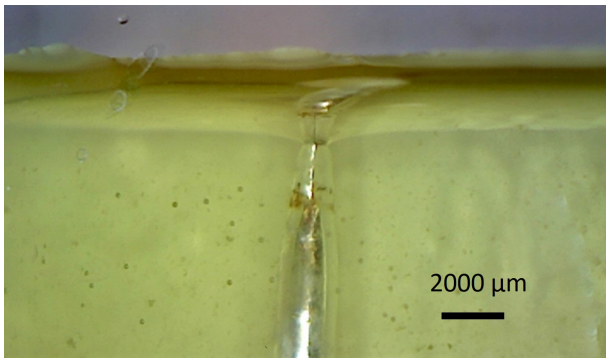

Figure 4.5: Micrograph of a submarine 25 µm diameter Pt disc coming back to the bulk of an aerated 1 mM FcMeOH in 500 mM NaCl solution dragging a stagnant layer of water.

The decrease of current at 3000 µm suggested that the diffusion field at the microelectrode was perturbed by the water-air interface from further away than theoretical expectations. The minimum of current observed at 4500 µm could be the effect of the meniscus being pushed and stretched by the microelectrode before being broken. Therefore, the rise of current observed at 4900 µm could be due to an increase of flux of redox species at the surface of the electrode by the convection created when the meniscus was being broken. After that, the surface of the electrode was free of solution, and the current dropped to zero.

This trend can be compared to what is observed when recording approach curves using a conventional shaped microelectrode. Figure 4.6 shows a conventional shaped Pt disc positioned at $d = 0\,\mu m$, which is about 500 µm below the water-air interface, and at $d = 1200\,\mu m$, outside the solution. The corresponding approach curves are shown in Figure 4.7.

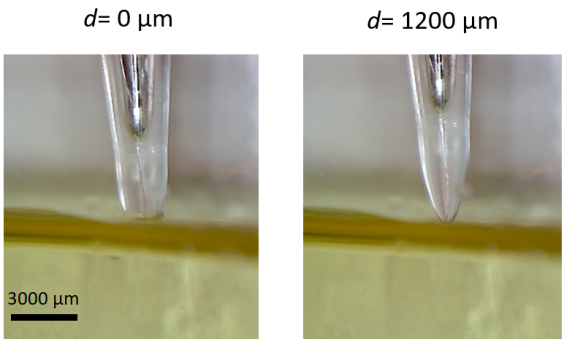

Figure 4.6: Micrographs of a conventional shaped 25 µm diameter Pt disc in an aerated 1 mM FcMeOH in 500 mM NaCl solution at the position set as $d = 0\,\mu m$ (left) and at $d = 1200\,\mu m$ (right).

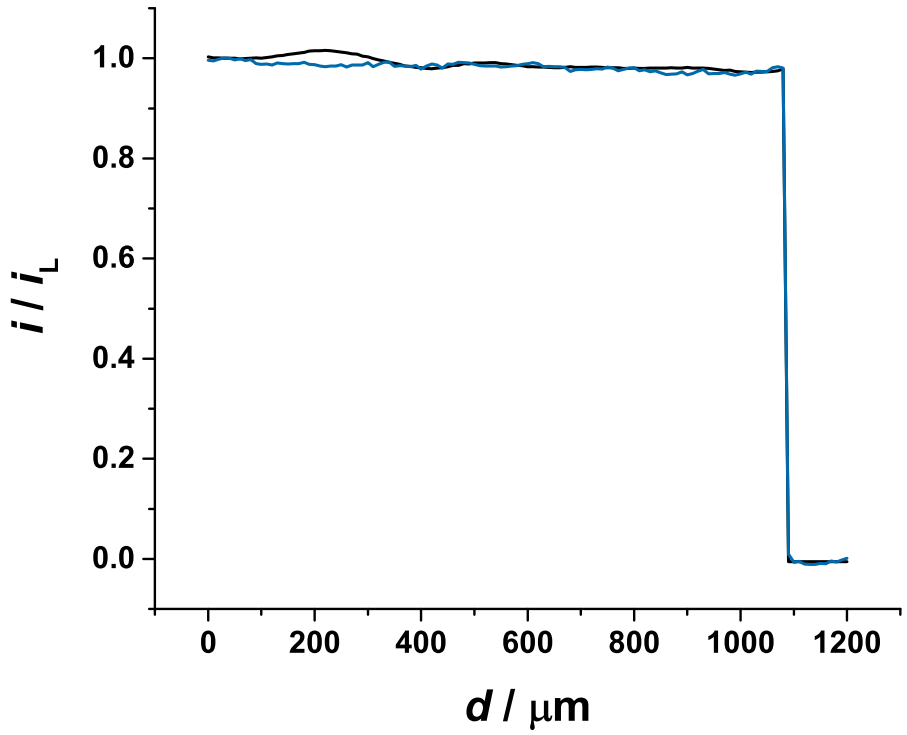

Figure 4.7: Approach curves recorded with a conventional shaped 25 µm diameter Pt disc in an aerated 1 mM FcMeOH in 500 mM NaCl solution holding the potential at 0.4 V vs SCE. The current was conditioned by holding the potential at 0.4 V for 100 s. The data was acquired using the step scan mode (black) and the sweep scan mode (blue) using a step size of 10 µm at $10\,\mu m\,s^{-1}$. At 1100 µm the electrode reached the water-air interface. The current was normalized by $i_L = 3.65 \times 10^{-9}$ A. $RG = 15$.

The approach curves in Figure 4.7 show significant differences compared to the ones recorded using the submarine microelectrode. In these the limiting current remained the same up to $d = 1100\,\mu m$ and when the electrode reached the water-air interface and went out of the solution the current dropped to zero. These did not show hindered diffusion or the trend observed close to the water-air interface in the curves shown in Figure 4.4. The reason behind this could be the orientation of the diffusion field in each case. The diffusion field of the conventional shaped microelectrode was facing the bulk of the solution rather than the water-air interface. Because of this, the convection created when the meniscus was being pushed and broken did not affect the current recorded. However, not only the shape of the electrode and the orientation of the diffusion field seemed to affect the response obtained when approaching the water-air interface. In order to investigate this, approach curves were recorded using submarine microelectrodes with different RG and scan velocity. The submarine 25 µm diameter Pt disc employed for these curves is shown in Figure 4.8 placed 500 µm below the meniscus of the solution at $d = 0\,\mu m$ and at $d = 500\,\mu m$ touching the meniscus.

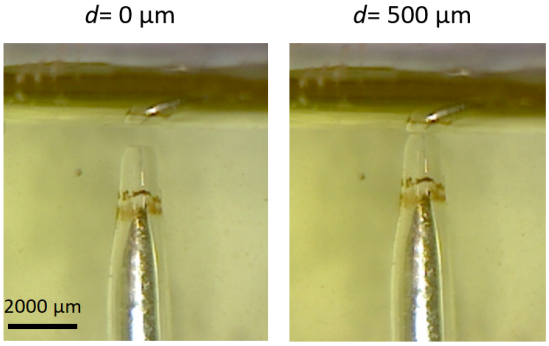

Figure 4.8: Micrograph of a submarine 25 µm diameter Pt disc in an aerated 1 mM FcMeOH in 500 mM NaCl solution at the position set as $d = 0\,\mu m$ (left), and at $d = 500\,\mu m$ (right). $RG = 25$.

Figure 4.9 shows the effect of the scan velocity in the approach curves recorded using an unconfined meniscus and a submarine microelectrode. For these curves the microelectrode was positioned 500 µm below the meniscus, and the approach curve was performed until the current measured was close zero.

These approach curves show that the higher the scan velocity, the higher the peak current. This is thought to result from the convection created when the electrode moved towards the water-air interface. A reference point to observe the increase of the convection could be the current spike observed when the electrode broke the meniscus,

which increases systematically with the scan velocity. After this feature, the current dropped to about 0.1 nA and then to zero as the electrode was coming out of the solution and its surface was uncovered by the solution. This experiment supports the interpretation of the approach curves shown in Figure 4.4. The current spike observed can then be related to the convection created by the electrode breaking the meniscus of the solution, however, these curves do not explain the current drop before this.

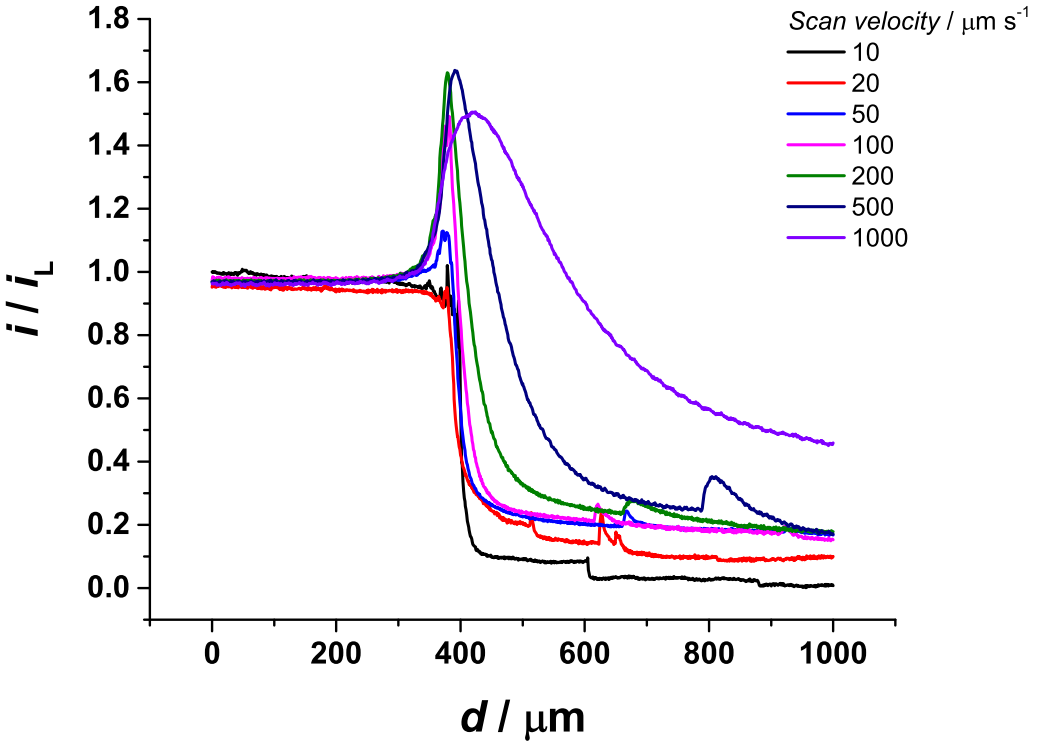

Figure 4.9: Approach curves recorded with a submarine 25 µm diameter Pt disc in an aerated 1 mM FcMeOH in 500 mM NaCl solution holding the potential at 0.4 V vs SCE. The electrode was conditioned by holding the potential at 0.4 V for 100 s. The data was acquired using the sweep scan mode with a step size of 1 µm and varied scan velocity. The current was normalized by $i_L = 4.33 \times 10^{-9}$ A. $RG = 25$.

Figure 4.10 shows the same experiment using a submarine electrode with $RG = 100$. A similar trend to the curves in Figure 4.9 is observed in these curves, however, with a larger amount of glass surrounding the electrode, the current seems to be less stable and there is a higher increase of current around 400 µm due to the convection created when the electrode breaks the meniscus.

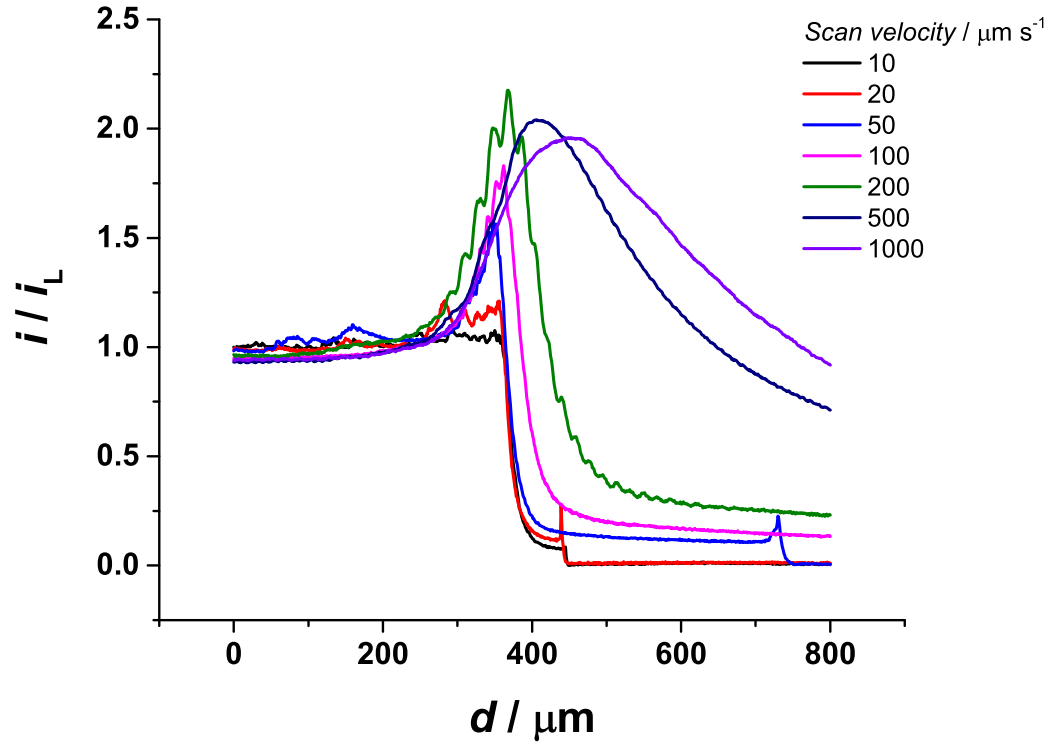

Figure 4.10: Approach curves recorded with a 25 µm diameter Pt disc in an aerated 1 mM FcMeOH in 500 mM NaCl solution holding the potential at 0.4 V vs SCE. The electrode was conditioned by holding the potential at 0.4 V for 100 s. The data was acquired using the sweep scan mode with a step size of 1 µm and varied scan velocity. The current was normalized by $i_L = 4.33 \times 10^{-9}$ A. $RG = 100$.

The investigation of the water-air interface using an unconfined meniscus seems to be susceptible to several experimental factors. An alternative to avoid the contribution of convection to the approach curves recorded in the region where hindered diffusion should be observed was to confine the meniscus. This is discussed in the next section.

4.1.1.2 Confined meniscus

The experiments in this section were performed using a confined meniscus in order to avoid contributions of convection in the amperometric response. In order to achieve this, a baffle with a 6 mm diameter hole was placed on top of the cell as described in section 3.5.1. The effect of the confinement is to force the meniscus to take a hemispherical shape. Figure 4.11 shows the confined water-air interface (left) and the same interface when the electrode was at $d = 4740$ µm (right).

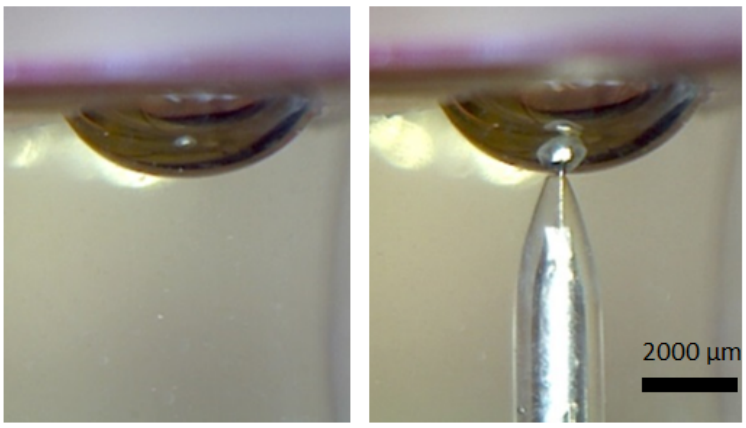

Figure 4.11: Micrograph of the confined water-air interface (left), and a submarine 25 µm diameter Pt disc in an aerated 1 mM FcMeOH in 500 mM NaCl solution at $d = 4740\,\mu m$ (right). $RG = 18$.

The methodology employed to investigate the confined water-air interface was the same as that used for the water-air interface with an unconfined meniscus. LSVs and chronoamperograms were recorded one after the other after moving the submarine microelectrode in 1000 µm steps from $d = 0\,\mu m$ to $d = 4000\,\mu m$, then every 100 µm, and 50 µm when getting closer to the confined water-air interface. After the electrode touched the water-air interface, the electrode was placed back in the bulk ($d = 0\,\mu m$) and electrochemically reconditioned by cycling the potential from 1 V to -1 V at $500\,mV\,s^{-1}$. Then approach curves from $d = 0\,\mu m$ to $d = 5000\,\mu m$ were recorded using step scan and sweep scan modes.

The LSVs and potential steps recorded at different electrode-interface positions are shown in Figure 4.12. Both figures show that the limiting current of the oxidation of FcMeOH from $d = 0\,\mu m$ to $d = 4720\,\mu m$ agrees with the theoretical expectations according to equation 2.11. Then, the current decreased when the electrode was positioned at $d = 4730\,\mu m$, which according to Figure 4.11 was 10 µm away from the water-air interface. The limiting current extracted from both experiments and plotted vs distance is shown in Figure 4.13.

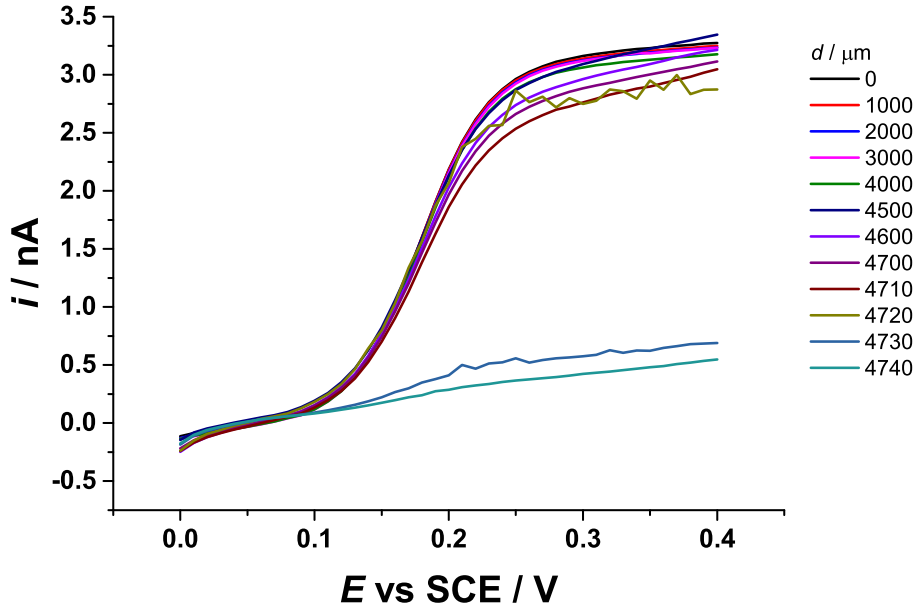

(a) LSVs

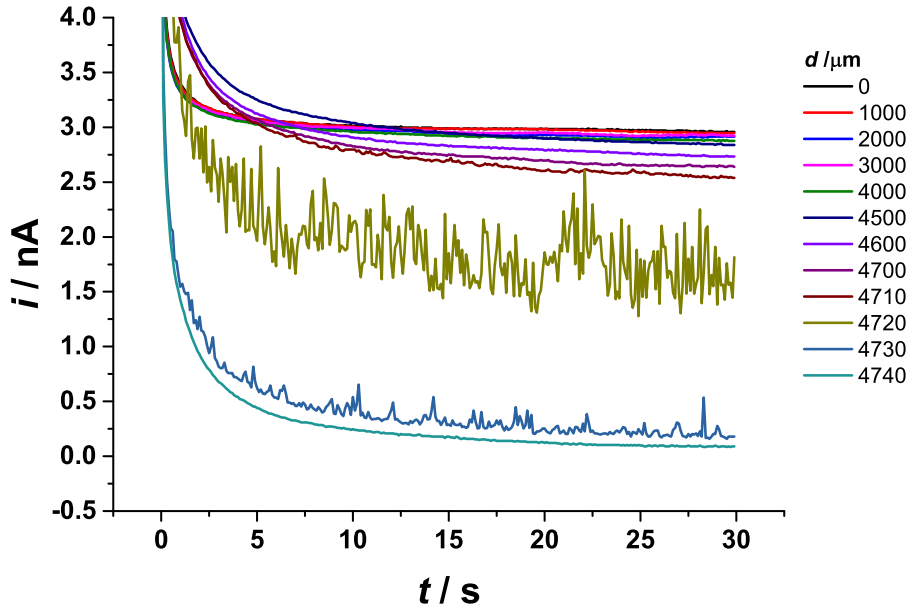

(b) Chronoamperograms

Figure 4.12: LSVs (a) and chronoamperograms (b) recorded with a submarine 25 µm diameter Pt disc at different distances to the water-air interface in an aerated 1 mM FcMeOH in 500 mM NaCl solution. The position $d = 0\,\mu m$ corresponds to the electrode in the bulk, and $d = 4740\,\mu m$ when it was touching the water-air interface. LSVs were acquired at $0.010\,V\,s^{-1}$. The potential was stepped from 0.0 V to 0.4 V vs SCE. $RG = 18$.

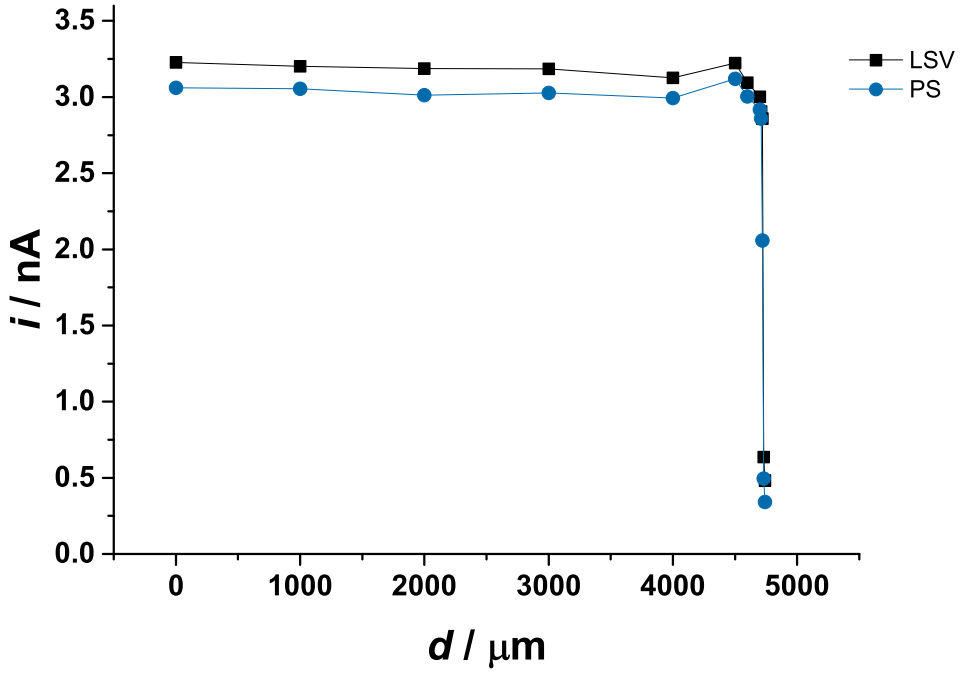

Figure 4.13: Limiting current from LSVs and potential steps (PS) from the experiments in Figure 4.12 as a function of the electrode water-air interface distance. The current from LSVs was extracted at E=0.4 V vs SCE, and at t=30 s in the chronoamperograms. The black points correspond to the limiting current from the LSVs, and the blue from the potential steps.

Once more the trend observed in the reconstructed approach curves shows agreement between the current from LSVs and chronoamperograms. Hindered diffusion is not observed at 125 µm away from the water-air interface as expected, but a slight increase of current before it dropped close to zero. This trend was then compared to the approach curves. Figure 4.14 shows micrographs of the submarine microelectrode at different distances with respect to the confined water-air interface that served as reference to record the approach curves. In the middle and right micrographs of Figure 4.14 it is possible to appreciate that the tip of the microelectrode is able to deform the water-air interface. This supports the hypothesis that an unconfined water-air interface is like an elastic barrier, and by confining the meniscus, we increase its mechanical stability.

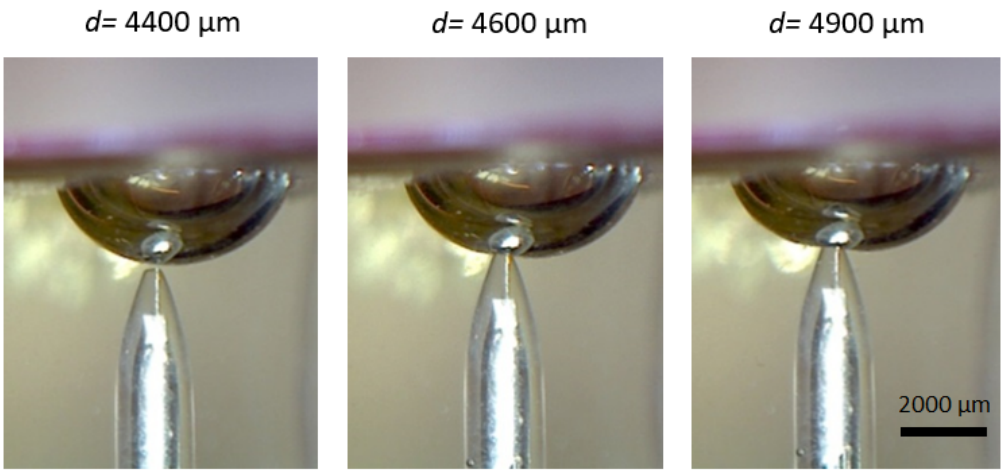

Figure 4.14: Micrographs of a submarine 25 µm diameter Pt disc in an aerated 1 mM FcMeOH in 500 mM NaCl solution at $d = 4400\,\mu m$ (left), $d = 4600\,\mu m$ (middle), and $d = 4900\,\mu m$ (right). $RG = 18$.

Figure 4.15 shows the approach curves recorded to investigate the region just before the rise of current observed in previous experiments. The reverse scan was acquired to further understand the reproducibility of the measurement. The step size in these curves was 5 µm, to acquire more data points, and the scan velocity was $10\,\mu m\,s^{-1}$ to avoid contributions of convection to the current. The first curve (black in Figure 4.15) was acquired from 4000 µm to 4900 µm and back. The second curve (blue in Figure 4.15) was recorded with the aim to approach the top 500 µm of the solution, but because the black curve showed that the electrode was out of the solution at 4600 µm it was acquired from 4400 µm to 4700 µm and back.

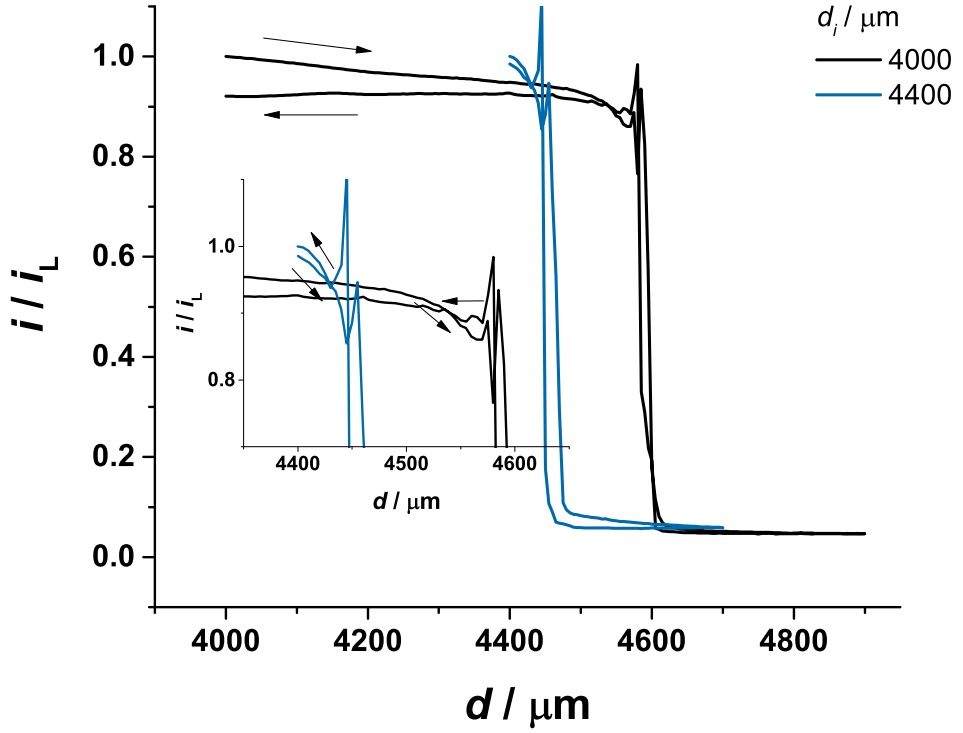

Figure 4.15: Approach curves recorded with a submarine 25 µm diameter Pt disc in an aerated 1 mM FcMeOH in 500 mM NaCl solution holding the potential at 0.4 V vs SCE. The electrode was conditioned by holding the potential at 0.4 V for 100 s. The data was acquired using the step scan mode with a step size of 5 µm at 10 µm s^{-1}. The forward and reverse scan are shown. The distance at which the experiment was started is indicated in the label (d_i). The insert is a closer look to the convection peaks created when the electrode approached the water-air interface. The current was normalized by $i_L = 2.87 \times 10^{-9}$ A. $RG = 18$.

The decrease of current from 4000 µm to 4500 µm in the forward scan of the black approach curve in Figure 4.15 is believed to ocurr due to an insufficient preconditioning time. However, the drop of current observed from 4500 µm to 4600 µm corresponds to the hindered diffusion of FcMeOH by the water-air interface.

As observed in previous measurements, a minimum followed by a current spike, which corresponded to the response recorded when the meniscus was being pushed and broken, was observed in these approach curves. After that, there was no solution left at the surface of the electrode, so the current dropped to zero. The reverse scan showed a hysteresis of 10 µm with respect to the forward scan, which could be related to how

much the electrode "stretched" the meniscus on its way out. On the way back to the solution, the surface of the electrode was covered with a stagnant layer of solution, and when it got detached from it, more convection was created than on its way out. This could be why the current spike was bigger on the reverse scan (at $d = 4590\,\mu m$) than on the forward scan (at $d = 4600\,\mu m$). The size of the convection peaks is highlighted in the insert of Figure 4.15.

An important observation is that the current on the way back was more stable than on the forward scan, which could be related to the fact that the electrode recorded current zero from $d = 4600\,\mu m$ to $d = 4900\,\mu m$. This could have worked like a potential step that reconditioned the electrode surface.

The blue approach curve in Figure 4.15 showed the features observed in the black curve previously recorded, including the minimum of current before the spike. What is remarkable is the fact that the blue curve is shifted 150 µm with respect to the black curve. This suggests that the electrode-interface distance decreased 150 µm during the time it took to perform the reverse scan of the black curve and the electrochemical cleaning of the electrode.

This observation is strong evidence that the water-air interface changed with time, and that the microelectrode was capable of tracking this change accurately. Because of this, the investigation of the water-SML interface was carried out employing a similar methodology to the water-air interface. The results are shown in the next section.

4.2 The water-SML interface

The experiments in section 4.1 showed that the approach curves recorded with the submarine microelectrodes are affected by convection created by the velocity at which the electrode moves towards the water-air interface. Also, that the amount of glass surrounding the microwire contributes to the convection created by the electrode, particularly because of the affinity of water to glass. Overall, the results suggested that the water-air interface behaves like an elastic barrier that is more stable when is confined. In this section we investigated the effect in the response after adding the synthetic SML. Therefore, this section is divided in 2 parts: the influence of the size of the meniscus in section 4.2.1 and the effect of the composition of the SML in section 4.2.2. To study the effect of the size of the meniscus we employed only the SECM feedback mode, but to investigate the effect of the composition of the SML we employed LSVs, chronoamperograms and approach curves.

4.2.1 Influence of the size of the meniscus

This section shows the investigation of the water-SML interface using submarine Pt microelectrodes and the SECM feedback mode.

The methodology consisted in recording approach curves after adding an aliquot of a 30% w.t. $C_{16}EO_8$ solution on top of the water-air interface to form a synthetic SML. Section 4.2.1.1 and 4.2.1.2 show the experiments performed using an unconfined and a confined water-SML interface respectively.

4.2.1.1 Unconfined meniscus

The water-SML interface was formed after adding a 100 µL aliquot of a 30% w.t. $C_{16}EO_8$ on top of the water-air interface. Figure 4.16 shows micrographs of the experimental arrangement employed with the microelectrode placed at $d = 0$ µm before adding the SML and at $d = 5000$ µm after adding the synthetic SML. These show a layer of synthetic SML at the water-air interface.

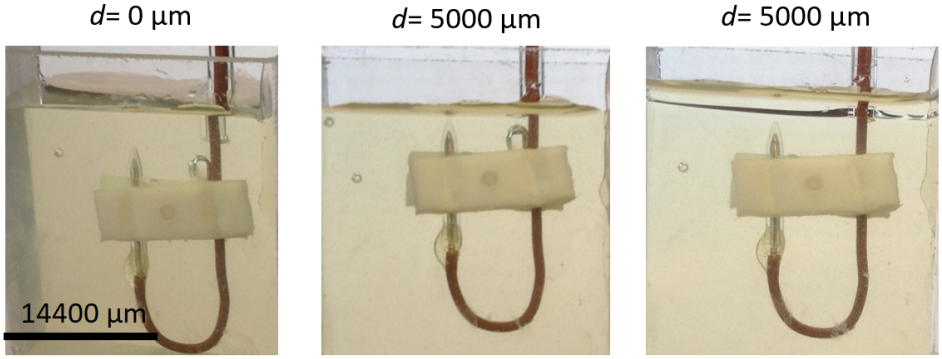

Figure 4.16: Micrographs of a submarine 25 µm diameter Pt disc in an aerated 1 mM FcMeOH in 500 mM NaCl solution before adding the synthetic SML at $d = 0$ µm (left) and $d = 5000$ µm (middle), and after adding the synthetic SML at $d = 5000$ µm (right).

Approach curves recorded before and after the synthetic SML was added to the solution are shown in Figure 4.17. These curves were recorded using a scan velocity of 100 µm s^{-1} to highlight the effect of the addition of the synthetic SML to the current spike that appears due to the convection created by the electrode breaking the meniscus.

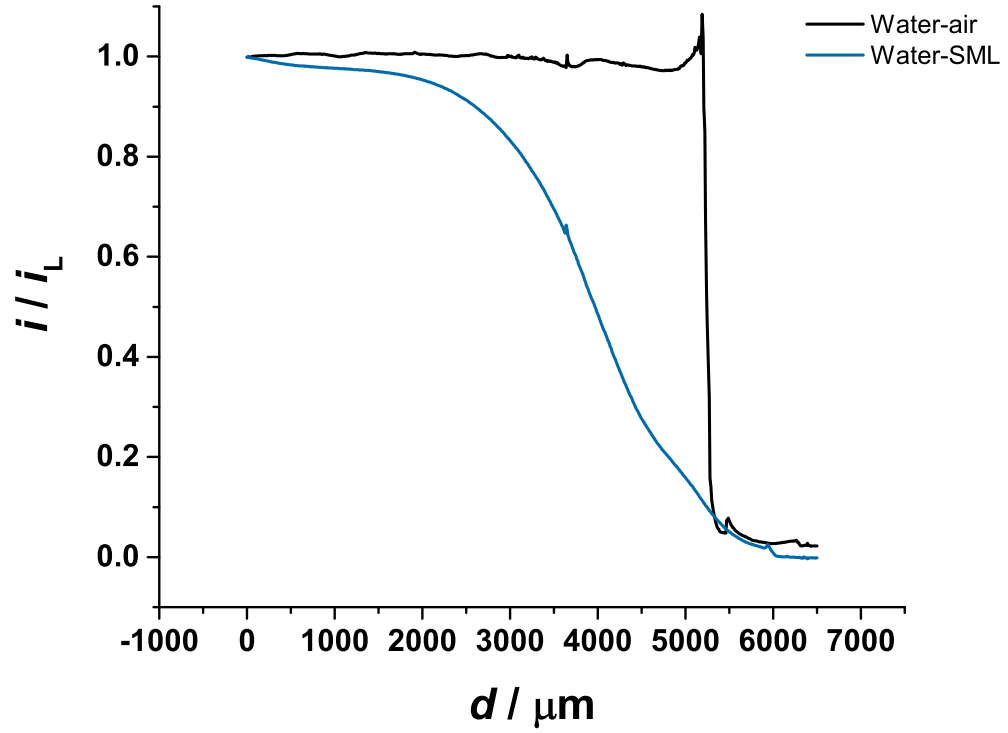

Figure 4.17: Approach curves recorded with a submarine 25 µm diameter Pt disc in an aerated 1 mM FcMeOH in 500 mM NaCl solution holding the potential at 0.4 V vs SCE. The electrode was conditioned by holding the potential at 0.4 V for 100 s. The data was acquired using the step scan mode with a step size of 10 µm at 100 µm s^{-1}. The SML consisted of 100 µL of a 30% w.t. $C_{16}EO_8$ solution. The current was normalized by $i_L = 3.65 \times 10^{-9}$ A. $RG = 18$.

Without SML, the approach curves in Figure 4.17 showed the features previously discussed: the current remains the same until the electrode reaches the water-air interface, then a spike is observed due to the meniscus being broken by the electrode. The curve recorded after adding the surfactant showed the current dropping when the electrode was 2000 µm way from the water-SML interface. This was remarkably far from the theoretical expectations for hindered diffusion, 87.5 µm to 125 µm ($7a$ -$10a$). The reason why this response was observed could be related to the viscosity gradient between the bulk and the water-air interface created after the synthetic SML was added. Also, it is possible that adding the surfactant made the interaction with the electrode glass less significant. This could be why the spike of current created when the electrode pops out of the solution is not observed after adding the synthetic SML.

Figure 4.18 shows that the approach curves recorded with a conventional shaped microelectrode follow a similar trend. The limiting current drops from the beginning of the measurement and the spike of current close to the water-SML interface is not observed. However, compared to the curves in Figure 4.17 that showed a continuous drop of current, in this curve the current decreased abruptly once the electrode was out of the solution at $d = 1150\,\mu m$. This is believed to be due to the orientation of the diffusion field, which is facing down the bulk rather than the viscous layer at the interface. In this case, when the electrode leaves the solution it does not push the meniscus on its way out.

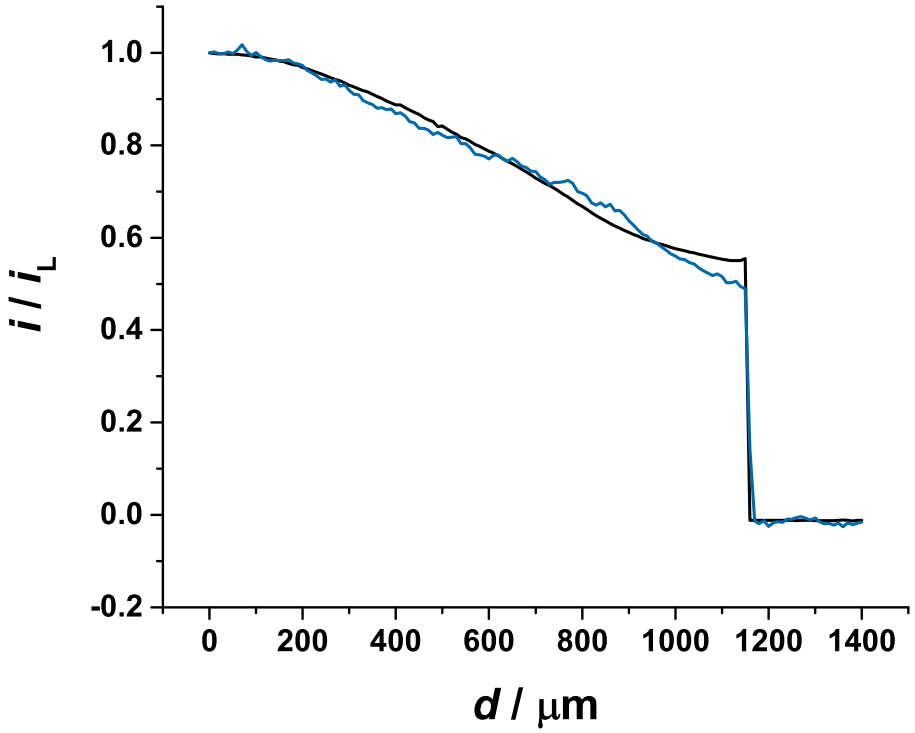

Figure 4.18: Approach curves recorded with a conventional shaped 25 µm diameter Pt disc electrode in a 1 mM FcMeOH + 0.5 M NaCl solution holding the potential at 0.4 V. The electrode was conditioned by holding the potential at 0.4 V for 100 s. The data was acquired using the step scan mode (black) and the sweep scan mode (blue) with a step size of 1 µm at $10\,\mu m\,s^{-1}$. The synthetic SML consisted of 100 µL of a 30% w.t. $C_{16}EO_8$ solution. The current was normalized by $i_L = 2.0 \times 10^{-9}$ A. $RG = 15$.

The next section shows the experiments performed to investigate the effect of confining the water-SML interface.

4.2.1.2 Confined meniscus

To investigate the confined water-SML interface, the electrode was positioned underneath the water-air interface as shown on the left of Figure 4.19. The micrograph in the middle ($d = 4500\,\mu m$) shows the electrode positioned 500 µm away from the water-air interface as 10 µL of the synthetic SML were added. The micrograph on the right ($d = 4500\,\mu m$) suggests that the distance between the electrode and the water-SML decreased after the addition of SML.

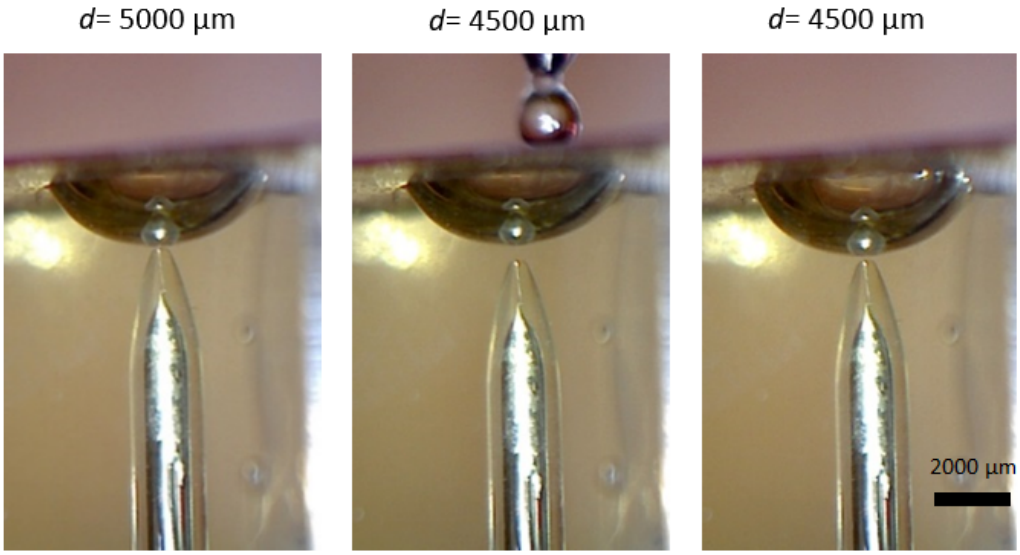

Figure 4.19: Micrographs of a submarine 25 µm diameter Pt disc in an aerated 1 mM FcMeOH in 500 mM NaCl solution at $d = 5000\,\mu m$ before adding the synthetic SML (left), at $d = 4500\,\mu m$ during the addition of the synthetic SML where a drop of the SML can be seen just above the hole in the baffle cover (middle), and at $d = 4500\,\mu m$ after the corresponding addition (right). The SML consisted in 10 µL of a solution made with 0.8 mL of a 30% w.t. $C_{16}EO_8$ in 0.2 mL of heptane. $RG = 18$.

The approach curves recorded before and after the addition of the synthetic SML are shown in Figure 4.20. These were recorded using a step size of 2 µm at $10\,\mu m\,s^{-1}$, which allowed us to acquire more data without inducing convection.

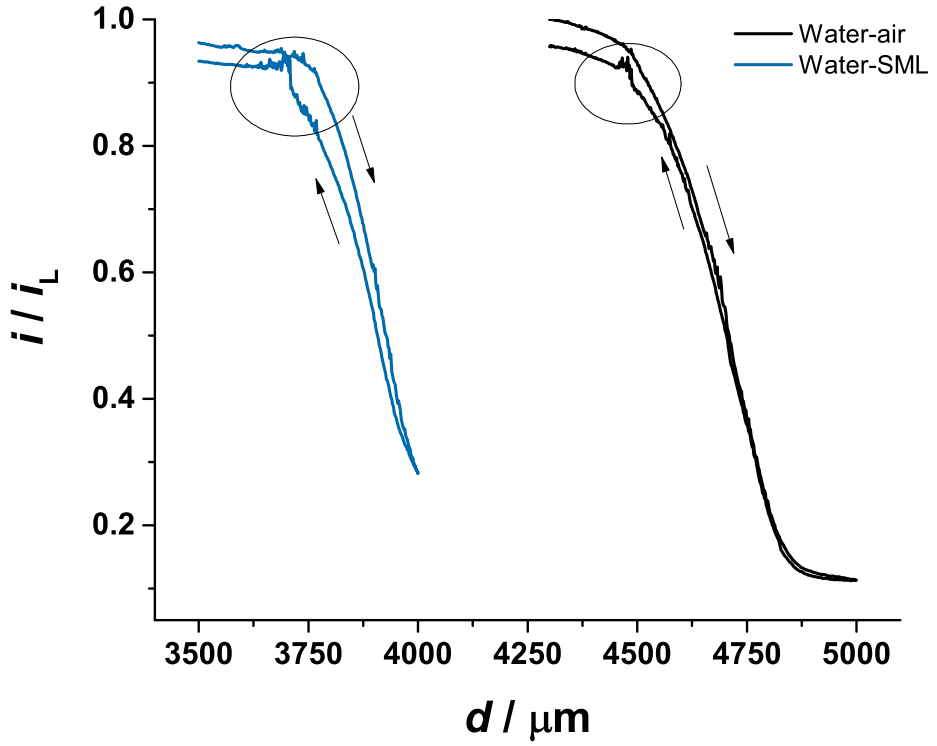

Figure 4.20: Approach curves recorded with a submarine 25 µm diameter Pt disc in an aerated 1 mM FcMeOH + 0.5 M NaCl solution holding the potential at 0.4 V. The current was conditioned by holding the potential at 0.4 V for 100 s. The data was acquired using the step scan mode with a step size of 2 µm at 10 µm s^{-1}. The forward and reverse scans are shown. The SML consisted in 10 µL of a solution made with 0.8 mL of a 30% w.t. $C_{16}EO_8$ in 0.2 mL of heptane. The current was normalized by $i_L = 3.08 \times 10^{-9}$ A. $RG = 18$.

For these curves the electrode was moved only 600 µm towards the water-air interface. The black curve recorded in absence of synthetic SML showed the current decreasing to 0.1 nA when presumably the electrode was out of the solution at $d = 5000$ µm. Then, on its way back to the solution, the current of the reverse scan showed the spikes previously observed when the electrode drags a layer of water towards the bulk (black circle in Figure 4.20). After adding the synthetic SML the electrode was moved back 1000 µm because the addition of the synthetic SML caused the tip-substrate distance to decrease as shown in Figure 4.19. The current in the approach curve recorded after adding the synthetic SML (blue curve) remained the same up to $d = 3650$ µm and then it dropped until the reverse scan started. The forward scan showed evidence of convec-

tion when the meniscus was pushed and broken by the electrode. In the reverse scan, the current spikes were bigger compared to the forward scan, and the hysteresis for this curve was higher compared to the black curve. It could be that after adding the SML the local viscosity changed but because the meniscus was confined, its stability did not decrease. This would explain why the current spikes that appear by the convection created by the electrode coming back to the solution are visible in the approach curve recorded after adding the synthetic SML. The change of the local viscosity could be the reason why the current after adding the SML was more stable compared to the black curve.

These approach curves were remarkably different to those acquired using an unconfined water-air interface. Using an unconfined meniscus provided approach curves that showed the current dropping not in agreement with hindered diffusion expectations. This very early decrease of current might be related to an increase of the local viscosity, which causes the drop of the diffusion coefficient of FcMeOH in the media. In order to investigate this, LSVs and chronoamperograms were recorded at different tip-substrate distances using two synthetic SML approximations. The effect of the variations of the diffusion coefficient, and concentration of the redox pair in the transient response was investigated through the fitting of the chronoamperometric data to the Mahon and Oldham equation. The results of these experiments are shown in section 4.2.2.

4.2.2 Influence of the SML composition

The experiments in this section were performed employing an unconfined meniscus because the contributions to the current due to convection were minimal using a low scan velocity and after adding the synthetic SML. Also, an unconfined meniscus is a more accurate representation of the water-SML interface in the field which is important for the application of this research. The two synthetic SML were made of a mixture of a 30% w.t. $C_{16}EO_8$ solution with an organic solvent. This was because when using only a 30% w.t. $C_{16}EO_8$ solution, the SML mixed with the solution below over time. We believe that the effect of adding an organic solvent to the synthetic SML allowed it to remain at the water-air interface for longer. The first synthetic SML consisted in a mixture of 0.8 mL of a 30% wt. $C_{16}EO_8$ + 0.2 mL of ethanol, referred as SML1 from now on. Figure 4.21 shows the electrode before adding the SML at $d = 4500\,\mu m$ and at $d = 5000\,\mu m$ after adding 0.8 g of the SML. Note that no boundary between the water and the SML was possible to appreciate, but a thickening of the meniscus.

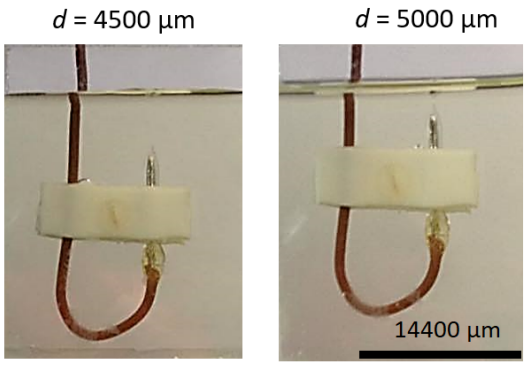

Figure 4.21: Micrographs of a submarine 25 µm diameter Pt disc in an aerated 1 mM FcMeOH in 500 mM NaCl solution at $d = 4500\,\mu m$ before adding the synthetic SML and at $d = 5000\,\mu m$ after adding of the synthetic SML. SML1: 0.8 mL of a 30% wt. $C_{16}EO_8$ + 0.2 mL of ethanol.

The second synthetic SML consisted in a mixture of 0.8 mL of a 30% wt. $C_{16}EO_8$ + 0.2 mL of heptane, and will be referred as SML2. Figure 4.22 shows the electrode before the addition, after the addition (at $d = 0\,\mu m$), and the interface an hour after the addition (at $d = 5000\,\mu m$). Using this synthetic SML it was clearly observed how the SML mixed with the solution below over time.

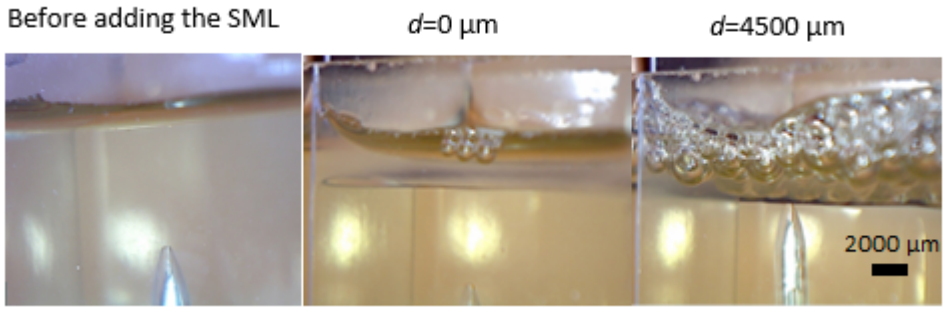

Figure 4.22: Micrographs of a submarine 25 µm diameter Pt disc in an aerated 1 mM FcMeOH in 500 mM NaCl solution at $d = 0\,\mu m$ before adding the SML, and at $d = 0\,\mu m$ and $d = 4500\,\mu m$ after adding the SML. SML2: 0.8 mL of a 30% wt. $C_{16}EO_8$ + 0.2 mL of heptane.

The methodology consisted in recording LSVs and chronoamperograms one after the other as the submarine microelectrode was moved in 1000 µm steps from $d = 0\,\mu m$ to $d = 3000\,\mu m$, then every 500 µm, and 100 µm when getting closer to the water-SML interface ($d = 5000\,\mu m$). After the electrode reached the water-SML interface, it was

placed back in the bulk ($d = 0\,\mu m$) and electrochemically reconditioned by cycling the potential from 1 V to -1 V at $500\,mV\,s^{-1}$. The approach curves were recorded using the step scan mode first and the sweep scan mode after.

The LSVs and chronoamperograms acquired at different electrode water-SML interface positions using SML1 and SML2 are shown in Figure 4.23 and Figure 4.24. Compared to the measurements acquired in the proximities of the water-air interface, the voltammetry close to the water-SML interface shows a uniform decay of the limiting current as the electrode approaches the interface. Once more, the current does not follow the theoretical expectations when approaching to an insulator.

The plots in Figure 4.25 were built by extracting the limiting current from the LSVs and chronoamperograms shown in Figure 4.24 and 4.23. The current from the LSVs was taken at E=0.4 V vs SCE and from the chronoamperograms at t=30 s. These showed agreement between both experiments. The current at the starting position agreed with theoretical expectations (circa 3 nA according to equation 2.11); however, it decreased systematically as the electrode was moved closer to the interface.

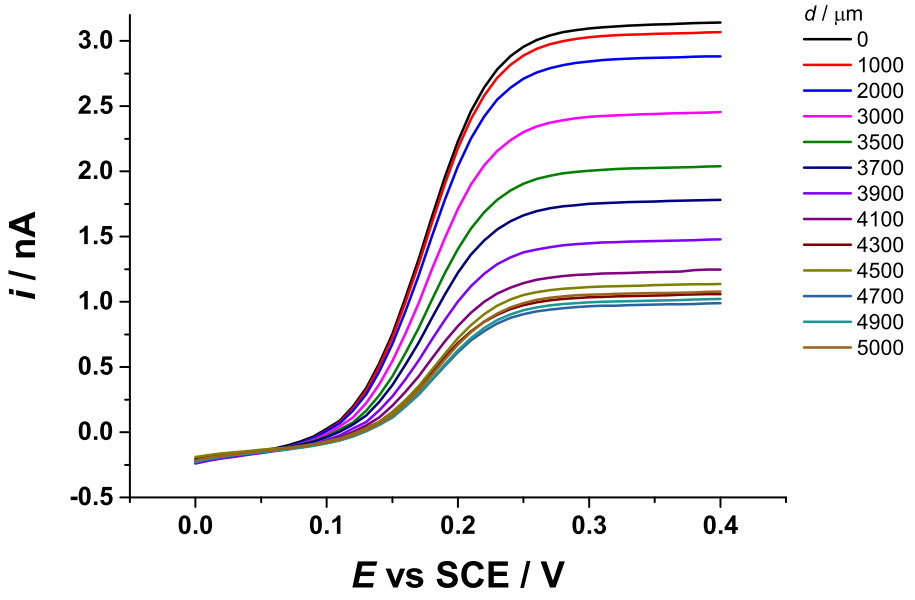

(a) LSVs

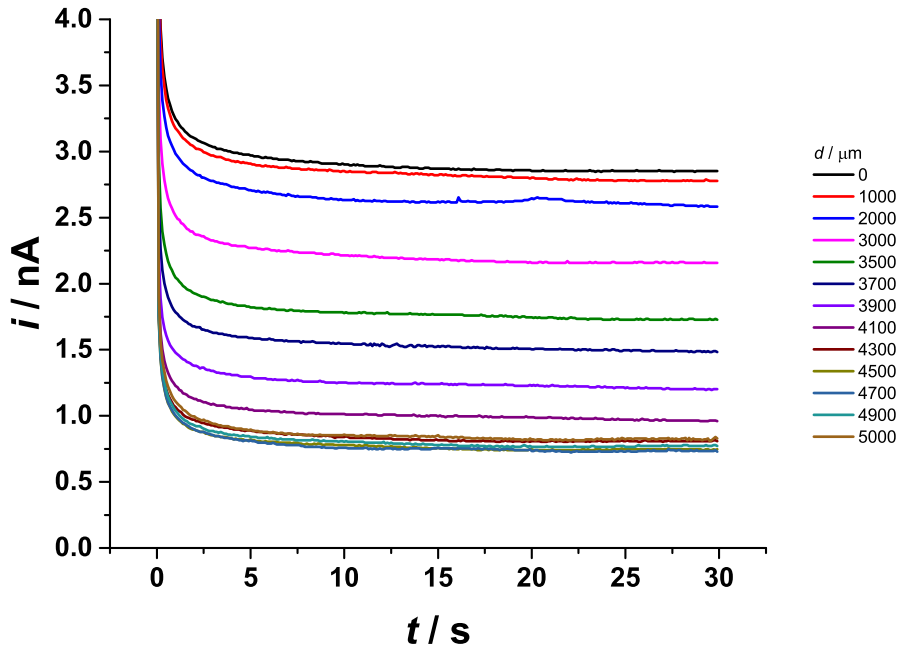

(b) Chronoamperograms

Figure 4.23: LSVs (a) and chronoamperograms (b) recorded with a submarine 25 µm diameter Pt disc at different distances to the water-SML interface in an aerated 1 mM FcMeOH in 500 mM NaCl solution + 0.8 g of SML1. The position $d = 0\,\mu m$ corresponds to the electrode in the bulk, and $d = 5000\,\mu m$ when it was touching the SML-air interface. LSVs were acquired at $0.010\,V\,s^{-1}$. The potential was stepped from 0.0 V to 0.4 V vs SCE. $RG = 18$.

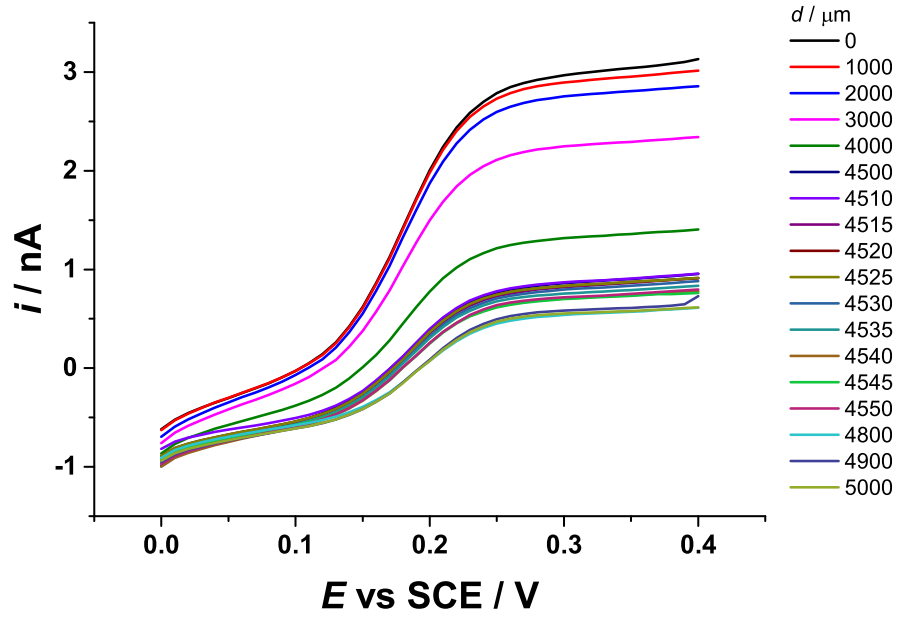

(a) LSVs

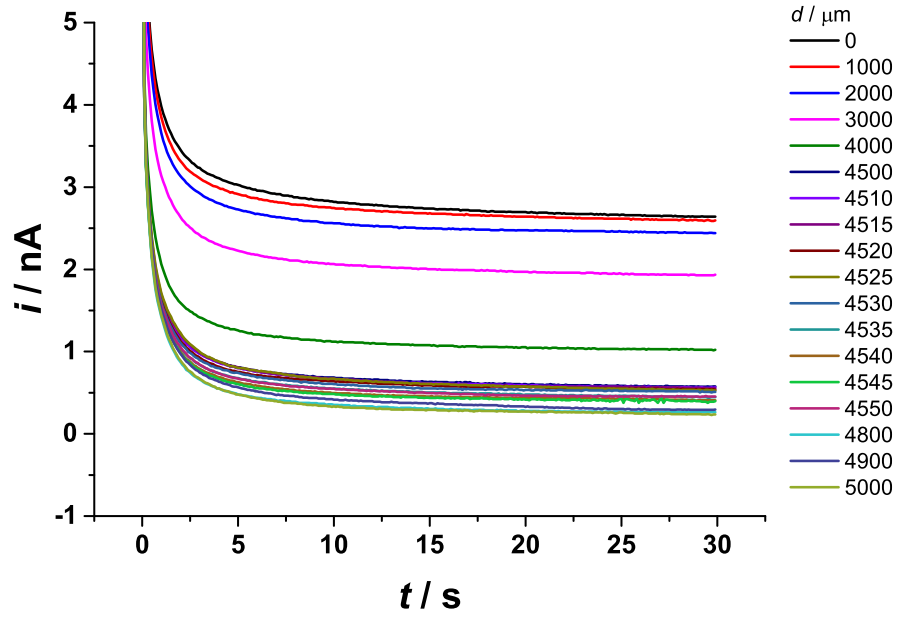

(b) Chronoamperograms

Figure 4.24: LSVs (a) and chronoamperograms (b) recorded with a submarine 25 µm diameter Pt disc at different distances to the water-SML interface in an aerated 1 mM FcMeOH in 500 mM NaCl solution + 0.8 g of SML2. The position $d = 0\,\mu m$ corresponds to the electrode in the bulk, and $d = 5000\,\mu m$ when it was touching the SML-air interface. LSVs were acquired at $0.010\,V\,s^{-1}$. The potential was stepped from 0.0 V to 0.4 V vs SCE. $RG = 18$.

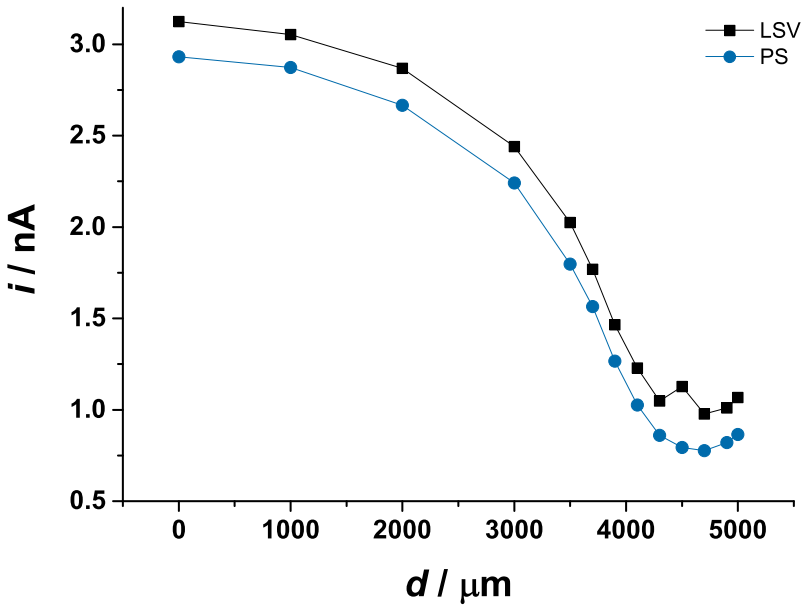

(a) SML1: 30% wt. $C_{16}EO_8$ + ethanol

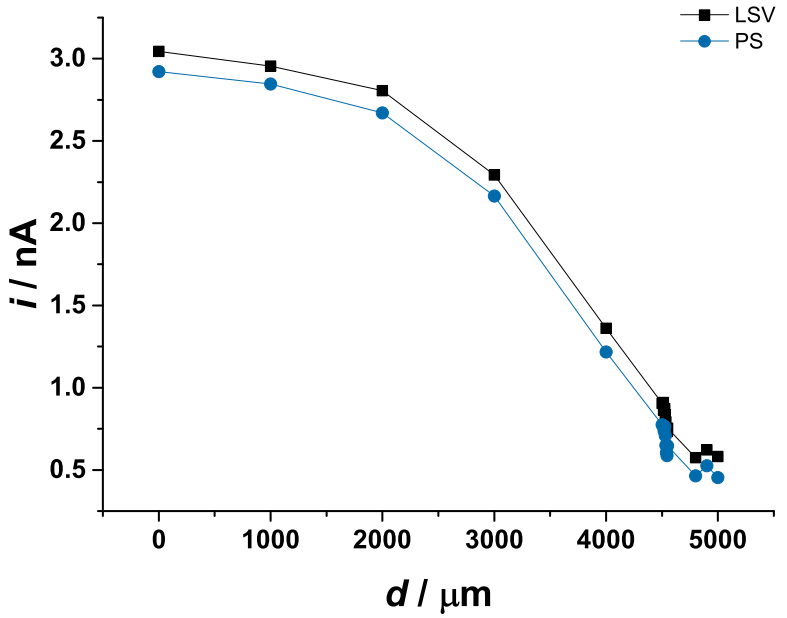

(b) SML2: 30% wt. $C_{16}EO_8$ + heptane

Figure 4.25: Limiting current from LSVs and potential steps (PS) from the experiments in Figure 4.23 and 4.24 as a function of the electrode water-SML interface distance. The current from LSVs was extracted at E=0.4 V vs SCE, and at t=30 s in the chronoamperograms. The black points correspond to the limiting current from the LSVs, and the blue from the potential steps.

The LSVs in Figure 4.23 show a more positive half-wave potential ($E_{1/2}$) as the electrode approached the water-SML interface. To investigate this, the $E_{1/2}$ was extracted from the LSVs using the "interpolate/extrapolate y from x" tool in Origin lab 9.0. The result is shown in Figure 4.26.

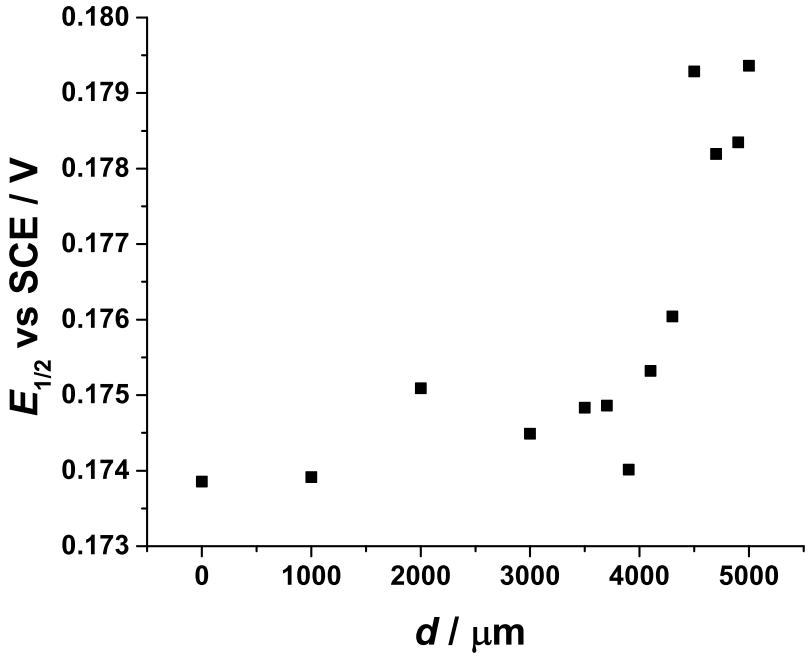

Figure 4.26: $E_{1/2}$ vs d extracted from LSVs in Figure 4.23.

The response seems to be in 2 groups: from 0 µm to 4000 µm (the bulk) and from 4000 µm to 5000 µm (the water-SML interface). In the bulk, the $E_{1/2}$ remained consistent, but at the water-SML interface it became more positive. This might occur because the oxidation of FcMeOH in the synthetic SML requires a larger driving force than in the bulk.

The trend observed in the LSVs and the chronoamperograms is comparable with the approach curves shown in Figure 4.27. The current in these also decreased earlier than expected.

The agreement between LSVs, chronoamperograms and approach curves for both SML1 and SML2 suggests that the composition of the SML does not determine the response. The trend in current might be given by the change of local viscosity at the water-air interface.

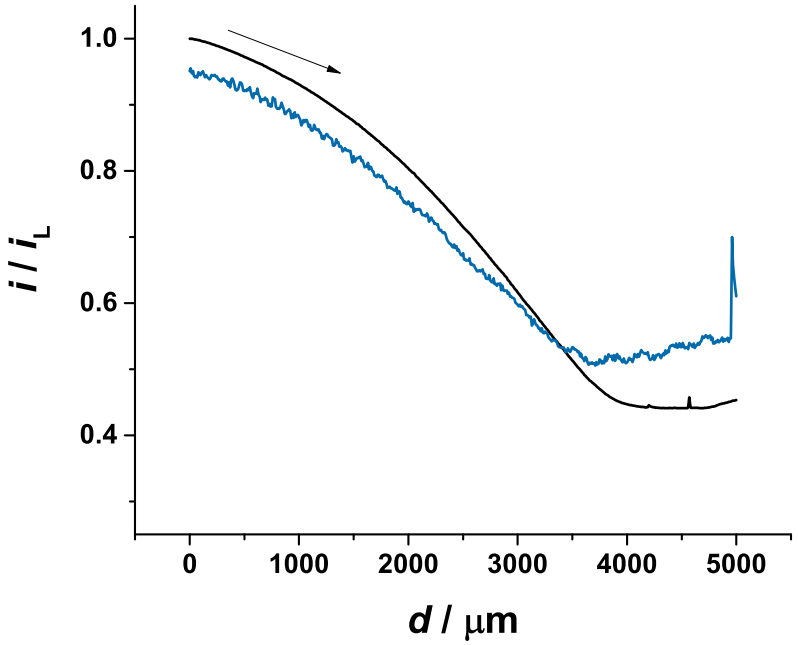

(a) SML1: 30% wt. $C_{16}EO_8$ + ethanol

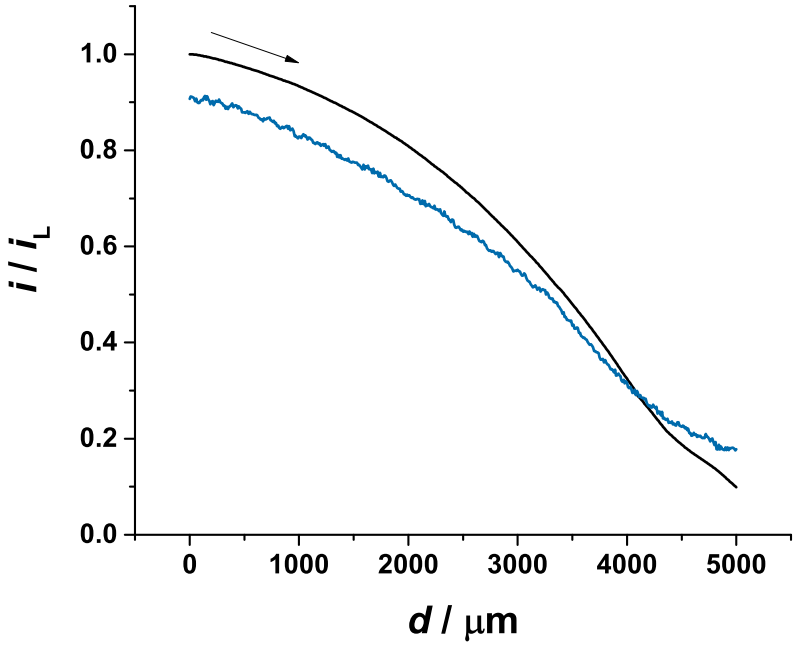

(b) SML2: 30% wt. $C_{16}EO_8$ + heptane

Figure 4.27: Approach curves recorded with a submarine 25 µm diameter Pt disc in an aerated 1 mM FcMeOH + 500 mM NaCl solution + 0.8 g of SML. The electrode was conditioned by holding the potential at 0.4 V for 100 s. The data was acquired using the step scan mode (black) and the sweep scan mode (blue) with a step size of 10 µm at 10 µm s^{-1}. The current was normalized by $i_L = 2.70 \times 10^{-9}$ A. $RG = 18$.

In order to investigate the dependence of the current with the changes of concentration (C) and diffusion coefficient (D) of FcMeOH, the chronoamperometric data obtained for each interface were fitted to the Mahon and Oldham equation through a non-linear regression. This was possible because the chronoamperometric current at short times is proportional to $D^{-1/2}$, and proportional to D at long times. This means that it is possible to decouple D and C when the number of electrons transferred (n) and the radius of the microdisc (a) are known [101].

The number of electrons and the size of the electrode were fixed parameters, and D and C of FcMeOH were free variables with limits from $1 \times 10^{-9}\,\mathrm{cm\,s^{-1}}$ to $1 \times 10^{-4}\,\mathrm{cm\,s^{-1}}$, and $1 \times 10^{-9}\,\mathrm{mol\,cm^{-3}}$ to $1 \times 10^{-4}\,\mathrm{mol\,cm^{-3}}$ respectively. The details of the fitting are shown in Appendix A.

A plot of the D and C values obtained for each SML as a function of distance (d) are shown in Figure 4.28.

Figure 4.28 (a) shows that D was consistent from $d = 0\,\mu\mathrm{m}$ to $d = 2000\,\mu\mathrm{m}$, then it decreased systematically as the microelectrode approached the water-SML interface. In Figure 4.28 (b) the FcMeOH diffusion coefficient in presence of SML2 showed a similar trend to the values obtained with SML1. From $d = 0\,\mu\mathrm{m}$ to $d = 2000\,\mu\mathrm{m}$ oscillated around the bulk value, and from $d = 3000\,\mu\mathrm{m}$ to $d = 5000\,\mu\mathrm{m}$ it decreased systematically.

This is in agreement to theoretical expectations. According to the Stokes-Einstein equation (diffusion of spherical particles through a liquid with low Reynolds number):

$$D = \frac{K_b T}{6\pi\eta r} \tag{4.1}$$

Where K_b is the Boltzmann constant, T is the absolute temperature, η is the dynamic viscosity and r is the radius of the spherical particle.

The diffusion coefficient is inversely proportional to the viscosity of the media. Therefore, as moving into the SML, a layer with higher viscosity, the diffusion coefficient of the redox species was expected to decrease.

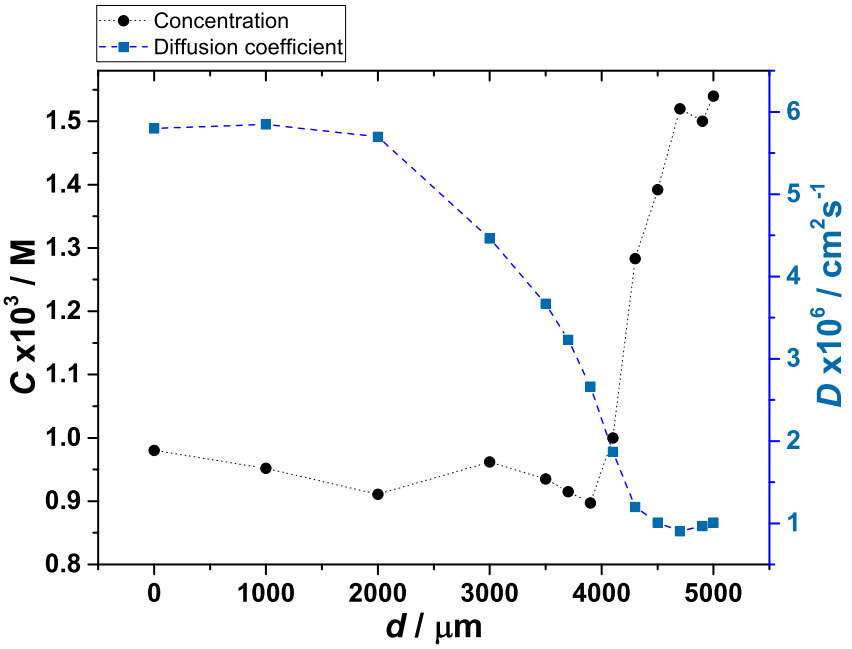

(a) SML1: 30% wt. $C_{16}EO_8$ + ethanol

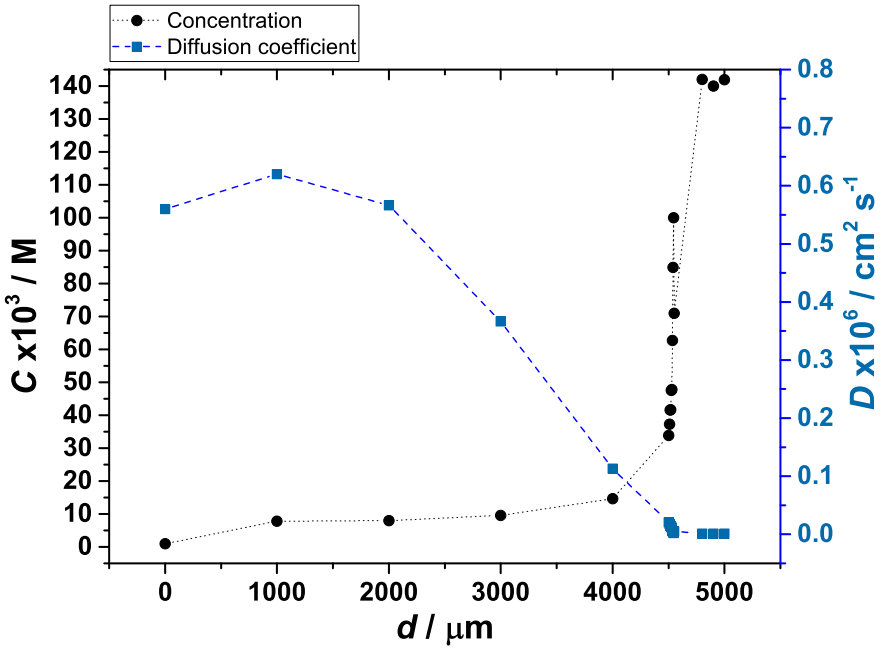

(b) SML2: 30% wt. $C_{16}EO_8$ + heptane

Figure 4.28: Diffusion coefficient (D) and concentration (C) as a function of the distance between the electrode and the water-SML interface derived from the fitting to the Mahon and Oldham equation of the chronoamperometric data shown in Figure 4.23 and Figure 4.24. The position $d = 0\,\mu m$ corresponds to the electrode in the bulk, and $d = 5000\,\mu m$ when it was touching the SML-air interface.

For SML1, the values of C oscillated around 1 mM from $d = 0\,\mu m$ to $d = 4000\,\mu m$, then they increased to 1.54 mM at $d = 5000\,\mu m$. For SML2, C was 1 mM at $d = 0\,\mu m$, then 7.81 mM at $d = 1000\,\mu m$ and it kept increasing until reaching a value of 141.9 mM at $d = 5000\,\mu m$. The fact that C increased as approaching the water-SML interface suggests that FcMeOH binds to the synthetic SML. However, the values obtained for SML2 are considerably higher than those for SML1. This might suggest a stronger partition of FcMeOH into the SML2.

The use of submarine microelectrodes allowed us to determine important parameters related to the water-air and water-SML interface under model conditions. The experiments shown in the next section were performed in order to obtain quantitative information from water samples using a conventional shaped microelectrode. This is because the end goal of this project is to perform similar measurements within the SML.

4.3 Detection of Pb^{2+} trace concentrations

The aim of the experiments shown in this section was to use a conventional shaped Bi film microelectrode (BiFMe) to characterise water samples in terms of Pb^{2+} trace concentrations. Using a BiFMe allowed us to implement a calibrationless method reported by Denuault *et al* [102]. These experiments were performed in the bulk of the solution with the aim to apply the same methodology within the SML.

Section 4.3.1 shows the optimization of the waveform in presence and in absence of Pb^{2+}. The effect of dissolved oxygen in the response is also discussed.

Section 4.3.1 shows the collection of data acquired to demonstrate the validity of the calibrationless method and also the calculation of the theoretical detection limits.

Section 4.3.3 shows the results of the calibrationless determination of Pb^{2+} trace concentrations in water samples collected in the Ravenglass estuary complex, in Cumbria, UK. This complex incorporates three rivers: the Mite, the Irt and the Esk. They join at a single point and flow into the estuary across a channel that connects the three rivers to the sea [103].

Figure 4.29 shows a map of the Ravenglass estuary complex and shows the area where the samples were taken:

1) Marine Ravenglass

2) Estuary mouth Ravenglass

3) Estuary mid Ravenglass

4) River Esk intertidal limit

These locations were chosen to investigate the trajectory of possible discharges from lead mining activity in the area.

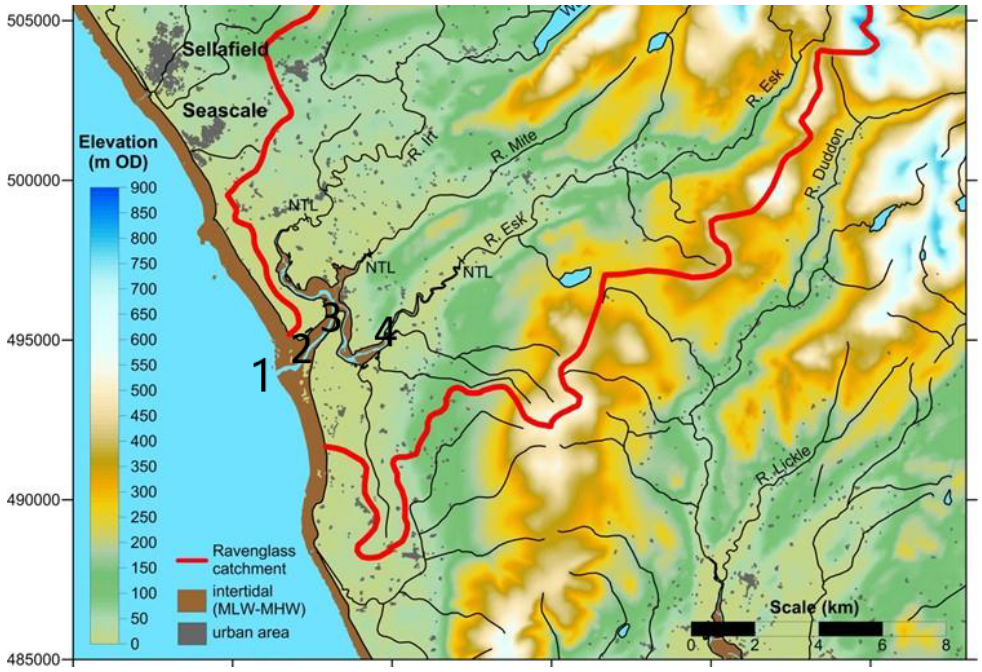

Figure 4.29: The catchment of the Rivers Irt, Mite and Esk which flow into the Ravenglass Estuary. NTL= Normal Tidal level. MHW= Mean Low Water. MHW= Mean High Water. Intertidal= The zone between the high and low water marks. Estuary= A semi-enclosed coastal body of water which has a free connection to the open sea and where freshwater mixes with saltwater. Taken from [103].

Anodic stripping voltammetry (ASV) was employed to determine trace concentrations of Pb^{2+} in the water samples obtained from the Ravenglass region. This is a technique that has been performed using Hg electrodes. Its low detection limits rely on a preconcentration step, in which the redox species accumulate onto the electrode surface (form an amalgam), and then are oxidised by sweeping the potential positively. The response is a stripping peak that is proportional to the concentration of the redox species in the solution. Nowadays, Hg electrodes are being replaced by Bi and Bi film electrodes because they are less toxic [104].

Plating Bi onto microelectrodes to fabricate Bi film microelectrodes (BiFMes) provides several advantages when performing trace metal analysis. Their small electroactive area ensures a high rate of mass transport of the electroactive species, which makes possible to perform analysis using shorter preconcentration times and avoid stirring the solution. Also, using microelectrodes allows measurements to be made in poor conducting media and without using the standard addition method.

In 2002, Denuault *et al* published a calibrationless method that involves using an equation in which the concentration of the redox species can be determined through the knowledge of the charge under the stripping peak, the preconcentration time and the expression of the limiting current at a microdisc [102]. This method is based on the premise that the deposited charge is equal to the stripping charge (equation 4.2). The stripping charge is proportional to current times the deposition time (equation 4.3) and by substitution of the equation of the limiting current at a microdisc (equation 4.4) a direct relationship between the stripping charge and the concentration is obtained (equation 4.5). Equation 4.6 shows the expression employed to determine the concentration of Pb^{2+} in this section.

$$Q_{strip} = Q_{dep} \tag{4.2}$$

$$Q_{dep} = i * t_{dep} \tag{4.3}$$

$$i = 4nFDCa \tag{4.4}$$

$$Q_{strip} = 4nFDCa * t_{dep} \tag{4.5}$$

$$C = \frac{Q_{strip}}{4nFDa} * t_{dep} \tag{4.6}$$

Where Q_{strip} is the stripping charge, Q_{dep} is the deposited charge, t_{dep} the deposition time, F is the Faraday constant, D is the diffusion coefficient, C is the concentration and n is the number of electrons. For the determination of Pb^{2+}: n= 2, D= $9.39 \times 10^{-6}\,cm^2\,s^{-1}$ [105] and the radius was determined using the limiting current for the reduction of $Ru(NH_3)_6{}^{3+}$ on a steady state LSV.

4.3.1 The waveform

A calibration curve was performed to prove the validity of the calibrationless method described earlier and to determine the theoretical detection limits. After the BiFMe was fabricated as described in section 3.3.2, aliquots of a 1.18 mM Pb^{2+} solution were added to 10 mL of a deaerated 0.5 M NaCl solution.

Figure 4.30 shows the E vs t plot for the potential waveform employed to record the response of the blank, a deaerated 0.5 M NaCl solution. In absence of Pb^{2+}, the perturbation included 5 cycles at $0.5\,V\,s^{-1}$ to ensure that the electrode surface was free of oxide. It was important to not cycle more positive than -0.3 V because the Bi stripping peak is found at 0.0 V vs SCE. Then, the preconcentration potential was held at -0.7 V vs SCE for 120 s and the potential was positively swept from -0.7 V to -0.3 V at $0.1\,V\,s^{-1}$.

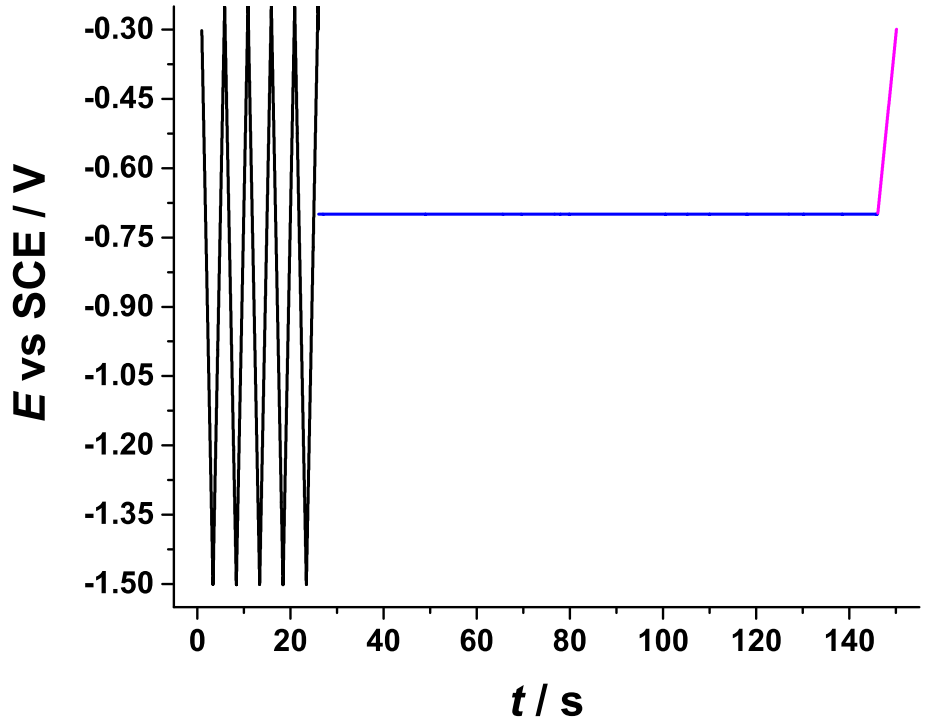

Figure 4.30: E vs t plot of the waveform used to condition the electrode and record the ASV-LSV. 5 cycles at $0.5\,\mathrm{V\,s^{-1}}$ (black), potential step from -0.3 V to -0.7 V for 120 s (blue) and the linear sweep at $0.1\,\mathrm{V\,s^{-1}}$ from -0.7 V to -0.3 V (pink).

Figure 4.31 shows i vs E plot for the potential waveform shown in Figure 4.30 in aerated and deaerated 0.5 M NaCl solution. The CV shows that when increasing the number of cycles, the current for the reduction of Bi oxide decreased. Also, that in presence of oxygen the LSV produced with a negative current sufficiently large to mask any lead stripping peaks. After adding the Pb^{2+} aliquot the waveform was modified by including a potential step at -0.4 vs SCE for 120 s to make sure any Pb deposited during the cycles was oxidised before the preconcentration step.
Figure 4.32 shows the waveform and the corresponding i vs E plot including this additional potential step.

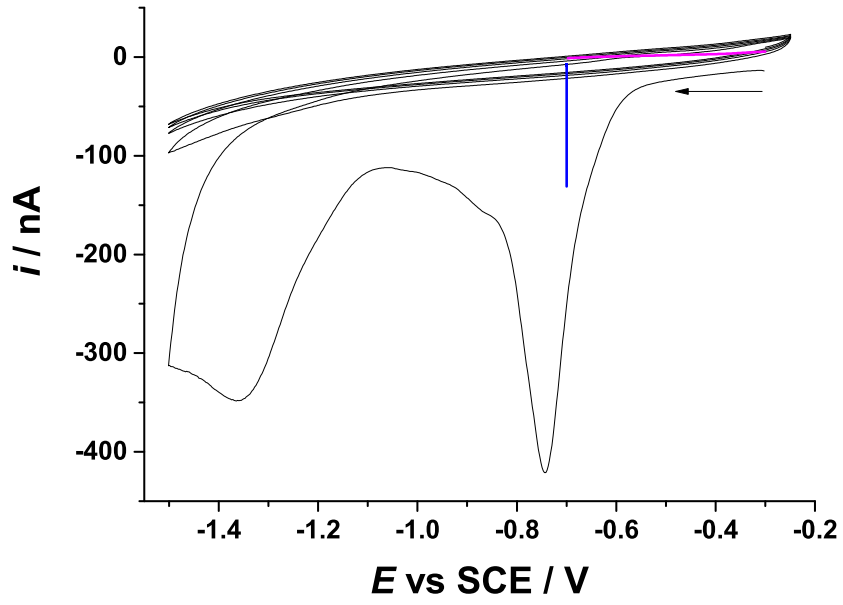

(a) Deaerated 0.5 M NaCl solution

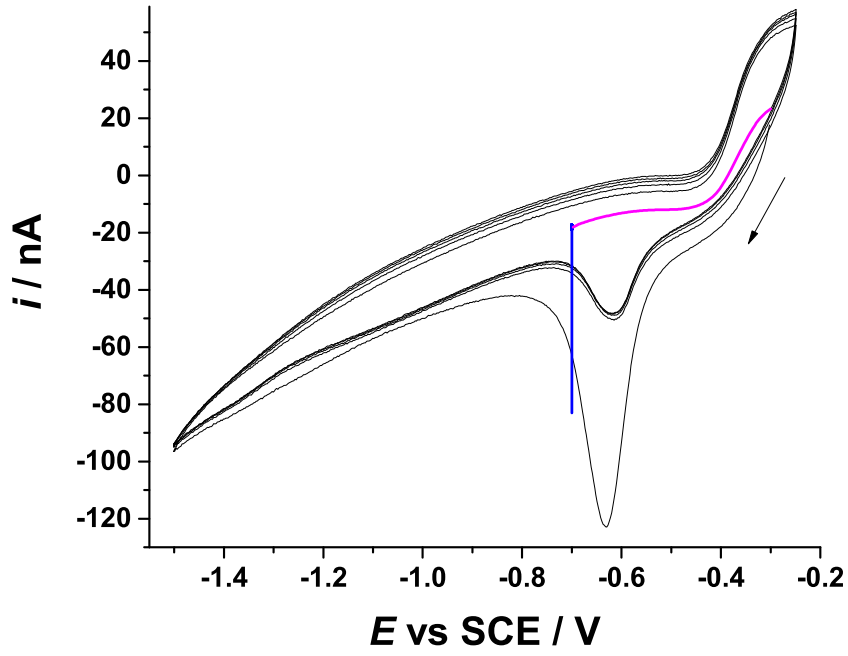

(b) Aerated 0.5 M NaCl solution

Figure 4.31: i vs E plot for the potential waveform shown in Figure 4.30 recorded in aerated and deaerated 0.5 M NaCl solution. In black, the CVs, in blue the current recorded during the preconcentration step and in pink the linear sweep.

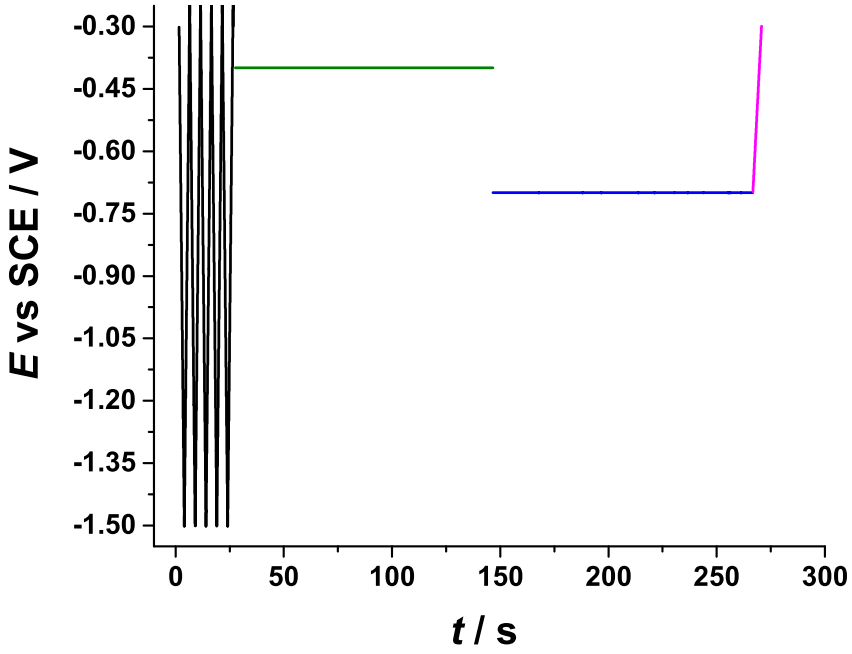

(a) E vs t

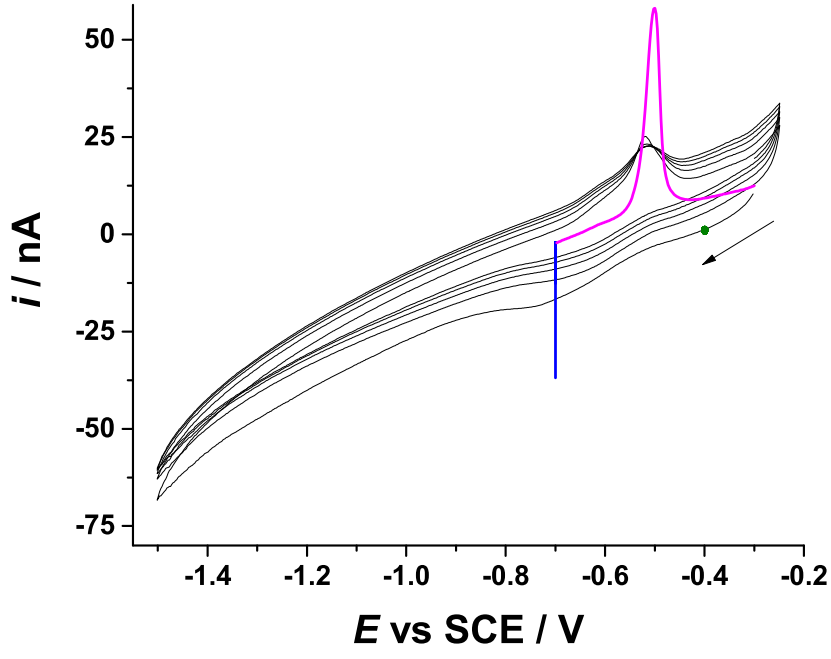

(b) i vs E

Figure 4.32: E vs t (a) and i vs E (b) plot for the potential waveform shown in Figure 4.30 recorded in deaerated 0.5 M NaCl solution after adding a 50 µL aliquot of a 1.18 mM Pb^{2+} solution. In black, the CVs, in blue the current recorded during the preconcentration step and in pink the linear sweep.

The preconcentration time and scan rate in the waveform were optimised for the analysis. Figure 4.33 shows the dependence of the size of the stripping peaks with the preconcentration time and the scan rate.

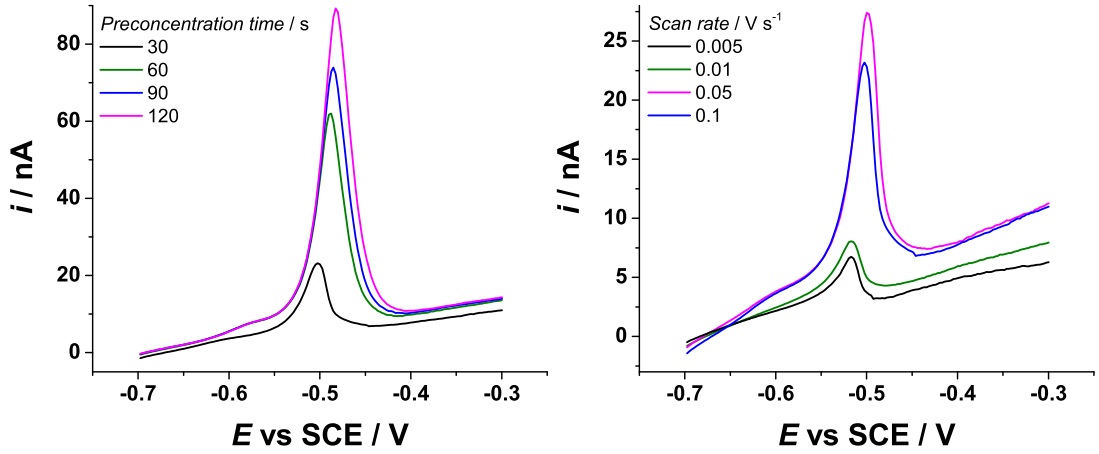

(a) Preconcentration time dependence

(b) Scan rate dependence

Figure 4.33: ASV-LSV recorded with a 64.6 µm diameter BiFMe in deaerated 0.5 M NaCl solution after adding a 50 µL aliquot of a 1.18 mM Pb^{2+} solution. a) Preconcentration time dependence: the potential was held at -0.7 V. b) Scan rate dependence: the potential was held at -0.7 V for 30 s.

The next section shows the response obtained after adding consecutive aliquots of a 1.18 mM Pb^{2+} solution to a deaerated 0.5 M NaCl NaCl solution. The aim was to obtain a collection of stripping peaks and the corresponding charge to determine the concentration of Pb^{2+} through equation 4.6 and compare it to the theoretical concentration. The data were also employed to calculate the detection limits of the method.

4.3.2 Validity of the calibrationless method

A calibration curve was performed by adding aliquots of a 1.18 mM Pb^{2+} solution to 10 mL of a deaerated 0.5 M NaCl solution to demonstrate the validity of equation 4.6. Figure 4.34 shows the ASV-LSV in absence of Pb^{2+} and after adding the corresponding aliquots. The measurement was performed in triplicate but only the first ASV is shown.

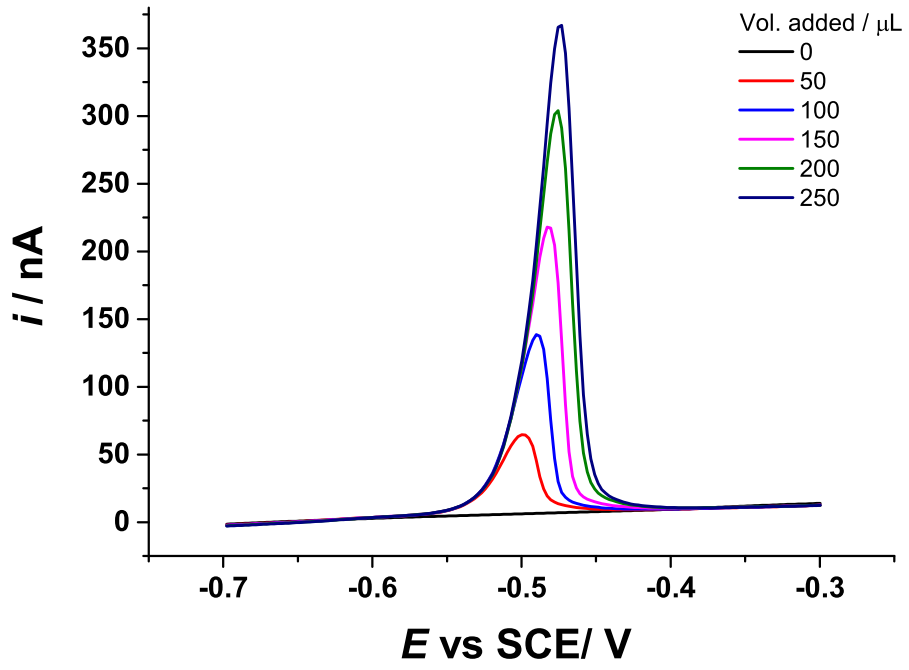

Figure 4.34: ASV-LSV recorded with a 64.6 µm diameter BiFMe in 10 mL of deaerated 0.5 M NaCl solution after adding aliquots of a 1.18 mM Pb^{2+} solution. The preconcentration potential was held at -0.7 V for 120 s. The scan rate of the stripping LSV was $0.1\,V\,s^{-1}$.

The corresponding stripping charges were determined by integrating the area under the anodic peak from the i vs E curve and correcting by the scan rate in Origin lab 9.0. Table 4.1 shows the average charge (Q) and standard deviation (σ) for each of the Pb^{2+} solution additions. The experimental concentration ($Exp.\ [Pb^{2+}]$) was calculated through equation 4.6. The theoretical concentration ($Theo.[Pb^{2+}]$) was calculated considering the dilution of the Pb^{2+} stock solution and corrected by the real volume delivered by the autopippete.

The error of $Exp.\ [Pb^{2+}]$ was calculated by combining the error associated to the charge and the radius of the electrode using the rules of propagation of uncertainty.

Table 4.1: Average charge under the stripping peak for the calibration curve performed (Q), the standard deviation (σ), the concentration calculated through equation 4.6 (*Exp.* $[Pb^{2+}]$), and the theoretical concentration (*Theo.* $[Pb^{2+}]$).

$\boldsymbol{Q}$ x10^9 / C	$\boldsymbol{\sigma}$ x10^9 / C	***Exp.*** $\boldsymbol{[Pb^{2+}]}$ x10^6 / M	***Theo.*** $\boldsymbol{[Pb^{2+}]}$ x10^6 / M
20.23	0.02	7.08 ± 1.10	7.94
45.50	1.05	15.95 ± 2.47	15.99
73.24	1.43	25.67 ± 4.55	23.95
104.20	0.90	36.52 ± 5.67	31.79
120.50	4.30	42.23 ± 6.54	39.57

Figure 4.35 shows a plot of *Exp.* $[Pb^{2+}]$, and *Theo.*$[Pb^{2+}]$ vs the volume of Pb^{2+} stock solution added. The experimental data showed a deviation from the theoretical values at concentrations above 25 µmol L^{-1}. This might be related to a systematic error induced by the delivery of the Pb^{2+} stock solution.

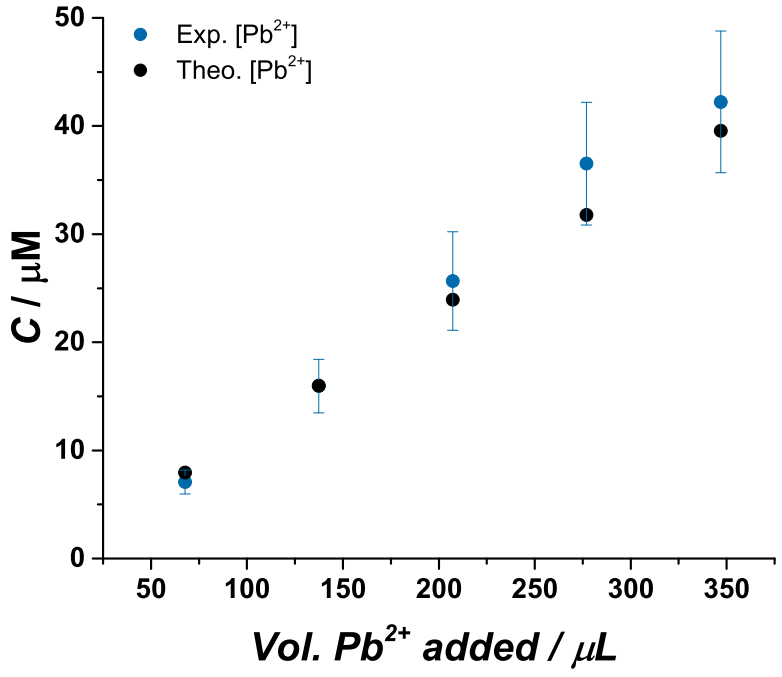

Figure 4.35: *C* vs *Vol.* Pb^{2+} *added* for the experimental concentration (*Exp.* $[Pb^{2+}]$) calculated through equation 4.6 and (*Theo.*$[Pb^{2+}]$).

The theoretical detection limits of the technique were determined to complement the analysis of the data. Figure 4.36 shows a plot of the charge under stripping peaks

shown in Figure 4.34 (Q_{Exp}) and the expected charge (Q_{Theo}) vs the theoretical Pb^{2+} concentration ($Theo.[Pb^{2+}]$).

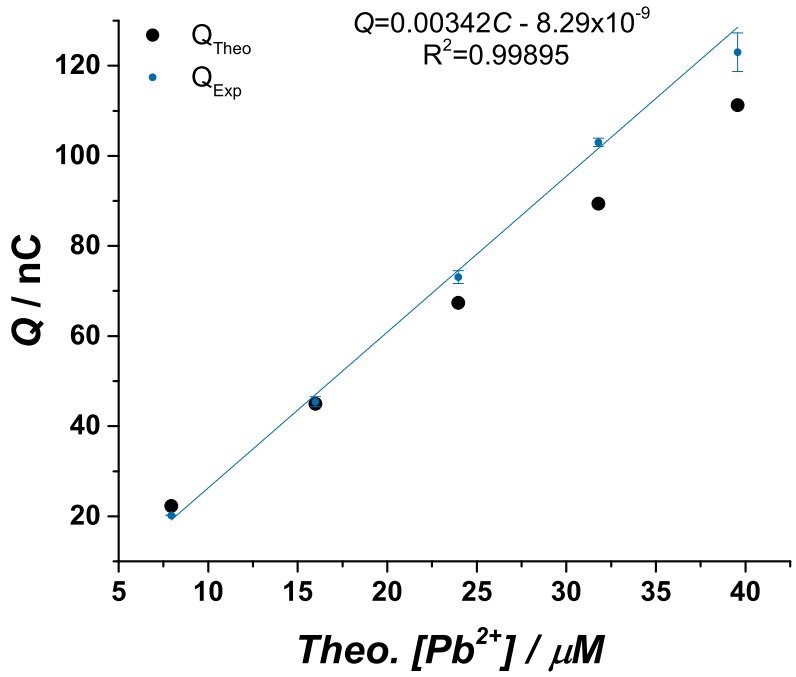

Figure 4.36: Q vs C plot for the data acquired (Q_{Exp}) compared to the expected charge (Q_{Theo}). The blue line is the linear regression performed. The equation of the linear fit and R^2 are shown in the plot. The error bars correspond to the standad deviation of the three repeats of (Q_{Exp}).

The minimum detectable concentration (C_{min}) was calculated through equation 4.7 [106].

$$C_{min} = \frac{3 * \sigma}{m} \tag{4.7}$$

Where σ is the standard deviation of the lowest concentration measured, and m is the slope of the Q_{Exp} vs C plot. For the data acquired the minimum detectable concentration was $0.018\,\mu mol\,L^{-1}$.

The results obtained showed that the response at the BiFMe is reliable and robust. More importantly, the calibration curve performed allowed us to confirm the validity of equation 4.6. Also, the magnitude of the detection limits suggest that is possible to implement the calibrationless method in real water samples as shown in the next section.

4.3.3 Determination of Pb^{2+} in water samples

The analysis of the samples was performed by measuring a 5 mL aliquot of each of the samples using a bulb pipette and placing it into a 5 neck cell. The sample was deaerated for 10 min and the waveform was applied three times.

Figure 4.37 shows the ASV-LSV corresponding to each sample at natural pH and at pH=1. The blank was a deaerated 0.5 M NaCl solution and samples were acidified adding 5 µL of $HClO_4$ 70%.

The samples were:

1) Marine Ravenglass

2) Estuary mouth Ravenglass

3) Estuary mid Ravenglass

4) River Esk intertidal limit

The results obtained at natural pH did not show any Pb^{2+} stripping peaks but a series of curves that looked very similar to the response of the blank. However, the low gradient observed for the current recorded in sample 4, suggests that it contained less species that could be oxidised during the anodic sweep.

On the other hand, sample 1 and sample 2 showed larger Pb^{2+} stripping peaks compared to sample 3 and 4 at pH=1. The low current for sample 4 was also observed at this pH.

In order to obtain the concentration of Pb^{2+} in each of the samples, the calculation using the charge under the stripping peak and equation 4.6 was performed. The results are shown in table 4.2.

Table 4.2: Charge under the stripping peak for sample 1 and 2 (Q), the standard deviation (σ) and the corresponding average concentration through equation 4.6 (C).

Water sample	***Q*** x10^9 / C	***C*** x10^6 / M	***Water sample***	***Q*** x10^9 / M	***C*** x10^6/ M
1	2.06	0.72 ± 0.11	2	0.55	0.19 ± 0.04
	2.09	0.73 ± 0.11		0.67	0.23 ± 0.04
	2.11	0.74 ± 0.11		0.59	0.21 ± 0.04
Average	2.09	0.73 ± 0.11		0.60	0.21 ± 0.04
σ	0.03	0.01		0.06	0.02

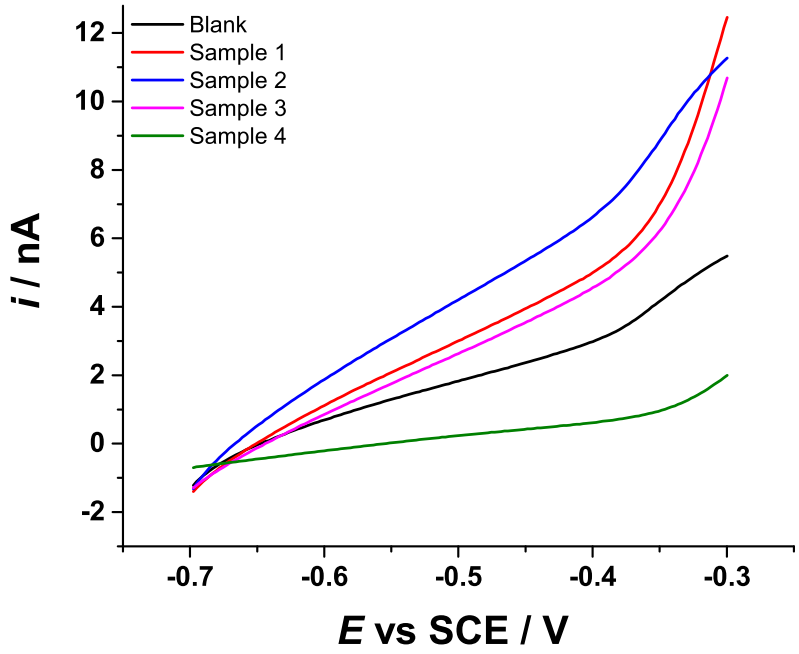

(a) Natural pH

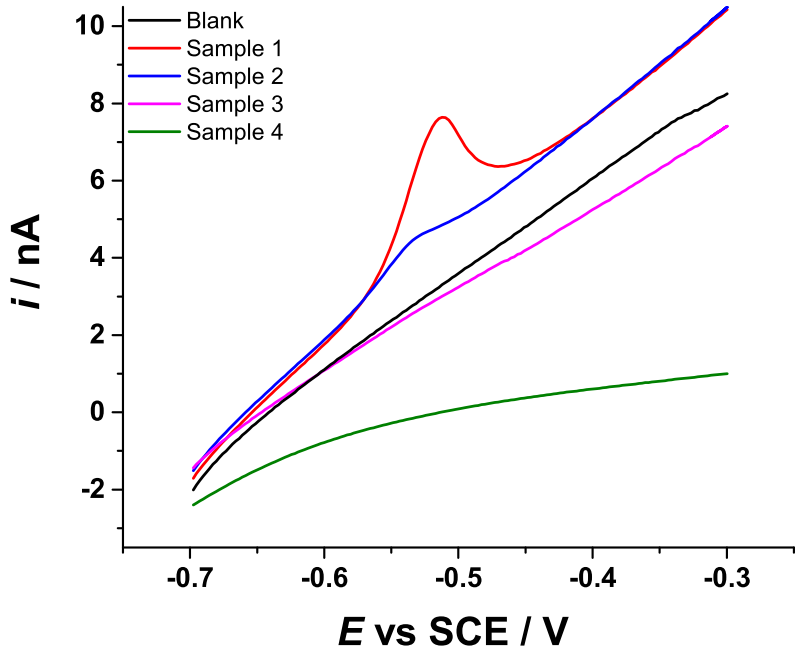

(b) pH=1

Figure 4.37: ASV-LSV recorded with a 64.6 µm diameter BiFMe in different water samples. The preconcentration potential was held at -0.7 V for 120 s. The scan rate of the stripping LSV was 0.1 V s^{-1}.

The concentration of Pb^{2+} for both sample 1 and 2 were very close to the detection limits determined through equation 4.7. However, the concentration of Pb^{2+} in the water samples was determined through equation 4.6 without using the standard addition method.
According to the location where the samples were taken we can infer that the accumulation of Pb^{2+} happen in the marine area rather than in the estuary complex.

4.4 Conclusions

The fabrication of submarine microelectrodes allowed the investigation of the water-air and water-SML interface. The submarine microelectrodes provided reproducible LSVs, chronoamperograms, and approach curves that were comparable between each other. The SECM investigation of the water-air interface showed that there are numerous factors affecting the approach curves recorded. The measurements are susceptible to the scan velocity: when this increases, the electrode creates convection. This enhances the flux of redox material to the surface of the electrode and produces a characteristic current spike in the approach curves recorded. We also learnt that the water-air interface interacts strongly with the glass surrounding the microwire. Because the glass is hydrophilic, the water molecules attach to it and travel with it as it is moved to the water-air interface.

These factors affected the response particularly in presence of an unconfined meniscus. The later was susceptible to convection; however, once the SML was added the convection created by moving the electrode and the interaction between the glass and the interface diminished. Confining the meniscus provided the meniscus with the necessary stability to investigate the top 500 µm of the solution. The approach curves recorded one after the other suggested that the water-air and the water-SML interface changes with time even when the meniscus is confined.

The two synthetic SML employed allowed us to investigate the unconfined water-SML interface. Both approximations produced a water-SML boundary, however, the SML2 ($C_{16}EO_8$ + heptane) produced a clearer interface. The LSVs, chronoamperograms, and approach curves acquired showed good agreement between each other and between both SML approximations. The chronoamperograms acquired at different tip-substrate distances allowed us to determine the concentration and diffusion coefficient of the redox species.

The fitting of the chronoamperometric data to the Mahon and Oldham equation showed that the changes in the limiting current of the redox pair are given by the drop

of the diffusion coefficient due to the increase of the local viscosity. On the other hand, the concentration of FeMeOH increased when approaching the water-SML interface. This suggests that the FcMeOH binds to the surfactant after added to the solution.

The concentration values obtained using SML1 were in good agreement with expectations: 0.98 mM in the bulk and 1.54 mM at the SML-air interface. In the case of SML2, the concentration in the bulk was 1 mM, and close to the SML-air interface 141.9 mM. This dramatic increase of concentration might suggest a higher partition of FcMeOH into SML2.

The fabrication of BiFMe allowed the determination of Pb^{2+} concentrations in water samples. The calibration curve obtained by adding aliquots of a Pb^{2+} solution to a deaerated 0.5 M NaCl allowed us to prove the validity of the calibrationless method reported by Denuault's group. The theoretical and experimental Pb^{2+} stripping charges were in good agreement.

The optimization of the waveform employed showed that the determination of trace Pb^{2+} is affected by the dissolved oxygen. The cleaning cycles performed before the preconcentration time showed that dissolved oxygen produced with a negative current that was capable of masking any Pb^{2+} stripping peaks. Also, the cleaning cycles showed that the Bi surface was covered with oxide, and by cycling the potential a baseline closer to zero was provided.

The determination of Pb^{2+} in water samples using the calibrationless method allowed us to distinguish between the samples without using the standard additions method. The results showed that the concentration of Pb^{2+} was higher in the sample taken in the marine area than in the estuary rest of the water samples. This suggests that the methodology could be implemented to water samples that contain SML.

Chapter 5

Investigation of the iron-groundwater interface

The results of the investigation of the iron-groundwater interface using the SECM generation/collection (G/C) mode, laser ablation inductively coupled plasma mass spectrometry (ICP-MS), scanning electron microscopy (SEM) and energy dispersive spectroscopy (EDX) are shown in this chapter. The aim of this investigation was to determine the suitability of iron from different sources and particle sizes as permeable reactive barrier (PRB) material. This was to follow up the experiments performed by colleagues from the National Oceanography Centre (NOC), which measured the TcO_4^- uptake of iron from different sources and particle sizes in synthetic groundwater. A review of these experiments is shown in section 5.1. In our experiments, we employed materials provided by the NOC researchers to compare their corrosion activity and determine their capacity to uptake model contaminants like ferrocyanide and perrhenate (ReO_4^-).

Section 5.2 shows the results obtained using the SECM G/C mode to investigate the corrosion activity of iron substrates made with iron provided by the NOC researchers. The results in section 5.2.1 show the tip-CVs recorded at different tip-substrate distances over time after exposing the iron substrates to a fixed volume of synthetic groundwater. The consumption of dissolved oxygen was monitored and served as a parameter to compare the corrosion activity of each material.

The results in section 5.2.2 show the voltammetry obtained when exposing the substrates to synthetic groundwater with a fixed concentration of ferrocyanide as a model contaminant. In this case the formation of Prussian blue served as a parameter to compare the corrosion activity of each material.

The experiments in section 5.2.3 show the investigation of the uptake of perrhenate

from groundwater through laser ablation ICP-MS, SEM and EDX.

Finally, in the open circuit potential measurements and Tafel plots for the electrodes made with iron flakes and iron powder are shown in section 5.5.

5.1 Batch experiments

Colleagues from the National Oceanography Centre performed experiments to determine the Tc uptake capacity of iron from different sources and particle sizes. For this, a fixed amount of ZVI (iron flakes), iron powder, haematite and magnetite were exposed to 5 mL of synthetic groundwater. After a period of exposure, the Tc residual concentration was measured and the distribution coefficients were determined for each of the materials. Haematite and magnetite were employed in order to determine the effect of having the iron surface covered with oxide in the Tc uptake efficiency. Figure 5.1 shows micrographs of the physical appearance of the vials employed in these experiments.

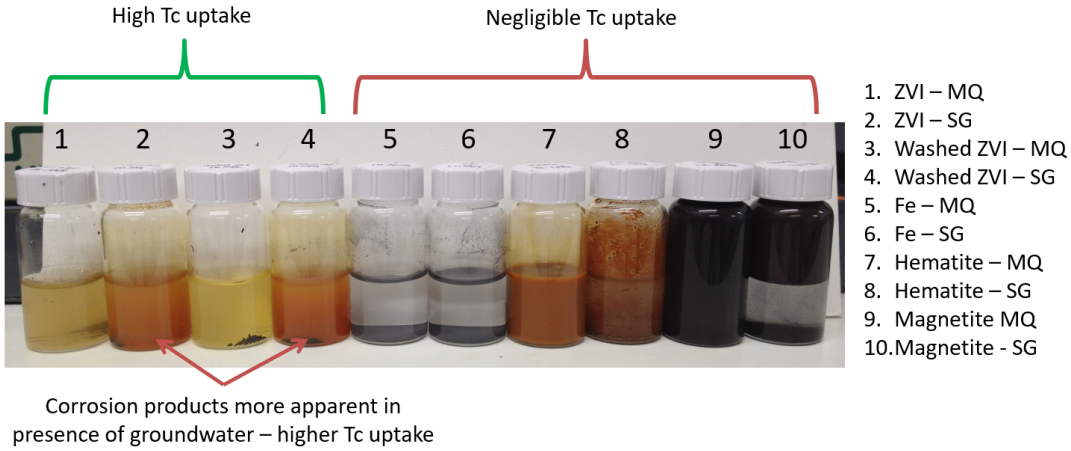

Figure 5.1: Micrographs of the physical appearance of the vials employed for the batch experiments. In the caption: ZVI = iron flakes, MQ = Milli-Q water, SG= synthetic groundwater, Fe= iron powder. Taken from [107].

Figure 5.2 shows the distribution coefficients for each of the vials shown in Figure 5.1. These are defined as the ratio of concentrations of a compound in a mixture of two immiscible phases at equilibrium. The higher distribution coefficients were found in vial 2 and 4, which corresponded to iron flakes in synthetic groundwater, and washed iron flakes in synthetic groundwater.

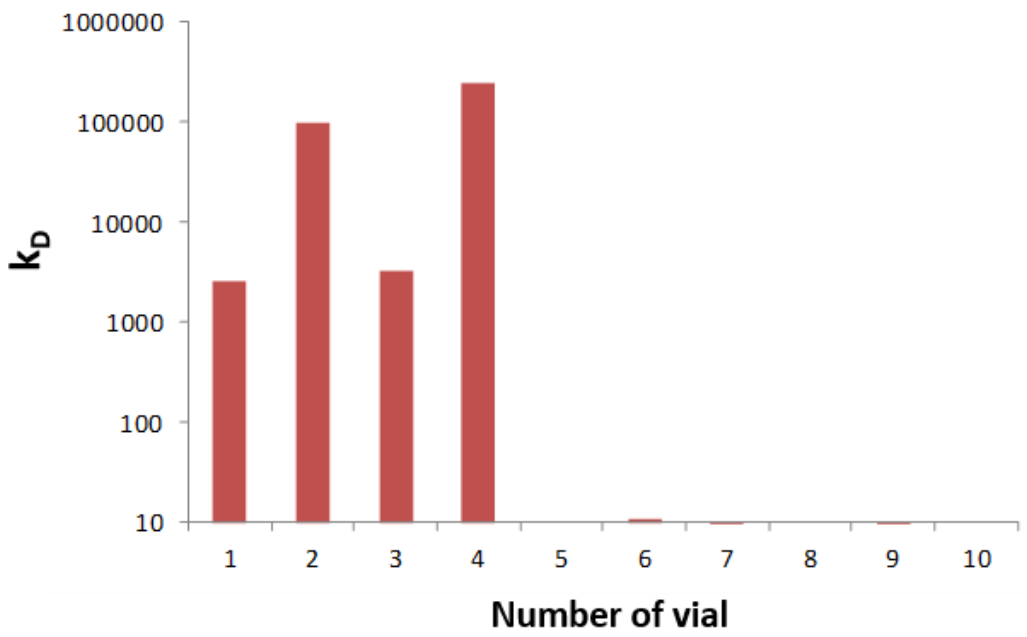

Figure 5.2: The distribution coefficients for each of the vials shown in Figure 5.1.

These results suggested that ZVI (iron flakes) were the most effective material to remove Tc from synthetic groundwater; however, this contradicted theoretical expectations. From the list of materials employed in this experiment, one would have expect that the iron powder showed higher corrosion rate and Tc uptake due to the larger surface area. These discrepancies motivated us to investigate the corrosion activity of the iron flakes and the iron powder employed in these experiments. In order to do this, iron substrates were fabricated by casting the materials in epoxy resin as explained in section 3.4.

Section 5.2 shows the investigation of the corrosion activity of these materials using the SECM G/C mode.

5.2 SECM experiments

The SECM experiments conducted to investigate the corrosion of the iron flakes and the iron powder were performed using the G/C mode. In our experiments, the iron substrate was the generator and a 25 µm Pt disc was the collector.

The methodology consisted in recording CVs at regular time intervals at two tip-substrate distances after exposing the iron substrates, made with iron flakes and iron powder, to a fixed volume of an electrolyte solution. The tip-substrate distance was fixed before the solution was added to the electrochemical cell, $d = 0$ µm was when the electrode touched the substrate, and 500 µm away was considered the bulk.

CVs were acquired when the Pt disc was 500 µm away from the substrate, then 50 µm once the electrode was reconditioned by recording 5 cycles at $0.5\,\mathrm{V\,s^{-1}}$ in the bulk. The results of the exposure of the iron substrates to synthetic groundwater are discussed in section 5.2.1. Section 5.2.2 shows the results of the exposure of the iron substrates to synthetic groundwater with ferrocyanide.

5.2.1 Exposure to synthetic groundwater

The iron substrates were polished using sand paper of 1200 grit until any rust on the surface was removed, then for 3, 5 and 8 minutes with alumina powder 5 µm, 1 µm and 0.3 µm respectively on a polishing pad prior the start of the experiment. The Pt disc was polished with alumina powder 0.3 µm in a polishing pad for 5 min and electrochemically cleaned by cycling the potential from -1 to 1 V vs SMSE at $0.5\,\mathrm{V\,s^{-1}}$ 5 times in a 1 M H_2SO_4 solution before being placed in the electrochemical cell.

Figure 5.3 shows a tip-CV recorded in synthetic groundwater to facilitate the interpretation of the CV acquired in presence of the iron substrates. It is possible to appreciate the typical features of Pt in a neutral aerated electrolyte: Pt oxide formation, Pt oxide stripping peak, H adsorption and desorption and the oxygen reduction reaction wave (ORR). The later served as a parameter to compare the corrosion activity between each of the iron substrates.

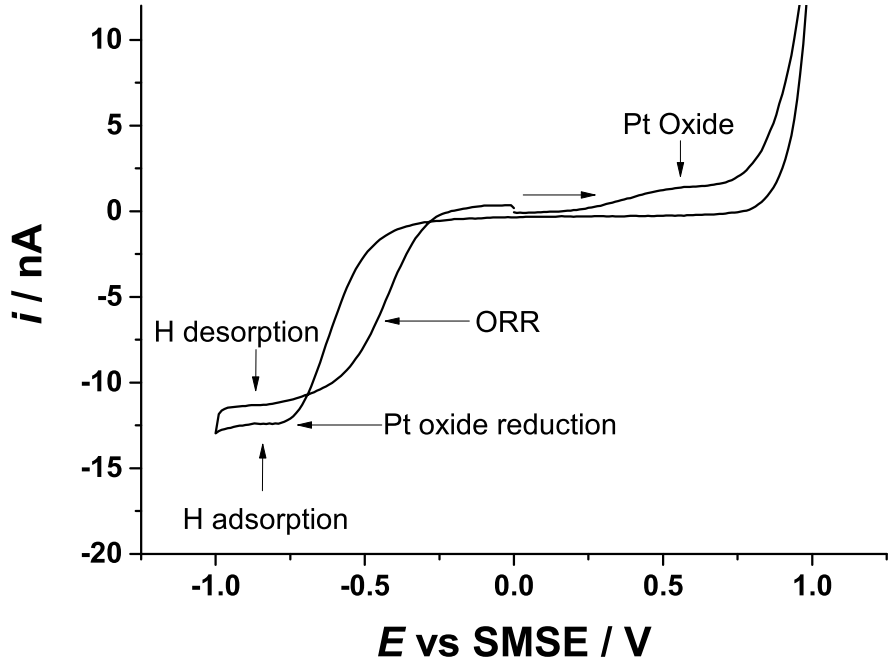

Figure 5.3: CV recorded with a 25 µm Pt disc at 0.1 V s^{-1} in 10 mL of aerated synthetic groundwater. $RG = 40$.

Figure 5.4 shows the CVs recorded in aerated synthetic groundwater over time when the tip was 500 µm and 50 µm away from the iron flake substrate.

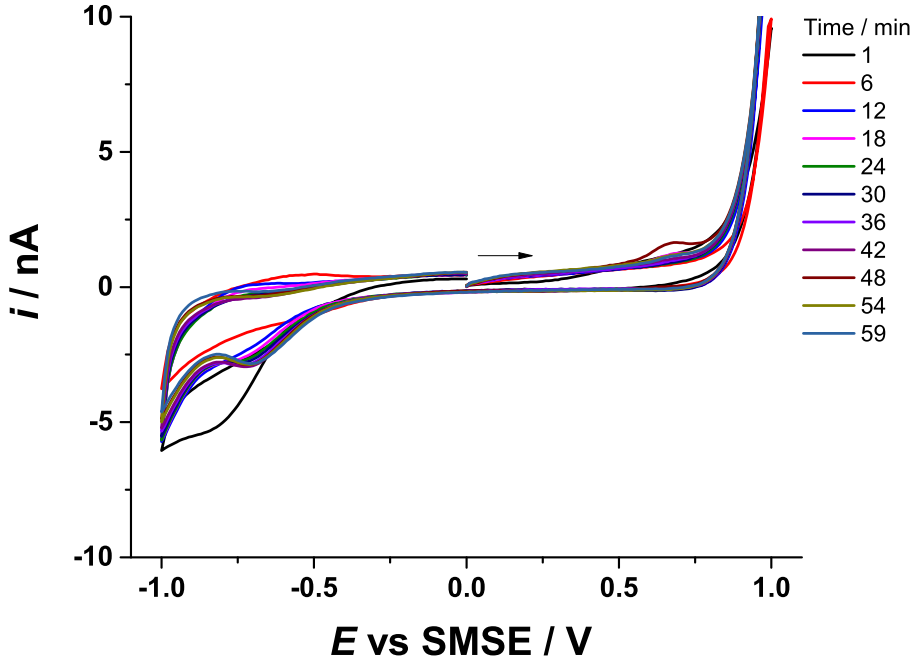

(a) 500 µm

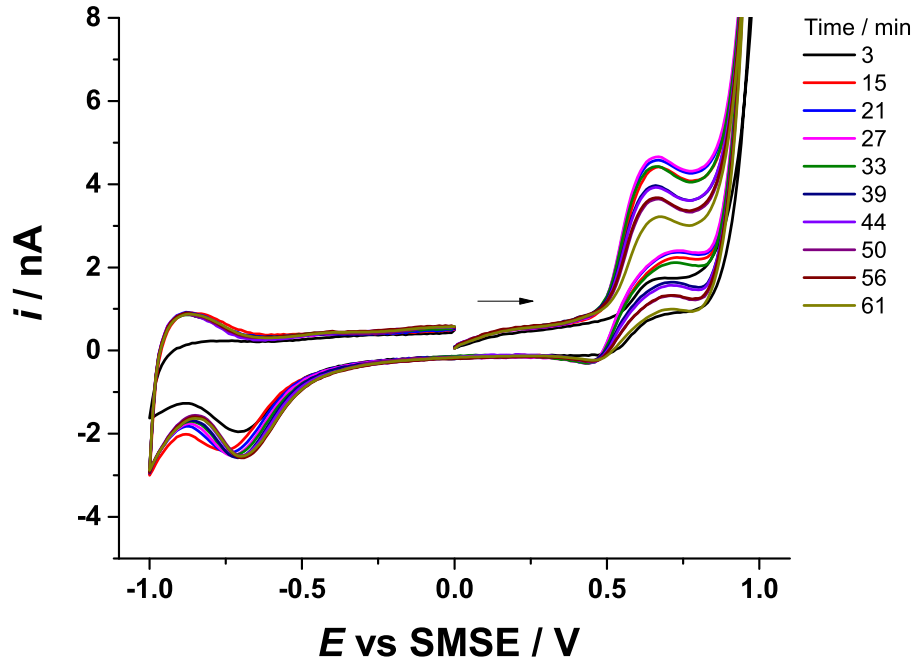

(b) 50 µm

Figure 5.4: Tip-CVs recorded with a 25 µm Pt disc located 500 µm (a) and 50 µm (b) above the iron flake substrate in 10 mL of aerated synthetic groundwater at 0.1 V s^{-1}. $RG = 15$.

The tip-CVs acquired 500 µm away from the iron flake substrate did not show an anodic wave. This could be because, according to the Fe Pourbaix diagram (Figure 5.5), at $pH = 7$ the Fe^{2+} released by the substrate reacts immediately with water to form iron hydroxides. On the other hand, the cathodic region did not show the typical features of the ORR, but an increase of the hydrogen region over time. This could be electrode fouling due to the saturation of the solution with corrosion products or simply because the substrate consumed the available oxygen in the bulk.

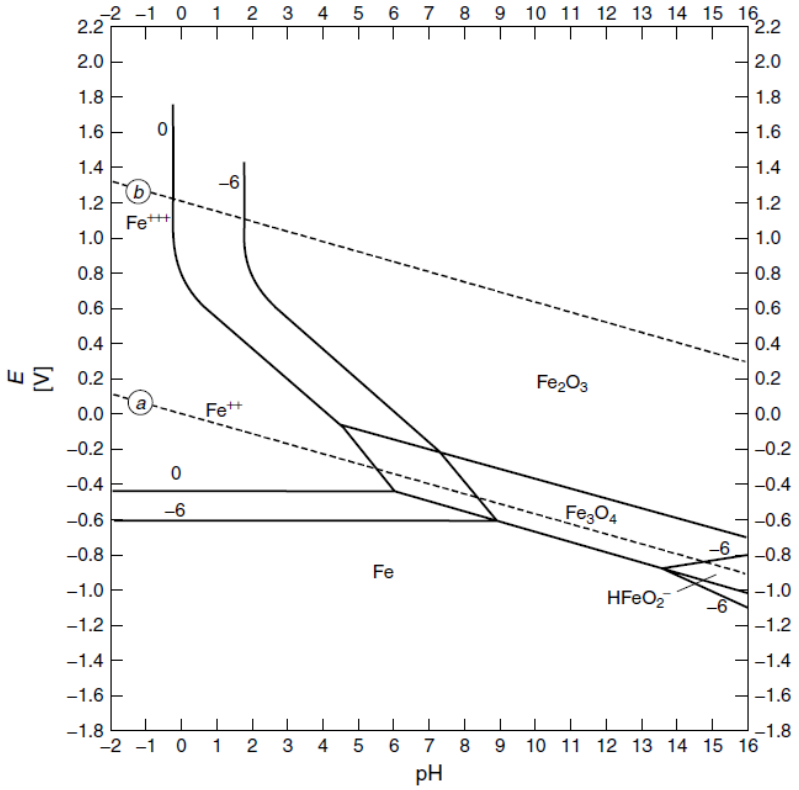

Figure 5.5: Fe Pourbaix diagram. The dashed lines marked with a) and b) correspond to the cathodic and anodic stability limits of water respectively. Lines marked with 0 correspond to $[Fe^{2+}] = 1M$, and those marked with -6 correspond to $[Fe^{2+}] = 10^{-6}M$. Taken from [108].

However, the tip-CVs recorded 50 µm away from the iron flake substrate showed a systematic increase of an anodic wave, that according to previous work in our group, correspond to the OH^- oxidation wave [109–111]. Figure 5.6 shows a plot of the limiting current extracted from the plateau of the OH^- oxidation wave with respect to exposure time to clarify the trend observed.

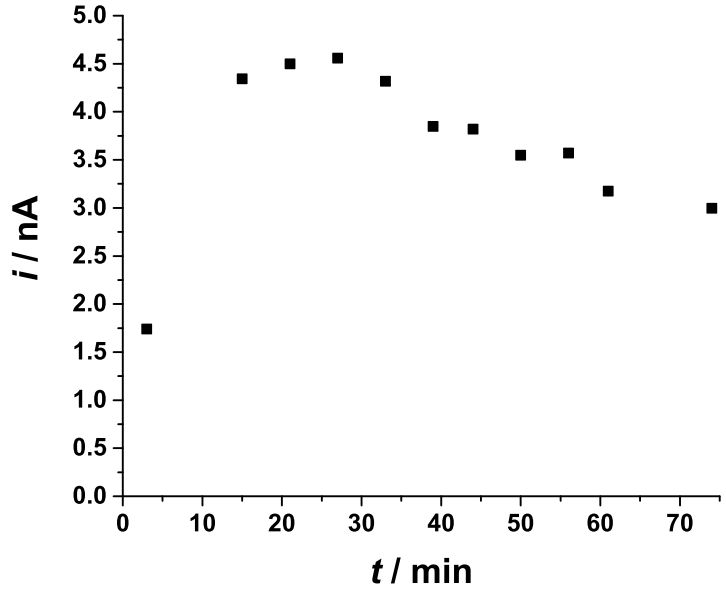

Figure 5.6: Limiting current vs exposure time for the oxidation of OH^-. The current was extracted from the plateau of the OH^- oxidation wave at 0.7 V vs SMSE.

According to Figure 5.6, the local pH increased from 0 min to 25 min of exposure. Then it decreased gradually from 30 min to 75 min, which could be due to the formation of passive film at the iron substrate. This agrees with the micrographs shown in Figure 5.7, where it is possible to appreciate the formation of a layer of rust at the surface of the substrate over time.

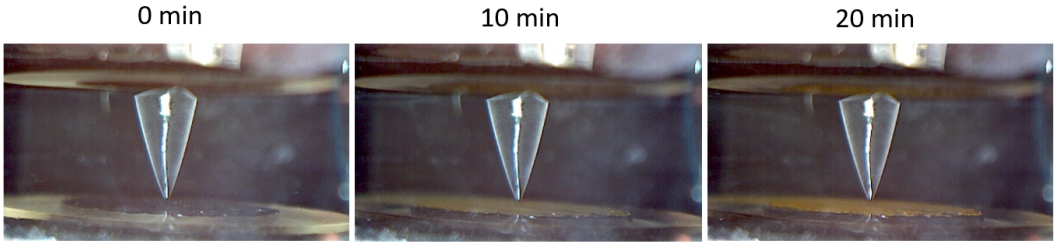

Figure 5.7: Micrographs of the experimental arrangement showing the changes at the surface of the iron flake substrate over time. The tip was located 500 µm above the iron substrate.

According to the tip-CVs recorded, it is possible to propose the reactions that occur at both the tip and the substrate.
Main reactions at the tip: the reduction of dissolved oxygen (equation 5.1) and the oxidation of OH^- ions (equation 5.2).

$$O_2 + 2\,H_2O + 4\,e^- \longrightarrow 4\,OH^- \tag{5.1}$$

$$OH^- + H_2O \longrightarrow \frac{1}{2}\,H_2O + \frac{1}{4}\,O_2 + e^- \tag{5.2}$$

Main reactions at the substrate: the reduction of dissolved oxygen (equation 5.1), the oxidation of Fe (equation 5.3) and the formation of $Fe(OH)_2$ and subsequent corrosion products (equation 5.4).

$$Fe^0 \longrightarrow Fe^{2+} + 2\,e^- \tag{5.3}$$

$$Fe^{2+} + 2\,OH^- \longrightarrow Fe(OH)_{2(s)} \tag{5.4}$$

Figure 5.8 shows a schematic representation of the reactions occurring at the substrate and at the tip when it was positioned 500 µm (a) and 50 µm (b) away from the iron flake substrate. In the bulk, the tip could only record the ORR current, however, in this experiment there was not a clear wave, which suggests the substrate consumed it avidly. When placed 50 µm away from the substrate the tip recorded the oxidation of the OH^- ions produced by the substrate.

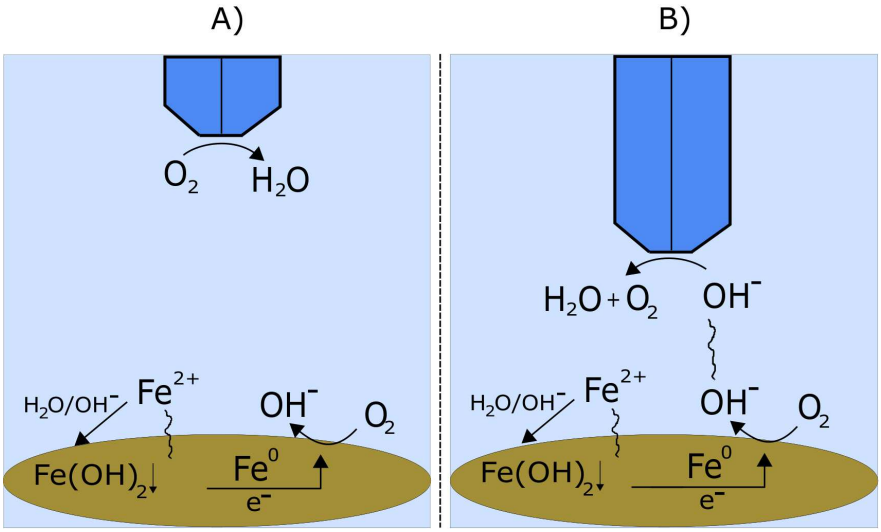

Figure 5.8: Schematic representation of the reactions occurring at the substrate, and at the tip when located 500 µm (a) and 50 µm (b) above the iron flake substrate.

The results suggest that the iron flakes undergo corrosion and form a passive film within the time scale of the experiment. On the other hand, the iron powder showed less signs of corrosion activity. Figure 5.9 shows micrographs of the experimental arrangement, where no obvious changes were observed at the surface of the iron powder substrate over time.

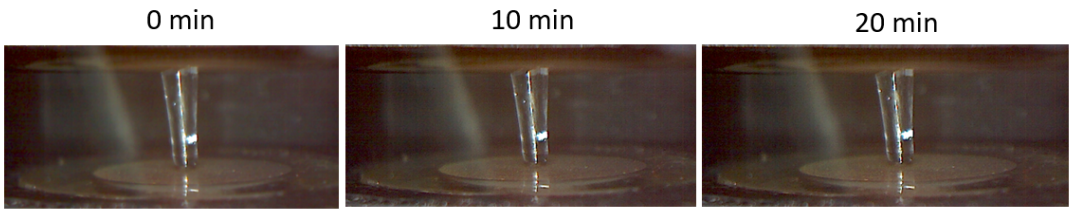

Figure 5.9: Micrographs of the experimental arrangement showing the changes at the surface of the iron powder substrate over time. The tip was located 500 µm above the substrate.

Figure 5.10 shows the CVs acquired 500 µm and 50 µm away from the iron powder substrate. Similarly to the CVs shown in Figure 5.4, no anodic wave is observed other than the formation of PtO. However, the ORR is observed when the electrode was placed 500 µm away from the substrate. Different to the tip-CVs recorded 50 µm away from the iron flake substrate, hindered diffusion of dissolved oxygen and no OH^- oxidation wave is observed in the tip-CVs recorded close to the iron powder substrate. This suggests that the iron powder was not producing any electroactive species, which means no corrosion activity.

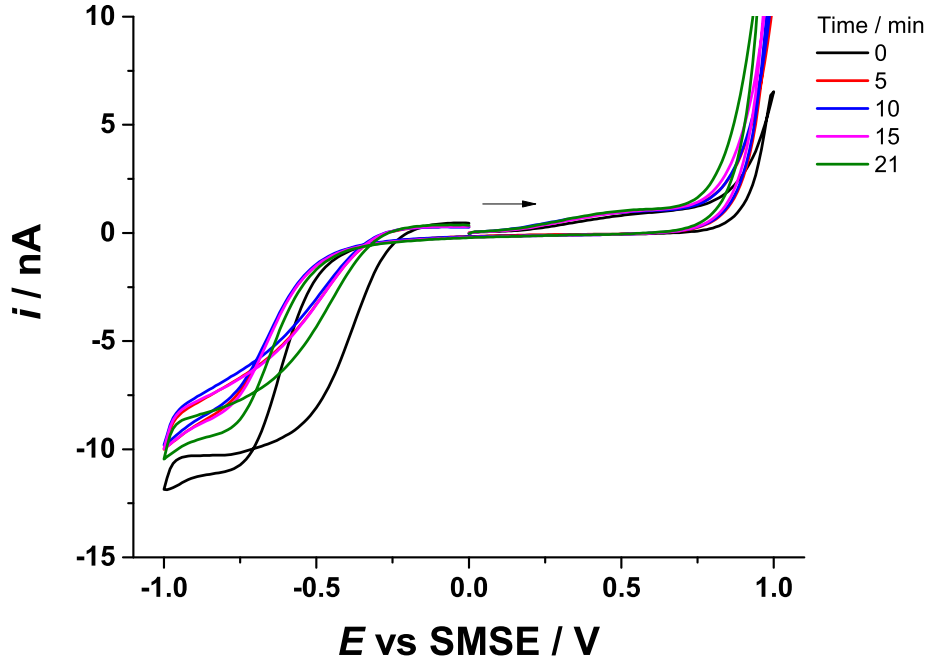

(a) 500 µm

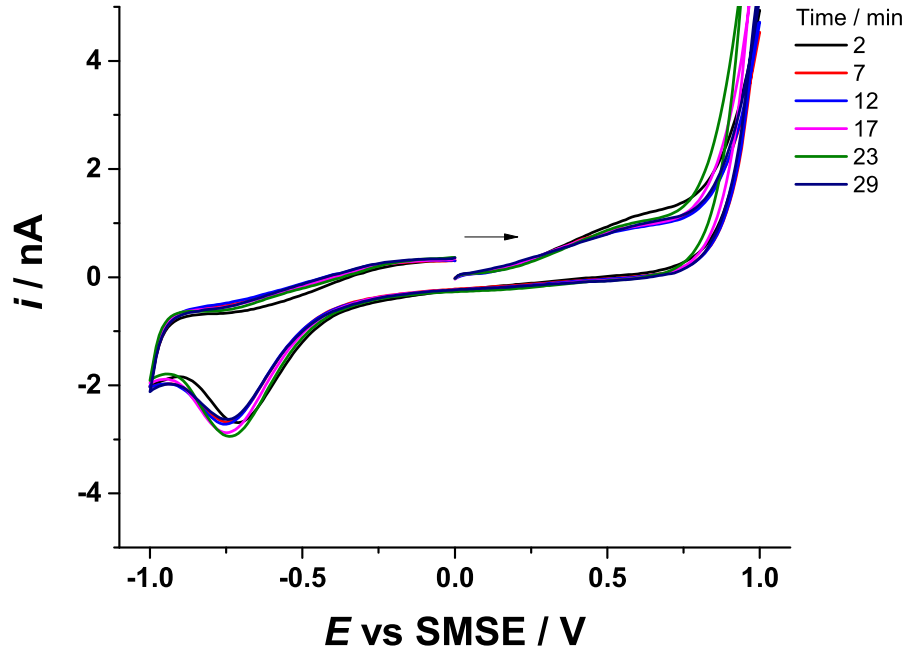

(b) 50 µm

Figure 5.10: Tip-CVs recorded with a 25 µm Pt disc located 500 µm (a) and 50 µm (b) above the iron powder substrate in 10 mL of aerated synthetic groundwater at $0.1\,\mathrm{V\,s^{-1}}$. $RG = 40$.

The tip-CVs shown in Figure 5.10 showed that the tip was only able to record the ORR when placed in the bulk. Because the substrate was not consuming O_2, its hindered diffusion was observed when the electrode was placed close to substrate. Figure 5.11 shows a schematic representation of the reactions occurring at the substrate and at the electrode when the tip-substrate distance was 500 µm (a) and 50 µm (b).

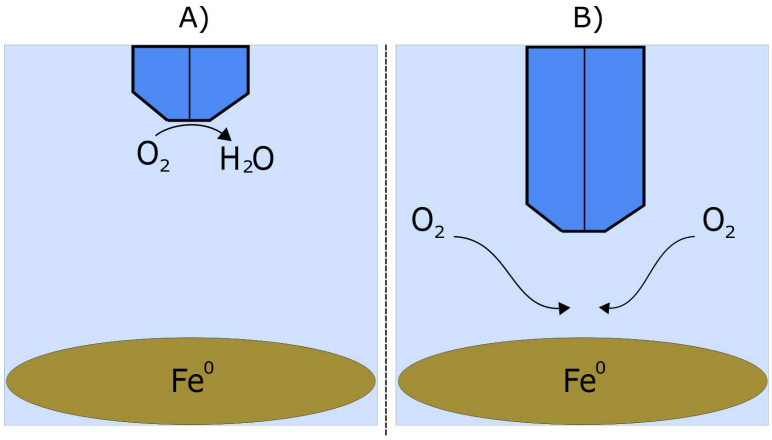

Figure 5.11: Schematic representation of the reactions occurring at the substrate, and at the tip when located 500 µm (a) and 50 µm (b) above the iron powder substrate.

The SECM experiments revealed once more that the iron flakes are unusually more active than the iron powder. The iron flakes showed a higher dissolved oxygen uptake, which suggests a higher corrosion activity. The next section shows experiments performed when the substrates were exposed to 10 mL of synthetic groundwater with ferrocyanide to compare the uptake efficiency of both materials towards a model contaminant.

5.2.2 Exposure to synthetic groundwater + ferrocyanide

In this experiment the substrates were exposed to 10 mL of a 5 mM ferrocyanide in synthetic groundwater. The methodology was carried out as in previous experiments, tip-CVs were recorded at a fixed interval of time. However, measurements were only acquired when the electrode was placed 500 µm away from the iron substrates because we were only interested in the uptake from the bulk. Figure 5.12 and Figure 5.14 show the tip-CVs acquired at a fixed time intervals above the iron flakes and iron powder substrates respectively.

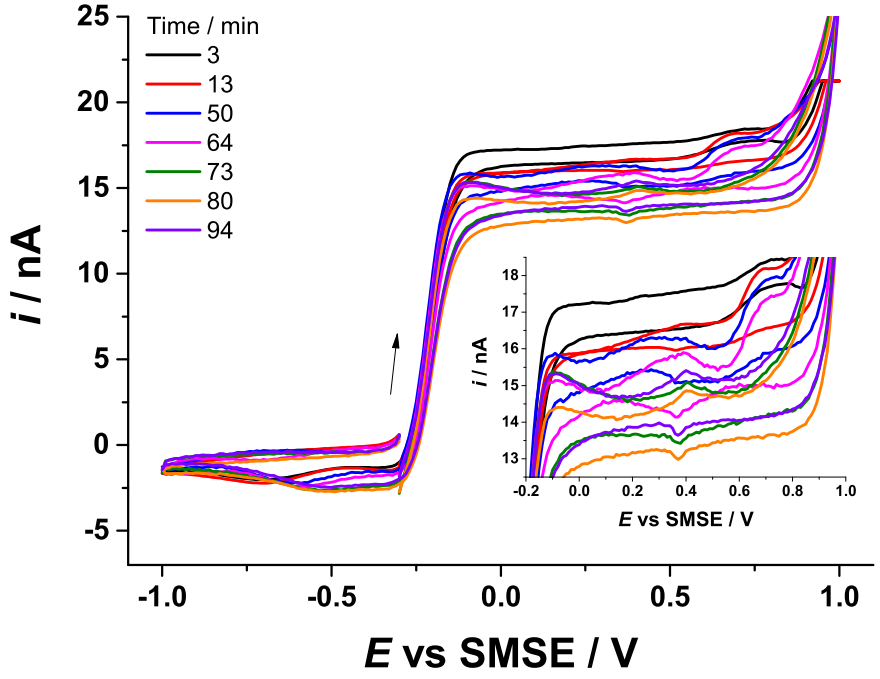

Figure 5.12: Tip-CVs recorded with a 25 µm Pt disc in 10 mL of a 5 mM ferrocyanide solution prepared in synthetic groundwater at 0.1 V s^{-1}. The electrode was positioned 500 µm away from the iron flakes substrate. The time in the caption corresponds to the time that the substrate was exposed to the solution. The insert is a closer look to the cathodic region. $RG = 15$.

The CVs recorded in presence of the iron flakes substrate showed that the limiting current for the oxidation of ferrocyanide decreased over time. This could be because as the substrate was undergoing corrosion it released Fe^{2+} and Fe^{3+} into the solution, which reacted with ferrocyanide to form Prussian blue. This is supported by the micrographs shown in Figure 5.13, where a blue film is observed at the iron flake substrate. The CVs also show a wave at about 0.8 V, which could correspond to the onset of OH^- oxidation, indicating the increasingly alkaline environment as the corrosion of the flakes progressed. Additionally, the ORR appears in the CVs acquired after 3 min and 13 min of exposure, but after that the cathodic region becomes wider and no signs of ORR are observed. This suggests oxygen consumption by the iron flakes.

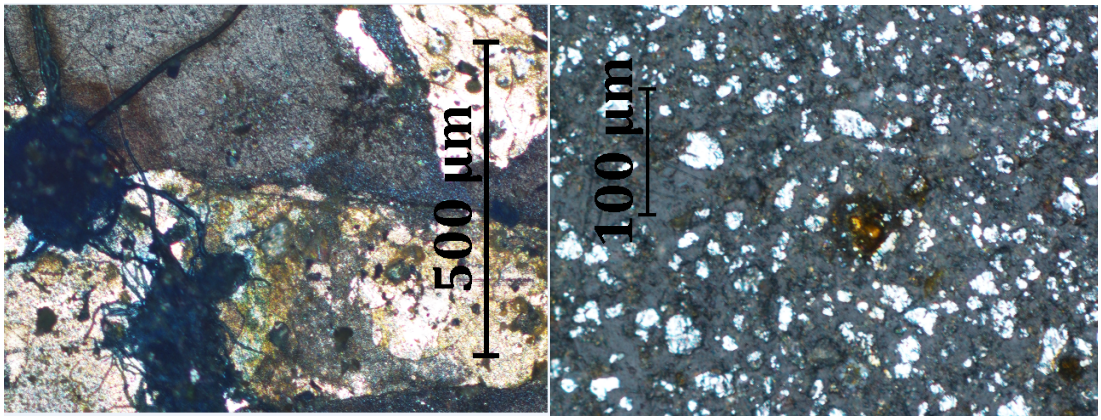

(a) Iron flake (b) Iron powder

Figure 5.13: Micrographs of the iron flake and iron powder substrate after being exposed to 10 mL of a 5 mM ferrocyanide solution prepared in synthetic groundwater.

In the case of the iron powder (Figure 5.14), the limiting current for the oxidation of ferrocyanide remained the same over time, there was no OH^- oxidation wave, and no oxygen consumption was seen in the voltammetry. This implied that the iron powder did not undergo corrosion in the time scale of the experiment. In contrast, the tip-CVs recorded 500 µm away from the iron flakes showed the consumption of ferrocyanide and dissolved oxygen.

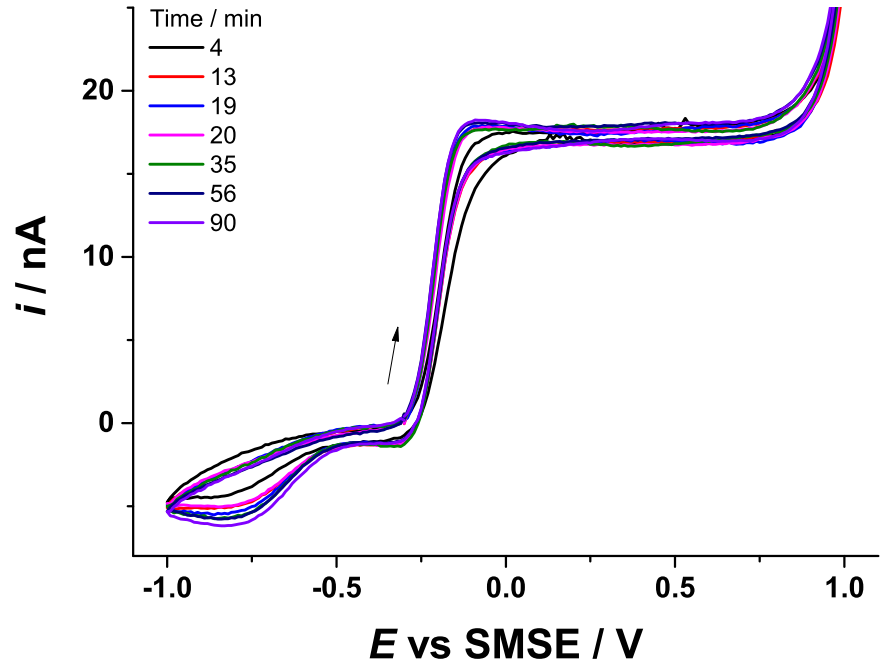

Figure 5.14: Tip-CVs recorded with a 25 µm Pt disc in 10 mL of a 5 mM ferrocyanide solution prepared in synthetic groundwater at $0.1\,\mathrm{V\,s^{-1}}$. The electrode was positioned 500 µm away from the iron powder substrate. The time in the caption corresponds to the time that the substrate was exposed to the solution. $RG = 15$.

According to the tip-CVs acquired and the micrographs obtained after the exposure we can propose the reactions occurring at the tip and the substrate.
Main reactions at the tip: the oxygen reduction reaction (equation 5.5) and the oxidation of ferrocyanide (equation 5.6).

$$\mathrm{O_2 + 2\,H_2O + 4\,e^- \longrightarrow 4\,OH^-} \tag{5.5}$$

$$\mathrm{Fe(CN)_6{}^{4-} \longrightarrow Fe(CN)_6{}^{3-} + e^-} \tag{5.6}$$

Main reactions at the substrate (corrosion): the oxygen reduction (equation 5.5), the oxidation of Fe (equation 5.7), and the production of $\mathrm{Fe(OH)_2}$ (equation 5.8).

$$\mathrm{Fe^0 \longrightarrow Fe^{2+} + 2\,e^-} \tag{5.7}$$

$$\mathrm{Fe^{2+} + 2\,OH^- \longrightarrow Fe(OH)_{2(s)}} \tag{5.8}$$

Reactions at the substrate (formation of Prussian blue): formation of the soluble form (equation 5.9), and the precipitate or true Prussian blue (equation 5.10).

$$K^+ + Fe(CN)_6{}^{4-} + Fe^{3+} \longrightarrow KFe^{III}[Fe(CN)_6{}^{4-}] \tag{5.9}$$

$$4\,Fe^{3+} + 3\,Fe(CN)_6{}^{4-} \longrightarrow Fe_4[Fe^{III}Fe(CN)_6{}^{4-}]_{3(s)} \tag{5.10}$$

All the experiments shown at the moment confirm what our colleagues from oceanography found: the iron flakes corrode quicker and also are more efficient at up taking redox species from solution (ferrocyanide like in this case).

The next stage was to determine the $ReO_4{}^-$ uptake capacity of each of the materials by measuring the residual $ReO_4{}^-$ through CV at a Pt microdisc. $ReO_4{}^-$ was chosen because it is a chemical analogue of $TcO_4{}^-$ as explained in section 2.2.3. This means that the results of the experiments performed using $ReO_4{}^-$ form the basis of a methodology to predict the reactivity of $TcO_4{}^-$ under the same conditions. Therefore, the voltammetry of $ReO_4{}^-$ in synthetic groundwater was investigated as shown in the next section.

5.2.3 Exposure to synthetic groundwater + perrhenate

A CV with a 50 µm diameter Pt disc in a deaerated 1 mM NH_4ReO_4 solution prepared in synthetic groundwater was recorded to investigate the response of the reduction of $ReO_4{}^-$. This was done in order to monitor its concentration over time and determine the uptake capacity of each of the materials as in the previous experiments. However, the CV in Figure 5.15 shows the lack of an oxidation or reduction wave for $ReO_4{}^-$ in synthetic groundwater.

Also, the ions in the synthetic groundwater seemed to mask some of the surface processes at the Pt electrode like the H adsorption and desorption.

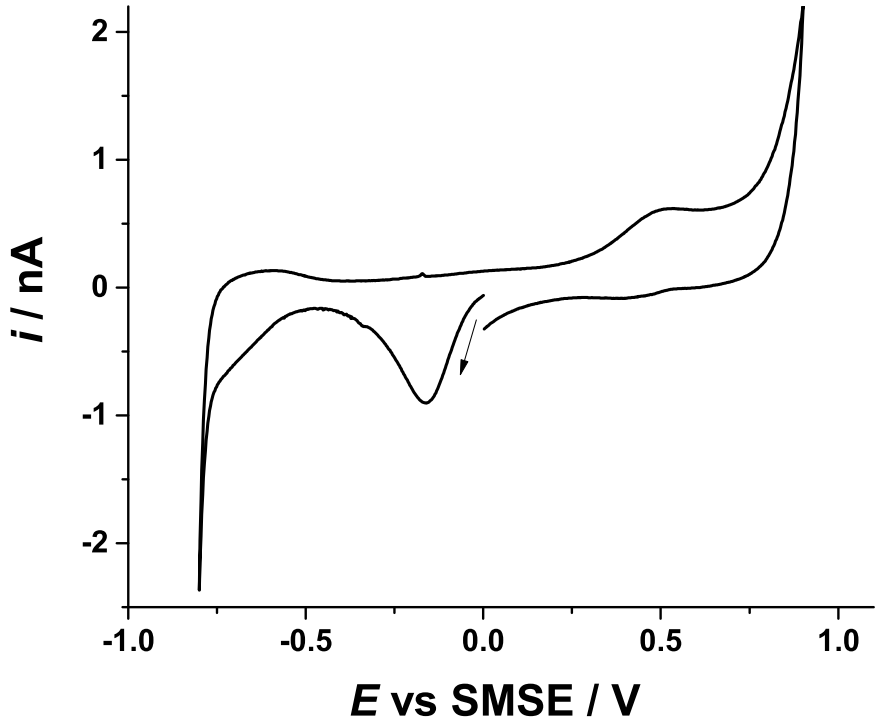

Figure 5.15: CVs recorded with a 50 µm diameter Pt disc in a deaerated 1 mM NH_4ReO_4 solution prepared in synthetic groundwater at $0.05\,V\,s^{-1}$.

On the other hand, the voltammetry performed in a 1 mM NH_4ReO_4 solution prepared in 1 M H_2SO_4 using Milli-Q water in Figure 5.16 showed a clear oxidation wave. No obvious cathodic wave is observed; however, the current offset of the blue curve with respect to the black curve at -0.45 V could be a consequence of the reduction of ReO_4^-. A decrease of the intensity of the H adsorption and desorption peaks, and the Pt oxide formation and stripping peaks compared to those in the CV with no ReO_4^- was observed.

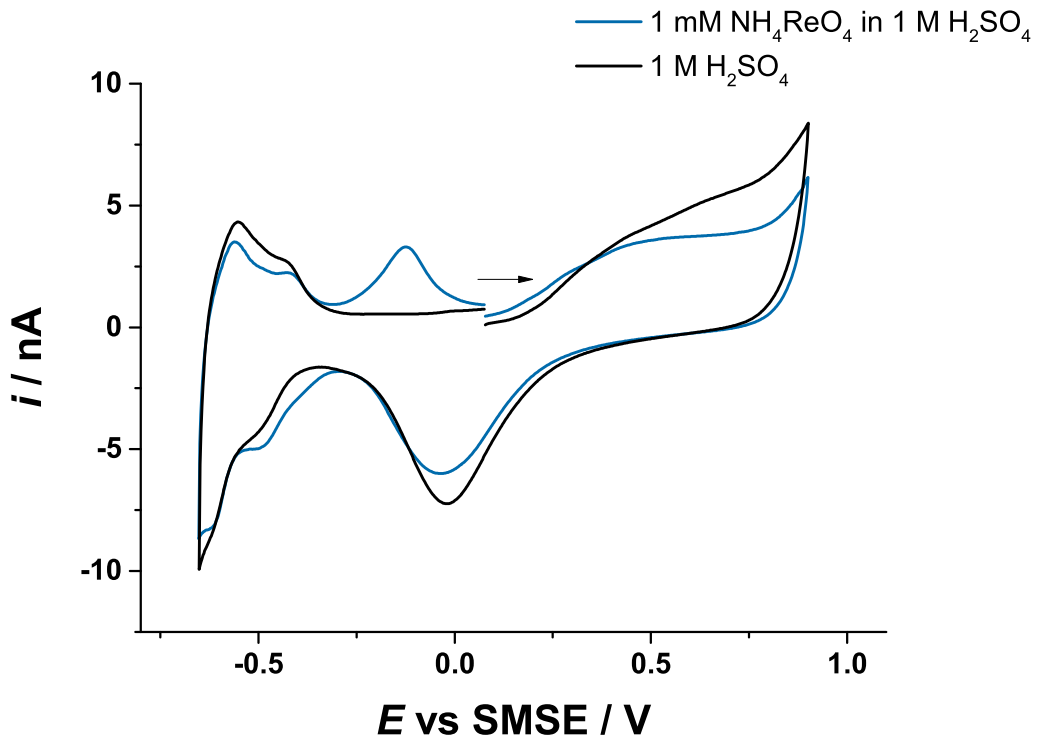

Figure 5.16: CV recorded with a 50 µm diameter Pt disc in a deaerated 1 mM NH_4ReO_4 in 1 M H_2SO_4 solution at 0.05 V s^{-1}.

Figure 5.17 shows CVs recorded using different negative potentials limits. These showed that the oxidation peak is not observed unless the potential is polarised beyond the H region. This demonstrate that the reduction of ReO_4^- at Pt requires Had to drive the reaction as mentioned in section 2.2.3. Had are electrochemically formed on the electrode surface and subsequently they reduce the ReO_4^- ions through a chemical reaction [78].

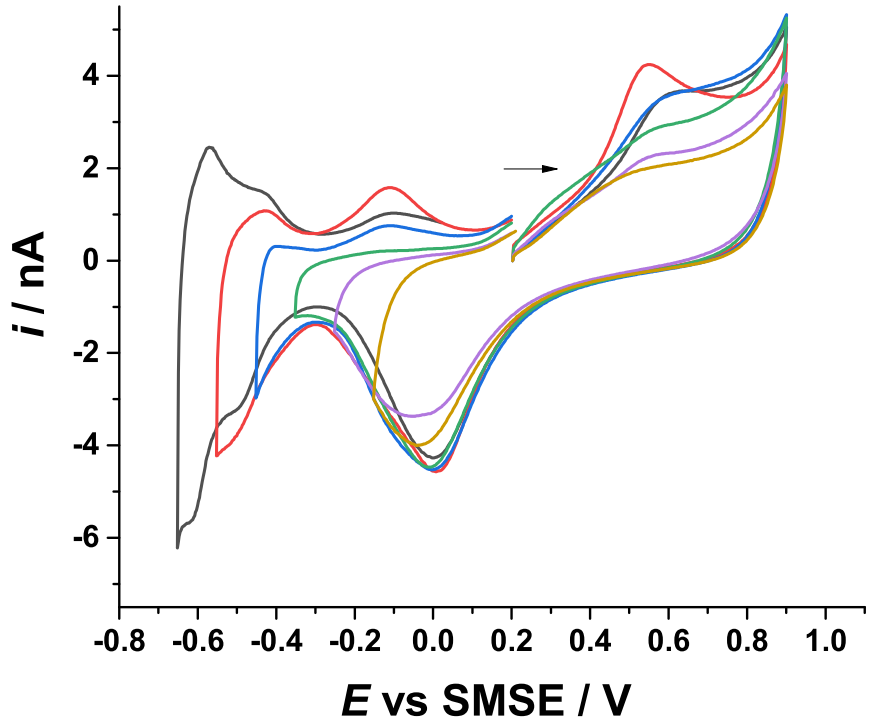

Figure 5.17: CVs recorded with a 50 µm diameter Pt disc in a deaerated 1 mM NH_4ReO_4 in 1 M H_2SO_4 solution at 0.05 V s^{-1}.

These measurements showed that we could not use CV to monitor the concentration of ReO_4^- in synthetic groundwater to compare its uptake by the different iron substrates. Because of this we exposed the iron substrates to a fixed volume of ReO_4^- solution and we interrogated the substrates surface using laser ablation inductively coupled plasma mass spectrometry (ICP-MS), scanning electron microscopy (SEM) and energy dispersive spectroscopy (EDX). The results of the interrogation of the iron surface through laser ICP-MS are described in the next section.

5.3 Laser ablation inductively coupled plasma mass spectrometry (ICP-MS)

Iron substrates made with iron powder from Aldrich (≈ 50 µm), and from large (≈ 750 µm) and medium (≈ 400 µm) size particles obtained from an iron chip were made by casting the materials in epoxy resin as shown in section 3.4.2.

Note that the size of the iron flakes provided by the oceanographers ranged from 100 µm to 1000 µm, which means the new materials were within this range. The mentioned

iron substrates were polished using sand paper of 1200 grit until any rust on the surface was removed, then for 3, 5 and 8 minutes with alumina powder 5 µm, 1 µm and 0.3 µm respectively on a polishing pad prior the start of the experiment. Then, they were exposed to 5 mL of a 1 mM NH_4ReO_4 solution prepared in synthetic groundwater for a week. After that, their surface was interrogated using laser ablation ICP-MS. In this technique a laser beam is focused on the sample surface to generate fine particles, which are then transported for rapid elemental and isotopic analysis. This technique was chosen because it can perform highly sensitive chemical analysis down to ppb (parts per billion) level without any sample preparation. The iron substrates were loaded into the laser's sample holder as shown in Figure 5.18 along with a polished chip of NIST 610 glass standard for calibration, an intact iron chip, and a piece of iron obtained after crushing the chip into smaller pieces with an industrial drill.

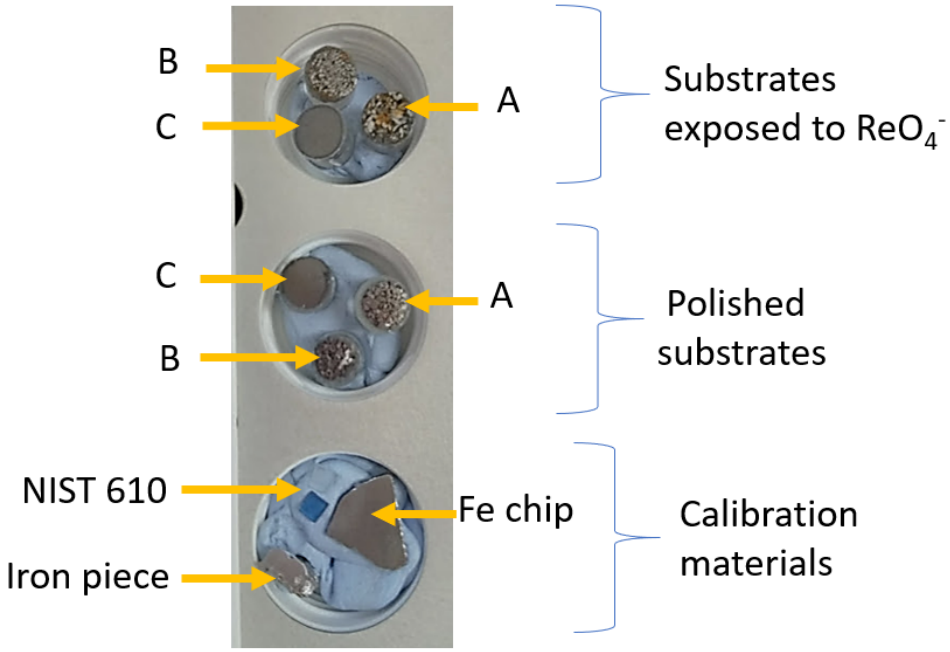

Figure 5.18: Micrograph of the sample holder employed during the laser ablation experiment. A= Large iron substrate. B= medium particle size. C= iron powder from Aldrich.

Ablated material was transported to the ICP-MS using a He carrier gas via a three port mixing bulb. Elemental data were acquired using a New Wave NWR193 excimer laser ablation system coupled to a Thermo X-Series II quadrupole ICP-MS. All ICP-MS and laser settings were optimised for optimal sensitivity and stability. Using the

New Wave laser system software shot locations were mapped across each sample and the calibration standards using the following parameters: Spot size: 10 µm, pulse rate: 5 Hz, energy: 50%, He flow: 1000 ml/min, Ar flow: 400 ml/min, acquisition time: 15-120 seconds, based on line raster length. "Wash" time between shots: 40 s.

Before and after the analysis multiple repeat measurements of the NIST 610 standard were made using the same parameters. The count per second recorded for each analysis were averaged and used to produce a calibration based on the known concentration of Re. The reference concentration values for Re (49.9 ppm), and for W (499 ppm) were extracted from the GeoReM database [112]. By comparing the counts per second measured in the standard to its known concentration, a calibration factor was determined. This factor was then applied to all the unknown shots and concentrations determined. For the analysis, we looked for W because we wanted to know if the composition of the material was affected by making the iron particles smaller using an industrial drill made of WC.

Figure 5.19 shows the plot of the % Re and concentration of W in ppm obtained for the iron chip, and the piece of iron made from it using an industrial drill shown in Figure 5.18. It is possible to appreciate that there was no Re at the iron surface before and after crushing the chip. On the other hand, the concentration of W increased up to 0.6 ppm after crushing the iron chip.

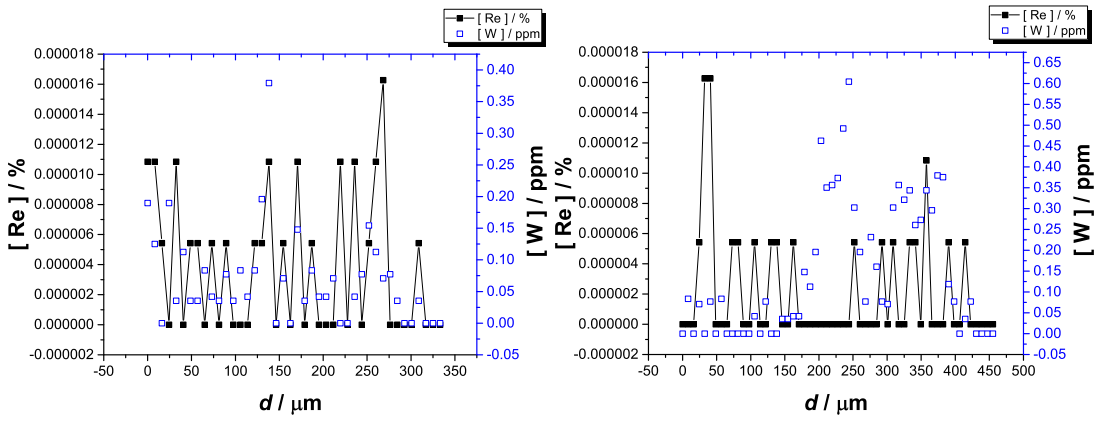

(a) Iron chip (intact)

(b) Iron chip (crushed)

Figure 5.19: Re (%) and W (ppm) concentration as a function of the distance travelled by the laser at the surface of the iron chip (left) and the piece of iron (right) shown in Figure 5.18.

After exposure to a 1 mM NH_4ReO_4 solution prepared in synthetic groundwater for a week the iron substrates made with large and medium size iron particles showed

various regions covered in rust. In contrast, the substrate made with iron powder from Aldrich showed a small area with signs of corrosion.

Figure 5.20 shows the plot of the % Re and concentration of W in ppm of a region in the large iron particles substrate that looked pristine after being exposed ReO_4^- for a week. According to the data acquired, the concentration of both W and Re was very close to zero, except below $d = 50\,\mu m$. This was because the laser was positioned in an area covered in rust at the start of the measurement and then it moved along the pristine area. This suggests that ReO^- does not reduce to ReO_2 at a freshly polished iron surface. On the other hand, when passing the laser through an area covered in rust in the same substrate, the signal for Re increased considerably as shown in Figure 5.21.

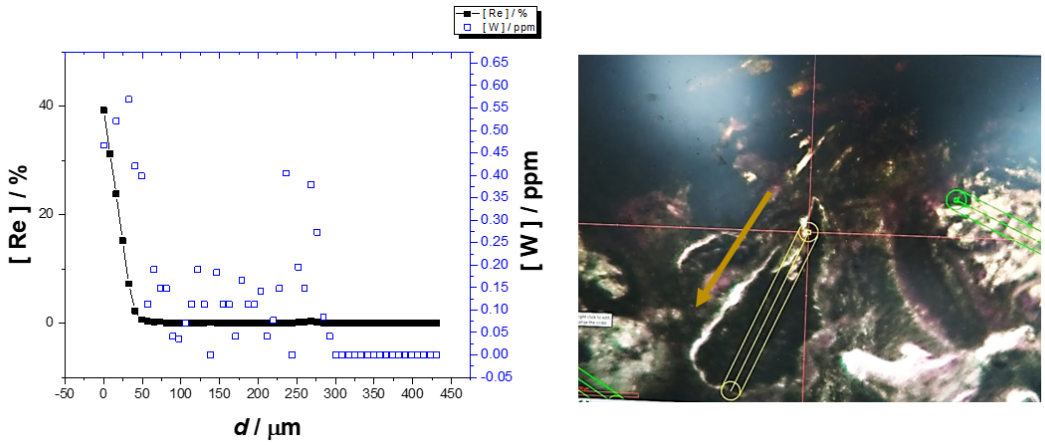

Figure 5.20: Re (%) and W (ppm) concentration as a function of the distance travelled by the laser at the large iron particles substrate (left), photograph of the location of the analysis (right). The orange arrow indicates the direction of the laser trajectory.

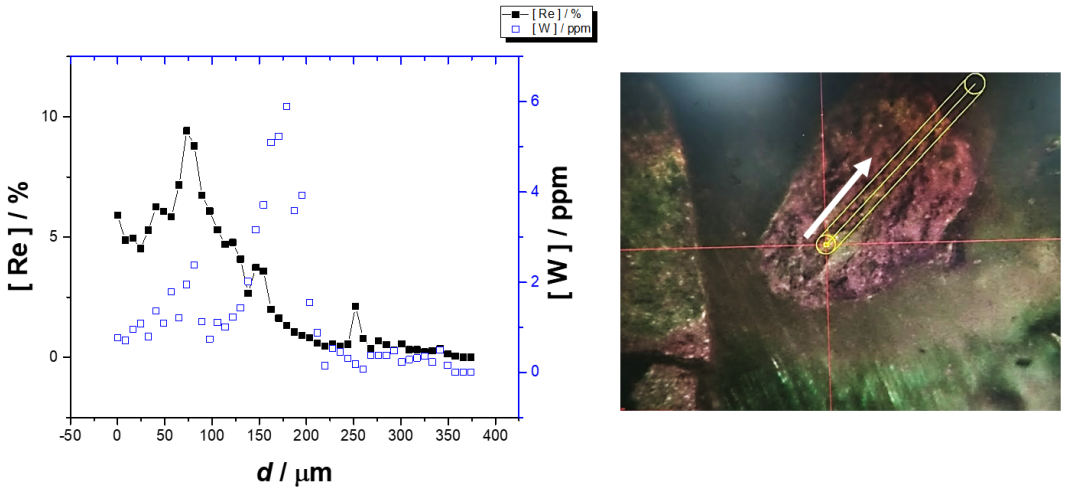

Figure 5.21: Re (%) and W (ppm) concentration as a function of the distance travelled by the laser at the large iron particles substrate (left), photograph of the location of the analysis (right). The white arrow indicates the direction of the laser trajectory.

The same occurred when interrogating the surface of the medium size iron particles substrate. Figure 5.22 shows the increasing concentration of Re as the laser went from a pristine area to a region covered in rust.

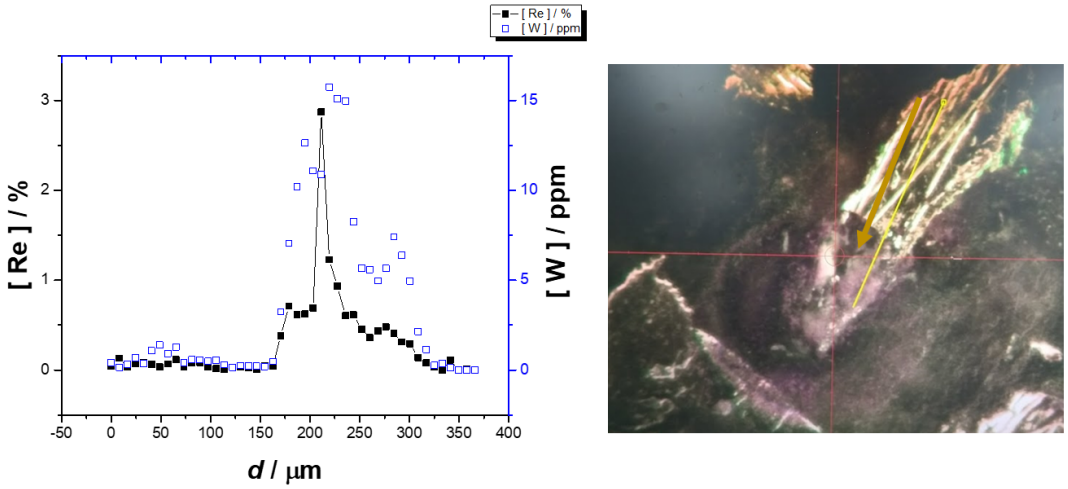

Figure 5.22: Re (%) and W (ppm) concentration as a function of the distance travelled by the laser at the medium size iron particles substrate (left), photograph of the location of the analysis (right). The orange arrow indicates the direction of the laser trajectory.

As previously mentioned, the substrate made with iron powder from Aldrich showed only a very small area covered in rust. This was explored by many ablation lines (green lines in Figure 5.23) but only the one indicated with the orange arrow showed a significant increase in the % of Re.

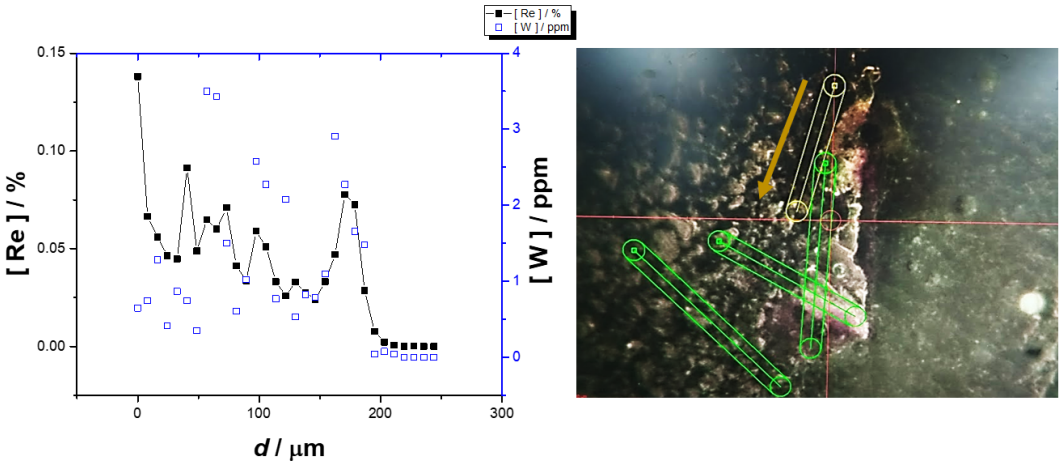

Figure 5.23: Re (%) and W (ppm) concentration as a function of the distance travelled by the laser at the substrate made with iron powder from Aldrich (left), photograph of the location of the analysis (right). The orange arrow indicates the direction of the laser trajectory.

From these experiments we learnt that ReO_2 co-deposits along with the iron corrosion products. The areas in the iron substrate that were not covered in rust did not show a signal for Re. On the other hand, in agreement with previous experiments, the iron powder from Aldrich showed very little reactivity compared larger iron particles. This suggests that the high reactivity observed on the iron flakes provided by our colleagues from the NOC was not related to the source of the material but to its size. In order to investigate the role of the particle size from the same source, we created iron particles with a size comparable to the iron powder from Aldrich using an iron chip as described in section 3.2. This would help to clarify if the trends observed were related to the source of the materials of to their particle size. The next section shows the results of the experiments performed using these materials, and the interrogation of the surface using SEM/EDX.

5.4 Scanning electron microscopy (SEM) and energy dispersive spectroscopy (EDX)

The experiments in this section were conducted to investigate the role of the particle size and the source of iron in its corrosion activity and ReO_4^- uptake from groundwater. The iron substrates made with large ($\approx$ 750 µm), medium ($\approx$ 400 µm) and small ($\approx$ 70 µm) iron particles from the same iron chip, and the substrate made with iron powder from Aldrich ($\approx$ 50 µm) were exposed to a 5 mL of 1 mM ReO_4^- solution for a week.

As in previous experiments, the substrates were polished using sand paper of 1200 grit until any rust on the surface was removed, then for 3, 5 and 8 minutes with alumina powder 5 µm, 1 µm and 0.3 µm respectively on a polishing pad prior the start of the experiment. The composition of the rust formed at the iron's surface after exposure to ReO_4^- was investigated using EDX. According to the results obtained through the laser ablation ICP-MS experiments, Re should be found within the corrosion products. SEM images and EDX spectra were obtained using a FEI XL30 environmental scanning electron microscope (ESEM) with a W filament as electron source, an UltaDry EDX, 10 mm^2 detector in the low vacuum mode (wet mode).

EDX uses the X-ray spectrum emitted by a solid sample bombarded with a beam of electrons to obtain localized chemical analysis. The EDX spectra is a plot of the the number of counts per channel as a function of the X-ray energy. The energy and intensity of the x-rays produced are related to the atomic number of the emitting element and the areal density of the examined layer. The penetration depth of the electrons depends on the electron accelerating voltage and the thickness of the sample. For standard electron probe beams (2 to 50 keV) it can be from 0.1 µm to about 5 µm [113].

The SEM images and all the EDX spectra of the substrates before and after exposed to ReO_4^- are shown in appendix B. These were acquired using 20.0 kV as accelerating voltage, however a higher resolution could have been achieved using a higher accelerating voltage. Figure 5.24 shows the substrates made from the same iron chip immersed in the ReO_4^- solution after a week. We can appreciate corrosion products in the proximities of the large iron particles substrate but not close to the rest of the substrates.

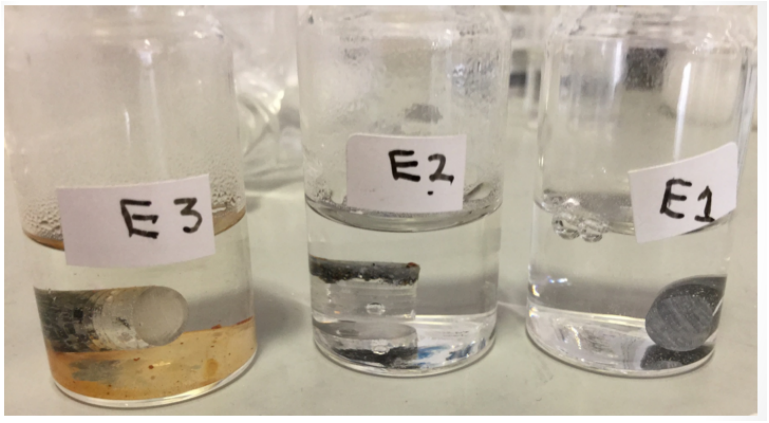

Figure 5.24: Photograph of the substrates made from the same iron chip after being exposed to 5 mL of a 1 mM ReO_4^- solution prepared in synthetic groundwater for a week. E1= the substrate made with small iron particles, E2= medium iron particles substrate, and E3= large iron particles substrate.

Figure 5.25 shows optical micrographs of the four substrates after a week of exposure to 5 mL of a 1 mM ReO_4^- solution prepared in synthetic groundwater. In these, the large and medium iron particles show a blue film what could be given by the ReO_2 deposited. The substrate made with small iron particles obtained from an iron chip showed an orange coloured rust. On the other hand, the iron substrate made with iron powder from Aldrich did not show the formation of rust.

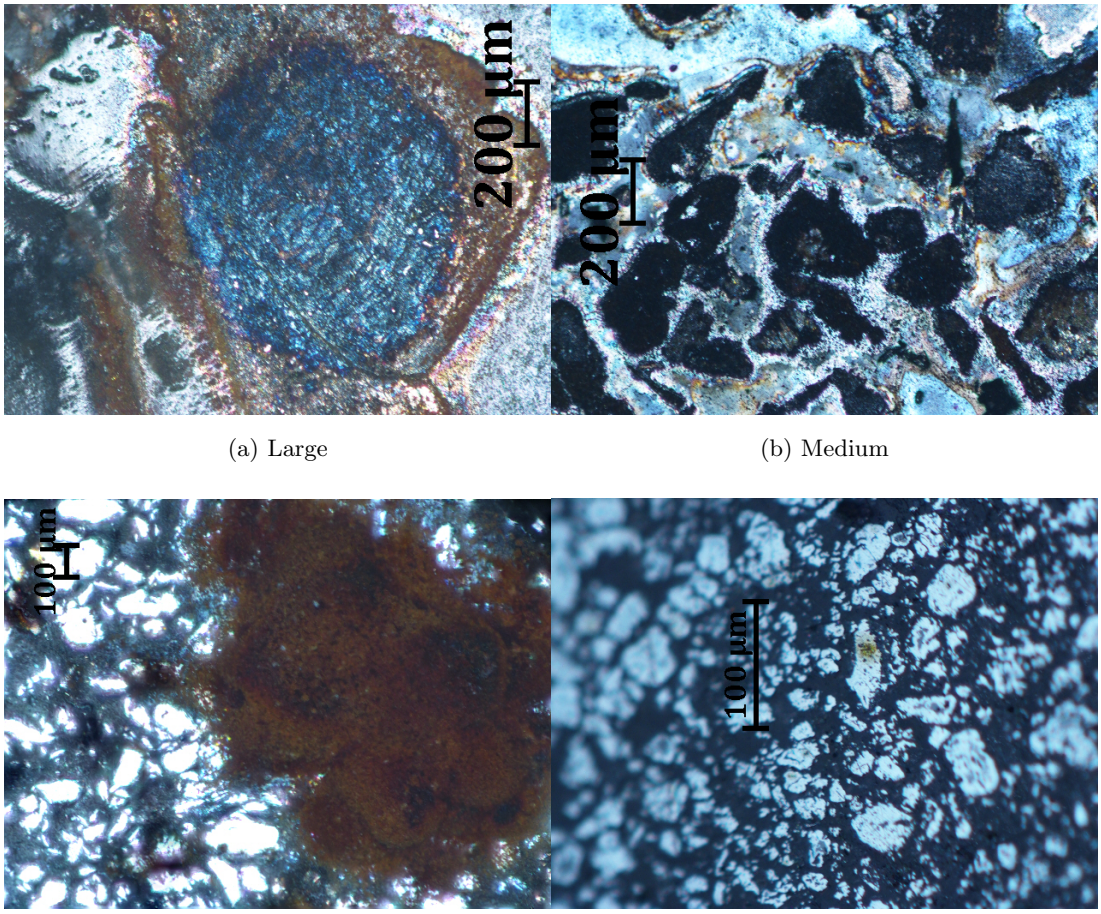

(a) Large (b) Medium

(c) Small (d) Iron powder from Aldrich

Figure 5.25: Micrographs of the substrates made from the same iron chip (a, b and c), and the iron powder from Aldrich (d) after being exposed for a week to 5 mL of a 1 mM ReO_4^- solution prepared in synthetic groundwater.

Figure 5.26 shows the SEM image obtained in one of the rust features observed in the large iron particles substrate. Table 5.1 shows the elemental composition of each of the points highlighted in the image. Table 5.2 shows the error corresponding to the data in Table 5.1.

Overall, the largest % atom found for Re in all the substrates was point 1 shown in Table 5.1 for the large iron particles. The medium size iron particles showed a lower % atom of Re in all of the points. The small iron particles obtained from an iron chip and the iron powder from Aldrich did not show any Re.

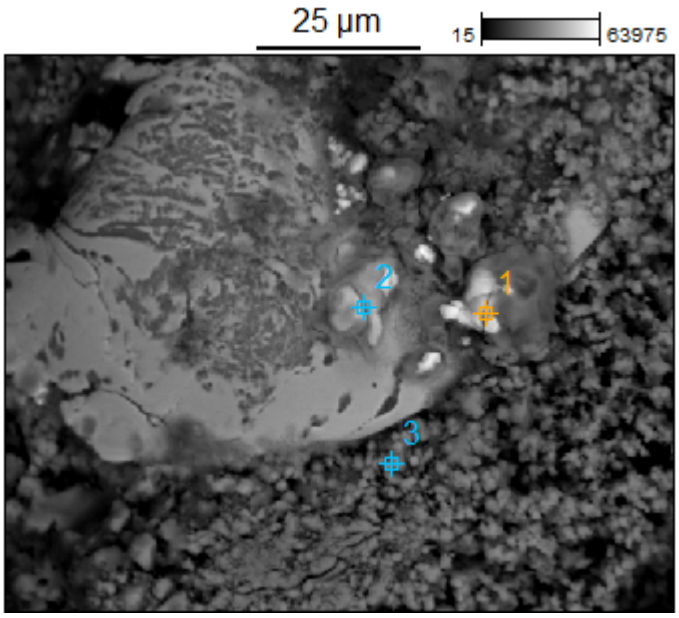

Figure 5.26: SEM image from the large iron particle size substrate. Image Resolution: 512 by 426. Image Pixel Size: 0.20 µm Acc. voltage: 20.0 kV, magnification: 1200.

Table 5.1: Atom % for the points in Figure 5.26.

	C-K	**O-K**	**Mg-K**	**Al-K**	**Si-K**	**S-M**	**Cl-K**	**Ca-L**	**Fe-K**	**Zn-K**	**Re-M**
Point 1	27.4	49.6			1.9	1.1	2.8		8.1	1.6	7.6
Point 2	18.0	65.2			1.2	2.6	0.5		7.3	0.6	4.5
Point 3	20.1	58.9	0.3	1.5	3.3	0.1		0.4	15.4		

Table 5.2: Atom % error for the points in Figure 5.26.

	C-K	**O-K**	**Mg-K**	**Al-K**	**Si-K**	**S-M**	**Cl-K**	**Ca-L**	**Fe-K**	**Zn-K**	**Re-M**
Point 1	± 0.4	± 0.4			± 0.1	± 0.0	± 0.0		± 0.1	± 0.1	± 0.1
Point 2	± 0.5	± 0.4			± 0.1	± 0.0	± 0.0		± 0.1	± 0.1	± 0.0
Point 3	± 0.4	± 0.3	± 0.0	± 0.0	± 0.0	± 0.0		± 0.0	± 0.1		

Figure 5.27 shows the SEM image obtained in one of the rust features observed in the medium size particles substrate. Table 5.3 shows the elemental composition of each of the points in the image. Table 5.4 shows the error corresponding to the data in Table 5.3.

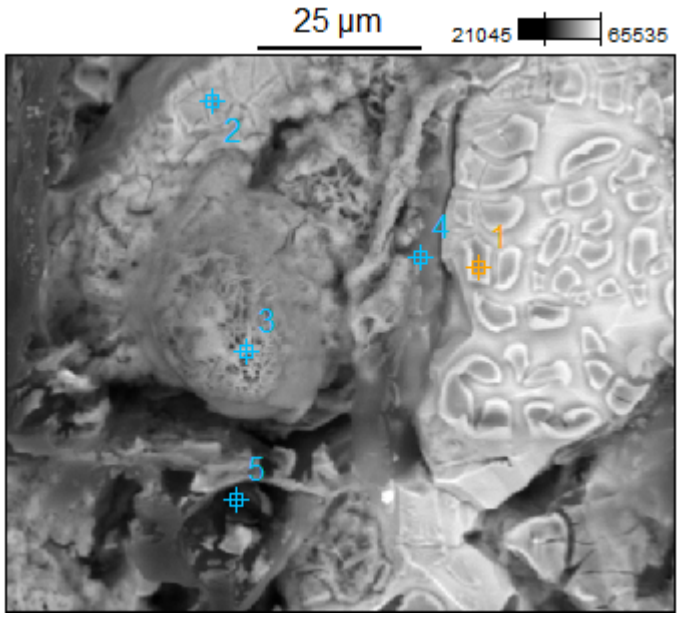

Figure 5.27: SEM image from the medium size iron particle substrate. Image Resolution: 512 by 426 Image Pixel Size: 0.20 µm. Acc. voltage: 20.0 kV Magnification: 1200.

Table 5.3: Atom % for the points showed in Figure 5.27.

	C-K	**O-K**	**F-K**	**Al-K**	**Si-K**	**Cl-K**	**Fe-M**	**Zn-K**	**Re-M**
Point 1	30.3	40.1		0.3	0.3		27.6	0.2	1.2
Point 2	29.9	36.1		0.2	0.2		33.2		0.5
Point 3	17.1	63.4	0.0		0.2		19.1		0.1
Point 4	43.7	29.0			0.2	0.1	26.9		0.2
Point 5	68.0	24.2	0.8		0.1	0.3	6.5		0.2

Table 5.4: Atom % error for the points in Figure 5.27.

	C-K	**O-K**	**F-K**	**Al-K**	**Si-K**	**Cl-K**	**Fe-M**	**Zn-K**	**Re-M**
Point 1	± 0.4	± 0.3		± 0.0	± 0.0		± 0.1	± 0.0	± 0.0
Point 2	± 0.4	± 0.3		± 0.0	± 0.0		± 0.1		± 0.0
Point 3	± 0.3	± 0.4	± 0.0		± 0.0		± 0.1		± 0.0
Point 4	± 0.4	± 0.2			± 0.0	± 0.0	± 0.1		± 0.0
Point 5	± 0.5	± 0.3	± 0.2		± 0.0	± 0.0	± 0.1		± 0.0

Figure 5.28 shows the SEM image obtained in the only rust feature observed in the

substrate made with small iron particles obtained from an iron chip. Table 5.5 shows the elemental composition of each of the points in the image.Table 5.6 shows the error corresponding to the data in Table 5.5.

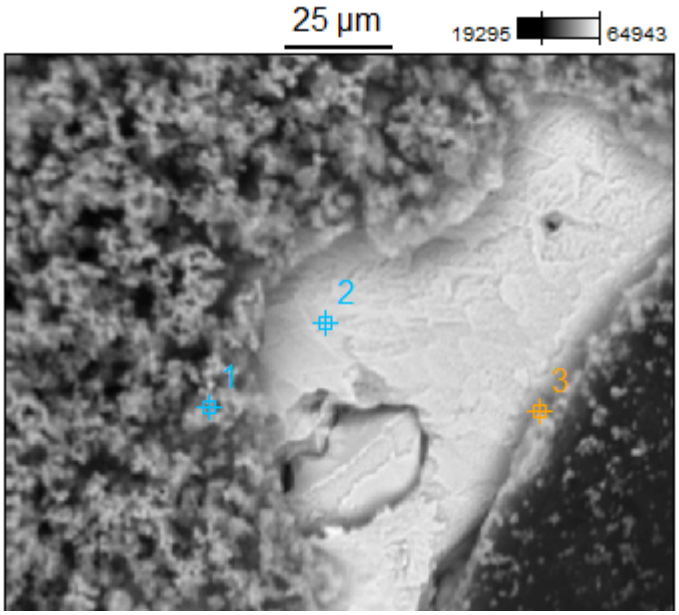

Figure 5.28: SEM image of the substrate made with small iron particles obtained from an iron chip. Image Resolution: 512 by 426. Image Pixel Size: 0.3 µm. Acc. voltage: 20.0 kV. Magnification: 800.

Table 5.5: Atom % for the points in Figure 5.28.

	C-K	**O-K**	**Al-K**	**Si-K**	**Cl-K**	**Fe-K**
Point 1	24.1	50.5	0.3	0.9	0.1	24.2
Point 2	28.7	28.1	0.3	0.7		42.2
Point 3	40.1	15.1	0.5	0.4	0.1	43.8

Table 5.6: Atom % for the points in Figure 5.28.

	C-K	**O-K**	**Al-K**	**Si-K**	**Cl-K**	**Fe-K**
Point 1	± 0.4	± 0.3	± 0.0	± 0.0	± 0.0	± 0.1
Point 2	± 0.5	± 0.3	± 0.4	± 0.0		± 0.2
Point 3	± 0.8	± 0.3	± 0.1	± 0.0	± 0.0	± 0.2

Figure 5.29 shows the SEM image obtained in the substrate made with iron powder from Aldrich. Table 5.7 shows the elemental composition of each of the points in the image. Table 5.8 shows the error corresponding to the data in Table 5.7.

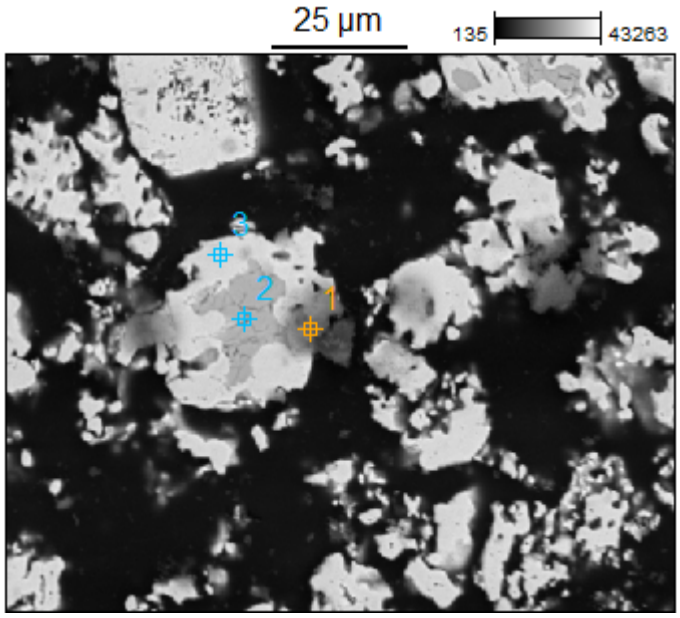

Figure 5.29: SEM image of the substrate made with iron powder from Aldrich. Image Resolution: 512 by 426. Image Pixel Size: 0.24 µm. Acc. voltage: 20.0 kV. Magnification: 1000.

Table 5.7: Atom % for the points in Figure 5.29.

	C-K	**O-K**	**Mg-K**	**Al-K**	**Si-K**	**Cl-K**	**Ca-K**	**Mn-K**	**Fe-K**
Point 1	43.2	31.2		18.2	0.0				7.3
Point 2	32.9	39.9	0.1	1.0	0.1		0.2	0.9	25.0
Point 3	58.0			0.8	0.1	0.1			40.9

Table 5.8: Atom % error for the points in Figure 5.29.

	C-K	**O-K**	**Mg-K**	**Al-K**	**Si-K**	**Cl-K**	**Ca-K**	**Mn-K**	**Fe-K**
Point 1	± 0.4	± 0.2		± 0.1	± 0.0				± 0.1
Point 2	± 0.4	± 0.3	± 0.0	± 0.0	± 0.0		± 0.0	± 0.0	± 0.1
Point 3	± 0.9				± 0.0	± 0.0			± 0.2

At the start of this chapter it was explained how the high Tc uptake by the iron flakes was unusual since one would expect smaller iron particles to be more reactive. However, our experiments showed a similar trend to those performed by our colleagues from oceanography: large iron particles show high corrosion activity and ReO_4^- uptake. The results in this section suggest that the formation of corrosion products and the uptake of Re are closely related; however still does not answer why this trend is observed. In order to investigate this, the corrosion rate of each material was determined using Tafel extrapolation and OCP measurements. The results are shown in the next section.

5.5 Tafel extrapolation and OCP measurements

The experiments in this section were conducted using iron electrodes that were fabricated as mentioned in section 3.3.4. These were exposed to a fixed volume of solution to measure the open circuit potential (OCP) over a period of time and to perform the Tafel extrapolation analysis.

The OCP for each iron electrode was measured over 3 hours in 10 mL of synthetic groundwater. Then, the potential was polarised ±30 mV at 0.001 V s^{-1} from the OCP to obtain the corresponding Tafel plots.

The OCP chronopotentiograms recorded using the iron flake and iron powder electrodes in 10 mL of aerated and deaerated synthetic groundwater are shown Figure 5.30.

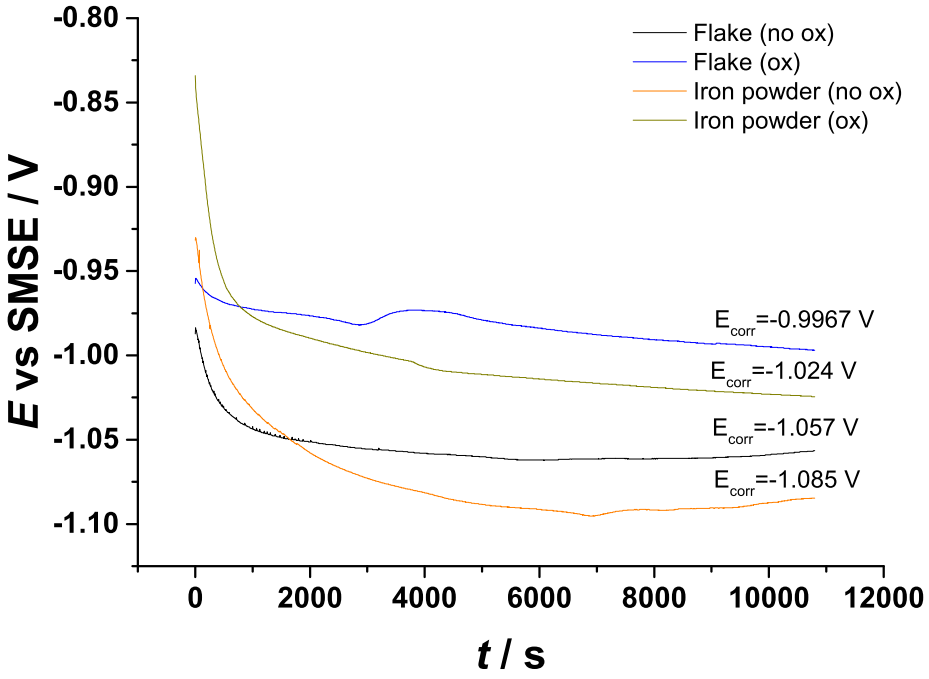

Figure 5.30: OCP chronopotentiograms recorded with the iron flake and the iron powder electrode in 10 mL of aerated and deaerated synthetic groundwater.

The OCP chronopotentiograms show that the corrosion potential for both electrodes acquired more negative values as the exposure time increased. This suggests that the metal surface reacts with the solvent and the dissolved oxygen to form a passive film that makes the corrosion potential more negative.

The potential plateau acquired by the iron flake was more positive than the plateau

for the iron powder electrode in both aerated and deaerated conditions. If we were to compare the corrosion potential of the two iron electrodes in a potential scale, the iron flake in aerated and deaerated conditions would be described as a more powerful reducing agent than the iron powder. This means that the iron flake will donate electrons more easily than the iron powder.

The results of the Tafel extrapolation analysis are summarised in Table 5.9. The corrosion potential (E_{corr}), corrosion current (i_{corr}) and Tafel slopes (b_a, b_c) were obtained by fitting a line to the anodic and cathodic branches in the Tafel plots shown in Figure 5.31 and 5.32.

Table 5.9: Corrosion potentials and currents extracted from the Tafel plots for each material in aerated and deaerated synthetic groundwater.

Electrode and solution	$\boldsymbol{E_{corr}}$ / V	i_{corr} x 10^6/ A cm^2	$\boldsymbol{b_a}$ / mV dec^{-1}	$\boldsymbol{b_c}$ / mV dec^{-1}
Iron flake (aerated)	-0.95	23.90	52	84
Iron flake(deaerated)	-0.96	13.27	43	90
Iron powder (aerated)	-0.91	14.58	94	124
Iron powder (deaerated)	-0.90	1.28	38	57

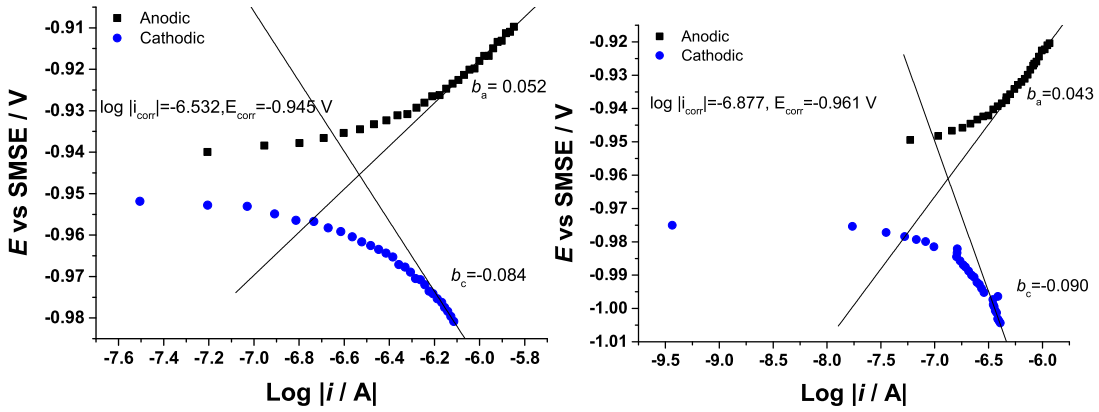

(a) Aerated (b) Deaerated

Figure 5.31: Tafel plots recorded using the iron flake electrode in 10 mL of aerated and deaerated synthetic groundwater. The graph shows the gradient of the linear fit (b_a and b_c) to the anodic and cathodic branches, and the intercept of the two lines.

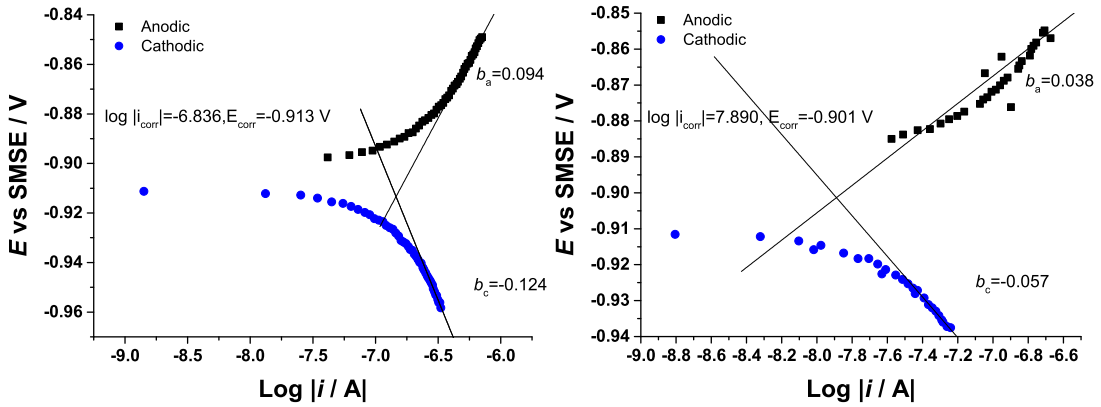

(a) Aerated (b) Deaerated

Figure 5.32: Tafel plots recorded using the iron powder electrode in 10 mL of aerated and deaerated synthetic groundwater. The graph shows the gradient of the linear fit (b_a and b_c) to the anodic and cathodic branches, and the intercept of the two lines.

In agreement with the OCP chronopotentiograms, the iron flake electrode acquired the most positive E_{corr}. The most negative E_{corr} was acquired with the iron powder electrode in deaerated synthetic groundwater.

The i_{corr} of iron in 5 mM $CaCl_2$ solutions has been reported as $35\,\mu A\,cm^{-2}$ with Tafel slopes $b_a = 83$ mV dec^{-1} and $b_c = 77$ mV dec^{-1} [59]. The i_{corr} measured with the iron flake electrode in aerated synthetic groundwater is comparable to this value. On the other hand, the i_{corr} for the iron powder was about 10 times lower than the iron flakes under these conditions. The Tafel slopes obtained for both iron powder and iron flakes are not comparable to those reported in the literature.

The OCP measurements and the Tafel extrapolation allowed us to quantitatively determine the corrosion rate of the iron powder and iron flake electrodes. The results agreed with what qualitatively we found out with the SECM, laser ablation ICP-MS, SEM and EDX: the iron flakes have a higher corrosion rate than the iron powder. However, the use of the Tafel extrapolation in this case has limitations because the surface area of the electrodes is not comparable. Also, the model assumes uniform corrosion, which ignores the effect on the corrosion activity of the of the individual in the synthetic groundwater. Additionally, the extraction of the information using graphical methods can lead to errors in the determination of the parameters.

5.6 Conclusions

The SECM G/C mode allowed the investigation of the corrosion activity of substrates made with iron powder and iron flakes provided by collaborators from the NOC. The current of electroactive species in the solution and released by the substrate was monitored by recording tip-CVs 500 µm and 50 µm above each substrate. The consumption of dissolved oxygen was monitored by recording the ORR limiting current over time and served as a parameter to compare the corrosion activity of both substrates. The tip-CVs acquired 500 µm above the iron powder substrate showed the ORR over time, which suggested poor dissolved oxygen consumption. The response observed when the tip was positioned 50 µm from the iron powder substrate showed the hindered diffusion of dissolved oxygen. This implied poor reactivity of the substrate.
On the other hand, the tip-CVs recorded 500 µm away from the iron flake did not show the distinctive ORR wave, but a more pronounced the H region. This suggested that the dissolved oxygen was consumed by the corrosion of the iron underneath. To support that, the tip-CVs acquired 50 µm showed a systematic increase of the OH^- produced by the corrosion of the iron flakes. Comparatively, the iron powder substrate showed poor dissolved oxygen consumption whereas the iron flake showed its avid consumption that implied a higher corrosion activity.

When the iron powder and flake substrates were exposed to synthetic groundwater with ferrocyanide as a model contaminant, the later acted like an indicator of the corrosion activity of the substrates. The decrease of the limiting current of ferrocyanide implied that it was being consumed by the reaction with $Fe^{2+/3+}$ to form Prussian blue. The tip-CVs acquired 500 µm above each substrate showed a systematic decrease of the ferrocyanide limiting current in the case of the iron flakes, and no changes for the iron powder. This suggested that the flakes undergo corrosion, which produced $Fe^{2+/3+}$ that reacted with ferrocyanide to form Prussian blue, but not the iron powder. Micrographs of the substrate's surface showed a blue film on the iron flakes substrate and none in the iron powder.

Iron particles created from an iron chip allowed the investigation of the role of the particle size and the source of the materials in the reactivity observed. These particles: large ($\approx$ 750 µm) and medium ($\approx$ 400 µm) put the iron flakes in the middle in a size scale, since they were $\approx$ 500 µm. When the iron powder (from Aldrich) provided by NOC colleagues and the new iron particules were made into substrates and exposed to a 5 mL of a 1 mM ReO_4^- solution prepared in synthetic groundwater for a week

we observed that the corrosion products increased as the size of the iron particles increased.

The voltammetry of perrhenate in Pt showed that the reduction of this species requires a high concentration of H in the media to occur, and that it is driven by the H electrochemically adsorbed at the Pt electrode surface. The CV in synthetic groundwater did not show ReO_4^- oxidation or reduction waves probably because this is a neutral solution, and the concentration of H^+ was not sufficient to drive the reaction. Also, it could be because this is made of a long list of ions that potentially can adsorb on the Pt surface. These could be competing with ReO_4^- for the reactive sites at the Pt surface. Because of this, it was not possible to monitor the concentration of ReO_4^- in synthetic groundwater using CV.

However, laser ablation ICP-MS allowed the interrogation of the surface of the iron substrates after exposure to a 1 mM ReO_4^- solution prepared in synthetic groundwater for a week. The results showed that the concentration of Re increased as areas covered in rust were ablated. This suggested that the reduction of ReO_4^- onto the iron surface occurs simultaneously with the precipitation of the corrosion products. The results showed that larger the iron particles, the quicker the iron surface was covered in a layer of corrosion products, and the higher the Re concentration at the iron surface.

The EDX spectra showed that not all rust areas had a high content of Re. Also, the EDX spectra did not show the presence of W in the composition of the raw iron. This suggests that the iron particles obtained from the same iron chip were not contaminated by the WC in the tools used to make then into smaller pieces. Therefore, the contamination of the materials by W is not involved in the "anomalous" behaviour of the materials provided by colleagues from the NOC.

Chapter 6

Conclusions and future work

The sea surface microlayer is a complex environmental interface that is responsible of the transfer of matter and gases between the sea and the atmosphere. It consists of a thin film made of surface active molecules that make its properties totally different compared to the bulk sea water. Its investigation has been performed using sampling methods that do not provide reproducible measurements. Efforts to overcome this issue had led the development of devices that combine a sampling method and an analytical technique. However, no device has been developed to avoid the sampling and perform measurements *in situ*. Because of this, the aim of this research was to exploit the properties of microelectrodes and SECM to develop a methodology to study the SML *in situ*.

Our approach consisted in fabricating submarine microelectrodes to investigate the properties of the water-air interface first, since the water-SML interface had to be more complicated. However, the results obtained showed that the behaviour of the water-air interface as an SECM substrate is dependant of the size of the meniscus. An unconfined water-air interface far from behaving like a solid wall, it showed particular susceptibility to convection created by the electrode moving towards the interface (the scan velocity). The speed at which the electrode was moved defined the shape of the approach curves recorded very close to the water-air interface. A current spike observed in approach curves related to the rupture of the meniscus changed proportional to the scan velocity.

Recording measurements at low scan velocities and confining the water-air interface decreased the effect of convection created by the electrode movement. The tip RG also contributed to the convection created by the electrode: the larger the RG the larger the current spike. Also, the hydrophilic character of the glass around the microwire provided a strong interaction between the microelectrode and the water-air interface.

This interaction and the effects of convection were diminished after adding the synthetic SML to the media. Future experiments could involve the use of submarine tips with silanized surfaces and very small RG to overcome the described factors affecting the response. On the other hand, the posibility of using a microelectrode array to investigate the water-air interface could provide several advantages. The convection would be avoid because a line of electrodes sampled the top millimetre of the solution.

The acquisition of LSVs and chronoamperograms allowed us to investigate the variations of the limiting current of the redox species at the proximities of the water-SML interface. Since both measurements were in agreement with each other and with approach curves recorded this is a clear indication that the methodology is worth implementing in water samples that contain SML.

The fitting of the *i vs t* data to the Mahon and Oldham equation showed that the changes in the limiting current of the redox pair are given by the drop of the diffusion coefficient due to the increase of the local viscosity.

The good agreement between experiments performed using two different synthetic SML suggested that the response is independent of the composition of the SML. However, future work could involve using different synthetic SML, like xanthan gum, which is a polysaccharide that forms globules as it increases its concentration in aqueous solution, and it is widely used to simulate marine snow.

Overall, the use of submarine microelectrodes allowed the investigation of the water-air and water-SML interface providing a reproducible amperometric response. The fabrication of BiFMe allowed the determination of Pb^{2+} concentrations in water samples. The calibration curve performed showed good agreement with the calibrationless method reported by Denuault's group. The cleaning cycles performed before the pre-concentration step and stipping LSV were necessary to make sure the Bi surface was free of oxide and obtain a baseline closer to zero current. The experiments also showed that the detection limits of the technique are affected by the presence of dissolved oxygen that produces a negative current that is capable of masking any Pb^{2+} stripping peaks. This is not favourable to implement the methodology to measurements *in situ*. However, the experiments suggested that the use of the calibrationless method allow the determination of lower concentrations than those predicted.

The second complex environmental interface investigated during this project was the iron-groundwater interface. This interface is of particular importance because of the implementation of permeable reactive barriers as a *in situ* remediation method of contaminated groundwater. The discharges to the environment of effluents with radioactive species had led to the contamination of groundwater. In the UK, the Sellafield nuclear plant discharges more than 90 TBq of 99Tc into the Irish sea annually. The removal of 99Tc from nuclear waste streams is a challenging because of its long lifetime, toxicity, and high mobility in the environment as pertechnetate ion (TcO_4^-).

This part of the project started as a follow up of the experiments performed by collaborators from the National Oceanography Centre (NOC). They measured the kinetics uptake of TcO_4^- by diverse iron materials and they found that the iron flakes provided by their industrial partner were particularly efficient. Their efficiency was compared to the poor reactivity of iron powder obtained from Aldrich.

In principle, the aim of the project was to compare the corrosion of these two materials using electrochemical methods. In order to do this, the materials were made into substrates and electrodes.

The SECM G/C mode was employed to compare the materials made into substrates. The tip-CVs recorded at different tip-substrate distances at various intervals of time allowed us to monitor electroactive species in the solution. These were dissolved gasses or species released by the corrosion activity of the substrates. The results showed that the iron powder substrate did not consume dissolved oxygen over time as exposed to a fixed volume of synthetic groundwater. On the other hand, the iron flakes substrate showed a high oxygen uptake which translates into a higher corrosion rate.

The reactivity of these two materials in presence of a redox species in solution other than dissolved oxygen showed that the iron flakes were more active than the iron powder. When ferrocyanide was a model contaminant, the magnitude of the limiting current of its oxidation allowed us to relate the corrosion activity of each substrate to its consumption.

On the other hand, when using ReO_4^- as a model contaminant the monitoring of its uptake could not be using amperometric methods. This was because the reduction of ReO_4^- requires a high concentration of H^+ in the media.

The investigation of the ReO_4^- uptake through laser ablation inductively coupled plasma mass spectrometry (ICP-MS), scanning electron microscopy (SEM) and energy dispersive spectroscopy (EDX) led to various useful conclusions. The iron powder

and iron flakes originally provided were not behaving weirdly. Creating the particles of different sizes from the same iron chip showed that the uptake increased as the corrosion products formed at the iron surface. Also, that the corrosion of the iron substrates increases with particle size. The results of the OCP measurements and the Tafel extrapolation agreed with what qualitatively we found out with the SECM, laser ablation ICP-MS, SEM and EDX: the iron flakes have a higher corrosion rate than the iron powder.

Future work on this is the characterisation of the corrosion products formed at the iron interface after exposure to using X-ray photoelectron spectroscopy.

In the literature, there is not agreement on the effect of decreasing the grain size boundary in the corrosion rate of a material. This seems to be strongly dependent on the media at which the materials are exposed to. Future work on this area could be comparing the corrosion and uptake by these materials in different electrolytes.

Appendices

Appendix A

The fitting of the chronoamperometric data to the Mahon & Oldham equation

The fitting of the chronoamperometric data to the Mahon and Oldham equation was conducted through Origin lab 9.0.

To include the Mahon and Oldham equation to the user defined equations:

1.-Menu tools

2.-Fitting function builder

3.-Create new function

4.-User defined: Mahon and Oldham equation

5.- Include the equation in C+ (Figure A.1) along with the parameters and the bounds as shown in Figure A.2.

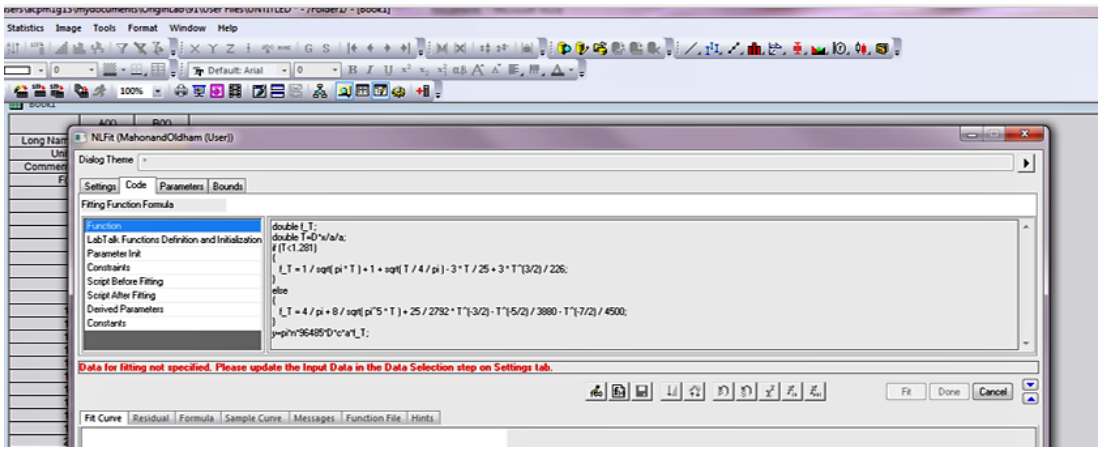

Figure A.1: Origin lab 9.0 fitting function builder dialogue showing the Mahon and Oldham equation written in C+.

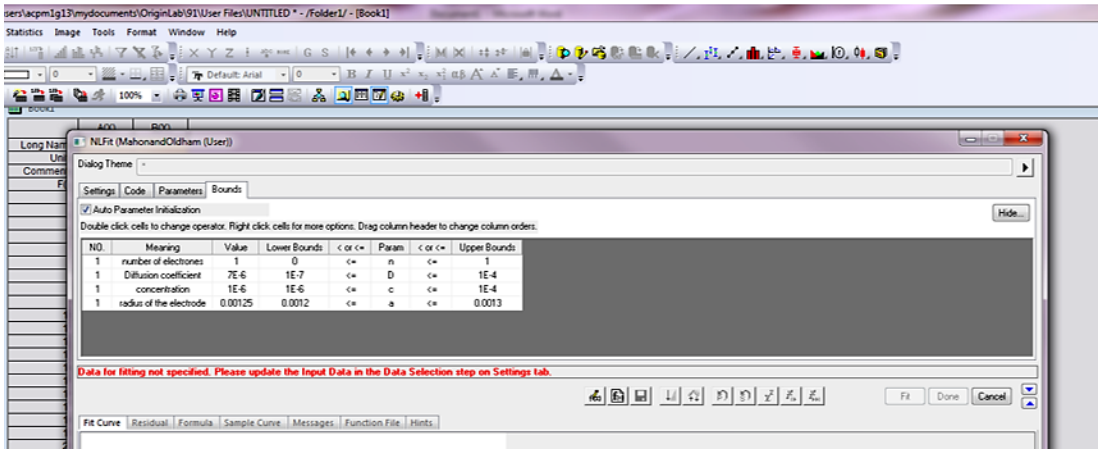

Figure A.2: Origin lab 9.0 fitting function builder dialogue showing the list of parameters and bounds employed.

To fit the data to a non-linear regression and determine D and C simultaneously:

1.-Select the data points to fit and make a plot of i vs t

2.-Open menu analysis

3.-Fitting

4.-Non-linear curve fit

5.-Open dialogue

The window shows the following menus:

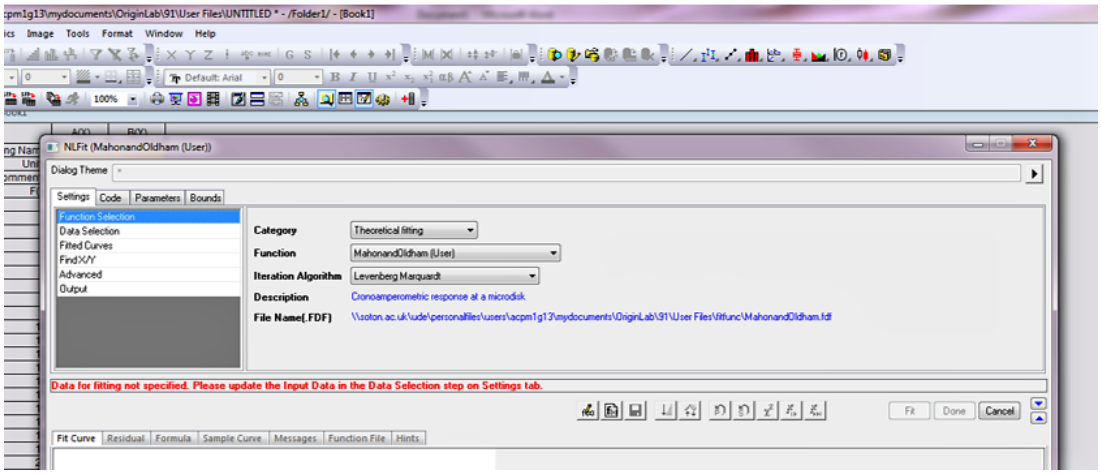

Figure A.3: Origin lab 9.0 non-linear fit dialogue.

Next step is to select the user defined equations and the Mahon and Oldham from the options. After that the following window appears:

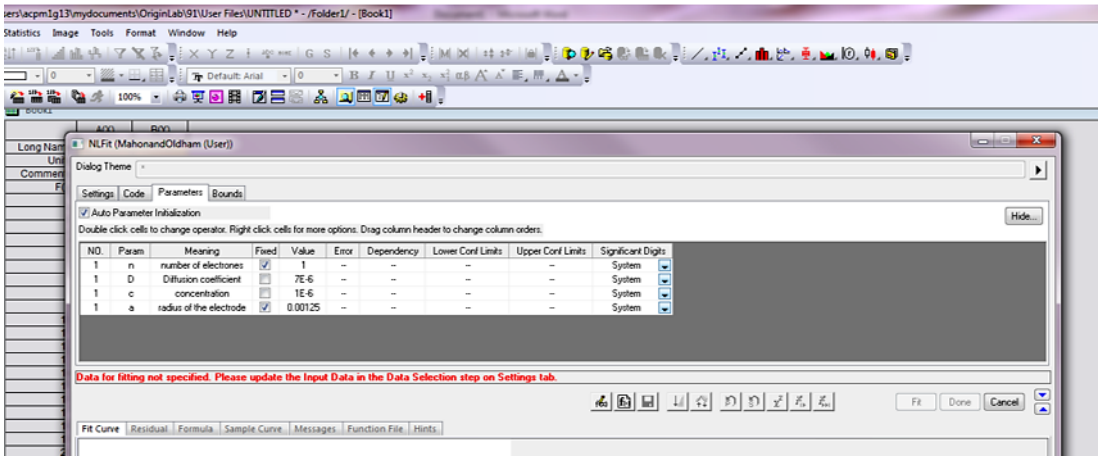

Figure A.4: Origin lab 9.0 non-linear fit dialogue showing the parameters with the bounds employed. n and a were fixed and D and C were unconstrained.

The "fixed" box was ticked for all parameters except D and C. The bounds for D and C are set by typing the approximate numbers as shown in Figure A.4. Then, click on the green button iterate.

Appendix B

SEM images and EDX spectra of the iron substrates

This section shows the SEM images and EDX spectra for the iron substrates made from an iron chip and the iron powder from Aldrich. They are displayed by size, showing first the data acquired when they were clean and polished, and after a week of exposure to a 1 mM ReO_4^- prepared in synthetic groundwater. SEM images and EDX spectra obtained using a FEI XL30 environmental scanning electron microscope (ESEM) with a W filament as electron source, an UltaDry EDX, 10 mm^2 detector in the low vacuum mode (wet mode).

B.0.1 Large iron particles ($\approx$ 750 µm)

Clean and polished

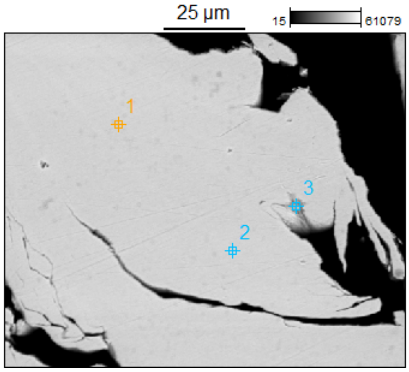

Figure B.1: Large iron particles substrate. Image Resolution: 512 by 426. Image Pixel Size: 0.24 µm. Acc. voltage: 20.0 kV. Magnification: 1000.

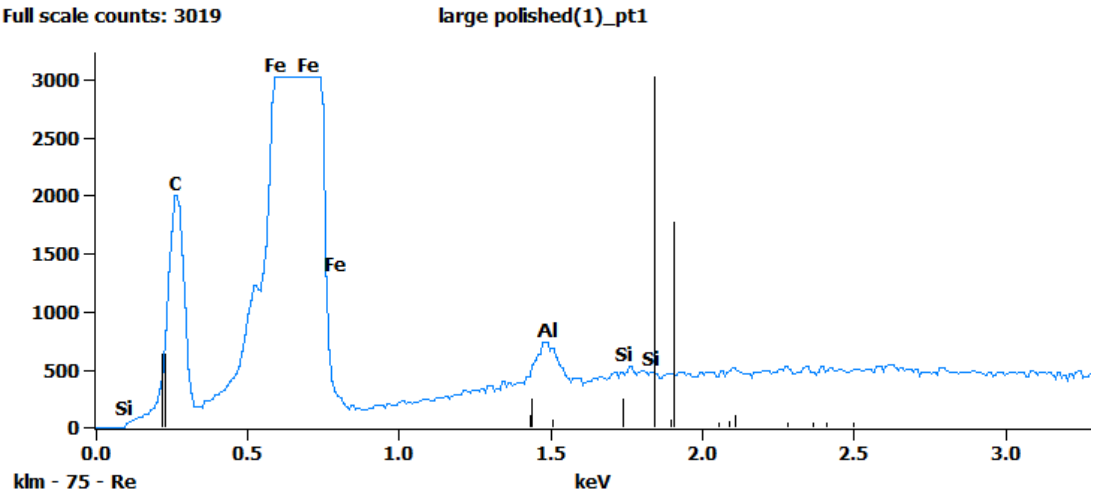

Figure B.2: EDX spectra of point 1 in the polished large iron particles substrate.

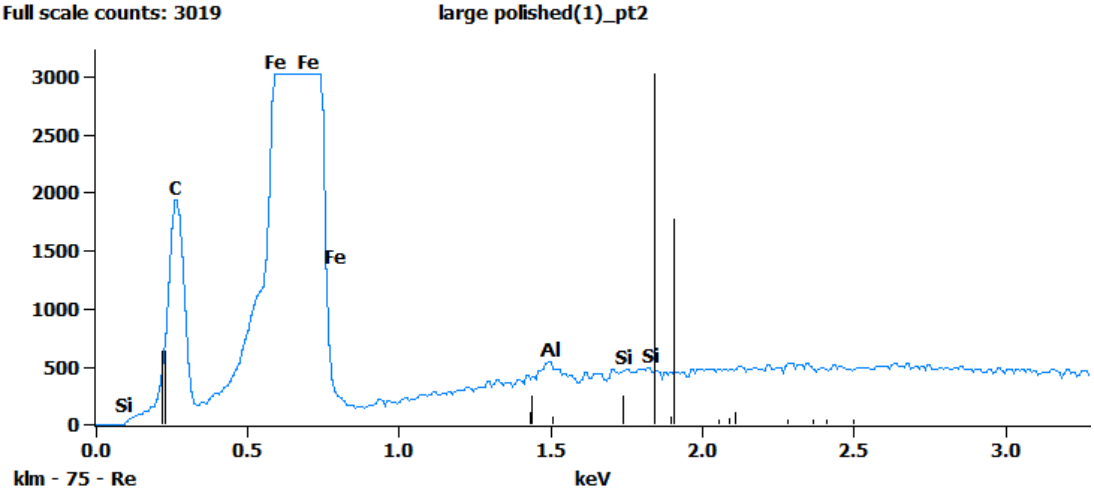

Figure B.3: EDX spectra of point 2 in the polished large iron particles substrate.

Table B.1: Atom % with error for the points showed in Figure B.1.

	C-K	O-K	Al-K	Si-K	Cl-K	Fe-K
Point 1	49.0 ± 0.6		1.0 ± 0.0	0.1 ± 0.0		49.9 ± 0.2
Point 2	48.1 ± 0.6		0.4 ± 0.0	0.1 ± 0.0		51.4 ± 0.2
Point 3	69.2 ± 0.7	2.4 ± 0.2	0.2 ± 0.0		0.1 ± 0.0	28.0 ± 0.1

After a week of exposure to ReO_4^-

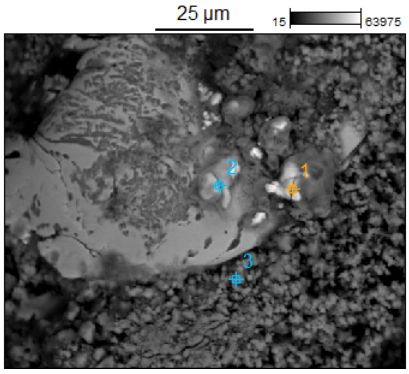

Figure B.4: Large iron particles substrate after exposed to 5 mL of 1 mM ReO_4^- solution in synthetic groundwater. Image Resolution: 512 by 426. Image Pixel Size: 0.20 m. Acc. voltage: 20.0 kV. Magnification: 1200.

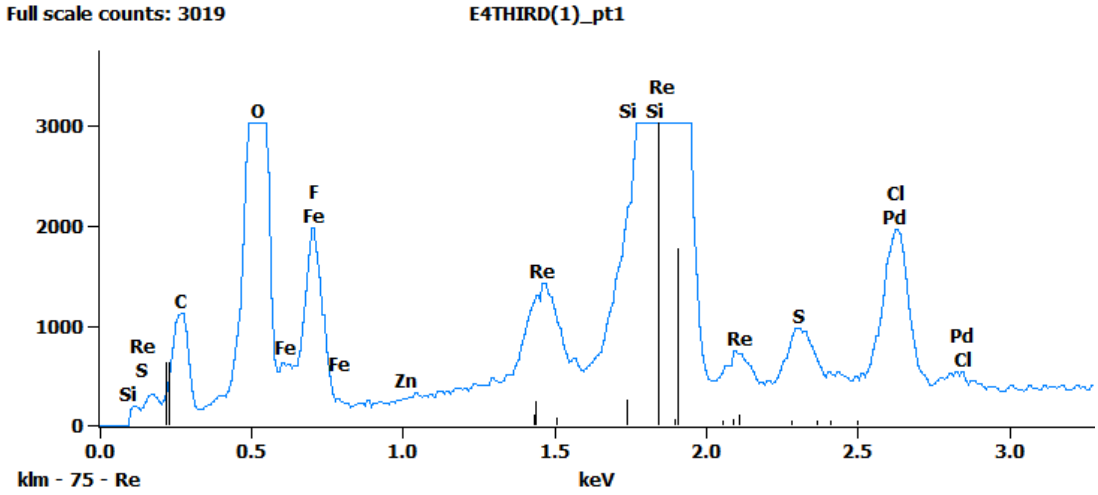

Figure B.5: EDX spectra of point 1 in the polished large iron particles substrate after exposed to 5 mL of a 1 mM ReO_4^- solution in synthetic groundwater.

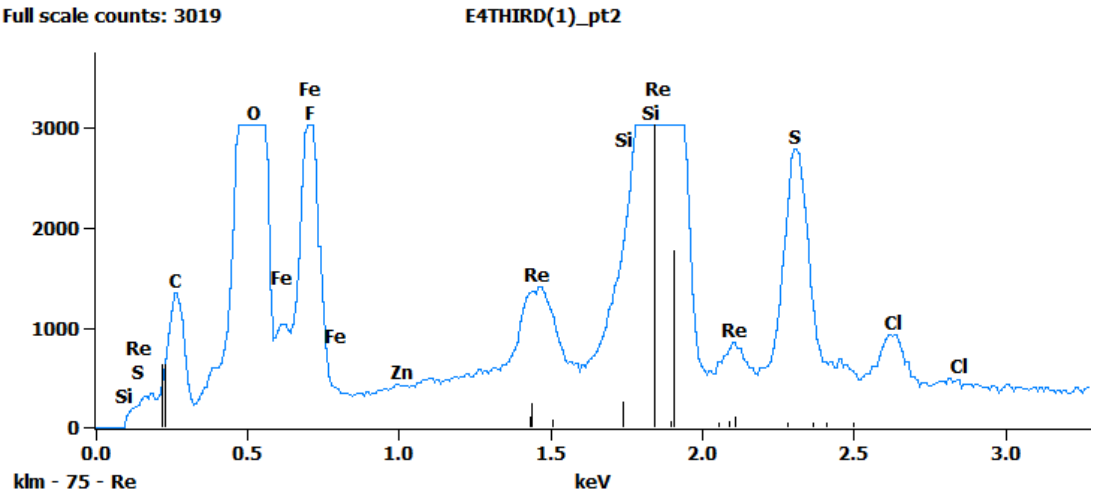

Figure B.6: EDX spectra of point 2 in the polished large iron particles substrate after exposed to 5 mL of a 1 mM ReO_4^- solution in synthetic groundwater.

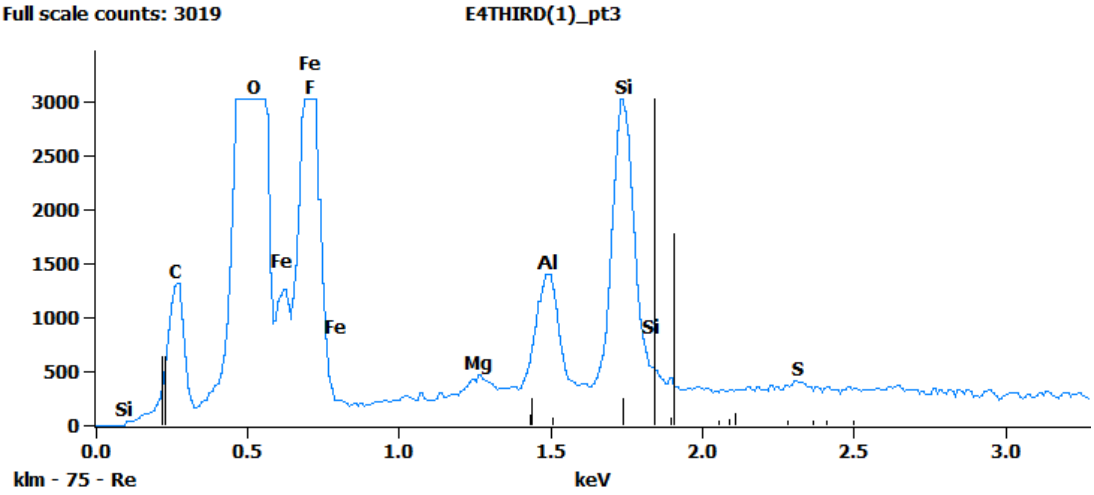

Figure B.7: EDX spectra of point 3 in the polished large iron particles substrate after exposed to 5 mL of a 1 mM ReO_4^- solution in synthetic groundwater.

Table B.2: Atom % for the points in Figure B.4.

	C-K	O-K	Mg-K	Al-K	Si-K	S-M	Cl-K	Ca-L	Fe-K	Zn-K	Re-M
Point 1	27.4	49.6			1.9	1.1	2.8		8.1	1.6	7.6
Point 2	18.0	65.2			1.2	2.6	0.5		7.3	0.6	4.5
Point 3	20.1	58.9	0.3	1.5	3.3	0.1		0.4	15.4		

Table B.3: Atom % error for the points in Figure B.4.

	C-K	O-K	Mg-K	Al-K	Si-K	S-M	Cl-K	Ca-L	Fe-K	Zn-K	Re-M
Point 1	± 0.4	± 0.4			± 0.1	± 0.0	± 0.0		± 0.1	± 0.1	± 0.1
Point 2	± 0.5	± 0.4			± 0.1	± 0.0	± 0.0		± 0.1	± 0.1	± 0.0
Point 3	± 0.4	± 0.3	± 0.0	± 0.0	± 0.0	± 0.0		± 0.0	± 0.1		

B.0.2 Medium size iron particles (≈ 400 µm)

Clean and polished

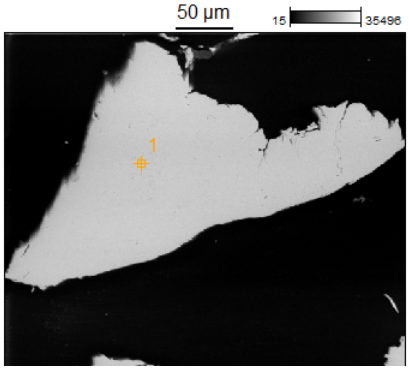

Figure B.8: Polished medium size iron particles substrate. Image Resolution: 512 by 426. Image Pixel Size: 0.68 µm. Acc. voltage: 20.0 kV. Magnification: 350.

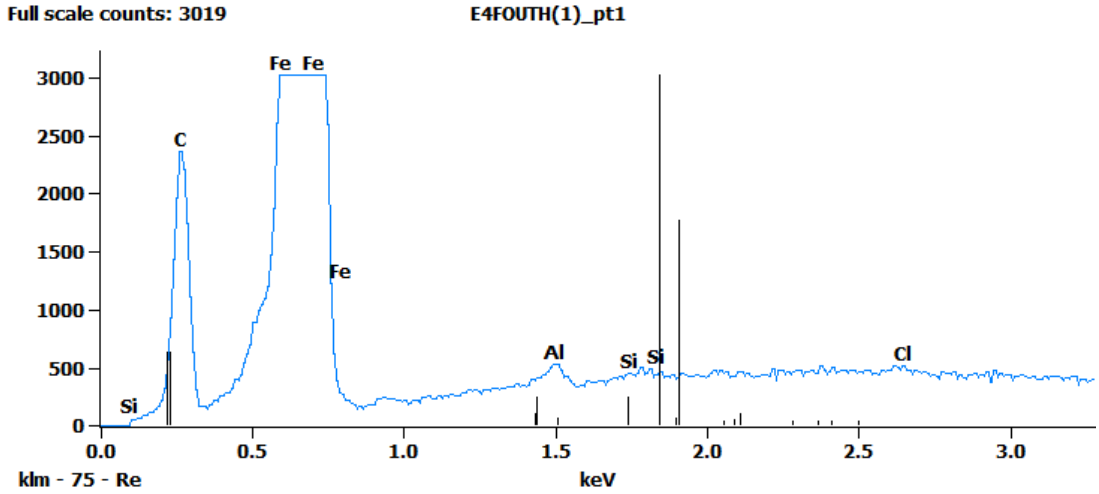

Figure B.9: EDX spectra of point 1 in the polished medium size iron particles substrate.

Table B.4: Atom % with error for the point showed in Figure B.8.

	C-K	Al-K	Si-K	Cl-K	Fe-K
Point 1	53.8 ± 0.6	0.4 ± 0.0	0.1 ± 0.0	0.1 ± 0.0	46.4 ± 0.2

After a week of exposure to ReO_4^-

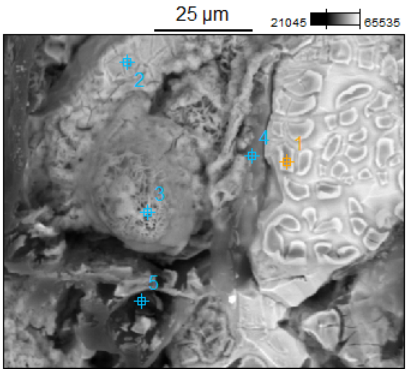

Figure B.10: Medium size iron particles substrate after exposed to 5 mL of 1 mM ReO_4^- solution in synthetic groundwater. Image Resolution: 512 by 426. Image Pixel Size: 0.20 µm. Acc. voltage: 20.0 kV. Magnification: 1200.

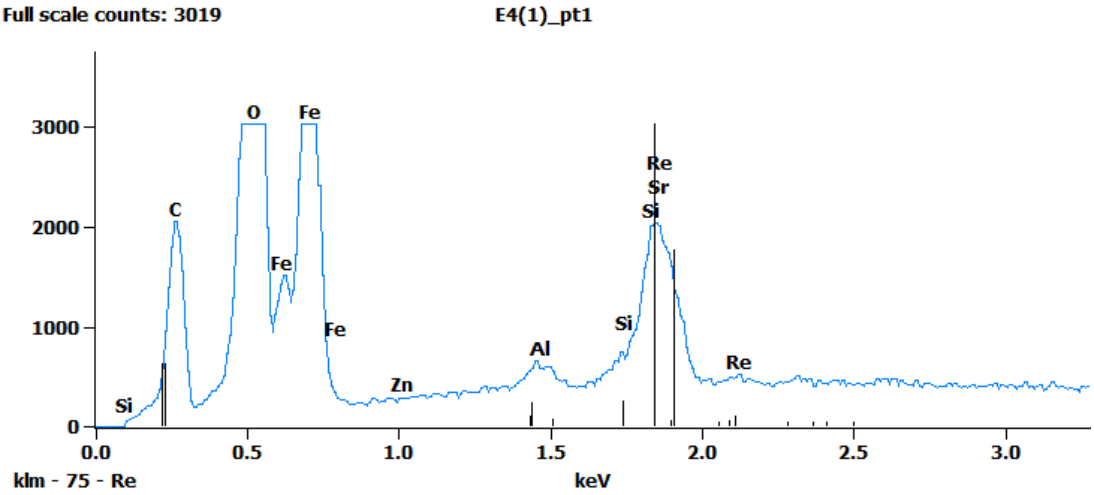

Figure B.11: EDX spectra of point 1 in medium size iron particles substrate after exposed to 5 mL of a 1 mM ReO_4^- solution in synthetic groundwater.

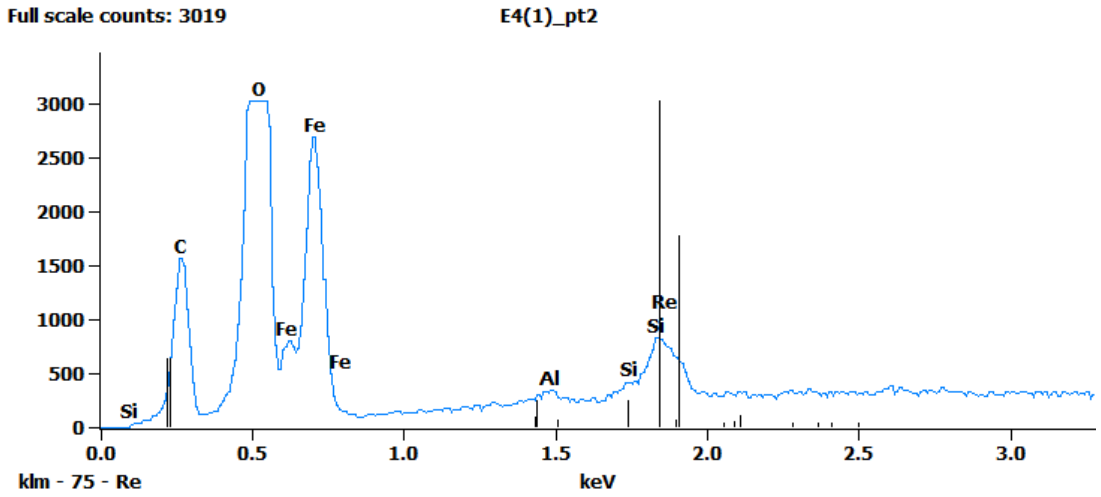

Figure B.12: EDX spectra of point 2 in medium size iron particles substrate after exposed to 5 mL of a 1 mM ReO_4^- solution in synthetic groundwater.

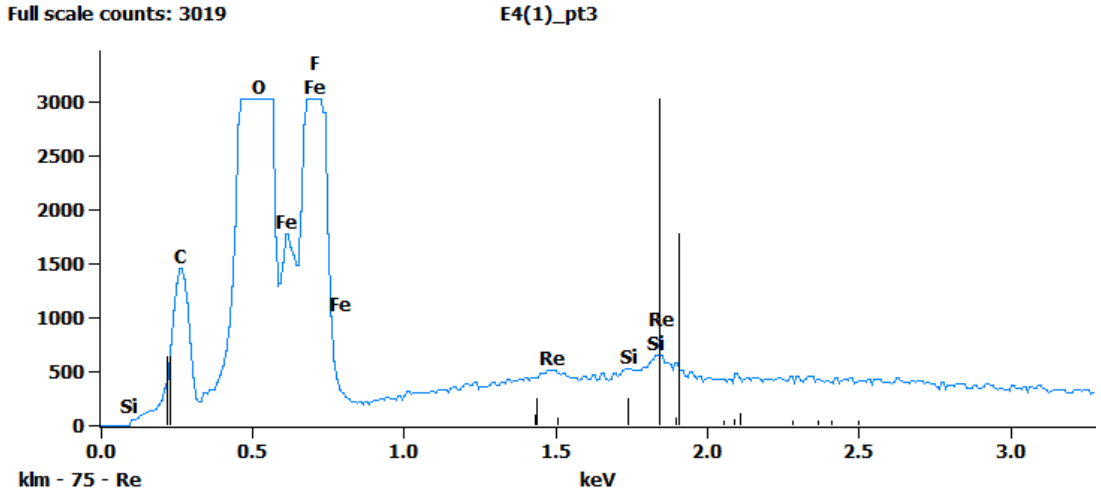

Figure B.13: EDX spectra of of point 3 in medium size iron particles substrate after exposed to 5 mL of a 1 mM ReO_4^- solution in synthetic groundwater.

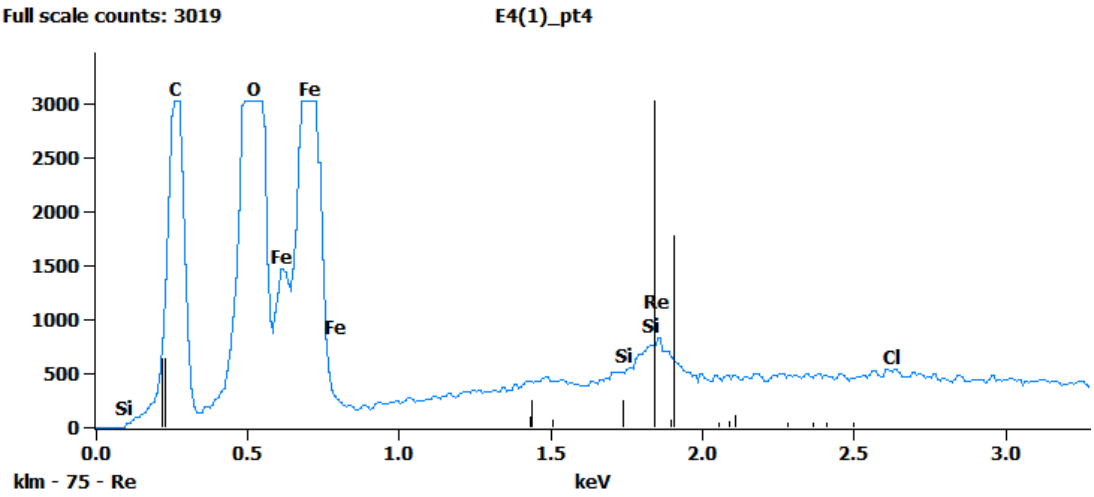

Figure B.14: EDX spectra of point 4 in medium size iron particles substrate after exposed to 5 mL of a 1 mM ReO_4^- solution in synthetic groundwater.

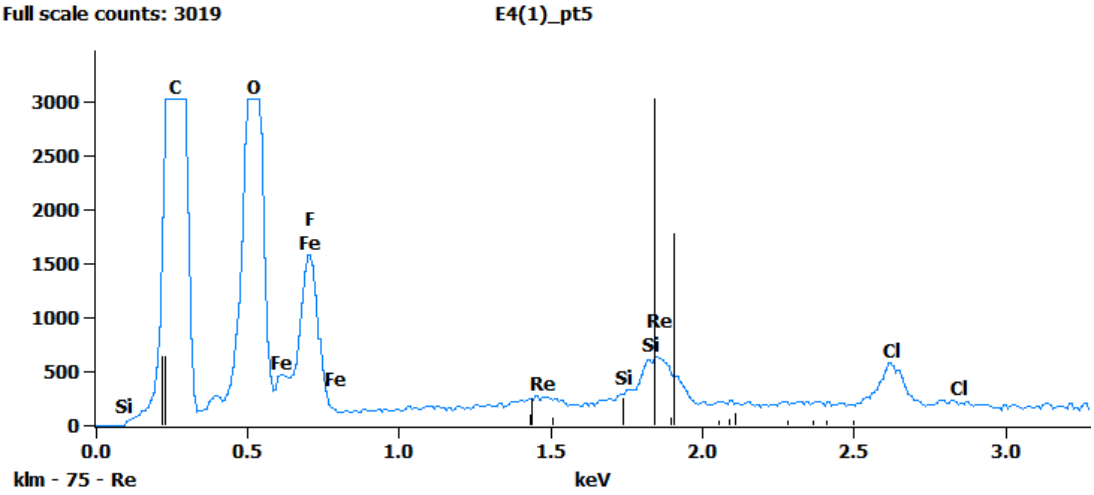

Figure B.15: EDX spectra of point 5 in medium size iron particles substrate after exposed to 5 mL of a 1 mM ReO_4^- solution in synthetic groundwater.

Table B.5: Atom % for the points showed in Figure B.10.

	C-K	**O-K**	**F-K**	**Al-K**	**Si-K**	**Cl-K**	**Fe-M**	**Zn-K**	**Re-M**
Point 1	30.3	40.1		0.3	0.3		27.6	0.2	1.2
Point 2	29.9	36.1		0.2	0.2		33.2		0.5
Point 3	17.1	63.4	0.0		0.2		19.1		0.1
Point 4	43.7	29.0			0.2	0.1	26.9		0.2
Point 5	68.0	24.2	0.8		0.1	0.3	6.5		0.2

Table B.6: Atom % error for the points in Figure B.10.

	C-K	O-K	F-K	Al-K	Si-K	Cl-K	Fe-M	Zn-K	Re-M
Point 1	± 0.4	± 0.3		± 0.0	± 0.0		± 0.1	± 0.0	± 0.0
Point 2	± 0.4	± 0.3		± 0.0	± 0.0		± 0.1		± 0.0
Point 3	± 0.3	± 0.4	± 0.0		± 0.0		± 0.1		± 0.0
Point 4	± 0.4	± 0.2			± 0.0	± 0.0	± 0.1		± 0.0
Point 5	± 0.5	± 0.3	± 0.2		± 0.0	± 0.0	± 0.1		± 0.0

B.0.3 Small iron particles obtained from an iron chip (≈ 70 µm)

Clean and polished

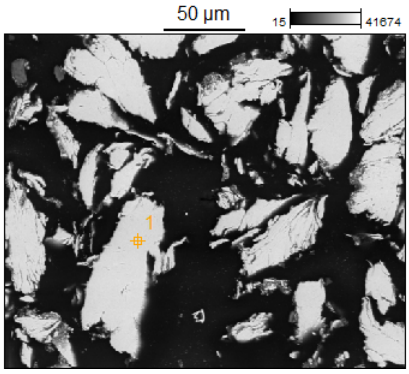

Figure B.16: Polished substrate made with iron powder produced in the lab. Image Resolution: 512 by 426. Image Pixel Size: 0.48 µm. Acc. voltage: 20.0 kV. Magnification: 500.

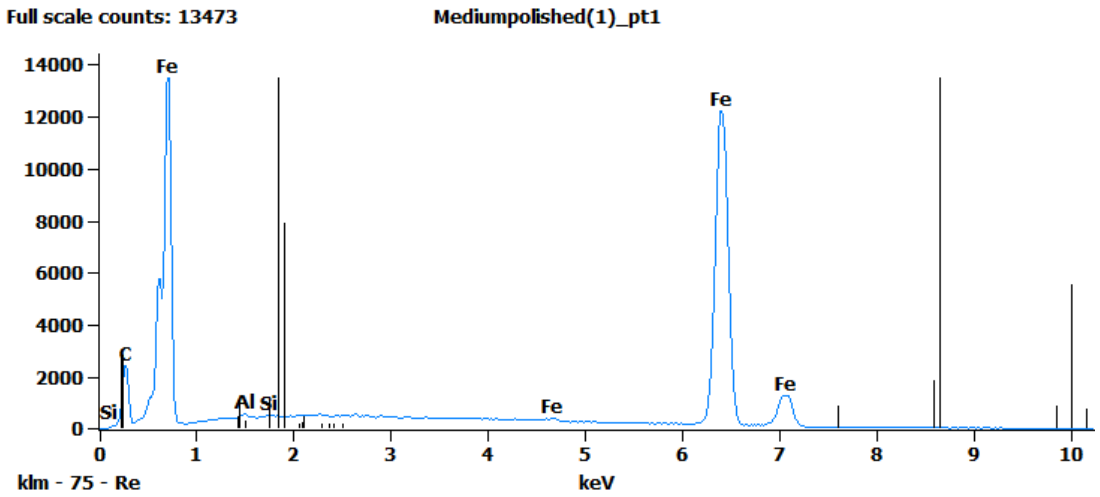

Figure B.17: EDX spectra of point 1 in the polished substrate made with small iron particles obtained from an iron chip.

Table B.7: Atom % with error for the point shown in Figure B.16.

	C-K	Al-K	Si-K	Fe-K
Point 1	53.8 ± 0.6	0.4 ± 0.0	0.2 ± 0.0	55.4 ± 0.2

After a week of exposure to ReO_4^-

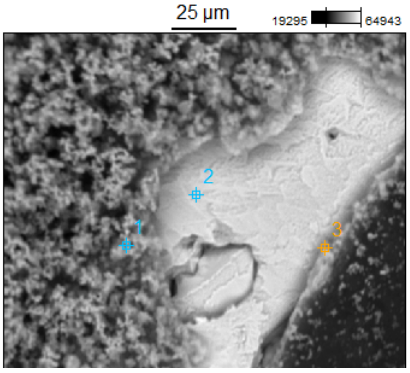

Figure B.18: The substrate made with small iron particles obtained from an iron chip after exposed to 5 mL of a 1 mM ReO_4^- solution in synthetic groundwater. Image Resolution: 512 by 426. Image Pixel Size: 0.3 µm. Acc. voltage: 20.0 kV. Magnification: 800.

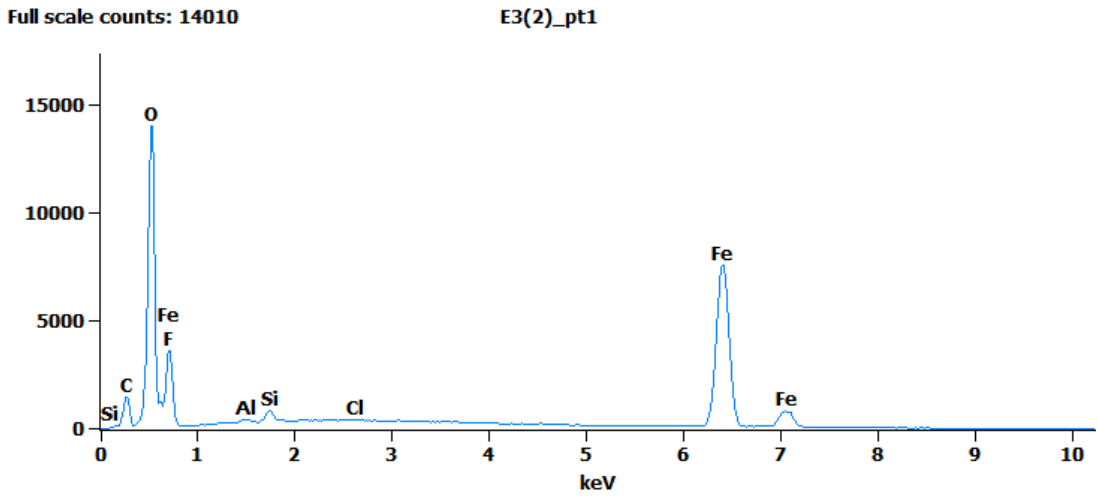

Figure B.19: EDX spectra of point 1 in the substrate made with small iron particles obtained from an iron chip after exposed to 5 mL of a 1 mM ReO_4^- solution in synthetic groundwater.

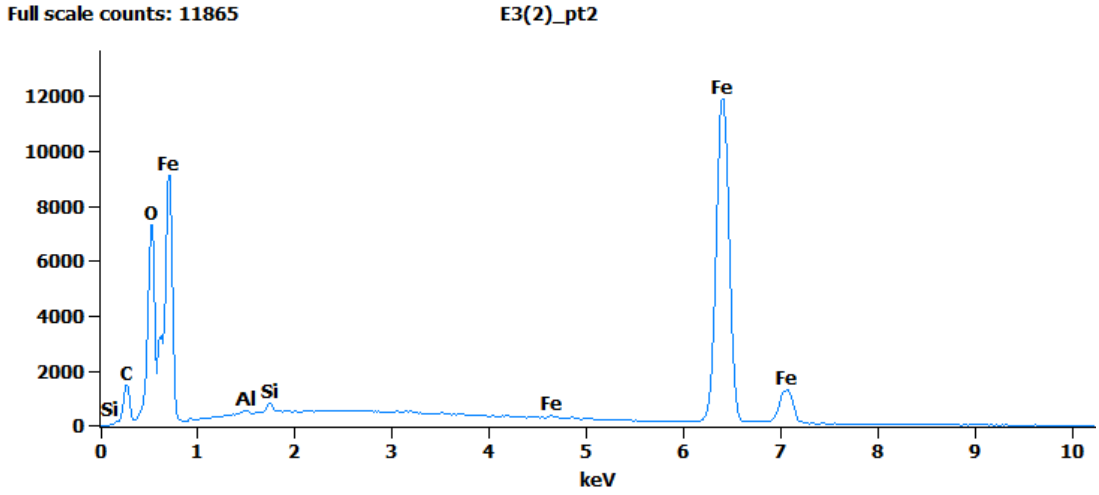

Figure B.20: EDX spectra of point 2 in the substrate made with small iron particles obtained from an iron chip after exposed to 5 mL of a 1 mM ReO_4^- solution in synthetic groundwater.

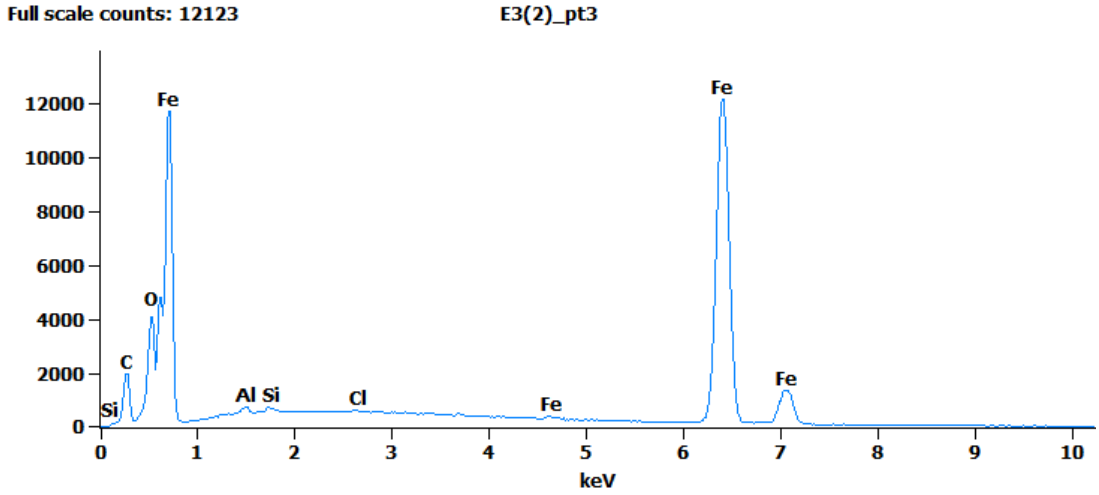

Figure B.21: EDX spectra of of point 3 in the substrate made with small iron particles obtained from an iron chip after exposed to 5 mL of 1 mM ReO_4^- solution in synthetic groundwater.

Table B.8: Atom % for the points in Figure B.18.

	C-K	**O-K**	**Al-K**	**Si-K**	**Cl-K**	**Fe-K**
Point 1	24.1	50.5	0.3	0.9	0.1	24.2
Point 2	28.7	28.1	0.3	0.7		42.2
Point 3	40.1	15.1	0.5	0.4	0.1	43.8

Table B.9: Atom % for the points in Figure B.18.

	C-K	O-K	Al-K	Si-K	Cl-K	Fe-K
Point 1	± 0.4	± 0.3	± 0.0	± 0.0	± 0.0	± 0.1
Point 2	± 0.5	± 0.3	± 0.4	± 0.0		± 0.2
Point 3	± 0.8	± 0.3	± 0.1	± 0.0	± 0.0	± 0.2

B.0.4 Iron powder from Aldrich (≈ 50 µm)

Clean and polished

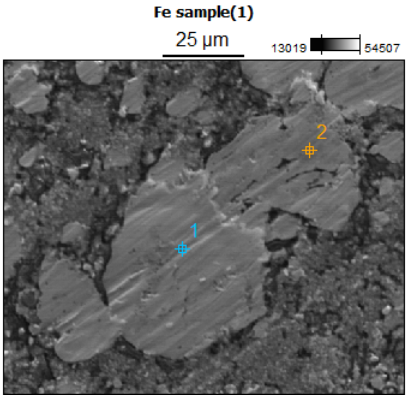

Figure B.22: Polished substrate made with iron powder from Aldrich. Image Resolution: 512 by 426. image Pixel Size: 0.24 µm. Acc. voltage: 15.0 kV. Magnification: 1000.

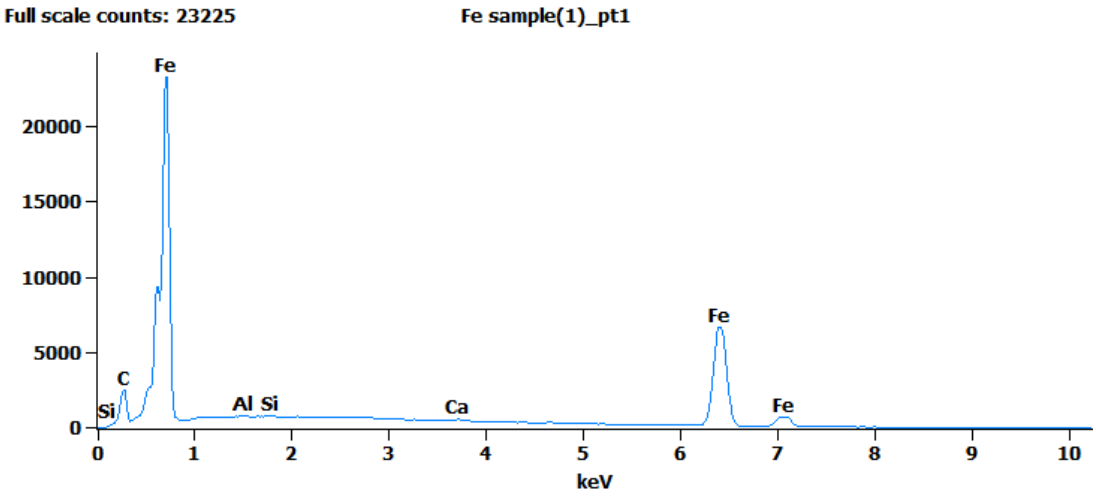

Figure B.23: EDX spectra of the polished substrate made with iron powder from Aldrich.

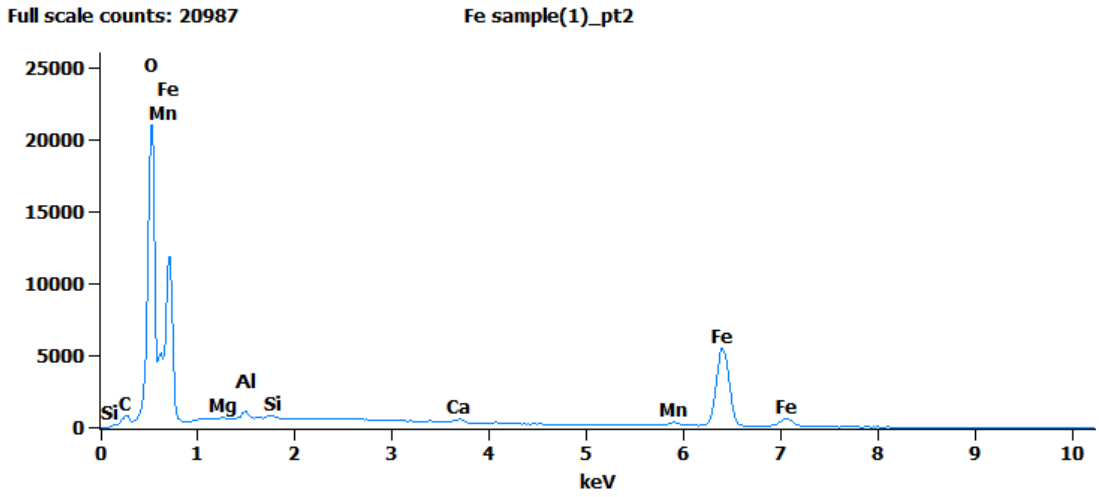

Figure B.24: EDX spectra of the polished substrate made with iron powder from Aldrich.

Table B.10: Atom % with error for the point shown in Figure B.22.

	C-K	O-K	Al-K	Si-K	Ca-K	Mn-K	Fe-K
Point 1	43.8 ± 0.5		0.3 ± 0.0	0.4 ± 0.1	0.1 ± 0.0		55.4 ± 0.3
Point 2	7.2 ± 0.3	53.3 ± 0.3 ± 0.0	0.6 ± 0.0	0.3 ± 0.0	0.4 ± 0.1	1.4 ± 0.1	36.5 ± 0.3

After a week of exposure to ReO_4^-

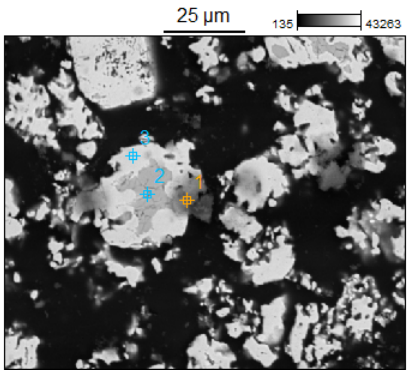

Figure B.25: The substrate made with iron powder from Aldrich after exposed to 5 mL of a 1 mM ReO_4^- solution in synthetic groundwater. Image Resolution: 512 by 426. Image Pixel Size: 0.24 µm. Acc. voltage: 20.0 kV. Magnification: 1000.

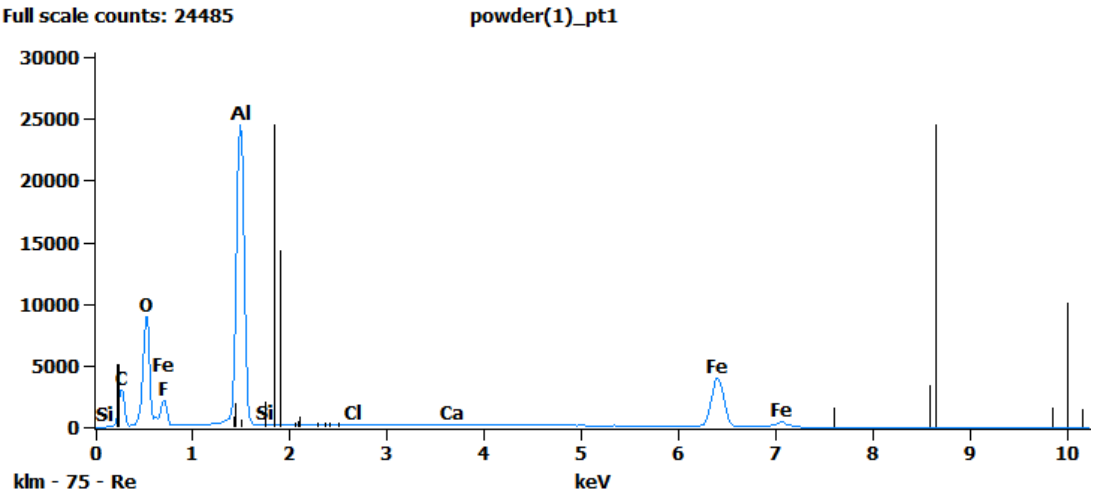

Figure B.26: EDX spectra of point 1 in in the substrate made with iron powder from Aldrich after exposed to 5 mL of a 1 mM ReO_4^- solution in synthetic groundwater.

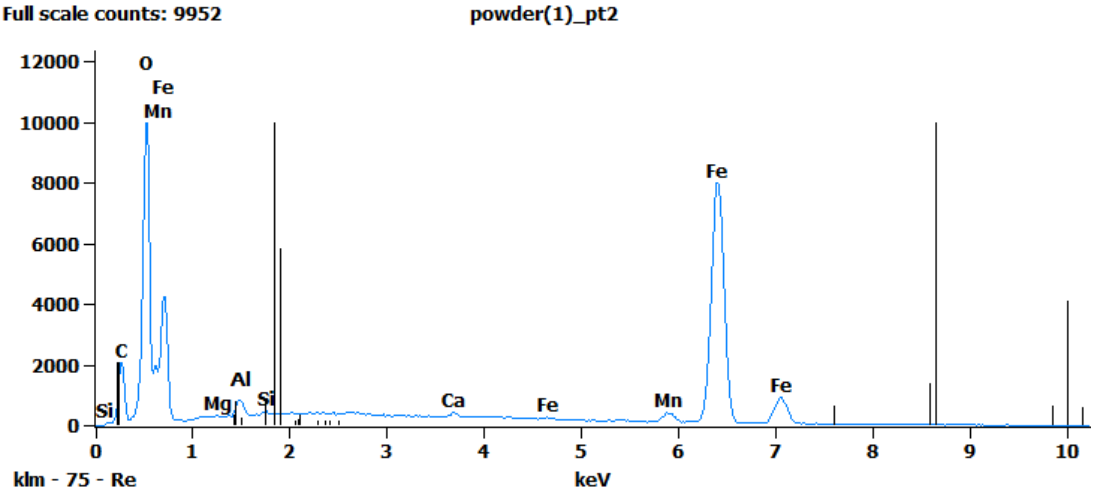

Figure B.27: EDX spectra of point 2 in the substrate made with iron powder from Aldrich after exposed to 5 mL of a 1 mM ReO_4^- solution in synthetic groundwater.

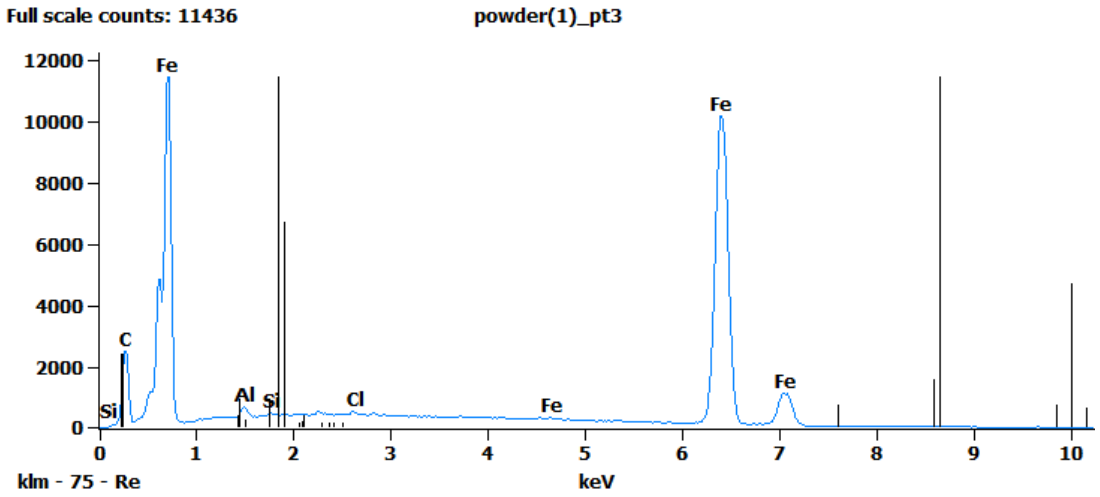

Figure B.28: EDX spectra of point 3 in the substrate made with iron powder from Aldrich after exposed to 5 mL of a 1 mM ReO_4^- solution in synthetic groundwater.

Table B.11: Atom % for the points shown in Figure B.25.

	C-K	**O-K**	**Mg-K**	**Al-K**	**Si-K**	**Cl-K**	**Ca-K**	**Mn-K**	**Fe-K**
Point 1	43.2	31.2		18.2	0.0				7.3
Point 2	32.9	39.9	0.1	1.0	0.1		0.2	0.9	25.0
Point 3	58.0			0.8	0.1	0.1			40.9

Table B.12: Atom % error for the points in Figure B.25.

	C-K	**O-K**	**Mg-K**	**Al-K**	**Si-K**	**Cl-K**	**Ca-K**	**Mn-K**	**Fe-K**
Point 1	± 0.4	± 0.2		± 0.1	± 0.0				± 0.1
Point 2	± 0.4	± 0.3	± 0.0	± 0.0	± 0.0		± 0.0	± 0.0	± 0.1
Point 3	± 0.9			± 0.0	± 0.0	± 0.0			± 0.2

References

[1] P. S. Liss et al. "Report group 1-Physical processes in the microlayer and the air-sea exchange of trace gases". In: *Sea Surf. Glob. Chang.* Cambridge, United Kingdom: Cambridge University Press, 1997, pp. 1–33.

[2] P. M. Williams et al. "Chemical and microbiological studies of sea-surface films in the Southern Gulf of California and off the West Coast of Baja California". In: *Mar. Chem.* 19.1 (1986), pp. 17–98.

[3] O. Wurl et al. "Formation and global distribution of sea-surface microlayers". In: *Biogeosciences* 8.1 (2011), pp. 121–135.

[4] J. Zhou et al. "The role of surface-active carbohydrates in the formation of transparent exopolymer of seawater particles by bubble adsorption". In: *Limnology* 43.8 (2011), pp. 1860–1871.

[5] O. Wurl and M. Holmes. "The gelatinous nature of the sea-surface microlayer". In: *Mar. Chem.* 110.1 (2008), pp. 89–97.

[6] M. Cunliffe et al. "Sea surface microlayers: A unified physicochemical and biological perspective of the air-ocean interface". In: *Prog. Oceanogr.* 109 (2013), pp. 104–116.

[7] C. M. Nichols et al. "Chemical characterization of exopolysaccharides from Antarctic marine bacteria". In: *Microb. Ecol.* 49.4 (2005), pp. 578–589.

[8] M. D. Kok, S. Schouten, and J. S. Sinninghe Damsté. "Formation of insoluble, nonhydrolyzable, sulfur-rich macromolecules via incorporation of inorganic sulfur species into algal carbohydrates". In: *Geochim. Cosmochim. Acta* 64.15 (2000), pp. 2689–2699.

[9] J. T. Hardy. "The sea-surface microlayer-Biology, Chemistry and anthropogenic enrichment". In: *Progr. Ocean.* 11.4 (1982), pp. 307–328.

[10] Z. Zhang et al. “Studies on the sea surface microlayer: II. The layer of sudden change of physical and chemical properties”. In: *J. Colloid Interface Sci.* 264.1 (2003), pp. 148–159.

[11] Z. Zhang et al. “Direct determination of thickness of sea surface microlayer using a pH microelectrode at original location”. In: *Sci. China Ser. B Chem.* 46.4 (2003), pp. 339–351.

[12] Z. Zhengbin et al. “Physicochemical Studies of the Sea Surface Microlayer: I. Thickness of the Sea Surface Microlayer and Its Experimental Determination”. In: *J. Colloid Interf. Sci.* 204.2 (1998), pp. 294–299.

[13] J. McN. Sieburth. “Microbiological and Organic-Chemical Processes in the Surface and Mixed Layers”. In: *Air-Sea Exch. Gases Part.* Ed. by Peter S Liss and W George N Slinn. Dordrecht: Springer Netherlands, 1983, pp. 121–172.

[14] A. Engel et al. “The Ocean’s Vital Skin: Toward an Integrated Understanding of the Sea Surface Microlayer”. In: *Front. Mar. Sci.* 4 (2017), pp. 1–14.

[15] P. S. Liss. “Gas Transfer: Experiments and Geochemical Implications”. In: *Air-Sea Exch. Gases Part.* Ed. by Peter S. Liss and W. George N. Slinn. Dordrecht: Springer Netherlands, 1983, pp. 241–298.

[16] R. C. Upstill-Goddard et al. “Bacterioneuston control of air-water methane exchange determined with a laboratory gas exchange tank”. In: *Global Biogeochem. Cycles* 17.4 (2003), pp. 1–15.

[17] E. J. Bock et al. “Relationship between air-sea gas transfer and short wind waves”. In: *J. Geophys. Res. Ocean.* 104.C11 (1999), pp. 25821–25831.

[18] S. P. McKenna and W. R. McGillis. “The role of free-surface turbulence and surfactants in air–water gas transfer”. In: *Int. J. Heat Mass Transf.* 47.3 (2004), pp. 539–553.

[19] K. Hasselmann. “Grundgleichungen der Seegangsvoraussage”. In: *Schiffstechnik* 1 (1960), pp. 191–195.

[20] F. Maclntyre. “The top millimeter of the ocean”. In: *Sci. Am. Inc* 230.5 (1974), pp. 62–77.

[21] W. Jin. “Evidence of Sea Spray Produced by Bursting Bubbles”. In: *Am. Assoc. Adv. Sci.* 212.4492 (1981), pp. 324–326.

[22] O. Wurl and J. P. Obbard. “A review of pollutants in the sea-surface microlayer (SML): A unique habitat for marine organisms”. In: *Limnol. Oceanogr.* 26.11-12 (2004), pp. 492–499.

[23] K. A. Hunter and P. S. Liss. “Principles and problems of modeling cation enrichment at natural air–water interfaces”. In: *Atmos. Pollut. Nat. Waters*. Ed. by S.J. (Ed.) Eisenreich. Ann Arbor, Press, 1981, p. 99.

[24] M. Heyraud and R. D. Cherry. “Correlation of 210 Po and 210 Pb enrichments in the sea-surface microlayer with neuston biomass”. In: *Cont. Shelf Res.* 1.3 (1983), pp. 283–293.

[25] Y. Belot, C. Caput, and D. Gauthier. “Transfer of americium from sea water to atmosphere by bubble bursting”. In: *Atmos. Environ.* 16.6 (1982), pp. 1463–1466.

[26] J. T. Hardy et al. “Report group 2-Biological effects of chemical and radiative change in the sea surface.” In: *Sea Surf. Glob. Chang.* 1997. Chap. Chapter 2, pp. 35–70.

[27] F. Azam. “Microbial Control of Oceanic Carbon Flux: The Plot Thickens”. In: *Science (80-.).* 280.5364 (1998), pp. 694–696.

[28] R. Conrad and W. Seiler. “Influence of the surface microlayer on the flux of nonconservative trace gases (CO, H_2, CH_4, N_2O) across the ocean-atmosphere interface”. In: *J. Atmos. Chem.* 6.1 (1988), pp. 83–94.

[29] R. Nakajima et al. “Enrichment of microbial abundance in the sea-surface microlayer over a coral reef: implications for biogeochemical cycles in reef ecosystems”. In: *Mar. Ecol. Prog. Ser.* 490 (2013), pp. 11–22.

[30] J. T. Hardy. “Ecology of a Temperate Marine Lagoon”. In: *Ecology* 18(4).July (1973), pp. 525–533.

[31] H. Ploug. “Cyanobacterial surface blooms formed by Aphanizomenon sp. and Nodularia spumigena in the Baltic Sea: Small-scale fluxes, pH, and oxygen microenvironments”. In: *Limnol. Ocean. 53* (2008), pp. 914–921.

[32] M. L. Calleja et al. “Control of air-sea CO_2 disequilibria in the subtropical NE Atlantic by planktonic metabolism under the ocean skin”. In: *Geophys. Res. Lett.* 32.8 (2005), pp. 1–4.

[33] J.T. Hardy. "Biological effects of chemicals in the sea-surface microlayer". In: *Sea Surf. Glob. Chang.* 1997. Chap. 11, pp. 339–370.

[34] J. T. Hardy and C. W. Apts. "The sea-surface microlayer: phytoneuston productivity and effects of atmospheric particulate matter". In: *Mar. Biol.* 82.3 (1984), pp. 293–300.

[35] R. Z. Riznyk et al. "Short-Term Effects of Polynuclear Aromatic Hydrocarbons on Sea-Surface Microlayer Phytoneuston". In: *Bull. Environ. Contam. Toxicol* (1987), pp. 1037–1043.

[36] S. A. Crow et al. "Densities of Bacteria and Fungi in Coastal Surface Films as Determined by a Membrane- Adsorption Procedure in coastal surface films Densities of bacteria and fungi by a membrane-adsorption as determined". In: *Limnol. Ocean.* 20.4 (1975), pp. 644–646.

[37] W. D. Garrett. "Collection of slick-forming materials from the sea surface". In: *Limnol. Ocean.* 10.4 (1965), pp. 602–605.

[38] M. Caccia et al. "Sampling sea surfaces with SESAMO: an autonomous craft for the study of sea-air interactions". In: *Robot. Autom. Mag. IEEE* 12.3 (2005), pp. 95–105.

[39] S. R. Piotrowicz et al. "Bursting bubbles and their effect on the sea-to-air transport of Fe, Cu and Zn". In: *Mar. Chem.* 7.4 (1979), pp. 307–324.

[40] M. I. Walker et al. "Actinide enrichment in marine aerosols". In: *Nature* 323.6084 (1986), pp. 141–143.

[41] H. Agogué et al. "Comparison of samplers for the biological characterization of the sea surface microlayer". In: *Limnol. Oceanogr.* (2004), pp. 213–225.

[42] M. J. O'Hara, S. R. Burge, and J. W. Grate. "Quantification of technetium-99 in complex groundwater matrixes using a radiometric preconcentrating minicolumn sensor in an equilibration-based sensing approach". In: *Anal. Chem.* 81.3 (2009), pp. 1068–1078.

[43] J. H. P. Watson and D. C. Ellwood. "The removal of the pertechnetate ion and actinides from radioactive waste streams at Hanford, Washington, USA and Sellafield, Cumbria, UK: The role of iron-sulfide-containing adsorbent materials". In: *Nucl. Eng. Des.* 226.3 (2003), pp. 375–385.

[44] US EPA. *Pump-and-Treat Ground-Water Remediation: A Guide for Decision Makers and Practitioners*. 1996.

[45] S. Y. Lee and E. A. Bondietti. "Removing uranium from drinking water by metal hydroxides and anion-exchange resin". In: *J. Am. Water Works Assoc.* 75.10 (1983), pp. 536–540.

[46] Y. Roh, Y. S. Lee, and P. M. Elless. "Characterization of corrosion products in the permeable reactive barriers". In: *Environ. Geol.* 40.1 (2000), pp. 184–194.

[47] R. M. Powell et al. "Permeable Reactive Barrier Technologies for Contaminant Remediation". In: *Epa/600/R-98/125* (1998), p. 113.

[48] J. Wantanaphong, S. J. Mooney, and E. H. Bailey. "Natural and waste materials as metal sorbents in permeable reactive barriers (PRBs)". In: *Environ. Chem. Lett.* 3.1 (2005), pp. 19–23.

[49] K. J. Cantrell, D. I. Kaplan, and T. W. Wietsma. "Zero-valent iron for the in situ remediation of selected metals in groundwater". In: *J. Hazard. Mater.* 42.2 (1995), pp. 201–212.

[50] Y. Roh et al. "Electro-enhanced remediation of trichloroethene contaminated groundwater using zero-valent iron". In: *J. Environ. Sci. Heal. Part A* 35.7 (2000), pp. 1061–1076.

[51] Y. Roh et al. "Electro-enhanced remediation of radionuclide contaminated groundwater using zero-valent iron". In: *J. Environ. Sci. Heal. Part A* 35.7 (2000), pp. 1043–1059.

[52] R. D Ludwig et al. "In situ chemical reduction of Cr(Vl) in groundwater using a combination of ferrous sulfate and sodium dithionite: a field investigation." In: *Environ. Sci. Technol.* 41.15 (2007), pp. 5299–5305.

[53] D. Fan et al. "Reductive sequestration of pertechnetate ($^{99}TcO_4^-$) by nano zerovalent iron (nZVI) transformed by abiotic sulfide". In: *Environ. Sci. Technol.* 47.10 (2013), pp. 5302–5310.

[54] R. A. Crane and T. B. Scott. "Nanoscale zero-valent iron: Future prospects for an emerging water treatment technology". In: *J. Hazard. Mater.* 211-212 (2012), pp. 112–125.

[55] S. R. A. J. Kanel. “Arsenic (V) Removal from Groundwater Using Nano Scale Zero-Valent Iron as a Colloidal Reactive Barrier Material”. In: *Environ. Sci. Technol.* V (2006), pp. 2045–2050.

[56] J. T Nurmi et al. “Characterization and Properties of Metallic Iron Nanoparticles: Spectroscopy, Electrochemistry, and Kinetics”. In: *Environ. Sci. Technol.* 39.5 (2005), pp. 1221–1230.

[57] I. Kielemoes, P. De Boever, and W. Verstraete. “Influence of denitrification on the corrosion of iron and stainless steel powder”. In: *Environ. Sci. Technol.* 34.4 (2000), pp. 663–671.

[58] M. R. Al-Agha et al. “Complex cementation texture and authigenic mineral assemblages in Recen concretion from the Lincolshire Wash (east cost, UK) driven by Fe(0) Fe (II) Oxidation”. In: *J. Geol. Soceity, London* 152.0 (1995), pp. 157–171.

[59] J. Farrell et al. “Investigation of the long-term performance of zero-valent iron for reductive dechlorination of trichloroethylene”. In: *Environ. Sci. Technol.* 34.3 (2000), pp. 514–521.

[60] K. Ritter, M. S. Odziemkowski, and R. W. Gillham. “An in situ study of the role of surface films on granular iron in the permeable iron wall technology”. In: *J. Contam. Hydrol.* 55.1-2 (2002), pp. 87–111.

[61] C. Su and R. W. Puls. “Significance of iron (II,III) hydroxycarbonate green rust in arsenic remediation using zerovalent iron in laboratory column tests”. In: *Environ. Sci. Technol.* 38.19 (2004), pp. 5224–5231.

[62] M. Abdelmoula et al. “Conversion Electron Mössbauer Spectroscopy and X-ray Diffraction Studies of the Formation of Carbonate-containing Green Rust one by Corrosion of Metallic Iron in $NaHCO_3$ and ($NaHCO_3$+ NaCl) solutions”. In: *Corros. Sci.* 38.4 (1996), pp. 623–633.

[63] S. C. B. Myneni, T. K. Tokunaga, and Jr G. E. Brown. “Abiotic Selenium Redox Transformations in the Presence of Fe (II , III) Oxides”. In: *Science (80-.).* 5340 (2008), pp. 1106–1109.

[64] A. D. Henderson and A. H. Demond. “Long-term performance of zero-valent iron permeable reactive barriers: a critical review”. In: *Environ. Eng. Sci.* 24.4 (2007), pp. 401–423.

[65] B. Gu et al. “Biogeochemical Dynamics in Zero-Valent Iron Columns: Implications for Permeable Reactive Barriers”. In: *Environ. Sci. Technol.* 33.13 (1999), pp. 2170–2177.

[66] L. J. Weathers, G. F. Parkin, and P. J. Alvarez. “Utilization of cathodic hydrogen as electron donor for chloroform cometabolism by a mixed, methanogenic culture”. In: *Environ. Sci. Technol.* 31.3 (1997), pp. 880–885.

[67] E. J. Weber. “Iron-Mediated Reductive Transformations: Investigation of Reaction Mechanism”. In: *Environ. Sci. Technol.* 30.2 (1996), pp. 716–719.

[68] M. Scherer et al. “Chemistry and Microbiology of Permeable Reactive Barriers for In Situ Groundwater Clean up”. In: *Crit. Rev. Microbiol.* 26.4 (2000), pp. 221–264.

[69] R. M. Powell et al. “Permeable Reactive Barrier”. In: *EPA/600/R-98/125* (1998).

[70] R. Thiruvenkatachari, S. Vigneswaran, and R. Naidu. “Permeable reactive barrier for groundwater remediation”. In: *J. Ind. Eng. Chem.* 14.2 (2008), pp. 145–156.

[71] R. A. Crane et al. “Magnetite and zero-valent iron nanoparticles for the remediation of uranium contaminated environmental water”. In: *Water Res.* 45.9 (2011), pp. 2931–2942.

[72] R. J. Drout et al. “Efficient Capture of Perrhenate and Pertechnetate by a Mesoporous Zr Metal-Organic Framework and Examination of Anion Binding Motifs”. In: *Chem. Mater.* 30.4 (2018), pp. 1277–1284.

[73] B. A. Lenell and Y. Arai. “Perrhenate sorption kinetics in zerovalent iron in high pH and nitrate media”. In: *J. Hazard. Mater.* 321 (2017), pp. 335–343.

[74] H. F. Liu, T. W. Qian, and D. Y. Zhao. “Reductive immobilization of perrhenate in soil and groundwater using starch-stabilized ZVI nanoparticles”. In: *Chinese Sci. Bull.* 58.2 (2013), pp. 275–281.

[75] K. Schwochau. “The Present Status of Technetium Chemistry”. In: *Radiochim. Acta* 2.32 (1983), pp. 139–152.

[76] E. Kim and J. Boulègue. “Chemistry of rhenium as an analogue of technetium: Experimental studies of the dissolution of rhenium oxides in aqueous solutions”. In: *Radiochim. Acta* 216.91 (2003), pp. 211–216.

[77] E. Méndez et al. “Electrochemical behavior of aqueous acid perrhenate-containing solutions on noble metals: Critical review and new experimental evidence”. In: *J. Colloid Interface Sci.* 263.1 (2003), pp. 119–132.

[78] J. O. Zerbino et al. “Electrochemical and optical study of rhenium layers formed on gold electrodes”. In: *J. Electroanal. Chem.* 521.1-2 (2002), pp. 168–174.

[79] S. Pons and M. Fleischmann. “The Behavior of Microelectrodes”. In: *Anal. Chem.* 59.24 (1987), pp. 1391–1399.

[80] M. I. Montenegro, M. A. Queiros, and J. L. Daschbach. *Microelectrodes: theory and applications*. 1st edition. Amsterdam, Netherlands: Springer, 1991, p. 5.

[81] C. Lefrou and R. Cornut. “Analytical expressions for quantitative scanning electrochemical microscopy (SECM)”. In: *ChemPhysChem* 11.3 (2010), pp. 547–556.

[82] C. G. Zoski. *Handbook of electrochemistry*. 1st edition. Amsterdam, The Netherlands: Elsevier Ltd, 2007, pp. 10–20.

[83] S. E. Pust, W. Maier, and G. Wittstock. “Investigation of localized catalytic and electrocatalytic processes and corrosion reactions with scanning electrochemical microscopy (SECM)”. In: *Zeitschrift fur Phys. Chemie* 222.10 (2008), pp. 1463–1517.

[84] D. P. Burt et al. “Scanning electrochemical microscopy as a probe Ag^+ binding kinetics at Langmuir phospholipid monolayers”. In: *Phys. Chem. Chem. Phys.* 7.15 (2005), pp. 2955–2964.

[85] P. R. Unwin and J. Zhang. “Scanning electrochemical microscopy (SECM) feedback approach for measuring lateral proton diffusion in langmuir monolayers: theory and application”. In: *Phys. Chem. Chem. Phys.* 4 (2002), pp. 3814–3819.

[86] J. Zhang and P. R. Unwin. “Effect of Fatty Alcohol Monolayers on the Rate of Bromine Transfer across the Water/Air Interface: Assessment of Candidate Models Using Scanning Electrochemical Microscopy”. In: *Langmuir* 18.4 (2002), pp. 1218–1224.

[87] J. Zhang and P. R. Unwin. “Scanning electrochemical microscopy (SECM) feedback approach for measuring lateral proton diffusion in langmuir monolayers: theory and application”. In: *Phys. Chem. Chem. Phys.* 4.15 (2002), pp. 3814–3819.

[88] C. J. Slevin et al. “A new approach for measuring the effect of a monolayer on molecular transfer across an air/water interface using scanning electrochemical microscopy”. In: *Langmuir* 14.19 (1998), pp. 5331–5334.

[89] L. Niu et al. “Application of scanning electrochemical microscope in the study of corrosion of metals”. In: *J. Mater. Sci.* 44.17 (2009), pp. 4511–4521.

[90] A. C. Bastos et al. “Imaging concentration profiles of redox-active species in open-circuit corrosion processes with the scanning electrochemical microscope”. In: *Electrochem. commun.* 6.11 (2004), pp. 1212–1215.

[91] J. Izquierdo et al. “Spatially resolved measurement of electrochemical activity and pH distributions in corrosion processes by scanning electrochemical microscopy using antimony microelectrode tips”. In: *Electrochim. Acta* 56.24 (2011), pp. 8846–8850.

[92] N. Perez. *Electrochemistry and corrosion science*. Ed. by Springer international. 2nd edition. Switzerland, 2004, pp. 115–117.

[93] E. Mccafferty. “Validation of corrosion rates measured by the Tafel extrapolation method”. In: *Corros. Sci.* 47 (2005), pp. 3202–3215.

[94] A. Hickling and D. J.G. Ives. “The electrochemical behaviour of iron oxides in dilute sulphuric acid and the interpretation of the flade potential of iron”. In: *Electrochim. Acta* 20.1 (1975), pp. 63–69.

[95] P. N. Bartlett et al. “The preparation and characterisation of H 1-e palladium films with a regular hexagonal nanostructure formed by electrochemical deposition from lyotropic liquid crystalline phases”. In: *Phys. Chem. Chem. Phys.* 4.15 (2002), pp. 3835–3842.

[96] P. N. Bartlett. “Electrodeposition of Nanostructured Films Using Self-Organizing Templates”. In: *Electrochem. Soc. Interface.* 13.4 (2004), pp. 28–33.

[97] M. Serrapede et al. “Nanostructured Pd Hydride Microelectrodes: In Situ Monitoring of pH Variations in a Porous Medium”. In: *Anal. Chem.* 86.12 (2014), pp. 5758–5765.

[98] N. A. Al Abass, G. Denuault, and D. Pletcher. “The unexpected activity of Pd nanoparticles prepared using a non-ionic surfactant template”. In: *Phys. Chem. Chem. Phys.* 16.10 (2014), pp. 4892–4899.

[99] D. J. Mitchell et al. "Phase behaviour of polyoxyethylene surfactants with water. Mesophase structures and partial miscibility (cloud points)". In: *J. Chem. Soc. Faraday Trans. 1 Phys. Chem. Condens. Phases* 79.4 (1983), pp. 975–1000.

[100] M. Sosna. "Oxygen reduction at microelectrodes: Applications to the Dissolved Oxygen Sensor for in situ Oceanographic Measurements". PhD thesis. University of Southampton, 2006.

[101] G. Denuault, M. V. Mirkin, and A. J. Bard. "Direct determination of diffusion coefficients by chronoamperometry at microdisk electrodes". In: *J. Electroanal. Chem.* 308 (1991), pp. 27–38.

[102] M. E. Abdelsalam, G. Denuault, and S. Daniele. "Calibrationless determination of cadmium, lead and copper in rain samples by stripping voltammetry at mercury microelectrodes: Effect of natural convection on the deposition step". In: *Anal. Chim. Acta* 452.1 (2002), pp. 65–75.

[103] Halcrow Group. *Ravenglass Estuary Complex Sefton Council*. 2013.

[104] A. Economou. "Bismuth-film electrodes: recent developments and potentialities for electroanalysis". In: *TRAC Trends Anal. Chem.* 24.4 (2005), pp. 334–340.

[105] H. Sato, M. Yui, and H. Yoshikawa. "Ionic Diffusion Coefficients of Cs^+, $Pb_2{}^+$, Sm^{3+}, $Ni_2{}^+$, $SeO_4{}^{2-}$ and $TcO_4{}^-$ in Free Water Determined from Conductivity Measurements". In: *J. Nucl. Sci. Technol.* 33.12 (1996), pp. 950–955.

[106] D. Harris. *Quantitative Chemical Analysis*. Ed. by W.H. and company Freeman. 7th edition. New York, 2007, pp. 84–87.

[107] P. Warwick, I. W. Croudace, and A. B. Cundy. *Assessment of sorbent materials for the in-situ remediation of 99Tc contaminated groundwater*. Tech. rep. 2017, pp. 1–29.

[108] A. J. Bard, M. Stratmann, and G. S. Frankel. *Encyclopedia of electrochemistry. Vol 4. Corrosion and Oxide Films*. WILEY-VCH Verlag, 2003, p. 755.

[109] M. E. Elsayed Abdelsalam et al. "Detection of Hydroxide Ions in Aqueous Solutions by Steady-State Voltammetry". In: *Electroanalysis* 13.4 (2001), pp. 289–294.

[110] S. Daniele et al. "Steady-State Voltammetry for Hydroxide Ion Oxidation in Aqueous Solutions in the Absence of and with Varying Concentrations of Supporting Electrolyte". In: *Anal. Chem.* 71.4 (1999), pp. 811–818.

[111] S. Daniele et al. “Steady-state voltammetry of hydroxide ion oxidation in aqueous solutions containing ammonia”. In: *Anal. Chem.* 74.14 (2002), pp. 3290–3296.

[112] K. P. Jochum et al. “GeoReM: A New Geochemical Database for Reference Materials and Isotopic Standards”. In: *Geostand. Geoanalytical Res.* 29.3 (2005), pp. 333–338.

[113] I. Prencipe et al. “Energy dispersive x-ray spectroscopy for nanostructured thin film density evaluation”. In: *Technol. Adv. Mater* 16.025007 (2015), pp. 1–9.